Evolution of Negative Streamers in Nitrogen: a Numerical Investigation on Adaptive Grids

Carolynne Montijn

Evolution of Negative Streamers in Nitrogen: a Numerical Investigation on Adaptive Grids

PROEFSCHRIFT

ter verkrijging van de graad van doctor
aan de Technische Universiteit Eindhoven,
op gezag van de Rector Magnificus,
prof.dr.ir. C.J. van Duijn,
voor een commissie aangewezen door
het College voor Promoties
in het openbaar te verdedigen
op dinsdag 20 december 2005 om 16.00 uur

door

Carolynne-Sireeh Montijn

geboren te Fréjus, Frankrijk

Typeset in LaTeX 2_ε. Figures made with Matlab® and Xfig.
Printed and bounded by Ponsen & Looijen bv., Wageningen, The Netherlands.
Cover design by Jan Montyn: Wave of Streamers, color etching (2005).

CIP-Data LIBRARY TECHNISCHE NATUURKUNDE EINDHOVEN

Montijn, Carolynne-Sireeh

Evolution of negative streamers in nitrogen: a numerical investigation on adaptive grids / by Carolynne-Sireeh Montijn.– Eindhoven: Technische Natuurkunde Eindhoven, 2005. – Proefschrift.
ISBN 90-386-2371-2
NUR 928
Trefwoorden: numerieke plasmafysica / numerieke simulatie / gasontladingen / nietlineaire dynamische systemen / plasma-instabiliteiten
Subject headings: plasma flow/ computational physics / discharges electric / electron avalanches / nonlinear dynamical systems / plasma instability

Dit proefschrift is goedgekeurd door de promotor:

prof.dr. U.M. Ebert

Copromotor:
dr. W.H. Hundsdorfer

Het onderzoek dat tot dit proefschrift heeft geleid werd mede mogelijk gemaakt door het Nederlandse Organisatie voor Wetenschappelijk Onderzoek (NWO) in het kader van het FOM-EW-onderzoeksprogramma Computational Science, en door het Centrum voor Wiskunde en Informatica (CWI).

Nederlandse Organisatie voor Wetenschappelijk Onderzoek

Voor Jan en Hien,
en voor Dico

CONTENTS

1

INTRODUCTION

1.1 What are streamers?

Stars, lightning, St. Elmo's fire, neon tubes, spark plugs, flat plasma displays panels– just a grip in the wide variety of natural phenomena and industrial applications in which plasmas are encountered. A plasma is a medium in which a number of neutral molecules has been ionized, creating a sufficient number of free charge carriers to affect the electromagnetic properties of the gas. The degree of ionization can vary from a complete separation of all electrons from their atoms in a fully ionized gas to very low values for partially ionized gasses where only every millionth molecule has freed an electron. Plasmas constitute the major part of the visible universe, not only in the form of stars, but all visible interstellar matter actually is in the plasma state.

Depending on the degree of equilibration of the plasma constituents, i.e. the neutral atoms or molecules, the excited states, the electrons, the ions, one speaks of thermal or non-thermal plasmas. A thermal – or high-temperature – plasma is close to thermal equilibrium, and can reach a temperature up to a billion Kelvin. The sun and other stars are typical examples of high-temperature plasmas, which are heated by nuclear fusion. Because of the enormous amount of energy released by nuclear fusion, and its relative safety compared to fission, a lot of effort has been put in extracting energy from fusion reactions. The most recent advance in this field of research is the announcement of the construction of the fusion reactor – or tokamak – ITER in Cadarache (France). Other examples of thermal plasmas, like arc discharges and thermal plasma torches, are treated by Kogelschatz [42].

Non-thermal – or low-temperature – plasmas on the other hand are generated by applying a strong electric or electromagnetic field on the gas. The energy is then transferred to the electrons rather than the gas, which stays at ambient temperature, whereas the electrons on the contrary can gain more and more energy, so that the plasma is not in thermal equilibrium. These non-equilibrium plasma discharges appear in various forms depending on the spatio-temporal characteristics of the electric field and on the pressure of the medium.

Glow discharges are typical examples of stationary low-temperature discharges, found in e.g. neon lights or plasma screen televisions. Low-temperature plasmas are widely used in industry, e.g. in the processing of semiconductors, flat panel displays, and gas cleaning. For a detailed review of the industrial applications of non-thermal plasmas we refer to Chen [21] and Bogaerts *et al.* [16]. U. Kogelschatz, in his von Engel Lecture at the XXXV ICPIG in Nagoya, 2001 [41], and in a more recent article [42] presents an overview of the most recent scientific advances in both thermal and non-thermal plasma physics.

Streamers are growing filaments of non-equilibrium, moderately or weakly ionized, non-stationary plasma, whose dynamics are controlled by highly localized and nonlinear space charge regions [80, 57]. A streamer can arise from a seed electron that moves in a gas under influence of an electric field. On its path, the electron collides with the neutral gas molecules (or atoms) and, if the electric field is strong enough, it eventually gains enough energy to ionize a molecule, thereby releasing a new electron and a positive ion. The two electrons now gain energy from the field, both colliding with and possibly ionizing other molecules, thereby creating an *electron avalanche*. The mobility of the electrons results in *space charge* regions, i.e. regions that are electrically non-neutral. Eventually, the amount of space charge can become strong enough to alter the background electric field, which in turn influences both the electron velocity and the ionization rate of the gas molecules. A *streamer* has then emerged, whose dynamics are controlled by nonlinear mechanisms. Streamers are typically the initial stage of sparks and arc discharges.

Industrial applications and natural occurrences

Because of the high energy of the electrons in streamers, they can collide inelastically with heavy particles in the gas. Such inelastic collisions result in e.g. ionization, excitation and dissociation of the heavy particles. Radicals able to crack larger molecules during collision can thereby be formed, making streamers very useful in the treatment of contaminated media. In particular, extensive scientific research has been carried out in the removal of polluting nitric oxide NO_x and sulfur dioxide SO_2 molecules from flue gasses [22, 25, 87, 73, 54, 90, 110], and the treatment of polluted water [31, 84, 52, 2, 1]. Streamers are also widely used in the microelectronics industry, in particular for the plasma enhanced chemical vapor deposition [51, 32, 7], and as sources of excimer radiation for material processing [61, 72, 41]. Recently, new advances have been made in airplane engineering by controlling the air flow around wings with discharges [14].

Streamers can also be observed in nature. They play a role in creating the paths of sparks and lightning [62, 10], and new techniques showed the existence of so-called sprites [33, 86, 60], and blue jets [108, 107, 77] in the higher regions of the atmosphere.

Streamer polarity: positive vs. negative streamers

Considering the evolution of streamers between two electrodes, two types can be distinguished: *cathode directed* or *positive* streamers, and *anode directed* or *negative* streamers. In positive streamers, positive space charge is flowing in the direction of the electric field, towards the cathode. In negative streamers, it is negative space charge that propagates in the electron drift direction, i.e. in the direction opposite to the electric field, towards the anode.

Positive streamers emerge relatively easily from a point or rod electrode, whereas negative streamers require a much higher electric field [82]. Experiments on positive streamers are therefore easier to obtain, and consequently the streamers of this polarity gained more scientific attention than negative ones. However, the observations of discharges structures in the atmosphere showed that negative streamer play a very important role in these, and called for a better understanding of negative streamers, from an experimental side as well as from the numerical and analytical side.

1.2 Electron avalanches and streamers: a literature survey

The emergence and propagation of streamers have been under great scientific attention for a long period of time. The basics of a new theory of spark breakdown were developed in the 1930's by Raether [80, 81], and also by Loeb and Meek [57, 58, 63, 55, 56, 64]. Since then, big scientific advances have been made on this subject, and we give a survey on the experimental, analytical and numerical investigations. We will mention work carried out both on positive and negative streamers, and in various gas types, but will mainly focus on negative streamers in nitrogen, which are the subject of this thesis.

1.2.1 Laboratory experiments

As mentioned above, Raether, Meek and Loeb developed their theory of emergence of a streamer from an electron avalanche. Raether carried out experiments in a cloud chamber, in which he made photographs of electron avalanches in air [80]. In this experimental setup a voltage pulse, lasting about a few nanoseconds, is applied to a gas gap. The region that is ionized within this time acts as a nucleation seed for water droplets. These droplets are then visualized with a camera, and Fig. 1.1, taken from the original paper by Raether, shows a picture obtained with this experimental method. These experiments lead Raether to develop his theory of streamers emerging from electron avalanches, and his measurements made him postulate that, at pressures close to atmospheric, the number of electrons in an avalanche should reach a critical value of around 10^8. Raether also developed the typical schematic picture of an electron avalanche evolving into a streamer, as used up to today (see Fig. 1.2). This figure shows a transient state, later a thin space charge layer develops. This was shown by the

FIGURE 1.1: Picture of an electron avalanche in a plane parallel gap filled with N_2 at 150 Torr ($\approx$ 0.2 bar). The picture originates from [80].

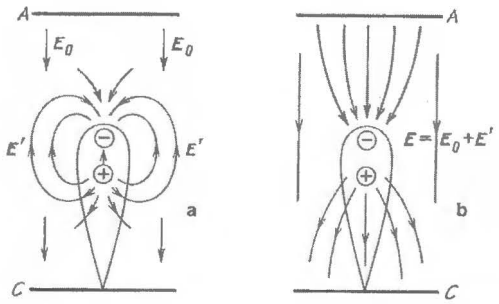

FIGURE 1.2: Schematic picture of an electron avalanche between plane parallel electrodes, as thought by Raether. The anode is denoted by *A*, the cathode by *C*. The left plot (a) shows the external field $\mathbf{E}_0$ and the field of the space charges $\mathbf{E}'$ separately. The right picture (b) shows the the total electric field $\mathbf{E} = \mathbf{E}_0 + \mathbf{E}'$. The pictures are taken from the textbook of Raizer [82], but originate from [80].

first two-dimensional simulations [24]. Loeb and Meek [63, 57], independently from Raether's work, analytically derived a similar criterion for the transition from avalanche to streamer.

Since then, large efforts have been made in obtaining time resolved measurements of electron avalanches and streamers. One method uses streak pictures. Streak photography gives pictures of the evolution along one spatial dimension as a function of time (see Fig. 1.3). However, since light emitted by streamers comes from the excited states, time resolved photographs only show the regions with high collision rates, which are typically situated at the tip of the streamer [104, 105, 20].

Recently, the development of ICCD (Intensified Charge Coupled Device)

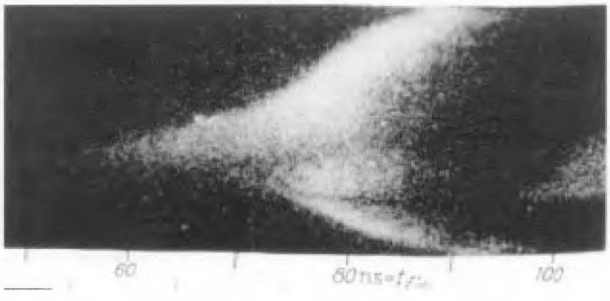

FIGURE 1.3: Streak photograph of a cathode (bottom) and anode (top) directed streamer in a 30 mm gap filled with N_2 at 378 Torr ($\approx$0.5 bar). The picture comes from [105].

cameras enabled researchers to obtain much higher temporal resolution, and at the same time a two-dimensional projection of the discharge, rather than the one-dimensional picture obtained with streak photography [96, 97, 112, 18]. These measurements enabled one to resolve much of the short time scale structure of streamers (see Fig. 1.4). On these figures, the light emitted from the growing tips of the streamers can be seen. From Fig. 1.4 we clearly see the filamentary structure of, in this case, positive streamers. They also show that these streamers branch, both in uniform and in a non-uniform field. The upper photographs of Fig. 1.4 show the time integrated picture of the streamer, while from the lower left picture, taken with the shortest possible shutter time, it is clear that it is at least on these short time scales that one should resolve the streamer propagation.

Most of the experimental work has been carried out on positive streamers in air [3, 97, 18, 19]. We wish to draw the reader's attention to the work done by Yi and Williams [112], who investigated the propagation of both anode and cathode-directed streamers, in pure N_2 and N_2/O_2 mixtures. Fig. 1.5 shows a photography that illustrates the streamer propagation under these conditions. These photographs show that both positive and negative streamers branch in N_2 and in N_2/O_2 mixtures. Moreover, Yi and Williams [112] measured that the propagation velocity of negative streamers is up to four times larger than that of positive streamers. One major limitation of experimental studies on streamers using photography is that they can only record the light emission which comes from the emission of excited states. At atmospheric pressure, the emission time is about 1 ns, and up to 10 ns at even lower pressures [95]. It is therefore not possible to obtain temporal resolutions below this threshold.

Other diagnostic tools comprise emission spectroscopy, absorption spectroscopy, and laser induced fluorescence [98]. These are typically used to obtain precise measurements on excited states and to identify the species present in a discharge. These methods, however, go well beyond the scope of this study and we restrain ourselves to only mention them.

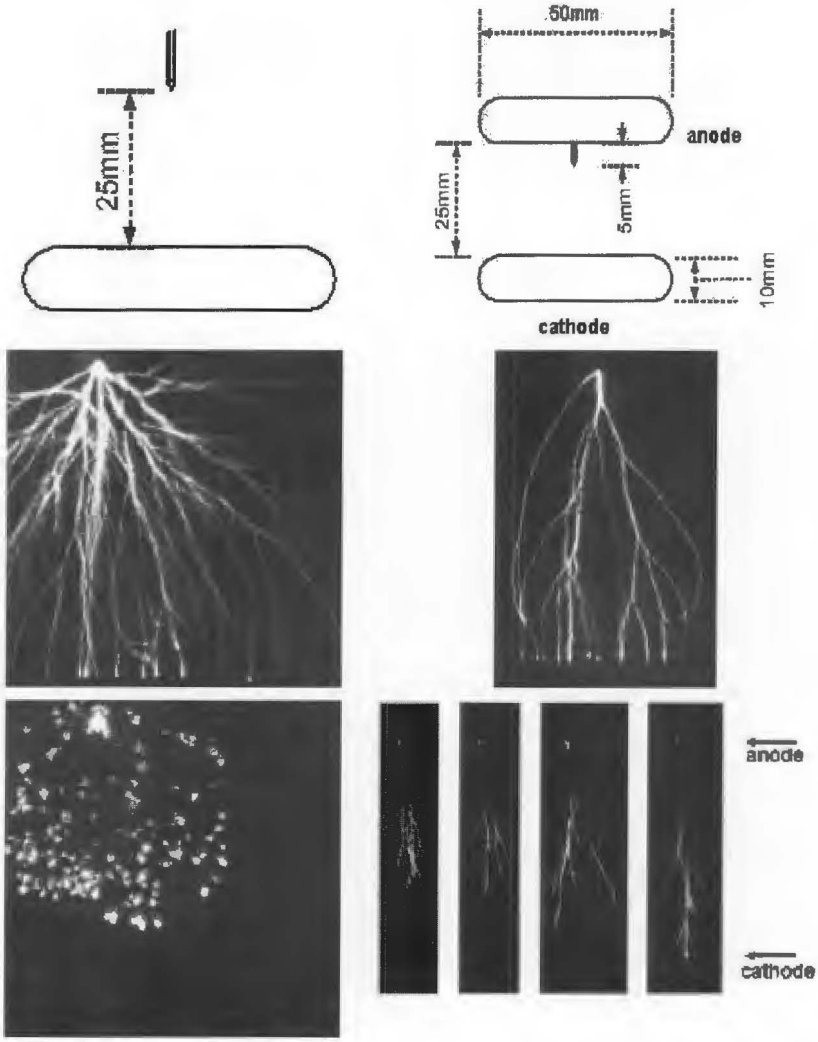

FIGURE 1.4: ICCD photographs of positive streamers in air. The electrode configuration is shown in the upper two figures; the left panel corresponds to a point to plane electrode configuration, resulting in in an inhomogeneous electric field, the right panel corresponds to a plane parallel electrode configuration, in which the field is uniform. The shutter time in the upper two photographs is of 5 μs, that in the lower left plot is of 0.8 ns, that in the lower right one of 50 ns. These photographs originate from [99] and [100].

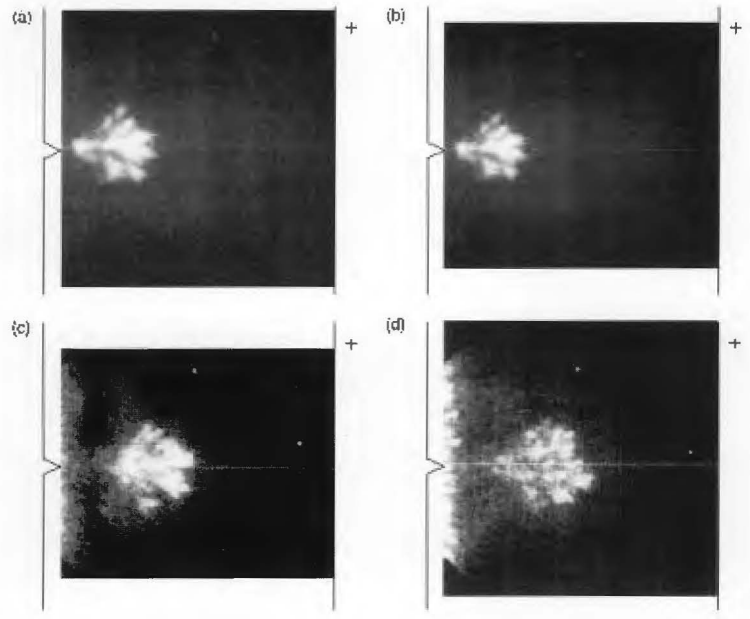

FIGURE 1.5: Photographs showing streamers in pure N_2 ((a) and (b)) and mixtures containing 15% (c) and 1% (d) O_2. Streamers in (a) and (c) are cathode directed, those in (b) and (d) anode directed. The gap is a point to plane gap, with an inter-electrode distance of 13 cm. The voltage applied to the anode is of approximately 123 kV, the pressure is of 1 bar. These photographs are taken from [112].

1.2.2 Discharges in the atmosphere

Lightning is a typical example of discharges encountered in the atmosphere. The initiation of the lightning channel in the thunderclouds is under great scientific attention nowadays, but falls beyond the scope of this study. The lightning channel is formed by the so-called leader whose path is created by a bunch of streamers. In contrast to streamers, the leader is hot which is required to maintain ionization and electric conductivity over a length of several kilometers. When the leader reaches the ground, a short circuit and further heating of the channel occurs. The high temperature of the lightning channel results in a fast thermodynamic expansion of the air, which in turn gives rise to a shock-front. The noise one hears during a typical thunderstorm emanates from this shock-front.

Streamers also play an important role in two types of discharges recently observed in the atmosphere, *sprites* and *blue jets*.

Sprites have been observed between about 40 and 90 km height in the atmosphere. Above 90 km, the dielectric relaxation of the ionosphere prevents streamer like phenomena to occur. Sprites can propagate from the ionosphere

FIGURE 1.6: Photograph of a sprite. The altitude is indicated at the right. Courtesy to H.C. Stenbaek-Nielsen, Department of Geophysics, University of Fairbanks, Alaska.

downwards or from some lower base upwards, or they can emerge at some intermediate height and propagate upwards and downwards like the event shown in Fig. 1.6. A variety of sprite forms have been reported [34, 92, 37]. The propagation direction and approximate velocity – their speed can exceed 10^7 m s^{-1} [91] –, is know since researchers succeeded in taking movies [76].

Blue jets on the other hand propagate upwards from the top of thunderclouds, at speeds that are typically two orders of magnitude lower than those of sprites [76], and they have a characteristic conical shape and appear in a blueish color [108, 107]. Blue jets are probably a sort of leaders, so streamers again play a role in their propagation as well.

Fig. 1.7 shows a photograph of a so-called gigantic jet. The lower part of the structure, up to an altitude of approximately 40 km, is similar to a blue jet, and the upper part of the structure is sprite-like. Blue jets and gigantic jets are very rare phenomena – only a few of them have been actually observed –, whereas sprites on the contrary, occur very often, and are likely to play an important role in the atmospheric chemistry.

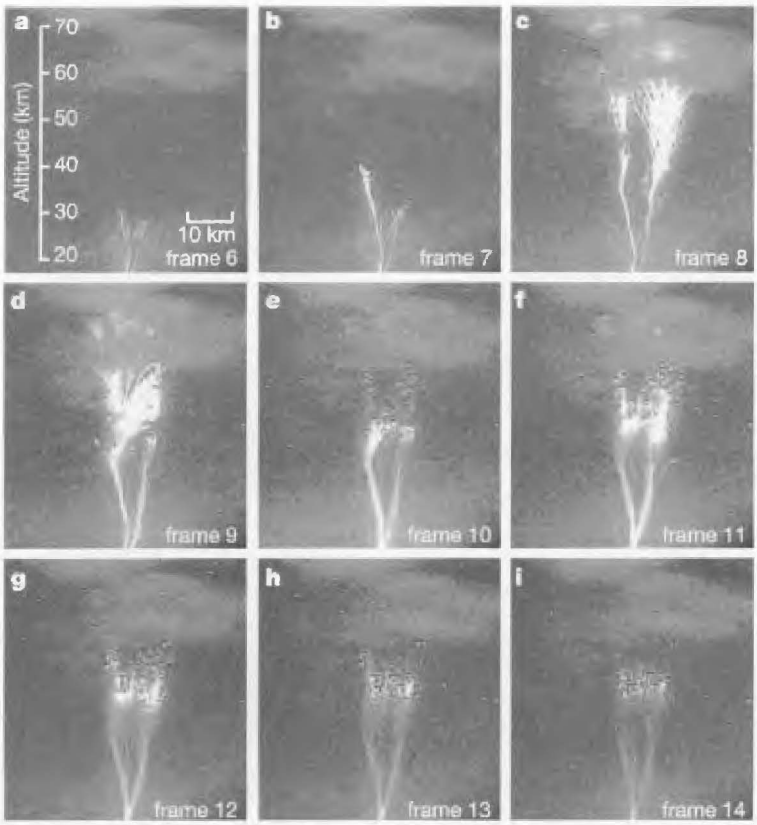

FIGURE 1.7: Evolution of a blue jet. The picture has been taken from [77].

The reason to interpret the gigantic sprite structures as streamers will be explained later in this thesis, namely in the section on dimensional analysis. There, it will become clear that the spatial dimensions of streamers scale with inverse gas density, while velocities are independent of gas density. All theoretical and experimental studies on streamers will therefore be applicable to sprites as well, at least in the simplest approximation.

1.2.3 Numerical streamer simulations

One major disadvantage of experiments is that it can be hard to determine the role of the multiple processes that are typically involved. It also often proves very difficult to measure certain features of the observed phenomenon. Moreover, changing an experimental set up for some scientific purpose often proves to be time and money consuming, or even impossible. Here the great advantage of numerical simulations becomes evident: it provides a tool to investigate the effect of any physical mechanism, simply by in- or excluding it from the numer-

ical model, and one can easily extract certain features, e.g. the evolution of the space charge layer, from the results. Of course, one should take care with the interpretation of numerical results as well, since both modeling and numerical implementation are prone to errors. However, once a model and its implementation in a computer have been tested successfully, numerical simulations make it possible to carry out a large variety of experiments, without having to make difficult and often expensive changes to the experimental setup. In fact, one may consider computer simulations as a compromise between experiments and analysis, making it possible to study much more complex systems than with analytical tools, without reaching the sometimes confusing complexity of experiments.

Now the difficulty for the simulations of streamers resides in the multiple spatial scales of the phenomenon:

1. **The whole, mainly non-ionized, background medium on which the electric field is applied**: in experimental laboratory investigations the background medium has a typical dimension in the order of at least centimeters in 3D space. Obviously it concerns the whole atmosphere in case of discharges like sprites or blue jets.

2. **The actual streamer, which is a narrow, quasi-neutral, ionized channel**: it can be as long as the whole system, but its width is typically in the order of hundreds of micrometers to millimeters in the laboratory experiments, and can reach up to hundreds of meters in the high atmosphere .

3. **The space charge region around the head of the streamer**: the self enhanced electric field of this region sets the dynamics of the streamer, and its dimensions are set by the ionization length, typically in the order of micrometers at atmospheric pressure.

Models for gas discharges: kinetic vs. fluid models

We mentioned previously that a streamer can emerge from an electron avalanche. Traditionally, one has used two different approaches to model the dynamics of the charged particles. The first is the *Monte Carlo* method, which aims to follow the individual particles and to capture their stochastic behavior [15, 50, 49, 106]. This method computes the trajectories of the individual particles using Newton's laws, and uses random numbers to determine the outcome of collisions between the particles. Such a model is very useful to describe the kinetics of the particles, but obviously, when the ionization degree is high, it becomes impossible to follow all the particles. The *Particle in Cell* method has been developed to face this difficulty, by clustering a representative number of particles into one single *superparticle*. The dynamics of the superparticles, including their interaction with the electric field, are then solved with the Monte Carlo method. Such models have been widely used for the modeling of a large variety of gas discharges [13, 71, 111], and for streamers [79, 88, 89] in particular.

The main disadvantage of these so called kinetic models is that they are computationally intensive, both from the point of view of time and memory. The use of a fluid model, in which the gas discharge species are described by means of averaged hydrodynamic quantities like density, velocity and momentum, permits to counteract these difficulties. Such models include particle drift and diffusion, source and sink terms for the charged particles, the Poisson equation that describes the interaction between the space charges and the electric field.

The main source for charged particles is the electron impact ionization, occurring when sufficiently energetic electrons collide with neutral atoms or molecules, thereby ionizing them. In the early twentieth century, Townsend gave an empirical formula describing the impact ionization source term as a function of the local electric field [93], which is still widely used nowadays. Other source and sink terms consist of photoionization, ionization by excited states, attachment, recombination, and dissociation [82].

In the following we review the work that has been done in simulating the propagation of both positive and negative streamers, using fluid models.

Positive and negative streamer propagation

In the last decade, substantial advances have been made in the simulations of positive streamers. As mentioned previously, one has to include mechanisms like photoionization or background ionization for such streamers to propagate, since a drift-diffusion model with a local reaction term only permits the propagation of negative streamers. The modeling of photoionization is, still nowadays, rather difficult because of the lack of accurate quantitative data. The first measurements that describe the rate of photoionization in air, nitrogen and oxygen date from 1970, by Penney and Hummert [78]. Later, Zhelenyak *et al.* [114] proposed a model for the photoionization in air, that was successfully matched to the measurements of Penney and Hummert by Kulikovsky [46]. The model proposed by Zhelenyak *et al.* gives the rate of photoionization as an integral formula of the rate of impact ionization, and has been widely used for the computation of positive streamers in air [45, 74, 53]. New developments question the role of photoionization versus that of background ionization in the dynamics of positive streamers [75].

Because they emerge relatively easily from point or wire electrodes, positive streamers have been under much more industrial attention than negative ones. As a consequence, most of the numerical simulations carried out up to now concerned positive streamers in air [6, 70, 45, 74, 75, 53]. These simulations mainly aimed at matching the models with the experimental measurements and applying the models for industrial purposes. The simulations focused on various electrode configurations and relatively low effective electric fields, typically in the order of 5 to 10 kV/cm. The gaps are then so-called *undervolted*, which means that, in the absence of the streamer induced field enhancement, the electric field is too low for a significant number of molecules to be ionized through impact ionization.

Because of the steep density gradients high electric fields give rise to, the simulations of negative streamers in *overvolted* gaps are computationally more demanding than those in undervolted gaps. Simulations on streamers in overvolted gaps have been carried out by Dhali and Williams [24] and Vitello *et al.* [101, 102]. However, their model did not include photoionization, but rather they used the presence of background ionization. The amount of background ionization in [24] was much too high and positive streamers did actually emerge. In [102] realistic values of background ionization were used, but the authors could not draw any conclusions with respect to positive streamers from the simulations in the parameter regime they investigated.

However, positive streamers were not the main focus of the work of Dhali and Williams and Vitello *et al.*, but rather negative streamers. Comparing their results with simulations of positive streamers by other authors show that the positive and negative streamers exhibit features generic to both cases. they are both characterized by a curved and thin space charge layer in the so-called *streamer head*. This layer enhances the field ahead of it, thereby creating a growth region for the streamer. The ionized channel left behind by the streamer head has become more conducting, which results in at least a partial screening of the channel from the exterior background electric field. On the other hand, the mechanism of ionization front propagation differs between positive and negative streamers.

Branching streamers

Earlier simulations of streamers in N_2 [5, 83] show that when the background electric field is high enough, the streamer tends to develop into an unstable state, leading to spontaneous branching. However, this conclusion was based partially on analytical arguments. No numerical tools were available to test convergence on different numerical mesh sizes.

The same branching phenomenon is later also observed in [53], where it is argued that inclusion of photoionization in a continuum approximation would in fact lead to stabilization.

The question on what underlying mechanism makes the streamer branch is under debate up to today. The first mechanism for streamer branching was proposed by Raether [80], who argued that electrons appear ahead of the streamer tip due to stochastic processes like photoionization, resulting in secondary electron avalanches, which would exhibit the form of branching streamers. This mechanism has been reproduced in figures in many textbooks that show a homogeneously charged streamers head preceeded by avalanches. That this mechanism works, has never been demonstrated. Actually, there is a strong reason to believe that a streamer with a homogeneous head charge (as it occurs in early stages of the evolution) never will branch. On the other hand, while a thin space charge layer is necessary, Ebert and co-workers have suggested that stochastic perturbations are not necessary for a streamer to branch [5, 83]. Their mechanism is that of a Laplacian instability, like that occurring in viscous fingering. This mechanism requires a charge layer with decreasing curvature, rather than

stochastic processes. The physical of the branching state of streamers is still a subject of scientific discussion [46, 74, 48, 27, 75], while experiments do show branching streamers, both in plane parallel gaps [112] and in other electrode geometries [99], both of positive and negative polarity and in pure N_2 as in N_2/O_2 mixtures [112]. In the scope of understanding the propagation of discharges in the atmosphere like sprites and blue jets, as well as for industrial application, there is a high need for a better understanding of the destabilizing mechanism.

1.2.4 Analytical investigations

Analysis allows clear statements, is one is lucky to find solutions. Typically, there are chances for limit cases. The first one is the case of the initial avalanche phase, when space charges are negligible and the problem is linear [63, 113, 82, 10, 67]. It will be treated in this thesis. However, once the space charges have grown so large that they affect the electric field, this linearization no longer holds and sophisticated analytical methods have to be applied to understand the dynamics of simplified models.

For planar streamer fronts, the analytical studies have shown some very interesting features, like the *pulled* nature of the ionization front. This pulled front character means that the long-term dynamics of the streamers are set in the *leading edge*, the unstable region ahead of the streamer front, where the particle densities decay exponentially [30, 29]. These analytical studies also showed that the steepness of planar streamer fronts increases with the electric field ahead of it. This will give raise to some major numerical difficulties, especially in high electric fields, since it is well known that fronts that approach the limit of shock fronts demand special numerical treatment to be captured adequately. Moreover, it has been shown using stability analysis that such planar fronts are unstable against transversal perturbations [5].

More recently, analytical efforts have been put in understanding curved ionization fronts. The streamer front was then approximated as a moving boundary, to which so-called conformal mapping techniques were applied [66, 65]. It was shown that, in the case of infinitesimally thin, curved, ionization fronts, branching indeed occurs but eventually cusps, i.e. singularities, would appear in the solution [66]. It was then necessary to look for some regularization mechanism to avoid the creation of cusps. Recent efforts [65] have shown some very encouraging results, in particular that fronts whose width are in the same order as their radius of curvature, are linearly stable, small perturbations on these fronts do not grow but are advected away.

1.3 Motivation and scope of this study

We have shown in Sect. 1.1 that a large variety of applications of electric discharges exists, both in industry and in geophysics. However, because of the complexity of the mechanisms involved in streamer dynamics, they still are not fully understood. Recent advances in imaging techniques enable researchers

to obtain high resolution measurements of streamers. However, as mentioned above, experiments are limited with respect to the temporal resolution, and not every quantity can be measured that one would be interested in. Moreover, the complexity of the phenomenon makes analytical studies rather difficult, so they can only be carried out on idealized situations. Numerical simulations provide a tool to carry out numerical experiments, which can be used to get a better understanding of the mechanisms involved in the emergence and propagation of streamers.

In this thesis, we focus on the propagation of negative streamers as described by the so called *minimal streamer model*. This model includes the basic physical features necessary for negative streamers to propagate, i.e. electron drift in the local electric field, diffusion and impact ionization. It was used in previous work on this kind of configurations [24, 102, 5, 83]. It gives the generic features of negative streamers in a non-attaching gas, and in particular holds for pure nitrogen, in which photoionization probably plays an insignificant role. Moreover, we will only consider very short time scales, during which sink terms of charged particles like recombination and the dynamics of the heavy ions can be neglected.

As mentioned in the previous section, this simple model already enables the description of physically interesting and experimentally observed behavior like branching, the mechanism of which is still subject of scientific research and discussion. It is therefore very beneficial to start with this minimal model and try to fully understand its implications, before including all kind of other mechanisms.

Throughout this thesis, we consider the streamer propagation in N_2 in a plane-parallel electrode configuration. Few laboratory experiments are able to make negative streamers in such a configuration, since a point-to-plane electrode configuration makes the inception much easier than a plane parallel one. However, this setting can very well be compared with that found in the atmosphere. Moreover, the use of a uniform background electric field will enable us to draw conclusions without needing to take into account effects of electrode geometry, which would make the interpretation of generic features much more difficult.

The simulations on negative streamers reported previously [24, 102, 5, 83], were all carried out on uniform grids. Their incapability to draw conclusions on the nature of the instabilities demanded for a development of a numerical code that could reach very high spatial resolutions within a reasonable computational time and, even more importantly, within the limits of computational memory. Now the simulations of negative streamers represents a great numerical challenge, and we summarize the main difficulties:

1. the multiscale character of the phenomenon, for which one needs to develop an efficient code, where refined grids move with the object;

2. the pulled character of the ionization front, due to which standard grid refinement procedures fail;

3. the density gradients that become steeper due to the growth of the electric

field;

4. the requirement to resolve not only the propagation, but also the instability of the streamer appropriately.

In addition to the question of branching, such a numerical code provides researchers with a very useful tool for the simulations of streamers in high electric fields in general, and opens the possibility of the exploration of a new parameter regime. In particular, the effect of the gap being overvolted or undervolted has not been thoroughly investigated up to today.

One other question arised, regarding the emergence of a streamer from an electron avalanche. This transition from avalanche to streamer is usually determined by Meek's criterion [63, 10], which neglects diffusion, and therefore demands some reconsideration.

1.4 Organization of the thesis

In Chapter 2 our model for negative streamers is derived. A literature survey enables us to identify those mechanisms that are important in the specific case of negative streamers propagating in non-attaching gases like (molecular) nitrogen or argon. For instance, we do not include photoionization, which is probably negligible in negative streamers in nitrogen. We end up with the so-called minimal streamer model, which consists of continuity equations for the charged particles, including diffusion, drift and reaction in the local electric field, coupled to the Poisson equation for the electric field. This model exhibits generic features of streamer propagation like the appearance of a space charge region, and the screening of the streamer body from the externally applied electric field. We then apply a dimensional analysis to the model, and discuss how the characteristic dimensions of the streamer scale with gas density. This finally leads to a dimensionless model for streamer propagation that makes it easy to translate the numerical results to any given gas density or gas type.

The minimal streamer model derived in Chapter 2 has been implemented in a numerical code. The algorithm developed to deal efficiently with the multiscale nature of the phenomenon is described in Chapter 3. It uses an adaptive grid refinement strategy for both the continuity equations and the Poisson equation. The refinement criterion takes into account the need for a high accuracy in the leading edge of the streamer. The code is tested on a planar streamer front, where the leading edge character is more pronounced then in the case when the front is curved. These tests show that the refinement procedure performs very well for the continuity equations, while the electric field can be calculated analytically in one dimension. We then test the code on a genuine, three-dimensional streamer with radial symmetry. The refinement strategy for the Poisson equation is now incorporated, and the results are in very good agreement with those obtained on uniform grids. Moreover, the gain in computational memory and time is substantial.

In Chapter 4 we give a brief overview of the evolution of an ionization seed in both undervolted and overvolted gaps. Three physical stages are identified. The first is the electron avalanche phase, characterized by its linearity. During this phase, space charge builds up, and once it has grown in a sufficient amount, it starts to significantly affect the background electric field, making the whole phenomenon nonlinear. The streamer regime is then entered. It exhibits characteristic features like a thin space charge layer, whose typical dimension is set by the ionization length, and which enhances the field ahead of it while suppressing it on the contrary in the strongly ionized channel. This space charge layer becomes flatter and eventually branches. These stages are encountered in both under- and overvolted gaps, and are the subject of a more detailed investigation in the rest of the thesis.

In Chapter refchapavstr we make an analytical side step to investigate in more detail the transition from avalanche to streamer. We linearize the minimal streamer model, including diffusion, around the background electric field. We use an exact expression for the electron density distribution, and use this expression to find exact analytical formulas for the spatial moments of the ion density. This leads to the derivation of a good approximation for the electric field induced by the charges, which is then used to derive an explicit, diffusion based criterion for the avalanche to streamer transition.

The streamer regime is the subject of Chapter 6. We use the code presented in Chapter 3 to compute the propagation of the discharge during this phase, in both undervolted and overvolted gaps. First, the spatial accuracy requirements are determined in different background electric fields. Then the buildup of the thin and curved space charge layer and the generic features of streamers evolving in an overvolted gap are discussed. The influence of the boundary conditions on the electrode as well as the initial ionization seed is investigated. We then continue with describing the evolution in undervolted gaps, which appears to be qualitatively different from that in strong background fields. Finally we interpret results of the numerical simulations in physical terms and compare them to previous analytical results or phenomenological concepts.

Chapter refchapbranch deals with branching streamers. We investigate how this branching is influenced by the grid size, and how the state of the streamer compares with analytical results on moving boundary problems. In particular, we investigate in how far the streamer approaches the limit of ideal conductivity, and we show that the space charge layer becomes flatter and thinner, thereby approaching the limit of a planar ionization front, which is known to be unstable.

We end with some concluding remarks and suggestions for further research in Chapter 8.

2

A FLUID MODEL FOR STREAMER DYNAMICS

In this chapter we give a sketch of the derivation of the fluid model, used to describe the streamer dynamics, from the Boltzmann equation. The several ionization processes occurring in a discharge are reviewed. Identifying the essential processes that are important for the dynamics of negative streamers in pure gasses, we derive our minimal streamer model. It consists of continuity equations for the particle densities, coupled to the Poisson equation for the electric potential. Hereafter we perform a dimensional analysis in order to identify the characteristic scales of the phenomenon. This dimensional analysis will appear to be very useful regarding the scaling when pressure varies on the one hand, and when the gas changes on the other hand.

2.1 Conservation of charge and momentum

When an electric field $\mathbf{E}$ is applied to a gas, particles with charge q and mass m_q in that gas will be accelerated along the line of force of this electric field. Collisions with neutral particles change the velocity of the electrons in a random way. The total velocity of the electrons is the sum of their random velocity and their drift velocity induced by the external electric force. If the gas is weakly ionized, electron-electron collisions are rare and electron-neutral collisions dominate. These can be either elastic – the direction of motion of the electron is randomly changed by the collision, but the electron loses a negligible amount of kinetic energy–, inelastic – the electron excites a molecule and carries less energy than before the collision –, or ionizing – the collision leads to ionization and the liberation of a second electron.

During their motion, the charged particles obey a continuity equation,

$$\frac{\partial n_q(\mathbf{r},t)}{\partial t} + \nabla \cdot \mathbf{j}_q(\mathbf{r},t) = S(\mathbf{r},t)\,, \tag{2.1.1}$$

where $S(\mathbf{r},t)$ is the source term for the charged particles. It corresponds to the ionization source and sinks in case we consider the densities of charged particles, and is zero if we consider the total charge density, since the total charge can not be created nor can it be annihilated.

The expression for the particle current density $\mathbf{j}_q(\mathbf{r},t)$ is

$$\mathbf{j}_q(\mathbf{r},t) = \mu_q n_q(\mathbf{r},t)\,\mathbf{E}(\mathbf{r},t) - D_q\,\nabla n_q(\mathbf{r},t)\,. \tag{2.1.2}$$

The first term of the left hand side gives the particle drift velocity induced by the local electric field,

$$\mathbf{v}_q^{\text{drift}} = \mu_q \mathbf{E}(\mathbf{r},t)\,. \tag{2.1.3}$$

The second term in (2.1.2) stands for the natural diffusion of the particles due to spatial gradients in their distribution.

Eqs. (2.1.1)-(2.1.2) can be derived through the Boltzmann equation [40, 82]. On a single particle level, the conservation of charge and momentum are described in the single-particle phase space $(\mathbf{r},\mathbf{v},t)$ – where r is the spatial coordinate, v the velocity and t the temporal coordinate – with the kinetic Boltzmann equation, that gives the temporal evolution of the particle density distribution $f_q(\mathbf{r},\mathbf{v},t)$,

$$\frac{df_q}{dt} = \frac{\partial f_q}{\partial t} + \mathbf{v}\cdot\nabla_{\mathbf{r}} f_q + \frac{q\mathbf{E}}{m_q}\cdot\nabla_{\mathbf{v}} f_q = \left(\frac{df_q}{dt}\right)_c\,. \tag{2.1.4}$$

Here the subscripts $\mathbf{r}$ and $\mathbf{v}$ indicate gradients in configuration space and velocity space, respectively, and the right hand side term stands for the sources and sinks of charged particles.

The number density distribution $n_q(\mathbf{r},t)$ in configuration space is defined as the average of the velocity distribution over velocity space,

$$n_q(\mathbf{r},t) = \int_V f_q(\mathbf{r},\mathbf{v},t)\,dV\,. \tag{2.1.5}$$

Likewise, the particle flux $j_q(\mathbf{r},t) = n_q(\mathbf{r},t)\,v_q(\mathbf{r},t)$ in configuration space is obtained by averaging the first moment of the distribution function over velocity space,

$$\mathbf{j}_q(\mathbf{r},t) = n_q(\mathbf{r},t)\,\mathbf{v}_q(\mathbf{r},t) = \int_V \mathbf{v}\,f_q(\mathbf{r},\mathbf{v},t)\,dV\,. \tag{2.1.6}$$

The continuity equation (2.1.1) in the hydrodynamic approximation is found by integrating the Boltzmann equation (2.1.4) over velocity space. To obtain the expression for the current density (2.1.1), the Boltzmann equation is multiplied by $\mathbf{v}$ and integrated over the entire velocity space,

$$\frac{\partial \mathbf{j}_q}{\partial t} + \frac{1}{3}\nabla(n_q(\mathbf{r},t)\langle v^2\rangle) - \frac{q\,n_q(\mathbf{r},t)}{m}\mathbf{E} = \nu_c(\overline{\cos\theta} - 1)\mathbf{j}_q(\mathbf{r},t)\,, \tag{2.1.7}$$

where

$$\langle v^2 \rangle = \frac{\int_V v^2 f_q \, dV}{n_q(\mathbf{r}, t)} \tag{2.1.8}$$

and $\overline{\cos\theta}$ is the mean cosine of the scattering angle.

We can now consider the quasi-stationary approximation for Eq. (2.1.7), which holds as long as the momentum and energy relaxation times of electrons in N_2 at atmospheric pressure are small compared to the time scale on which the macroscopic changes occur. In Fig. 2.1, taken from [102], the electron momentum and energy relaxation times are plotted as a function of the electric field, showing that indeed these times are at least two orders of magnitude smaller than the characteristic discharge development time, which is in the order of nanoseconds, or larger. The curves of Fig. 2.1 have been computed by solving the Boltzmann equation using the code ELENDIF [69]. We introduce the effective collision frequency of the particles ν_q as,

$$\nu_q = \nu_c(1 - \overline{\cos\theta}) \,, \tag{2.1.9}$$

the particle mobility μ_q as,

$$\mu_q = \frac{q}{m\nu_q} \,. \tag{2.1.10}$$

and the diffusion coefficient as,

$$D_q = \frac{m\mu_q\langle v^2 \rangle}{3q} \,. \tag{2.1.11}$$

This finally leaves us with Eq. (2.1.2).

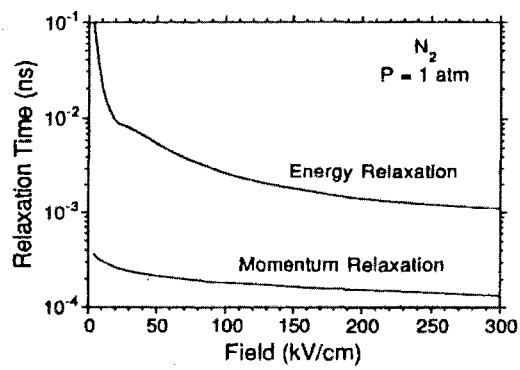

FIGURE 2.1: Energy and momentum relaxation times as a function of the electric field strength, for electrons in N_2 at atmospheric pressure

2.2 Ionization sources and sinks

2.2.1 Ionization by electron impact

The most important source of ionization in the bulk of a weakly ionized gas discharge comes from the collisions between electrons and neutral gas molecules. Such collisions will result in an ionization event of a neutral molecule, provided the kinetic energy of the electrons is larger than the ionization energy. If there are only elastic collisions, the electron will eventually gain enough energy after having traveled a sufficient distance. But if there are also inelastic events, the electric field E needs to be above a certain threshold E_0. This threshold field is dependent on the gas species and the pressure. For a species A the reaction can be written as

$$A + e^- \xrightarrow{|\mathbf{E}|>E_0} A^+ + 2e^- , \tag{2.2.1}$$

for a gas of species A. The impact ionization rate can be characterized by the ionization frequency ν_i. In a gas with density N, ν_i is defined through the electron energy distribution $n(\epsilon)$ and the ionization cross section of atoms in their ground state $\sigma_i(\epsilon)$,

$$\nu_i = N\langle v\sigma_i\rangle = N\frac{\int n(\epsilon)v\sigma_i(\epsilon)d\epsilon}{\int n(\epsilon)d\epsilon} . \tag{2.2.2}$$

The ionization coefficient α is more widely used to characterize the impact ionization rate, and is defined as the number of ionization events performed by an electron along a path of unit length,

$$\alpha = \frac{\nu_i}{|\mathbf{v}_e^{\text{drift}}|} , \tag{2.2.3}$$

where $\mathbf{v}_e^{\text{drift}}$ is the electron drift velocity as given by Eq. (2.1.3). Since the electric field determines the particle energy, Townsend suggested an empirical formula to describe the ionization coefficient as a function of the field [82],

$$\alpha(|\mathbf{E}|) = \alpha_0 \exp(-E_0/E) , \tag{2.2.4}$$

in which the ionization length α_0 and threshold field E_0 are determined by fitting the experimental curves. For N_2 the fitting leads to [23]

$$\begin{aligned} \alpha_0 &= 4332\,(N/N_0)\,\text{cm}^{-1} , \\ E_0 &= 200\,(N/N_0)\,\text{kV cm}^{-1} , \end{aligned} \tag{2.2.5}$$

where N is the gas density and N_0 is the gas density under normal conditions. The source term for electrons and positive ions due to impact ionization then becomes,

$$\left(\frac{dn}{dt}\right)_i = \nu_i n_e = n_e\mu_e\,|\mathbf{E}|\alpha(|\mathbf{E}|). \tag{2.2.6}$$

2.2.2 Other ionization processes

Another source of ionization is photoionization. This occurs when a neutral molecule absorbs a high-energy photon. It has been shown in [78, 74] that in the case of pure nitrogen, the effect of photoionization could be neglected, since the photoionization rate is much smaller than that from impact ionization. In [74], it has also been shown that this is not the case as soon as a small amount of oxygen is added to the nitrogen, since the characteristic absorption length of ionizing radiation then increases significantly. Moreover, the photoionization coefficients being not very well known, it is useful to study a situation rather independent of photoionization: negative streamers in pure gases.

In [82], two other bulk ionization processes are described, namely the ionization by excited atoms or molecules, the so-called Penning-ionization, and associative ionization. These are two step processes, and therefore slow. Moreover the first only plays a role in gas mixtures, since the energy of the excited molecule has to be larger than the ionization energy of the other molecule. Associative ionization comes from the reaction between an ion and an atom into a molecular ion. Since we will only consider molecular nitrogen, this ionization process is not taken into account as well.

Finally, the electrodes can also be sources of electrons. We will consider only cold electrodes in this thesis, excluding any thermoionic emissions. Cold cathodes, however, can also release electrons due to secondary emission. The most important secondary emission mechanism is the ion-electron emission: an ion reaching the cathode can knock out an electron. Since we concentrate on processes in free space, electrodes are treated schematically. Depending on our choice, the boundary conditions can be a much stronger source of electrons than secondary emission.

2.2.3 Ionization sink processes

Attachment is a main sink of electrons in electronegative gases like oxygen. However, in this thesis we investigate the streamer dynamics in nitrogen, which is a non-attaching gas. Therefore attachment can be omitted from our model.

Another sink of ionization is the electron-ion recombination. In nitrogen, electrons and positive ions have comparable densities $n_e \approx n_+$, they decay through recombination like,

$$\left(\frac{\partial n_e}{\partial t}\right)_r = -\beta_{ei} n_e n_+ \approx= -\beta_{ei} n_e^2, \quad n_e \approx \frac{n_e^0}{1+\beta_{ei} n_e^0 t} \tag{2.2.7}$$

where n_e^0 is the initial plasma density and β_{ei} is the electron ion recombination coefficient. The characteristic decay time of a plasma with initial density n_e^0 due to this process therefore becomes $\tau_r = (\beta_{ei} n_e^0)^{-1}$. A numerical determination through the Boltzmann equation reports a value of $\beta_{ei} \simeq 2.8 \cdot 10^{-7}$ cm^{3}s^{-1} for N_2 under normal conditions [43]. So, for a plasma density n_e^0 in the order of 10^{14} cm^{-3}, which will appear to be a reasonable value, the characteristic decay time due to electron-ion recombination becomes in the order of 10^{-7} s. This is

much larger than the total time of discharge development in high electric fields, and in the same order of magnitude at low fields. However, the high densities are generated by a rapidly propagating ionization front. The separation of time scales therefore leads to a spatial separation, and recombination only takes place in the channel far behind the active tip. Following earlier work [24, 102, 74], recombination is not taken into account in this thesis.

2.3 The minimal streamer model

2.3.1 A fluid approximation for the particles

In the fluid approximation, the motion of charged particles is described by the continuity equations for the electron and ion densities $n_e(\mathbf{R}, t)$ and $n_+(\mathbf{R}, t)$ [82],

$$\begin{aligned} \frac{\partial n_e}{\partial t} + \nabla \cdot \mathbf{j_e} &= S_e \,, \\ \frac{\partial n_+}{\partial t} + \nabla \cdot \mathbf{j}_+ &= S_+ \,, \end{aligned} \tag{2.3.1}$$

coupled to the Poisson equation for the electric field,

$$\nabla^2 \phi = \frac{e}{\epsilon_0}(n_e - n_+) \,, \quad \mathbf{E} = -\nabla\phi \,, \tag{2.3.2}$$

where $\mathbf{j_e}$ and $\mathbf{j}_+$ denote the particle current densities, and S the ionization source and sink terms.

The particle currents are determined by the sum of the drift and diffusive fluxes, as described in Sect. 2.1,

$$\begin{aligned} \mathbf{j_e} &= -n_e \mu_e \mathbf{E} - D_e \nabla n_e \,, \\ \mathbf{j}_+ &= n_+ \mu_+ \mathbf{E} - D_+ \nabla n_+ \,. \end{aligned} \tag{2.3.3}$$

However, the mobility of the positive ions being two orders of magnitude smaller than that of the electrons [102], we can consider them to be immobile on the short time scales that will be investigated in this thesis, $\mu_+ = 0 = D_+$. In general, mobility and diffusion constant will depend on the electric field, but we will take them as constant. Diffusion and mobility of the electrons are related to temperature through the Einstein relation,

$$\frac{D_{e/+}}{\mu_{e/+}} = kT/e \,. \tag{2.3.4}$$

Since we here do not take into account thermal effects in the plasmas, we consider the temperature to be constant.

In Sect. 2.2, it has been argued that in the specific case of streamers propagating in molecular nitrogen, the main source of charged particles is impact ionization. This would not be true if the gas were, for example, air, which contains oxygen and therefore is attaching, and where photoionization might

not be neglected. However, considering the simple case of N_2 will allow us to investigate generic features of the streamer propagation. The impact ionization term in Eqs. (2.3.1) can be written using Townsend's approximation (2.2.4),

$$\begin{aligned} S_e = S_+ &= n_e \mu_e |\mathbf{E}| \alpha(|\mathbf{E}|) \\ &= n_e \mu_e |\mathbf{E}| \alpha_0 \mathrm{e}^{-E_0/|\mathbf{E}|} \end{aligned} \tag{2.3.5}$$

where the source terms for electrons and positive ions are taken equal due to the conservation of charge during such an impact ionization event.

2.3.2 Dimensional analysis

This model has been implemented in dimensionless form. The characteristic length and field scales emerge directly from Townsend's ionization formula (2.2.4) as $l_0 = \alpha_0^{-1}$ and E_0, respectively. The characteristic velocity is then given as $v_0 = \mu_e E_0$, which leads to a characteristic timescale $t_0 = \frac{l_0}{v_0} = \frac{l_0}{\mu_e E_0}$. The characteristic diffusion then becomes $D_0 = l_0^2/t_0$. The number density scale emerges from the Poisson equation (2.3.2), $n_0 = \epsilon_0 E_0 / e l_0$. We use the values from [23], which have been used subsequently in [24, 102], for μ_e, E_0 and α_0 in N_2 at 300 K, which depend on the pressure p in bar,

$$\mu_e \simeq \frac{380}{(N/N_0)} \ \mathrm{cm^2\,V^{-1}\,s^{-1}}, \tag{2.3.6}$$

$$\alpha_0 \simeq 4332 (N/N_0) \ \mathrm{cm^{-1}}, \tag{2.3.7}$$

$$E_0 \simeq 2 \cdot 10^5 (N/N_0) \ \mathrm{V\,cm^{-1}}. \tag{2.3.8}$$

Inserting these values in the characteristic scales we obtain,

$$l_0 \simeq \frac{2.3 \cdot 10^{-4}}{(N/N_0)} \ \mathrm{cm}, \qquad t_0 \simeq \frac{3 \cdot 10^{-12}}{(N/N_0)} \ \mathrm{s}, \tag{2.3.9}$$

$$n_0 \simeq 4.7 \cdot 10^{14} (N/N_0)^2 \ \mathrm{cm^{-3}}, \qquad D_0 \simeq \frac{1.8 \cdot 10^4}{(N/N_0)} \ \mathrm{cm^2 s^{-1}}. \tag{2.3.10}$$

The dimensionless quantities are then defined as follows,

$$\begin{aligned} \mathbf{r} &= \mathbf{R}/l_0, & \tau &= t/t_0, \\ \sigma &= n_e/n_0, & \rho &= n_+/n_0, \\ \boldsymbol{\mathcal{E}} &= \mathbf{E}/E_0, & \boldsymbol{\Gamma}_{e/+} &= \mathbf{j}_{e/+}/(n_0 \mu_e E_0), \\ \phi &= V/(E_0 l_0), & D &= D_e/D_0. \end{aligned} \tag{2.3.11}$$

Here σ and ρ denote the dimensionless electron and ion number densities, respectively, τ the dimensionless time, $\boldsymbol{\mathcal{E}}$ the dimensionless electric field, and D the dimensionless diffusion coefficient. For the diffusion coefficient we use the value given in [26], D_e=1800 $\mathrm{cm^2 s^{-1}}$, which gives a dimensionless diffusion coefficient of 0.1.

Inserting these dimensionless quantities into the continuity equations (2.3.1) we obtain

$$\begin{aligned} \frac{\partial \sigma}{\partial \tau} + \nabla \cdot \mathbf{\Gamma}_e &= \sigma |\boldsymbol{\mathcal{E}}| \exp(-1/|\boldsymbol{\mathcal{E}}|), \\ \frac{\partial \rho}{\partial \tau} + \nabla \cdot \mathbf{\Gamma}_+ &= \sigma |\boldsymbol{\mathcal{E}}| \exp(-1/|\boldsymbol{\mathcal{E}}|), \end{aligned} \tag{2.3.12}$$

where the expressions for the dimensionless particle fluxes defined by Eq. (2.3.3) are

$$\begin{aligned} \mathbf{\Gamma}_e &= -\sigma \boldsymbol{\mathcal{E}} - D \nabla \sigma, \\ \mathbf{\Gamma}_+ &= \mathbf{0}. \end{aligned} \tag{2.3.13}$$

The Poisson equation (2.3.2) can also be rescaled,

$$\nabla^2 \phi = \sigma - \rho, \quad \boldsymbol{\mathcal{E}} = -\nabla \phi, \tag{2.3.14}$$

ϕ being the dimensionless electric potential. We refer to the equations (2.3.12-2.3.14) as the minimal streamer model, since it contains all the basic physics needed to investigate the propagation of streamers in a non-attaching gas. The big advantage of using these dimensionless quantities is the easy rescaling of the results to any gas density, therefore making the translation to either laboratory conditions or high altitude sprites straightforward. Moreover, it also makes it possible to translate the results to other gasses, for which different values for μ_e, α_0, E_0 and D_e should be used.

2.3.3 Boundary and initial conditions

In narrow geometries, streamers frequently are growing from pointed electrodes, that create strong local fields in their neighborhood and a pronounced asymmetry between the initiation of positive and negative streamers [97]. On the other hand, in many natural discharges and, in particular, for sprites above thunderclouds [53], it is appropriate to assume that the electric field is homogeneous. Of course, dust particles or other nucleation centers can play an additional role in discharge generation, but in this thesis we will focus on the effect of a homogeneous field on a homogeneous gas.

The computational domain is bounded by two planar electrodes. The model is implemented in a cylindrical, radially symmetric coordinate system $(r, z) \in (0, L_r) \times (0, L_z)$, such that the electrodes are placed perpendicular to the axis of symmetry, the cathode at $z = 0$ and the anode at $z = L_z$. To obtain a uniform background field $\boldsymbol{\mathcal{E}}_b$, a potential difference is imposed on the electrodes. The radial boundary at L_r is virtual, and only present to create a finite computational domain. In order for the boundary conditions for the electric potential not to influence the solution, we need to take this boundary relatively far away from the symmetry axis, along which the streamer propagates. The boundary condition at $r = 0$ follows from symmetry conditions, and a homogeneous Neumann boundary condition is imposed at $r = L_r$. The boundary conditions for

the electric potential read,

$$\phi(r,0,\tau)=0,\ \phi(r,L_z,\tau)=|\boldsymbol{\mathcal{E}}_b|L_z,\ \frac{\partial\phi}{\partial r}(L_r,z,\tau)=0\,. \tag{2.3.15}$$

The background electric field $\boldsymbol{\mathcal{E}}_b$ is then directed in the z-direction.

Throughout this thesis, we use a Gaussian initial ionization seed, placed on the axis of symmetry, at a distance $z=z_0$ from the cathode,

$$\sigma(r,z,0)=\rho(r,z,0)=\sigma_0\exp\left(\frac{r^2+(z-z_0)^2}{r_b^2}\right)\,. \tag{2.3.16}$$

The maximal density σ_0 of this seed, the radius r_b at which the density drops to $1/\mathrm{e}$ of its maximal value (the so-called e-folding radius), and the value of z_0 differ from case to case, and will be specified where needed.

The continuity equation for the electron density σ has a second order spatial derivative, and therefore requires two boundary conditions for each direction in space. Again the condition at $r=0$ follows from symmetry considerations. At $r=L_r$ and $z=L_z$ we use Neumann boundary conditions, so that electrons that arrive at those boundaries may flow out off the system. At the cathode, both homogeneous Neumann or Dirichlet boundary conditions will be investigated. The use of Neumann boundary conditions permits electrons to flow into the system if the initial seed is attached to the cathode ($z_0=0$). Dirichlet boundary conditions are only used to ensure that there is no inflow of electrons if the seed is placed in the bulk of the gap ($z_0\gg r_b$). To recapitulate, the boundary conditions for the electrons read

$$\begin{aligned}&\sigma(r,0,\tau)=0\ \text{ or }\ \frac{\partial\sigma}{\partial z}(r,0,\tau)=0\,,\\&\frac{\partial\sigma}{\partial z}(r,L_z,\tau)=0\,,\\&\frac{\partial\sigma}{\partial r}(L_r,z,\tau)=0\,.\end{aligned} \tag{2.3.17}$$

The boundary conditions at $r=0$ simply follow from symmetry.

We notice that, if $z_0\gg r_b$ in Eq. (2.3.16), the ionization seed is detached from the cathode, and this results in practice in a vanishing inflow of electrons through the boundary, which is further ensured by imposing Dirichlet boundary conditions at the cathode . On the other hand, placing the seed on the cathode and using Neumann boundary conditions will result in an inflow of electrons. Varying the value of z_0 and the boundary conditions will therefore enable us to investigate the influence of the inflow of electrons on the streamer propagation. Furthermore, the use of dense seed, in particular in low fields, accelerates the emergence of a streamer. We remark that the initial seed is charge neutral.

3

AN ADAPTIVE GRID STRATEGY FOR STREAMER SIMULATIONS

We present an algorithm that deals efficiently with the different spatial scales involved in the evolution of streamers. This algorithm has moreover be designed to take into account the leading edge of the ionization front, which sets the dynamics of the streamer. Because the spatial density gradients in the leading edge are not necessarily steep, standard refinement methods, which usually refine regions with steep gradients, fail. The algorithm is based on the decoupling of the grids for the continuity equations on the one hand and those for the Poisson equation on the other hand. The refinement criterion uses error estimates of the solutions. It is applied at each time step, and the grids therefore adapt to the solution. The discretizations are based on finite volume methods. A flux limiting scheme for the drift term is used to deal with the steep gradients. Tests on planar and curved ionization fronts are carried out successfully.

3.1 Numerical discretizations

In our numerical simulations we shall mainly consider the streamer model with radial symmetry, making it effectively two dimensional. The system and the initial and boundary conditions are described in Sect. 2.3.3. To illustrate some of the difficulties we will also deal with the one-dimensional case.

In the cylindrically symmetric coordinate system the continuity equation (2.3.12) for the electrons, together with the expression for their fluxes (2.3.13), gives

$$\begin{aligned} \frac{\partial \sigma}{\partial t} &= \nabla \cdot (\sigma \boldsymbol{\mathcal{E}}) + D\nabla^2 \sigma + \sigma |\boldsymbol{\mathcal{E}}| e^{-1/|\boldsymbol{\mathcal{E}}|} \\ &= \frac{1}{r}\frac{\partial (r\sigma \mathcal{E}_r)}{\partial r} + \frac{\partial (\sigma \mathcal{E}_z)}{\partial z} + \frac{D}{r}\frac{\partial}{\partial r}(r\frac{\partial \sigma}{\partial r}) + D\frac{\partial^2 \sigma}{\partial z^2} + \sigma |\boldsymbol{\mathcal{E}}| e^{-1/|\boldsymbol{\mathcal{E}}|} . \end{aligned} \tag{3.1.1}$$

The continuity equation (2.3.12) for the positive ions, that are immobile, simply

is

$$\frac{\partial \rho}{\partial t} = \sigma |\boldsymbol{\mathcal{E}}| e^{-1/|\boldsymbol{\mathcal{E}}|}, \tag{3.1.2}$$

and the Poisson equation (2.3.14) reads

$$\nabla^2 \phi = \frac{1}{r}\frac{\partial}{\partial r}(r\frac{\partial \phi}{\partial r}) + \frac{\partial^2 \phi}{\partial z^2} = \sigma - \rho. \tag{3.1.3}$$

The electric field $\boldsymbol{\mathcal{E}} = (\mathcal{E}_r, \mathcal{E}_z)^{\mathrm{T}}$ can be computed from the electric potential as

$$\boldsymbol{\mathcal{E}} = -\nabla\phi = -\Big(\frac{\partial \phi}{\partial r}, \frac{\partial \phi}{\partial z}\Big)^{\mathrm{T}}. \tag{3.1.4}$$

The boundary conditions for this system have been treated in Sect. 2.3.3.

3.1.1 Spatial discretization of the continuity equations

The equations will be solved on a sequence of (locally) uniform grids with cells

$$\mathcal{C}_{ij} = [(i-1)\Delta r, i\Delta r] \times [(j-1)\Delta z, j\Delta z],\ i = 1...M_r,\ j = 1...M_z,$$

where $M_r = L_r/\Delta_r$ and $M_z = L_z/\Delta_z$ are the number of grid points in the r- respectively z-direction, and cell centers $(r_i, z_j) = ((i-\frac{1}{2})\Delta r, (j-\frac{1}{2})\Delta z)$. We denote by $\sigma_{i,j}$ and $\rho_{i,j}$ the density approximations in the cell centers. These can also be viewed as cell averages. The electric potential ϕ_{ij} and field strength $|\boldsymbol{\mathcal{E}}|_{i,j}$ are taken in the cell centers, whereas the electric field components are taken on the cell vertices, where they determine the mass fluxes. For the moment we assume that the electric field is known, its computation will be discussed later on.

The equations for the particle densities are discretized with finite volume methods, based on mass balances for all cells. Rewriting the continuity equations (3.1.1) and (3.1.2) will result in the semi-discrete system

$$\begin{aligned}
\frac{d\sigma_{i,j}}{dt} &= \frac{1}{r_i \Delta r}(r_{i-\frac{1}{2}} F^a_{i-\frac{1}{2},j} - r_{i+\frac{1}{2}} F^a_{i+\frac{1}{2},j} + r_{i-\frac{1}{2}} F^d_{i-\frac{1}{2},j} - r_{i+\frac{1}{2}} F^d_{i+\frac{1}{2},j}) \\
&\quad + \frac{1}{\Delta z}(F^a_{i,j-\frac{1}{2}} - F^a_{i,j+\frac{1}{2}} + F^d_{i,j-\frac{1}{2}} - F^d_{i,j+\frac{1}{2}}) + S_{i,j}, \\
\frac{d\rho_{i,j}}{dt} &= S_{i,j},
\end{aligned}$$

in which F^a and F^d denote the advective and diffusive electron fluxes through the cell boundaries, and S_{ij} stands for the source term in the grid cell $\mathcal{C}_{ij}$.

The discretization of the advective terms requires care. A first order upwind scheme as used in [75] appears to be much too diffusive [12], leading to a totally different asymptotic behavior on realistic grids. Moreover, it is expected that the numerical diffusion will over-stabilize the numerical scheme, thereby suppressing interesting features of the solutions. Higher order linear discretizations, however, lead to numerical oscillations and negative values for the electron density, that

will grow in time due to the reaction term. This holds in particular for central discretizations [39]. The choice was made to use an upwind-biased scheme with flux limiting. This gives mass conservation and monotone solutions without introducing too much numerical diffusion. For the limiter we will take the Koren limiter function, which is slightly more accurate than standard choices such as the van Leer limiter function [39].

Denoting $\mathcal{E}^+ = \max(-\mathcal{E}, 0)$ and $\mathcal{E}^- = \min(-\mathcal{E}, 0)$ to distinguish upwind directions for the field components $\mathcal{E}_r, \mathcal{E}_z$, the advective fluxes are computed by

$$\begin{aligned} F^a_{i+\frac{1}{2},j} &= \mathcal{E}^+_{r;\,i+\frac{1}{2},j}\Big[\sigma_{i,j} + \psi\big(p_{i,j}\big)\big(\sigma_{i+1,j} - \sigma_{i,j}\big)\Big] \\ &\quad + \mathcal{E}^-_{r;\,i+\frac{1}{2},j}\Big[\sigma_{i+1,j} + \psi\big(1/p_{i+1,j}\big)\big(\sigma_{i,j} - \sigma_{i+1,j}\big)\Big]\,, \qquad (3.1.5) \\ F^a_{i,j+\frac{1}{2}} &= \mathcal{E}^+_{z;\,i,j+\frac{1}{2}}\Big[\sigma_{i,j} + \psi(q_{i,j})(\sigma_{i,j+1} - \sigma_{i,j})\Big] \\ &\quad + \mathcal{E}^-_{z;\,i,j+\frac{1}{2}}\Big[\sigma_{i,j+1} + \psi(1/q_{i,j+1})(\sigma_{i,j} - \sigma_{i,j+1})\Big]\,, \qquad (3.1.6) \end{aligned}$$

in which

$$p_{i,j} = \frac{\sigma_{i,j} - \sigma_{i-1,j}}{\sigma_{i+1,j} - \sigma_{i,j}} \quad , \quad q_{i,j} = \frac{\sigma_{i,j} - \sigma_{i,j-1}}{\sigma_{i,j+1} - \sigma_{i,j}}\,,$$

and ψ is the limiter function

$$\psi(\theta) = \max\Big(0, \min\Big(1, \frac{1}{3} + \frac{\theta}{6}, \theta\Big)\Big)\,.$$

Note that in regions where the solution is smooth we will have values of p_{ij}, q_{ij} close to 1, and then the scheme simply reduces to the third-order upwind-biased discretization corresponding to $\psi(\theta) = \frac{1}{3} + \frac{1}{6}\theta$. In non-smooth regions where monotonicity is important the scheme can switch to first-order upwind, which corresponds to $\psi(\theta) = 0$.

The diffusive flux is calculated with second-order central differences as

$$F^d_{i+\frac{1}{2},j} = \frac{D}{\Delta r}(\sigma_{i,j} - \sigma_{i+1,j})\,, \qquad (3.1.7)$$

$$F^d_{i,j+\frac{1}{2}} = \frac{D}{\Delta z}(\sigma_{i,j} - \sigma_{i,j+1})\,. \qquad (3.1.8)$$

Finally, the reaction term S_{ij} in (3.1.5) is computed in the cell centers as

$$S_{i,j} = \sigma_{i,j}|\boldsymbol{\mathcal{E}}|_{ij} e^{-1/|\boldsymbol{\mathcal{E}}|_{ij}}\,. \qquad (3.1.9)$$

Boundary values will be either homogeneous Dirichlet or homogeneous Neumann type. For example, if $\sigma = 0$ for $z = 0$, we introduce virtual values [39]

$$\sigma_{i,0} = -\sigma_{i,1}\,, \quad \sigma_{i,-1} = -\sigma_{i,2}\,. \qquad (3.1.10)$$

If $\sigma_z = 0$ for $z = 0$ then we set

$$\sigma_{i,0} = \sigma_{i,1}\,, \quad \sigma_{i,-1} = \sigma_{i,2}\,. \qquad (3.1.11)$$

These formulas follow from the approximations

$$\begin{aligned} \sigma(r_i, z_{\frac{1}{2}}) &= \frac{1}{2}(\sigma(r_i z_0) + \sigma(r_i, z_1)) + \mathcal{O}(\Delta z^2) \\ \sigma_z(r_i, z_{\frac{1}{2}}) &= \frac{1}{\Delta z}(\sigma(r_i, z_1) - \sigma(r_i, z_0)) + \mathcal{O}(\Delta z^2) \end{aligned} \tag{3.1.12}$$

3.1.2 Spatial discretization of the Poisson equation

The electric potential ϕ is computed through a second-order central approximation of Eq. (2.3.14), and is defined at the cell centers:

$$\begin{aligned} \sigma_{i,j} - \rho_{i,j} &= \frac{\phi_{i+1,j} - 2\phi_{i,j} + \phi_{i-1,j}}{\Delta r^2} + \frac{\phi_{i+1,j} - \phi_{i-1,j}}{2r_i \Delta r} \\ &+ \frac{\phi_{i,j+1} - 2\phi_{i,j} + \phi_{i,j-1}}{\Delta z^2} . \end{aligned} \tag{3.1.13}$$

The electric field components are then computed by using a second-order central discretization of $\boldsymbol{\mathcal{E}} = -\nabla\phi$, and are defined in the cell boundaries,

$$\begin{aligned} \mathcal{E}_{r;i+\frac{1}{2},j} &= \frac{\phi_{i,j} - \phi_{i+1,j}}{\Delta r} , \\ \mathcal{E}_{z;i,j+\frac{1}{2}} &= \frac{\phi_{i,j} - \phi_{i,j+1}}{\Delta z} . \end{aligned} \tag{3.1.14}$$

The electric field strength is computed at the cell centers, therefore the components are first determined in the cell centers by averaging the cell boundary values, and the electric field strength then becomes:

$$|\boldsymbol{\mathcal{E}}|_{i,j} = \frac{1}{2}\sqrt{(\mathcal{E}_{r;i-\frac{1}{2},j} + \mathcal{E}_{r;i+\frac{1}{2},j})^2 + (\mathcal{E}_{z;i,j-\frac{1}{2}} + \mathcal{E}_{z;i,j+\frac{1}{2}})^2} . \tag{3.1.15}$$

We notice here that, discretizing $\nabla \cdot \boldsymbol{\mathcal{E}}$ with a second-order central scheme gives

$$\frac{\partial}{\partial t}(\nabla \cdot \boldsymbol{\mathcal{E}}) = \frac{\partial(\sigma_{i,j} - \rho_{i,j})}{\partial t} .$$

Therefore, the total current conservation following from Eqs. (2.3.12)-(2.3.14),

$$\nabla \cdot (\frac{\partial \boldsymbol{\mathcal{E}}}{\partial t} + \boldsymbol{\Gamma}_e) = 0 , \tag{3.1.16}$$

also holds on the level of the discretizations.

3.1.3 Temporal discretization

After the spatial discretization, the system of equations (3.1.5) can be written in vector form as a system of ordinary differential equations,

$$\begin{aligned} \frac{d\sigma}{d\tau} &= G(\sigma, \boldsymbol{\mathcal{E}}) , \\ \frac{d\rho}{d\tau} &= S(\sigma, \boldsymbol{\mathcal{E}}) , \end{aligned} \tag{3.1.17}$$

where the components of G and S are given by the spatial discretizations in (3.1.5). The electric field $\mathcal{E}$ and the field strength $|\mathcal{E}|$ are computed from given σ, ρ by discretized versions of (3.1.3) and (3.1.4). Therefore the full set of semi-discrete equations actually forms a system of differential-algebraic equations.

The particle densities are updated in time using the explicit trapezoidal rule, which is a two-stage method, with step size $\Delta\tau$. In the following the superscript n denotes the time step. Starting at time $\tau^n = n\Delta\tau$ from known particle distributions $\sigma^n(r,z) \approx \sigma(r,z,\tau^n)$, $\rho^n(r,z) \approx \rho(r,z,\tau^n)$ and known electric field $\mathcal{E}^n(r,z) \approx \mathcal{E}(r,z,\tau^n)$, the predictors $\bar{\sigma}^{n+1}$ and $\bar{\rho}^{n+1}$ for the electron and ion densities at time τ^{n+1} are first computed by

$$\begin{aligned} \bar{\sigma}^{n+1} &= \sigma^n + \Delta\tau\, G(\sigma^n, \mathcal{E}^n)\,, \\ \bar{\rho}^{n+1} &= \rho^n + \Delta\tau\, S(\sigma^n, \mathcal{E}^n)\,. \end{aligned} \tag{3.1.18}$$

After this the Poisson equation (3.1.3) is solved with source term $\bar{\sigma}^{n+1} - \bar{\rho}^{n+1}$, leading to the electric field $\bar{\mathcal{E}}^{n+1}$ at this intermediate stage by Eq. (3.1.4). The final densities at the new time level τ^{n+1} are then computed as

$$\begin{aligned} \sigma^{n+1} &= \bar{\sigma}^{n+1} + \frac{\Delta\tau}{2} G(\sigma^n, \mathcal{E}^n) + \frac{\Delta\tau}{2} G(\bar{\sigma}^{n+1}, \bar{\mathcal{E}}^{n+1})\,, \\ \rho^{n+1} &= \bar{\rho}^{n+1} + \frac{\Delta\tau}{2} S(\sigma^n, \mathcal{E}^n) + \frac{\Delta\tau}{2} S(\bar{\sigma}^{n+1}, \bar{\mathcal{E}}^{n+1})\,, \end{aligned} \tag{3.1.19}$$

after which the Poisson equation is solved once more, but now with the source term $\sigma^{n+1} - \rho^{n+1}$, giving the electric field $\mathcal{E}^{n+1}$ induced by the final particle densities at time τ^{n+1}. This time discretization is second-order accurate, which is in line with the accuracy of the spatial discretization.

The use of an explicit time integration scheme implies that the grid spacing and time step should obey restrictions for stability. For the advection part we get a Courant-Friedrichs-Lewy (CFL) restriction

$$\max \mathcal{E}_r \frac{\Delta\tau}{\Delta r} + \max \mathcal{E}_z \frac{\Delta\tau}{\Delta z} \quad < \quad \nu_a\,, \tag{3.1.20}$$

and the diffusion part leads to

$$D\frac{\Delta\tau}{\Delta r^2} + D\frac{\Delta\tau}{\Delta z^2} \quad < \quad \nu_d\,. \tag{3.1.21}$$

Actually, to be more precise, the minimal time step $\Delta\tau$ determined by (3.1.20) or (3.1.21) should be used. In our simulations, condition (3.1.20) will determine this minimal $\Delta\tau$ and the time step will be chosen well inside this constraint.

For the first order upwind advection scheme combined with a two-stage Runge-Kutta method, the maximal Courant number is [39] $\nu_a^1 = 1$, while for the third order upwind scheme it is $\nu_a^3 = 0.87$. The second order central discretization demands a maximal Courant number $\nu_d = 0.5$.

A third restriction for the time step comes from the dielectric relaxation time. The ions are considered to be immobile, which leaves us with the following time step restriction in dimensional units [8],

$$\Delta t \leq \frac{\epsilon_0}{e\mu_e \max n_e}, \tag{3.1.22}$$

where we refer to Chap. 2 for the meaning of these quantities. If we apply the dimensional analysis of Chap. 2, we obtain the time step restriction in dimensionless units,

$$\Delta\tau \leq \frac{1}{\sigma}. \tag{3.1.23}$$

In fact, this restriction is much weaker than that for the stability of the numerical scheme, as is shown in Fig. 3.1 (this figure has been obtained with the simulations which will be treated in more detail in Chap. 6).

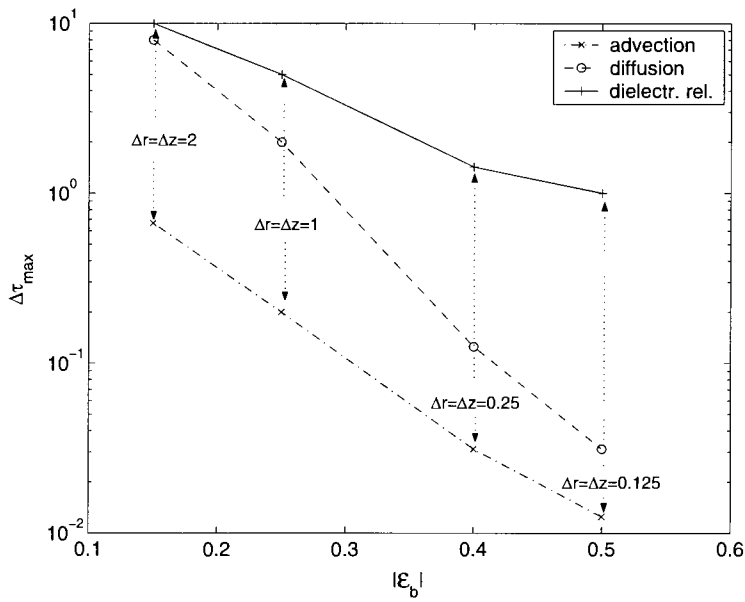

FIGURE 3.1: Maximal time step allowed by the advection discretization (dash dotted line with crosses), the diffusion discretization (dashed lines with circles) and the dielectric relaxation time (solid line with pluses), as a function of the background electric field. The minimal mesh size is indicated in the plot.

The choice for an explicit time stepping scheme was made after tests with VLUGR [11], a local refinement code that uses –computationally much more intensive– implicit schemes (BDF2). These tests showed that these implicit schemes also needed relatively small time steps to obtain accurate solutions, so

that in the end an explicit scheme would be more efficient in spite of stability restrictions for the time steps. Moreover the use of an explicit scheme allows us to decouple the computation of the particle densities from that of the electric potential and electric fields. With a fully implicit scheme all quantities are coupled, leading to much more complex computations.

Another reason for preferring explicit time stepping is monotonicity. The solutions in our model have very steep gradients for which we use spatial discretizations with limiters to prevent spurious oscillations. Of course, such oscillations should also be prevented in the time integration. This has led to the development of schemes with TVD (total variation diminishing) or SSP (strong stability preserving) properties; see [36, 39]. In contrast to stability in the von Neumann sense (i.e., L_2-stability for linear(ized) problems with (frozen) constant coefficients), such monotonicity requirements under implicit methods do not allow step sizes larger than one. Among the explicit methods, the explicit trapezoidal rule is optimal with respect to such monotonicity requirements.

3.1.4 Remarks on alternative discretizations

The above combination of spatial and temporal discretizations provide a relatively simple scheme for the streamer simulations. The accuracy will be roughly $O(\Delta x^2) + O(\Delta \tau^2)$ in regions where the solution is smooth (also for the limited advection discretization [39, p. 218]). In our tests, step size restrictions mainly originate from the advective parts in the continuity equations. The above scheme is stable and monotone (free of oscillations) for Courant numbers up to one, approximately. Usually we take smaller step sizes than imposed by this bound to reduce temporal errors.

As mentioned before in Sect. 3.1.1 using a first-order upwind discretization for the advective term will usually introduce too much diffusion, whereas second-order central advection discretizations lead to numerical oscillations and negative concentrations.

Higher-order discretizations can certainly be viable alternatives. However, we then will have larger spatial stencils, which creates more difficulties with local grid refinements where numerical interfaces are created. The above discretization is robust and easy to implement.

It is well known that limiting as in (3.1.5), (3.1.6) gives some clipping of peak values in linear advection tests, simply because the limiter does not distinguish genuine extrema from oscillations induced numerically. This can be avoided by adjusting the limiter near extrema, but in the streamer tests it was found that such adjustments were not necessary. In the streamer model the local extrema in each spatial direction are located in the streamer head, and the nonlinear character of the equations give a natural steepening there which counteracts local numerical dissipation.

In [102] a flux-corrected transport (FCT) scheme was used. The advantage of our semi-discrete approach is that is becomes easier to add source terms without having to change the simulation drastically. Also the transition from 1D discretizations to 2D or 3D becomes straightforward conceptually; the imple-

mentations for higher dimensions are still difficult, of course, in particular for the Poisson equation. Moreover, in [12] comparisons of the FCT scheme with a scheme using the van Leer limiter (which is closely related to the limiter used in our scheme) show that the FCT scheme, in contrast to the limited scheme, gives somewhat irregular results for simple advection tests in regions with small densities. In the leading edge the densities decay exponentially, and we do not want such irregularities to occur.

3.2 The adaptive refinement procedure

3.2.1 The limitations of the uniform grid approach

Up to now, all simulations that have been carried out on the minimal streamer model were performed on a uniform grid [24, 102, 5, 83]. However the use of a uniform grid on such a large system has numerous limitations.

The first limitation is the size of the system. In [5, 83] the simulations were performed in a radially symmetric geometry with $2000 \times 2000 = 4 \cdot 10^6$ grid points. Since the number of variables is of at least 10 per grid point (the electron and ion densities both at old and new time step, the electric potential, the electric field components and strength, and the terms containing the temporal derivatives of both electrons and ions), the total number of variables will be of at least $40 \cdot 10^6$. So, when computing in double precision (64 bits or 8-bytes values) the memory usage is then in the order of several hundreds MB, depending on the compiler. Moreover, these simulations show that the streamer will eventually branch, and up to now there was no convergence of the branching time with respect to the mesh size. In order to investigate the branching, it would be necessary to rerun the simulation with a smaller grid size. Moreover it would be interesting to investigate larger systems. So from that point of view it is worth looking at an algorithm that would require much less memory usage.

The second limitation is the use of fast solvers for the Poisson equation. For this we use the FISHPAK routine, described in [109, 85]. One of the major limitations of this routine is its inaptitude to deal accurately with large grids, due to numerical instabilities with respect to round-off errors.

We illustrate this by an example. Consider the Laplace equation in a radially symmetric coordinate system $(r, z) \in (0, L_r) \times (0, L_z)$,

$$\left\{ \begin{array}{rcl} \nabla^2 \phi & = & (-6A + 4A^2(r^2 + (z - \frac{L_z}{2})^2))e^{-A(r^2+(z-\frac{L_z}{2})^2)}, \\ \phi(r,0) & = & \phi(r,L_z) = e^{-A(r^2+(\frac{L_z}{2})^2}, \\ \frac{\partial \phi}{\partial r}(0,z) & = & 0, \frac{\partial \phi}{\partial r}(L_r,z) = -2Are^{-A(r^2+(\frac{L_z}{2})^2}, \end{array} \right. \tag{3.2.1}$$

with $L_r = L_z = 1$, giving the analytical solution $\phi(r,z) = e^{-A(r^2+(z-L_z/2)^2)}$.

The accuracy of the method can be characterized by the discrete L_1, L_2 and L_∞-norms of the errors. For a grid function $v = (v_{ij})$ on a $m \times m$ grid these

norms are defined as

$$\begin{aligned} ||v||_1 &= \sum_{i,j=1}^{m} \Delta r \Delta z |v_{i,j}| , \\ ||v||_2 &= \sqrt{\sum_{i,j=1}^{m} \Delta r \Delta z |v_{i,j}|^2} , \\ ||v||_\infty &= \max_{i,j}(|v_{i,j}|) . \end{aligned} \tag{3.2.2}$$

Fig. 3.2 shows these L_p-norms of the numerical error e_ϕ of the results obtained with the FISHPAK routine on a $(m \times m)$-grid, as a function of m, with $A = 100$. The upper and lower panel show the error of the single respectively double precision computations.

In a similar way we determine the L_p-norms of the numerical error in the electric field strength $|\tilde{\mathcal{E}}|_{ij}$, computed with Eq. (3.1.15). They are shown in Fig. 3.3.

Up to a number of grid points of approximately 2000, the errors in the electric potential are of second order, in agreement with the discretization. The errors in the field are also of second order, even though, at first sight, a first-order behavior might be expected, since it's the derivative of a quantity of second order accuracy. This can be explained through an asymptotic error expansion, which,

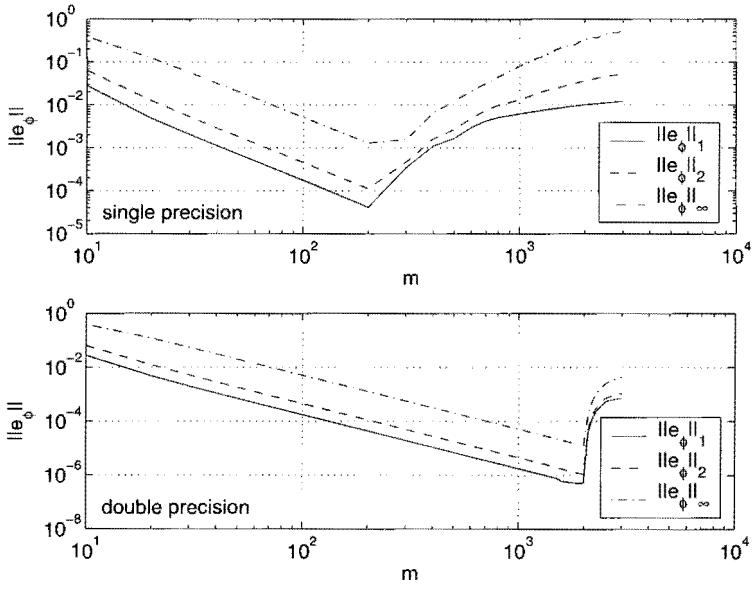

FIGURE 3.2: The L_1-errors (solid), L_2-errors (dashed) and L_∞-errors (dash-dotted) for ϕ in Eq. (3.2.1) on $m \times m$ grids, as a function of m. Upper panel, single precision; lower panel, double precision.

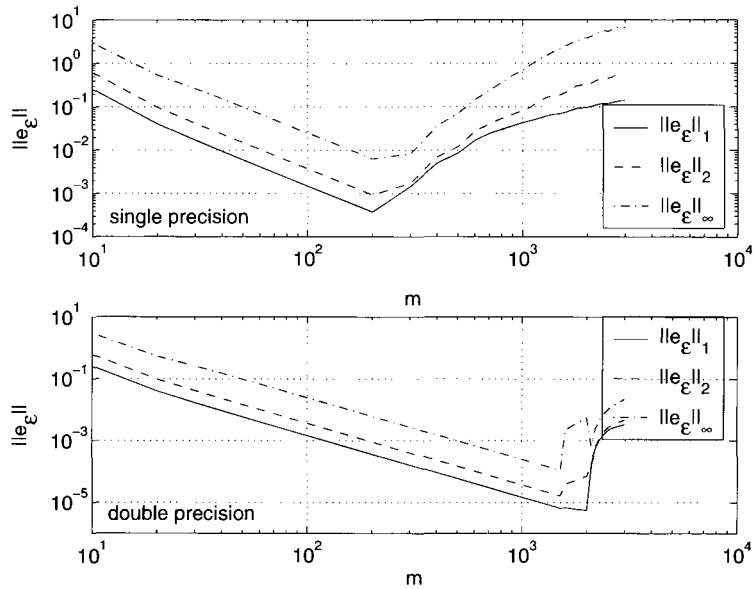

FIGURE 3.3: The L_1-errors (solid), L_2-errors (dashed) and L_∞-errors (dash-dotted) for $|\mathcal{E}|$ in Eq. (3.2.1) on $m \times m$ grids, as a function of m. Upper panel, single precision; lower panel, double precision.

for simplicity, will be carried in one-dimension. The second order discretization for ϕ will give

$$\phi_j = \phi(z_j) + \Delta z^2 v(z_j) + O(\Delta z^4)\,, \tag{3.2.3}$$

with a principal error function v which will be smooth if the solution ϕ is so. By considering local truncation errors it is seen that v should satisfy $\partial_{zz} v = \partial_z^4 \phi/12$ with corresponding homogeneous boundary conditions. Then the discretized value of the field at the cell boundary becomes:

$$\begin{aligned} \mathcal{E}_{j+\frac{1}{2}} &= \frac{\phi_j - \phi_{j-1}}{\Delta z} \\ &= \frac{\phi(z_j) - \phi(z_{j+1})}{\Delta z} + \Delta z(v(z_j) - v(z_{j+1})) + O(\Delta z^3), \end{aligned} \tag{3.2.4}$$

which, using a Taylor expansion around $z_{j+\frac{1}{2}}$, yields

$$\begin{aligned} \mathcal{E}_{j+\frac{1}{2}} &= -\partial_z \phi(z_{j+\frac{1}{2}}) + O(\Delta z^2) - \Delta z^2 \partial_z v(z_j) + O(\Delta z^3) \\ &= \mathcal{E}(z_{j+\frac{1}{2}}) + O(\Delta z^2) \end{aligned} \tag{3.2.5}$$

It is clear that the performance of the FISHPAK routine decreases dramatically when more than approximately 2000 grid points (in double precision) are

used. We note that these numerical instabilities also show up on a $m_r \times m_z$ grid if either m_r or m_z are larger than 2000, approximately, in double precision.

It is necessary to develop some strategy to counteract these limitations. This will be done by choosing separate grids with suitable local refinements for the continuity equations (2.3.12)-(2.3.12) and the Poisson equation (2.3.14).

3.2.2 General structure of the locally uniform refined grids

Both the continuity equations (3.1.1)-(3.1.2) and the Poisson equation (3.1.3) are computed on a set of uniform, radially symmetric grids, that are refined locally where needed. The approach of solving these equations separately rather than simultaneously allows the use of different sets of grids for each equation, thereby making it possible to decouple the grids for the continuity equation from those of the Poisson equation, thus allowing grids that are tailored for the particular task at hand. We emphasize that it is the use of an explicit time stepping method that allows us to decouple the grids.

In both cases the equations are first solved on a coarse grid. This grid is then refined in those regions where a refinement criterion – which will be treated in more detail below – is met. These finer grids can be further refined, wherever the criterion is still satisfied. Both the grids and the refinement criteria may be different for the continuity equations on the one hand and the Poisson equation on the other hand, but the general structure of the grids is the same for both type of equations. It consists of a series of nested grids Ω^k, k being the grid number, with level $l(k)$. This level function gives the mesh width of a grid, $l(1) = 1$ corresponding to the coarsest grid Ω^1 with mesh width Δr_c and Δz_c. We notice that one single grid $k = 1$ exists at this coarsest level $l = 1$, whereas several, non-overlapping grids might exist on the finer levels. A certain grid

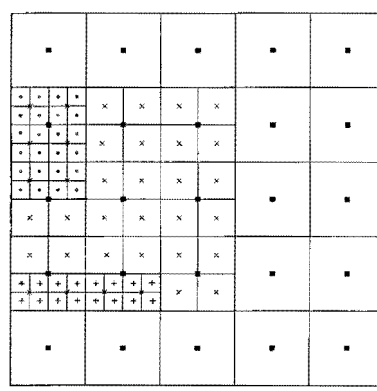

FIGURE 3.4: An example of nested grids: ■ cell centers on Ω^1 with $l(1) = 1$, × cell centers on Ω^2 with $l(2) = 2$, + cell centers on Ω^3 with $l(3) = 3$, ○ cell centers on Ω^4 with $l(4) = 3$.

will have a mesh twice as fine as the grid one level coarser – which we will call its parent grid – so that the mesh widths of a grid with level l become $\Delta r^l = \Delta r_c/2^{l-1}$ and $\Delta z^l = \Delta z_c/2^{l-1}$.

Fig. 3.4 shows an example of four nested grids on three levels. We will denote a quantity u on a certain grid Ω^k with level $l = l(k)$ as $u^k_{ij} = u(r^l_i, z^l_j)$. Recall that $r^l_i = (i - 1/2)\Delta r^l$, $z^l_j = (j - 1/2)\Delta z^l$.

Throughout this thesis, the grids for the Poisson equation are designated by $\mathcal{G}$, those for the continuity equations by $\mathcal{H}$. For the Poisson equation the grids are structured as follows: we determine all grid points of a grid $\mathcal{G}^l$ at a certain level l that, following some refinement monitor (we will give more details later), have to be refined. This results in one or more connected sets of finer grid cells. The finer *child grids* $\{\mathcal{G}^{l+1}\}$ of the *parent grid* $\mathcal{G}^l$ cover the smallest rectangular domain enclosing each of these sets (see the left picture of Fig. 3.5).

For the continuity equations, the placement of child grids is somewhat different. Again we find the set of grid points that have to be refined on a grid $\mathcal{H}^l$ at a certain level l. However instead of taking one single rectangular grid that encloses the entire connected set of refined grid points, we now use a series of smaller rectangular domains $\{\mathcal{H}^{l+1}\}$, each of which covers a part of the region that has to be refined. The union of the sets $\{\mathcal{H}^{l+1}\}$ obviously should cover the whole refined region (see the right picture of Fig. 3.5). We notice that all the grids $\mathcal{H}^{l+1}$ are chosen such that they contain an identical, user defined, number of grid points M_0 in the radial direction. This is only for convenience of programming.

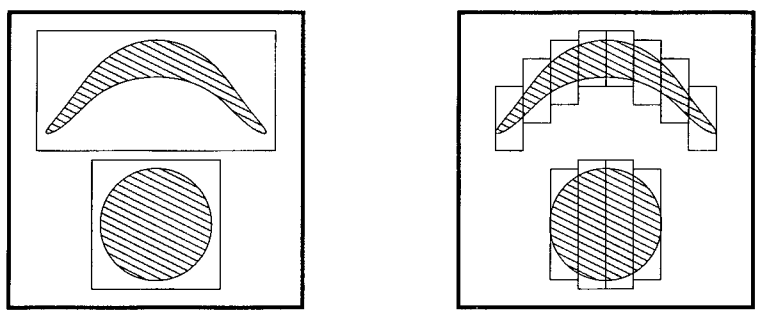

FIGURE 3.5: Schematic grid structure. The thick rectangles indicate the position of the coarse grid that has to be refined. The filled regions indicate where the refinement criterion is met. In the left plot the rectangular grids such as used for the Poisson equation are shown. In the right plot, the set of rectangles such as used for the continuity equations are shown, they all contain the same number of grid points in the radial (horizontal) direction.

In what follows, to make the distinction between the indices on a coarse and on a fine grid, we use capital indices I and J for the coarse grid and small indices i and j for the fine grid, as indicated in Fig. 3.6. Notice that a coarse grid cell with the cell center (r_I, z_J) contains four finer cells with centers (r_i, z_j), (r_i, z_{j+1}), (r_{i+1}, z_j), (r_{i+1}, z_{j+1}), with $i = 2I - 1$ and $j = 2J - 1$.

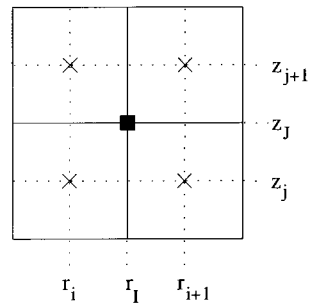

FIGURE 3.6: Coarse grid cell with cell center (r_I, z_J) and the four finer grid cells within.

3.2.3 Refinement scheme for the continuity equation

Let us assume that the particle distributions and electric field at time τ^n are known on a set S^n of m rectangular grids $\mathcal{H}^{n,k}$ with level $l = l(k)$, $1 \leq k \leq m$, as shown in Fig. 3.7. Then, using the explicit time stepping method introduced in Sect. 3.1.3, the particle distributions at time τ^{n+1} can be computed on all the grids of S^n (Fig. 3.7b). Now the new set S^{n+1} of nested grids that is best suitable for the solution at τ^{n+1} has to be found, as in Fig. 3.7c.

Moreover, the computational domain for the continuity equations can be reduced substantially by the following physical consideration: our model is a fluid model based in the continuum hypothesis, which is not valid anymore if the densities are below a certain threshold, that can be taken as 1 mm^{-3}. In nitrogen at atmospheric pressure, this corresponds roughly to a dimensionless density of 10^{-12}. The regions where all densities are below this threshold can simply be ignored. Therefore, after each time step the densities below this threshold are set to zero. The computational domain for the continuity equations for the next time step is then taken as the region where σ or ρ are strictly positive. In view of our two-stage Runge-Kutta time stepping we use a four point extension of this domain in all directions.

Restriction of fine grid values to a coarse grid

At first, when a grid $\mathcal{H}^{n,K}$ at level $L = L(K)$ contains a finer grid $\mathcal{H}^{n,k}$ at level $l = L + 1$, the particle densities on $\mathcal{H}^{n,k}$ are restricted to $\mathcal{H}^{n,K}$ in such a way that the total mass of each particle species is conserved locally. From Fig. 3.4 and Fig. 3.6 it can be seen that one cell of $\mathcal{H}^{n,K}$ contains four cells on $\mathcal{H}^{n,k}$, and the mass conservation implies that for each particle species the total mass in the coarse grid cell is equal to the sum of the masses in the finer grid cells, which, taking into account the cylindrical geometry of the cells, translates in the following restriction formula $U^K = Res(U^k)$ for the grid functions $U^K = \{u^K_{IJ}\}$

and $U^k = \{u_{ij}^k\}$,

$$U_{IJ}^K = Res(U^k)_{IJ} = \frac{1}{4r_I^L} \sum_{m=2I-1}^{2I} \sum_{n=2J-1}^{2J} r_m^l u_{mn}^l , \tag{3.2.6}$$

in which u stands for either the electron or the ion density. This restriction step is carried out because time stepping on a too coarse grid may lead to erroneous values, which are now overwritten by the better restricted values.

Refinement criterion: curvature monitor

It is now possible to find the regions where the grids should be refined at t^{n+1}. The decision whether a finer grid should be used on a certain region is made with a relative curvature monitor. This monitor is defined on a grid with level l as the discretization of

$$M_u(r^l, z^l) = (\Delta r^l)^2 \left| \frac{1}{r} \frac{\partial}{\partial r} (r \frac{\partial u}{\partial r}) \right| + (\Delta z^l)^2 \left| \frac{\partial^2 u}{\partial z^2} \right| . \tag{3.2.7}$$

Although this expression does not provide an accurate estimate of the discretization errors, it does give a good indication of the degree of spatial difficulty of

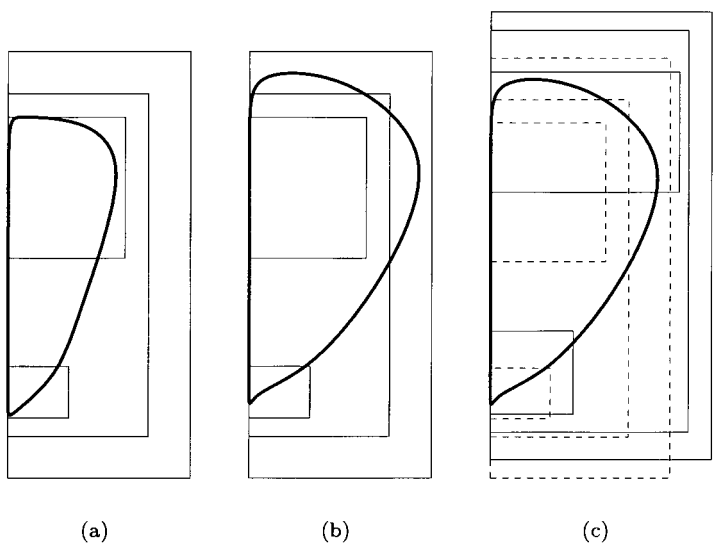

FIGURE 3.7: (a): Contour line of the solution and the set of rectangular computational grids, both at τ^n. (b): Contour line of the solution at τ^{n+1} and computational grids at τ^n. (c): Contour line and computational grids at τ^{n+1}, the dashed lines are the grids at τ^n.

the problem [94]. It is applied first on the electron density σ, since that is the quantity which advects and diffuses, and therefore the quantity in which some discretization error will appear. The monitor is also applied on the total charge density $\sigma - \rho$ since this is the source term of the Poisson equation, and the accuracy of the solution of the Poisson equation is of course dependent on the accuracy of the source term. The monitor is taken relative to the maximum value of each quantity, and the refinement criterion through which the need to refine a certain grid $\mathcal{H}^k$ with level l then reads:

$$\text{refine all grid cells } i,j \text{ where } \frac{M_u(r_i^l, z_j^l)}{\max u_{ij}^l} \geq \epsilon_u^l, \quad u = \sigma,\, \sigma - \rho \tag{3.2.8}$$

in which ϵ_σ^l and $\epsilon_{\sigma-\rho}^l$ are grid-dependent refinement tolerances that still have to be chosen.

Now, starting from the coarsest grid, the monitors are computed by approaching them with a second order central discretization, and the regions that should be refined are determined. For this set of finer grids again the regions to be refined are computed, and so on until the finest discretization level is reached, or until the monitor is small enough on every grid. Now the new set of nested grids S^{n+1} has been determined, but the particle densities are still only known on the set S^n (in Fig. 3.7c this means that we have to convert the density distributions on the dashed grids to distributions on the solid rectangles).

Criteria such as (3.2.7) are common for grid refinements. As we shall see in experiments, it will be necessary to extend the refined regions to include (a part of) the leading edge of a streamer. This leading edge is the high field region into which the streamer propagates, and where the densities decay exponentially. This modification, due to the pulled front character of the equations [29], is discussed in Sect. 3.3.

Mapping coarse grid values to the interior of the finer grids

In the following we consider mapping functions from a coarse grid $\mathcal{H}^K$ with level L to a child grid $\mathcal{H}^k$ with level l. There are three possible relations between a grid $\mathcal{H}^{n+1,k}$ at time τ^{n+1} and the older grids $\{\mathcal{H}^{n,k}\}$, as illustrated in Fig. 3.8. First it is possible that at the previous time step a finer grid $\mathcal{H}^{n,K}$ existed on some region of $\mathcal{H}^{n+1,k}$ (as in the vertically striped region of Fig. 3.8). Then the values of the densities on the new grid are computed by the restriction (3.2.6):

$$U^{n+1,k} = Res(U^{n,K}) \quad \text{on } \mathcal{H}^{n+1,k} \cap \mathcal{H}^{n,k}, \tag{3.2.9}$$

where U again stands for the set of grid values of either electron- or ion densities. Secondly, there is the possibility that (part of) the new grid already existed at the previous time step, in which case there is no need for projecting the density distributions from one grid to the other. And finally it may occur that the new grid lies on a region where only a coarser grid $\mathcal{H}^{n,K}$ existed at the previous time level (as in the horizontally striped region in Fig. 3.8). Then we have to make a prolongation of the coarse grid values $U^{n+1,K}$ to the new fine grid. One main

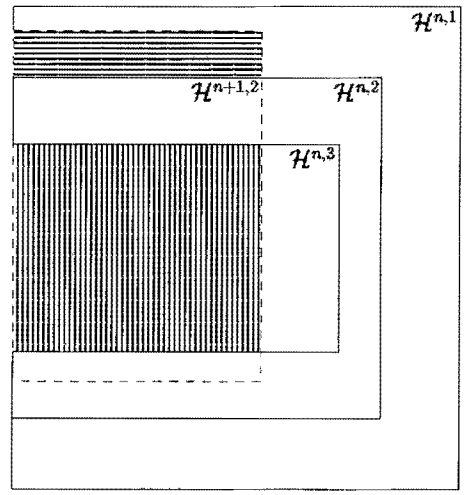

FIGURE 3.8: Three grids at time τ^n (solid lines) and a grid at the next time step τ^{n+1} (enclosed by the dashed lines) with the same level as $\mathcal{H}^{n,2}$. In the vertically striped region the new grid coincides with a finer grid at the previous time step, in the horizontally striped region only a coarser grid existed at τ^n, and in the region that is not filled a grid at the same level existed at τ^n.

consideration in the choice of the prolongation is the conservation of charge in the discretizations. For simplicity, we will first consider a one-dimensional prolongation, which is then easily extended to more dimensions.

We consider coarse grid values $U^K = \{u_I^K\}$. Then a mass conserving interpolation for values $U^k = \{u_i^k\}$ on a grid twice as fine is,

$$u_i^k = U_I^K + D_I\,, \quad u_{i+1}^k = U_I^K - D_I\,, \tag{3.2.10}$$

which obviously implies mass conservation,

$$\Delta z^l u_i^k + \Delta z^l u_{i+1}^k = \Delta z^L U_I^K\,. \tag{3.2.11}$$

Using a three-points stencil, the coefficient D_I can be written as

$$D_I = \alpha_{-1} U_{I-1} + \alpha_0 U_I + \alpha_1 U^{I+1}\,. \tag{3.2.12}$$

Then the interpolation is second order accurate if

$$D_I = \frac{1}{8}(U_{I-1} + U_{I+1})\,. \tag{3.2.13}$$

In the case of a three-dimensional geometry with axial symmetry, the expression for the interpolated value becomes, in cylindrical coordinates,

$$u_{i,j}^k = \tilde{u}_{i,J} + D_{i,J}^z\,, \quad \tilde{u}_{i,J} = \frac{R_I}{r_i} U_{I,J}^K + \frac{1}{r_i} D_{I,J}^r\,, \tag{3.2.14}$$

with

$$D^z_{i,J} = \frac{1}{8}(\tilde{u}_{i,J-1} - \tilde{u}_{i,J+1}), \; D^r_{I,J} = \frac{1}{8}(R_{I-1}U^K_{I,J-1} - R_{I+1}U^K_{I,J+1}), \quad (3.2.15)$$

in which $I = (i + i \mod 2)/2$ and $J = (j + j \mod 2)/2$.
Remark: This mass conserving interpolation might lead to new extrema or negative values. That could be prevented automatically by limiting the size of the slopes. However, in our simulations this turned out not to be necessary.

Boundary conditions

Finally, we need boundary values for all grids. On the coarsest grid these simply follow from the discretization of the boundary conditions (2.3.15)-(2.3.17), as explained in Sect. 3.1.1. On finer grids they are interpolated from coarse grid values. We will consider both bi-linear and bi-quadratic interpolations.

The bi-linear interpolation of $U^k = \{u^k_{ij}\}$ from the coarse grid values $U^K = \{u^K_{IJ}\}$ reads

$$\begin{aligned} u^k_{i,j} &= U^K_{I,J} + \frac{r_i - R_I}{\Delta r^K}(U^K_{I+1,J} - U^K_{I,J}) + \frac{z_j - Z_J}{\Delta z^K}(U^K_{I,J+1} - U^K_{I,J}) + \\ &\quad + \frac{r_i - R_I}{\Delta r^K}\frac{z_j - Z_J}{\Delta z^K}(U^K_{I+1,J+1} - U^K_{I+1,J} - U^K_{I,J+1} + U^K_{I,J}), \end{aligned} \quad (3.2.16)$$

where $I = (i - i \mod 2)/2$ and $J = (j - j \mod 2)/2$.

The quadratic interpolation is derived using the Lagrange interpolation formula to find $U^k = \{u^k_{ij}\}$ from the coarse grid values $U^K = \{u^K_{IJ}\}$. The interpolated value becomes

$$\begin{aligned} u^k_{ij} &= Int(U^K)_{ij} \\ &= \frac{1}{r^{l(k)}} \sum_{p=-1}^{1} \sum_{q=-1}^{1} r^{l(K)}_{I+p} u^K_{I+p,J+q} \prod_{\substack{P\neq p \\ P=-1}}^{1} \frac{r^{l(k)}_i - r^{l(K)}_{I+P}}{r^{l(K)}_{I+p} - r^{l(K)}_{I+P}} \prod_{\substack{Q\neq q \\ Q=-1}}^{1} \frac{z^{l(k)}_j - z^{l(K)}_{J+Q}}{z^{l(K)}_{J+q} - z^{l(K)}_{J+Q}} \end{aligned} \quad (3.2.17)$$

in which $I = (i+i \mod 2)/2$ and $J = (j+j \mod 2)/2$. The definition of I and J is different from the one for the linear interpolation because of the different stencil used for the interpolation. Note that the interpolated quantity is not σ but $r\sigma$ because of the cylindrical coordinate system.

As we shall see below, mass conservation at the grid interfaces is ensured by matching the fluxes, but we note that this interpolation is mass conserving in a global sense. The interpolation (3.2.14)-(3.2.15) conserves mass locally, that is, per cell. For notational convenience this will be demonstrated here only for the case of a one-dimensional polar coordinate system, but the proof is similar in the radially symmetric case. We denote by U_I the density on the coarse grid in the point $R_I = (I - \frac{1}{2})\Delta R$, and u_i the density on the grid twice as fine in the

point $r_i = (i - \frac{1}{2})\Delta r$. In this case the above interpolation formula reduces to

$$u_i = \frac{1}{r_i} \sum_{p=-1}^{1} r_{I+p} u_{I+p} L_{I,p}(r_i) \tag{3.2.18}$$

with

$$I = I(i) = (i + i \mod 2)/2\,, \qquad L_{I,p}(r) = \prod_{\substack{P=-1 \\ P \neq p}}^{1} \frac{r - R_{I+P}}{R_{I+p} - R_{I+P}}\,.$$

We have

$$\sum_{p=-1}^{1} L_{I,p}(r) \equiv 1\,, \tag{3.2.19}$$

which follows from the observation that interpolating a constant function will be exact. The interpolation results in two different values of the densities in the two fine grid cells i and $i+1$ that are contained in the coarse cell I, so the total mass μ on the fine grid can be written as

$$\begin{aligned} \Delta r \sum_i r_i u_i &= \Delta r \sum_{i \text{ odd}} (r_i u_i + r_{i+1} u_{i+1}) \\ &= \Delta r \sum_{i \text{ odd}} \Big(\sum_{p=-1}^{1} L_{I,p}(r_i) R_{I+p} U_{I+p} + \sum_{p=-1}^{1} L_{I,p}(r_{i+1}) R_{I+p} U_{I+p} \Big)\,. \end{aligned}$$

We can thus write

$$\mu = \Delta r \sum_I \sum_{p=-1}^{1} (L_{I,p}(r_i) + L_{I,p}(r_{i+1})) R_{I+p} U_{I+p}\,,$$

which, rearranging the terms and using property (3.2.19), leads to:

$$\mu = 2\Delta r \sum_I R_I U_I = \Delta R \sum_I R_I U_I\,,$$

which is the total mass on the coarse grid. Hence the interpolation is mass conserving in a global sense.

Flux conservation at grid interfaces

The mapping from one grid to the other must take into account a flux correction on grid interfaces, in order to ensure mass conservation. This correction yields that the total mass going through one coarse grid cell must be the same as the sum of total mass going through two fine grid cells (see Figure 3.9). Taking into

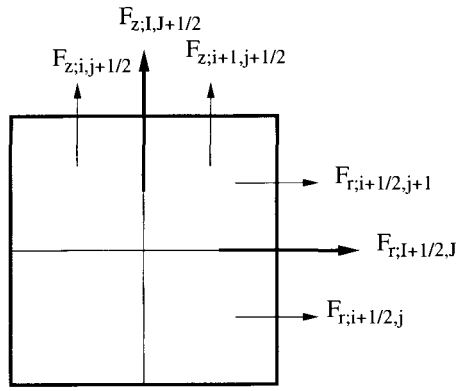

FIGURE 3.9: The fluxes on coarse and fine grids; the mass fluxes through the coarse grid cell should be the same as the sum of the fine cell fluxes.

account the cylindrical geometry of the system, the fluxes through coarse grid cells become, in terms of the fine grid fluxes,

$$\begin{aligned} F^K_{r;I+1/2,J} &= \frac{\Delta r^l}{\Delta r^L}(F^k_{r;i+1/2,j} + F^k_{r;i+1/2,j+1}), \\ F^K_{z;I,J+1/2} &= \frac{\Delta r^l}{\Delta r^L R_I}(r^l_i F^k_{z;i,j+1/2} + r^l_{i+1} F^k_{z;i+1,j+1/2}), \end{aligned} \tag{3.2.20}$$

where $i = 2I - 1$ and $j = 2J - 1$.

3.2.4 Refinement scheme for the Poisson equation

The refinement strategy for the computation of the electric potential is also based on a static regridding approach, where the grids are adapted after each complete time step. In this case, however, the refinement criterion is not based on a curvature monitor but on an iterative error estimate approach. The FISHPAK routine will be used on a sequence of nested grids $\mathcal{G}^m$. The solution on a coarse grid will be used to provide boundary conditions for the grid on the finer level, which will in general extend over a smaller region. This approach is explained in full detail in [103]; here we will discuss the main features of the scheme.

Starting from the (known) charge density distribution $\sigma - \rho$ on a set of grids $\{\mathcal{H}^k\}$, the Poisson equation is first solved on the two coarsest grids $\mathcal{G}^1$ and $\mathcal{G}^2$, both covering the entire computational domain $(0, L_r) \times (0, L_z)$. The finest of these two grids is coarser or as coarse as the coarsest grid of $\{\mathcal{H}^k\}$. The densities should then first be mapped onto the coarse grids $\mathcal{G}^1$ and $\mathcal{G}^2$, using the restriction formula (3.2.6). The source term of the Poisson equation is then known on these two coarse grids, and the Poisson equation is solved using a

FISHPAK routine that discretizes Eq. (3.1.3) using second-order differences:

$$\begin{aligned} \sigma_{i,j}^m - \rho_{i,j}^m &= \frac{\phi_{i+1,j}^m - 2\phi_{i,j}^m + \phi_{i-1,j}^m}{(\Delta r^l)^2} + \frac{\phi_{i+1,j}^m - \phi_{i-1,j}^m}{2r_i^l \Delta r^l} \\ &+ \frac{\phi_{i,j+1}^m - \phi_{i,j}^m + \phi_{i,j-1}^m}{(\Delta z^l)^2} \end{aligned} \tag{3.2.21}$$

in which $l = l(m)$ is the level of grid $\mathcal{G}^m$. This system of linear equations is then solved using a cyclic reduction algorithm, see [35]. The details of FISHPAK are described in [85]. The subroutine was used as a black box in our simulations. A comparison with iterative solvers, multigrid or conjugate gradient type, can be found in [17]. For the special problem we have here – Poisson equation on a rectangle – such iterative solvers are not only much slower than FISHPAK, but they also require much more computational memory.

The boundary conditions that are used for the grids that cover the entire computational domain are:

$$\begin{aligned} &\phi(r,0,t) = 0\,, \qquad \phi(r,L_z,t) = -E_0 L_z\,, \\ &\frac{\partial\phi}{\partial r}(0,z,t) = 0\,, \qquad \frac{\partial\phi}{\partial r}(L_r,z,t) = 0\,. \end{aligned} \tag{3.2.22}$$

These boundary conditions correspond to a constant background electric field $\boldsymbol{\mathcal{E}} = (0, E_0)^{\mathrm{T}}$. It is assumed here that L_r has been chosen sufficiently large, so that the results near the symmetry axis $r = 0$ will have a very small effect on the field at $r = L_r$. As a next step, the coarse grid electric potentials ϕ^1 on $\mathcal{G}^1$ and ϕ^2 on $\mathcal{G}^2$ are compared with each other, by mapping ϕ^1 onto $\mathcal{G}^2$ with a quadratic interpolation based on a nine-point stencil as shown in Fig. 3.10.

For the prolongation that gives a continuous map of an electric potential $\phi^M = \{\phi_{IJ}^M\}$ onto a finer grid $\mathcal{G}^m$ we use the following formula, based on a least square fit:

$$\begin{aligned} \phi^m(r,z) &= Pro(\,\phi^M\,(r,z)) \\ &= \phi_{IJ}^M + c_{10}(r - r_I^M) + c_{01}(z - z_J^M) + \\ &+ c_{11}(r - r_I^M)(z - z_J^M) + \\ &+ c_{20}(r - r_I^M)^2 + c_{02}(z - z_J^{l-1})^2 \end{aligned} \tag{3.2.23}$$

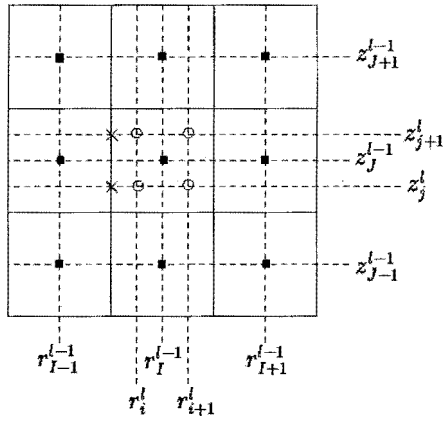

FIGURE 3.10: The nine-points stencil used to map coarse grid values of the electric potential ϕ^{l-1}_{IJ} onto the fine grid, thus obtaining $\phi^{l}_{i,j}$, $\phi^{l}_{i+1,j}$, $\phi^{l}_{i,j+1}$ and $\phi^{l}_{i+1,j+1}$. The cell centers of the coarse grid are marked with ■, those of the fine grids with ○, and the boundary points of the fine grids are marked with ×.

with coefficients

$$
\begin{aligned}
c_{10} &= \frac{1}{6\Delta r}(-\phi^M_{I-1,J-1} - \phi^M_{I-1,J} - \phi^M_{I-1,J+1} \\
&\quad +\phi^M_{I+1,J-1} + \phi^M_{I+1,J} + \phi^M_{I-1,J+1}), \\
c_{01} &= \frac{1}{6\Delta z}(-\phi^M_{I-1,J-1} - \phi^M_{I,J-1} - \phi^M_{I+1,J-1} \\
&\quad +\phi^M_{I-1,J+1} + \phi^M_{I,J+1} + \phi^M_{I+1,J+1}), \\
c_{11} &= \frac{1}{4\Delta r\Delta z}(\phi^M_{I-1,J-1} + \phi^M_{I+1,J-1} - \phi^M_{I-1,J+1} + \phi^M_{I+1,J+1}), \\
c_{20} &= \frac{1}{10\Delta r^2}(\phi^M_{I-1,J-1} - 2\phi^M_{I,J-1} + \phi^M_{I+1,J-1} \\
&\quad +3\phi^M_{I-1,J} - 6\phi^M_{I,J} + 3\phi^M_{I+1,J} \\
&\quad +\phi^M_{I-1,J+1} - 2\phi^M_{I,J+1} + \phi^M_{I+1,J+1}), \\
c_{02} &= \frac{1}{10\Delta z^2}(\phi^M_{I-1,J-1} + 3\phi^M_{I,J-1} + \phi^M_{I+1,J-1} \\
&\quad -2\phi^M_{I-1,J} - 6\phi^M_{I,J} - 2\phi^M_{I+1,J} \\
&\quad +\phi^M_{I-1,J+1} - 2\phi^M_{I,J+1} + \phi^M_{I+1,J+1}),
\end{aligned}
\tag{3.2.24}
$$

This interpolation will primarily be used to generate boundary conditions for the finer level, as illustrated in Fig. 3.10 for the boundary points on the finer grid marked with ×, but it will also be used for error estimation. The interpolation for the boundary conditions will be done such that there is a bias in the stencil toward the smooth region to enhance the accuracy.

The error of the solution on a grid $\mathcal{G}^m$ is then estimated by the point-wise difference between the solution on that grid and the interpolation of the solution on the underlying coarser grid $\mathcal{G}^M$:

$$g^m_{i,j} = \phi^m_{i,j} - (Pro\ \phi^M)_{i,j}\,. \tag{3.2.25}$$

The refinement criterion is as follows:

$$\text{refine all grid cells } i,j \text{ where } |g^m_{i,j}| \geq \epsilon_\phi \tag{3.2.26}$$

where ϵ_ϕ is a small parameter that still has to be chosen. This leads to new and finer grids on which the whole procedure of mapping the charge densities onto it, solving the Poisson equation using the FISHPAK routine and estimating the error is repeated, and so on until the error is smaller than ϵ_ϕ everywhere or until the finest desired level is reached. Notice that, since the grids do not cover the whole computational domain anymore, the boundary conditions (3.2.22) do no longer hold. We now have Dirichlet boundary conditions on each boundary that lies in the interior of the computational domain, and they are computed by interpolating the electric potential on the finest grid that is known using Eq. (3.2.23). Using this third order interpolation formula implies that the error introduced by the interpolation is negligible compared to to discretization error, which is second order. With this method there is an upper bound for the maximum error e^m on grid m with level l [103]:

$$e^m \leq \max_{i,j} g^m_{ij} + (l-1)\epsilon_\phi, \tag{3.2.27}$$

where $g^m = \max g^m_{ij}$ as been defined in Eq. (3.2.25). This means that the extra error due to the refinement can be made as small as wanted provided ϵ_ϕ is taken small enough.

The electric field has to be known on the continuity grids $\mathcal{H}^k$, since it appears in the continuity equations (2.3.12)-(2.3.12). However it has to be computed from the electric potential that is only known on the Poisson grids, using Eq. (3.1.4). We consider the grid $\mathcal{H}^k$ with level $l(k)$ on which the electric field has to be known, and the finest potential grid $\mathcal{G}^m$ with level $l(m)$, which has a non-empty intersection with $\mathcal{H}^k$.

There are three possible situations: the potential grid can be either coarser, as fine as, or finer than the continuity grid. If both grids have the same size ($l(k) = l(m)$), or if the continuity grid is coarser than the Poisson grid ($l(k) < l(m)$), then the field components are set directly with a second order central approximation of Eq. (3.1.4), using the neighboring points of the point where the field components need to be known. If the Poisson grid is coarser than the continuity grid ($l(k) > l(m)$), the electric field is first computed on the Poisson grid with a second order central approximation of Eq. (3.1.4), and then this field is interpolated to the continuity grid. The interpolation is performed with a piecewise bilinear approximation.

3.2.5 Overall algorithm

In the previous sections, the refinement algorithms for the continuity equations and the Poisson equation have been treated separately. We here describe the overall algorithm.

We start from known density distributions of the charged particles σ^n and ρ^n at a certain time τ^n, on a set of grids $\mathcal{H}^{n,k}$. The electric field induced by the charges on the grids $\mathcal{H}^{n,k}$ is computed using the refinement method described in Sect. 3.2.4.

The step size for the time integration is then set in such a way that the stability conditions (3.1.20)-(3.1.21) of both advection and diffusion discretizations are met on the finest grid. The values of both ν_a and ν_d have been taken as 0.1, which is smaller than the maximal values of 0.87 and 0.37 respectively, specific to the third-order upwind scheme for the advection and the second-order central discretization for diffusion, together with a two-stage Runge Kutta time integration method [39].

Then, starting on the finest grid level, the particle fluxes are computed on each grid and corrected using the flux correction formulas (3.2.20). The first stage of the Runge Kutta step (3.1.18) can then be carried out. The field induced by the density predictors $\bar{\sigma}^n$ and $\bar{\rho}^n$ is again computed using the procedure described in Sect. 3.2.4. The new boundary conditions for the particle densities are then computed on all grids $\mathcal{H}^{n,k}$, and the second stage of the Runga-Kutta method is carried out in the same way as the first stage. We then obtain the density distributions σ^{n+1} and ρ^{n+1} on the set of grids $\mathcal{H}^{n,k}$.

Following the procedure described in Sect. 3.2.3, after restriction of fine grid values to the parent grids, the grids $\mathcal{H}^{n+1,k}$ for the next time step are computed using the refinement monitor (3.2.8). The densities are then mapped from the grids $\mathcal{H}^{n,k}$ to the grids $\mathcal{H}^{n+1,k}$, and the new boundary conditions are computed. We thus obtain the density distributions σ^{n+1} and ρ^{n+1} on the set of grids $\mathcal{H}^{n+1,k}$ at the new time τ^{n+1}.

3.3 Tests of the algorithm on a planar ionization front

3.3.1 Governing equations

In order to test the implementation of the grid refinements, we first consider the evolution of a planar streamer front, which has been investigated theoretically [29, 30]. This will exhibit clearly any errors in the implementation. Moreover, this will allow us to draw some conclusions on the tolerances and interpolations to use in the more general two-dimensional simulations.

Initially we have an ionization seed

$$\sigma(r,z,0) \;=\; \rho(r,z,0) \;=\; 10^{-4}\exp\left(-\frac{(z-z_0)^2}{100}\right) \tag{3.3.1}$$

situated as $z = z_0$, and a constant background electric field $\boldsymbol{\mathcal{E}}_b = -|\boldsymbol{\mathcal{E}}_b|\hat{\mathbf{e}}_z$. The spatial region in this specific example is $(r, z) \in [0, L] \times [0, L]$ with $L = 1024$. The boundary conditions for the electron density and the electric field are

$$\begin{aligned} \sigma(r,0,\tau) &= 0\,, & \frac{\partial\sigma}{\partial z}(r,L,\tau) &= 0\,, \\ \frac{\partial\sigma}{\partial r}(0,z,\tau) &= 0\,, & \frac{\partial\sigma}{\partial r}(L,z,\tau) &= 0\,, \\ \phi(r,0,\tau) &= 0\,, & \frac{\partial\phi}{\partial z}(r,L,\tau) &= |\boldsymbol{\mathcal{E}}_b|\,. \\ \frac{\partial\phi}{\partial r}(0,z,\tau) &= 0\,, & \frac{\partial\phi}{\partial r}(L,z,\tau) &= 0\,. \end{aligned} \tag{3.3.2}$$

In this effectively one-dimensional case, because of the independence of all the unknowns on the radial coordinate, we write the electric field as $\boldsymbol{\mathcal{E}}(r, z, \tau) = \mathcal{E}(z, \tau)\hat{\mathbf{e}}_z$. It is then possible to obtain the electric field directly from the charge densities by integrating Eq. (2.3.14) along the z-direction and using the boundary condition $\mathcal{E} = -|\boldsymbol{\mathcal{E}}_b|$ for the electric field at $z = L$,

$$\mathcal{E}(z,\tau) = -|\boldsymbol{\mathcal{E}}_b| + \int_z^L (\sigma(z',\tau) - \rho(z',\tau))\, dz' \tag{3.3.3}$$

From the electron and positive ion density at time t^n, the electric field $\mathcal{E}^n$ can be solved at each cell vertex by discretizing Eq. (3.3.3). Starting from the value at $z = L$, which corresponds to $j = M$ on a grid with M grid points in the z-direction, we thus obtain:

$$\begin{aligned} \mathcal{E}^n_{M+\frac{1}{2}} &= -|\boldsymbol{\mathcal{E}}_b| \\ \mathcal{E}^n_{j+\frac{1}{2}} &= \mathcal{E}^n_{j+\frac{3}{2}} + \Delta z(\sigma^n_{j+1} - \rho^n_{j+1})\,. \end{aligned} \tag{3.3.4}$$

The electric field strength in the cell centers is then taken as the average field of the corresponding vertices,

$$|\mathcal{E}|^n_j = \frac{1}{2}\left|\mathcal{E}^n_{j-\frac{1}{2}} + \mathcal{E}^n_{j+\frac{1}{2}}\right| \tag{3.3.5}$$

Fig. 3.11 shows the temporal evolution of the initial ionization seed (3.3.1) situated at $z_0 = 51$, with a background field $|\boldsymbol{\mathcal{E}}_b| = 1$ and a diffusion coefficient $D = 0.1$, on a uniform grid with grid size $\Delta_r = 32$ and $\Delta_z = 1/2$. The choice for the z_0 comes from the wish to compare it later on with a coarse grid computation ($\Delta_z = 2$), and the requirement to have the maximal value of the seed being well captured on this coarse grid. After an initial growth the electron density saturates after $\tau \approx 100$ into an uniformly translating front, growing into the direction opposite to the background field.

The front velocity is plotted as a function of time in Fig. 3.12. It has been evaluated numerically by tracking the displacement, within a time interval of 12.5, of the maximal net charge density $\sigma - \rho$. Up to $\tau \approx 100$, the space charge

layer that is being traced is formed. After this time, the velocity of the front approaches the asymptotic front velocity [30],

$$v^* = |\mathcal{E}_b| + 2\sqrt{D|\mathcal{E}_b|e^{-1/|\mathcal{E}_b|}}, \tag{3.3.6}$$

which, for these particular values of the background electric field and the diffusion coefficient, is equal to 1.3836.

3.3.2 Importance of the leading edge

In the following illustrations we have computed the temporal evolution of the densities and the electric field on a fine and on a coarse uniform grid as well as on locally refined grids. The refinement algorithm for the continuity equations is as explained in Sect. 3.2.3. In order to demonstrate the need for the leading edge to be included in the refinement, results with the "standard" refinement (i.e. without including the leading edge) will be compared to those that do include the leading edge. In this leading edge of the ionization front the densities decay exponentially, but the electric field strength is such that the reaction term is non-negligible. From theoretical studies [29, 30] it is known that this region is very important since it determines the asymptotic dynamics of the front.

For the present problem we use the a priori knowledge that the front moves to the right and the leading edge is the region ahead of the front. The standard

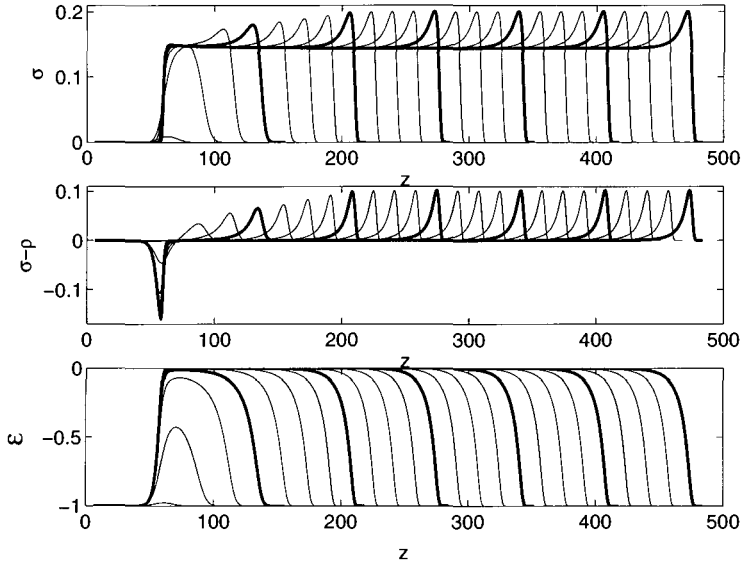

FIGURE 3.11: Uniform grid solutions of the planar streamer front with $|\mathcal{E}_b| = 1$ and $D = 0.1$, for $0 \leq \tau \leq 300$ with time steps of 12.5. The thick lines correspond to τ multiple of 50.

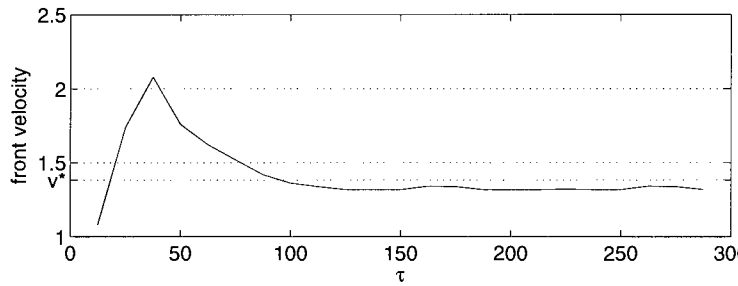

FIGURE 3.12: Numerical front velocity (solid line) as a function of time, compared to the theoretical asymptotic front velocity $v^* = 1.3863$

criterion reads,

$$\text{refine all grid cells } j \text{ where } \left|\frac{\partial^2 u}{\partial z^2}(z_j)\right| \geq \epsilon_u, \quad u = \sigma, \sigma - \rho \tag{3.3.7}$$

Second, we use the same criterion but now with the inclusion of the so-called leading edge in the refined region, taking into account the cut-off of densities below the continuum threshold of 10^{-12}, i.e.:

$$\begin{aligned} &\text{refine all grid cells } j \text{ obeying criterion (3.3.7),} \\ &\text{extend the refined region in the propagation direction} \\ &\text{to all } \{z_j | \sigma_j > 10^{-12}\}. \end{aligned} \tag{3.3.8}$$

Fig. 3.13 shows the results of the one-dimensional streamer simulation with tolerance values of 10^{-3} and 10^{-5} at $\tau = 300$, with a time step such that the Courant numbers for both advection and diffusion are at most 0.1, which is sufficiently small to render the temporal errors negligible.

The value of x_0 in the initial pulse (3.3.1) has been chosen such that the maximum of this Gaussian pulse was situated in a coarse grid cell center. Moreover, if a grid refinement is needed at the very first time step, the initial condition on the finer grids is not interpolated from the coarser grid values, but is calculated directly from Eq. (3.3.1), so that the initial pulse on the finer grids is computed without interpolation errors.

The results with a fine uniform grid can be considered as a reference solution, and it is clear that on the coarse uniform grid the front moves too fast and is too smooth, whereas the front computed on the standard refined grid moves too slowly. The coarse grid solution moving too fast is due to the large amount of numerical diffusion introduced by the coarse grid. As discussed in [29], this smoothening leads to less localized front solutions, which in turn may result in faster front speeds.

The method in which the leading edge is included in the refined region gives much better results than the standard refinement strategy with respect to the moving ionization front. This can be explained as follows: the region that is

refined does not necessarily have a fine grid at the previous time step, and therefore the values at previous time step must be interpolated from coarser grid values, leading significant errors in the front velocity.

3.3.3 Quadratic interpolation of the boundary conditions

In the previous section we showed that the use of a linear interpolation to map coarse grid values onto fine grid cells introduces artificial diffusion, and therefore requires a relatively strict tolerance in order for the front to be well captured. We here investigate whether the use of a quadratic instead of linear interpolation helps to overcome this.

Fig. 3.14 shows the results at $\tau = 300$ when a quadratic interpolation is used for the computation of the boundary conditions. It appears that in this case, if the leading edge is not included in the refinement, the front still moves too fast, however the error is reduced compared to when a linear interpolation is used.

In the case that the leading edge is included in the refinement, the choice of the interpolation does not appear to affect significantly the results.

In Table 3.1 the front velocities v_f are listed for the fine ($\Delta x = \frac{1}{2}$) and the coarse ($\Delta x = 2$) uniform grids, as well as for refined grids without inclusion

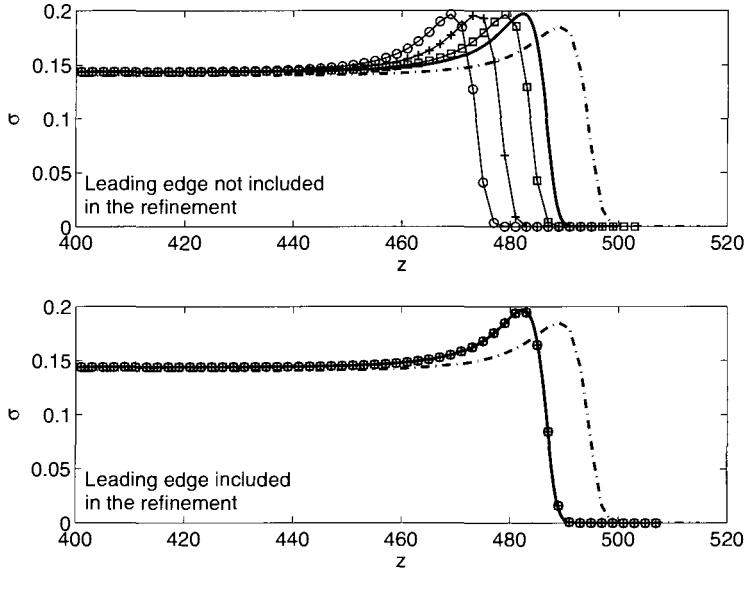

FIGURE 3.13: Approximations for $\sigma(z,\tau)$ at $\tau = 300$ on a fine grid ($\Delta z = \frac{1}{4}$), a coarse grid ($\Delta z = 2$) and refined grids ($\Delta z = 4, 2, 1, \frac{1}{2}, \frac{1}{4}$) with either the standard criterion (upper figure) or with leading edge included in the refined region (lower figure). *Dash dotted line*: uniform, $\Delta z = 2$; *solid line*: uniform, $\Delta z = \frac{1}{4}$; ○, refined, $\epsilon_\sigma = \epsilon_{\sigma-\rho} = 10^{-1}$; +, refined, $\epsilon_\sigma = \epsilon_{\sigma-\rho} = 10^{-3}$; □, refined, $\epsilon_\sigma = \epsilon_{\sigma-\rho} = 10^{-5}$.

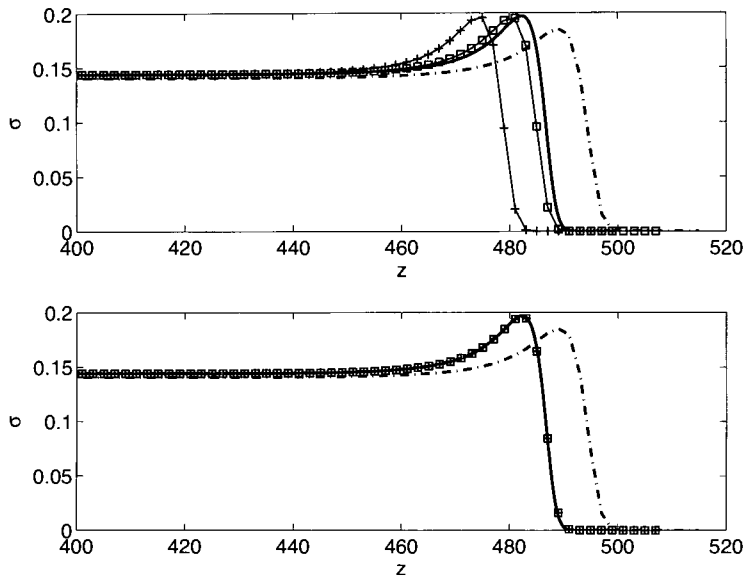

FIGURE 3.14: Comparison of the uniform grid solutions at $\tau = 300$ with those on refined grids with a refined grid computation with standard refinement (upper panel) and including the leading edge (lower panel), with a quadratic interpolation of the boundary conditions. *Solid line*: uniform grid $\Delta z = \frac{1}{2}$. *Dash dotted line*: coarse grid $\Delta z = 2$. +: $\epsilon_\sigma = \epsilon_{\sigma-\rho} = 10^{-3}$. □: $\epsilon_\sigma = \epsilon_{\sigma-\rho} = 10^{-5}$.

of the leading edge, and with linear or quadratic interpolation of the boundary conditions, with tolerances $\epsilon_\sigma = \epsilon_{\sigma-\rho} = 10^{-3}$. The given velocities have all been computed through the displacement of the maximal electron density between τ=250 and 262.5.

method	v_f
uniform $\Delta z = \frac{1}{4}$, 1st order upwind scheme	1.585
uniform $\Delta z = \frac{1}{4}$, flux limited scheme	1.380
uniform $\Delta z = 2$, flux limited scheme	1.440
standard refinement, linear interpolation	1.360
refinement including leading edge, lin. int.	1.380
refinement including leading edge, quad. int.	1.380

Table 3.1: Front velocities v_f on various grids. The refinements have been carried out with $\epsilon_\sigma = \epsilon_{\sigma-\rho} = 10^{-3}$. The exact asymptotic velocity is $v^* = 1.3836$.

It should be noticed here that the importance of the tolerance criterion for the total charge density will not appear in the one-dimensional case, since in this case, with the Neumann boundary condition at $z = L$, the electric field only

depends on the total charge, which is conserved within the grid refinements. In the two-dimensional case the electric potential, and thus the electric field, also depends on the distance to the charges, and consequently the curvature of the total charge density then will also play an important role.

From these tests it appears that the grid refinement based on a simple curvature monitor works well provided the leading edge is included in the regions of refinement. This is in accordance with [29] where the importance of the leading edge for dynamics of a planar front is discussed. The interpolation from coarse to fine grids should be quadratic. Using linear interpolation may introduce artificial diffusion, smoothing the front and thereby accelerating it.

We also looked at the results obtained by discretizing the advective term with a first-order upwind scheme. We concluded from those tests that, contrarily to what is said in [75], this scheme perform very badly. The amount of numerical diffusion introduced by that scheme completely changes the asymptotic velocities on realistic grids. Moreover, it is expected that the numerical diffusion will over-stabilize the numerical scheme thereby suppressing interesting features of the solutions.

We will continue with the propagation of curved ionization fronts at the tip of the streamer channels with cylindrical symmetry (2D case), which differs substantially from the planar front (1D case). For instance, the electric field cannot be found explicitly as in the 1D case, but has to be computed through the Poisson equation for the electric potential. Also, due to the curvature of the particle densities the electric field also will vary in space in the non-ionized region $\sigma = 0 = \rho$, restricting the forward extension of the leading edge by a decrease of the field, and the tolerance $\epsilon_{\sigma-\rho}$ will play a non-negligible role in that case.

3.4 Performance of the code on streamer propagation with axial symmetry

A planar ionization front as treated in the previous section is mainly of theoretical interest. Genuine streamers emerge from single electrons, thereby losing the planar characteristics. In such a case, it is no longer possible to compute the electric field by integrating it as in Eq.(3.3.3), and the use of a more sophisticated Poisson solver is needed.

3.4.1 Initial and boundary conditions for the test case

In this section the refinement algorithm as presented in Sect. 3.2 will be applied on a streamer initiated by a Gaussian ionization seed situated on the axis of symmetry at $z = z_0$.

$$\sigma(r, z, 0) = \rho(r, z, 0) = 10^{-4} \exp\left(-\frac{r^2 + (z - z_0)^2}{100}\right). \tag{3.4.1}$$

The computational domain is given by $(r, z) \in [-L_r, L_r] \times [0, L_z]$. Of course, because of the axial symmetry, the actual computations are carried out for $r \in [0, L_r]$. In contrast to the planar ionization front, we now impose the electric potential at the electrodes in such a way that a uniform background field $\boldsymbol{\mathcal{E}}_b = -|E_b|\hat{\mathbf{e}}_\mathbf{z}$ is applied over the gap. The boundary conditions for the electron densities and the electric potential now become,

$$\begin{aligned} &\frac{\partial \sigma}{\partial z}(r,0,\tau) = 0\,, \quad \frac{\partial \sigma}{\partial z}(r,L_z,\tau) = 0\,, \quad \frac{\partial \sigma}{\partial r}(L_r,z,\tau) = 0\,, \\ &\phi(r,0,\tau) = 0\,, \quad \phi(r,L_z,\tau) = |E_b|L_z\,, \quad \frac{\partial \phi}{\partial r}(L_r,z,\tau) = 0\,. \end{aligned} \tag{3.4.2}$$

We use homogeneous Neumann boundary conditions at the cathode ($z = 0$), which, together with the ionization seed placed on the cathode, means that electrons flow into the system.

3.4.2 Reference solution on a uniform grid

Let us first present the temporal evolution of the ionization seed (3.4.1) placed on the cathode at $z = 0$ in a background field $|E_b| = 0.5$, on a domain with dimensions $L_r = 1024$ and $L_z = 2048$. A uniform grid with grid size $\Delta r = \Delta z = 1$ covers the domain where both the electron and positive ion densities are strictly positive. This is a relatively coarse grid, but, as mentioned in Sect. 3.2.1, the use of finer grids would require too many grid points for the FISHPAK routine to handle within an acceptable accuracy. Therefore we will use this uniform grid computation as a reference to test the performance of the adaptive refinement method. Fig. 3.15 shows the snapshots of the electron and net charge density distributions as well as the electric field, at $\tau = 75$, 150, 225 and 300.

At $\tau = 75$, the maximal deviation of the electric field strength from its background value is around 0.4%, and space charges do not play a significant role yet. This is the electron avalanche phase, during which the Gaussian electron density distribution advects with an almost constant velocity, undergoes a diffusive widening, and grows due to the impact ionization, leaving behind a small trail with positive ions [67].

At $\tau = 150$ the space charges concentrate in a layer around the streamer head, as can be seen in the second column of Fig. 3.15. Due to its curvature, this space charge layer focuses the electric field ahead of the layer and the field is strongest near the axis of symmetry. The body of the streamer is highly ionized, its conductivity therefore is enhanced, and the electric field in the streamer body is lower than the background field. The space charge layer becomes thinner and denser in time, and the electric field is increasingly enhanced, as can be seen in the third column of Fig. 3.15. Eventually, the streamer becomes unstable, and branches. The beginning of this branching state is shown in the rightmost column of Fig. 3.15.

The space charge layer can be characterized by its half maximum width w and half maximum radius r_e, as depicted in Fig.3.16. The width of the

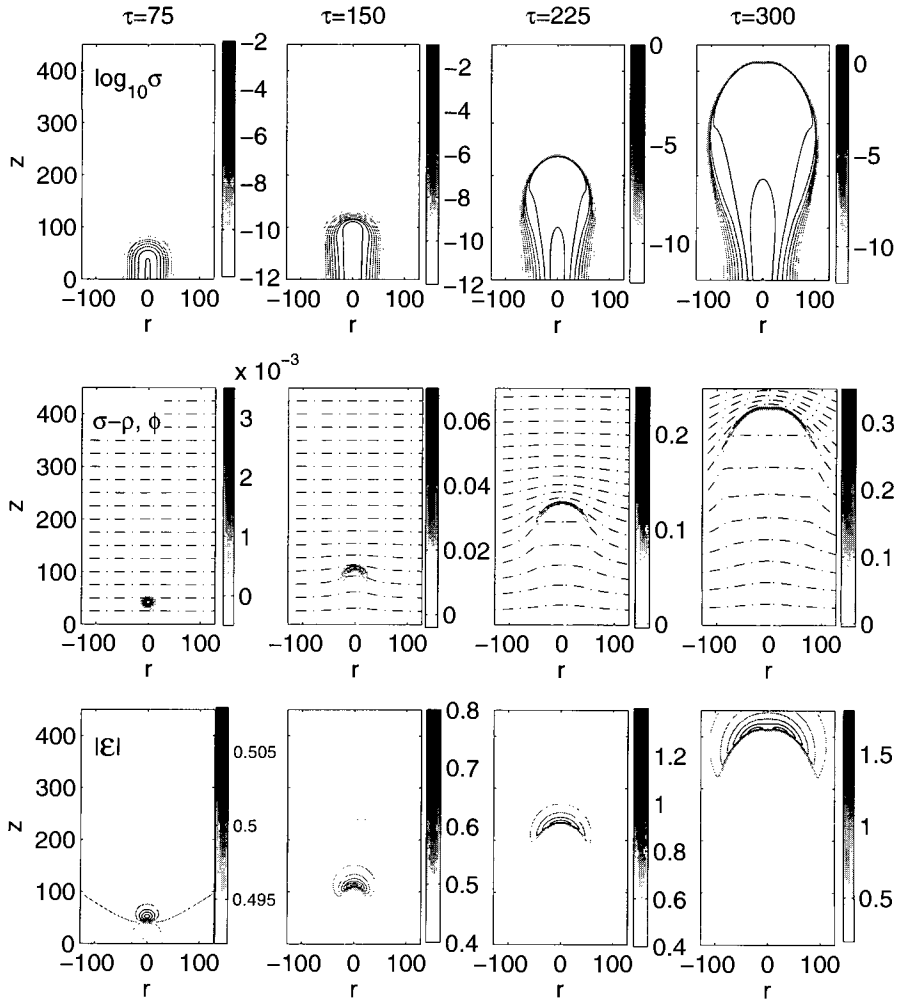

FIGURE 3.15: Propagation of a Gaussian ionization seed as given by Eq.(3.4.1) in a background field $|\mathcal{E}_b| = 0.5$. The snapshots correspond to times τ=75, 150, 225 and 300. *Upper row*: the logarithm of the electron density σ. *Middle row*: the net charge density $\sigma - \rho$. *Lower row*: the electric field strength $|\mathcal{E}|$. The grid covers the region where the particles densities are strictly positive, which is up to $z \approx 450$ for $\tau = 75$.

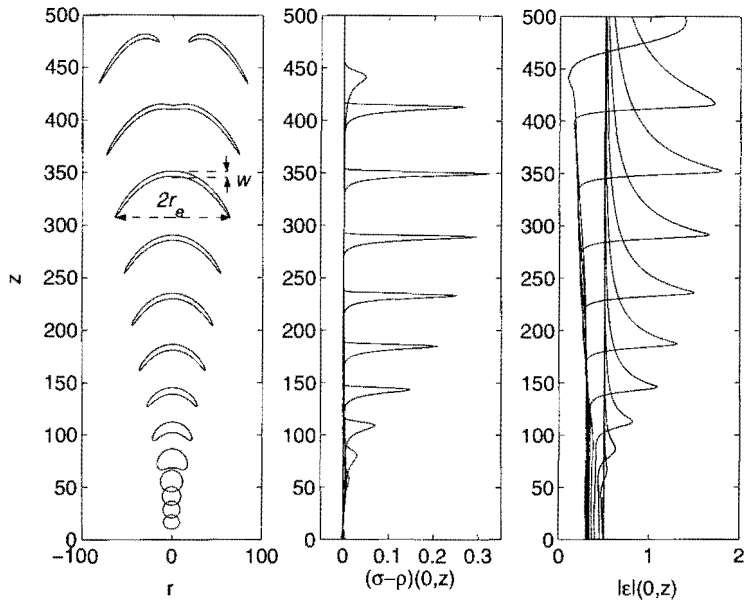

FIGURE 3.16: Left: contour lines of $\sigma - \rho = (\sigma - \rho)_{max}/2$ at $\tau = 25$ to 325 with steps of 25. The definition of the half maximum width w and radius r_e are depicted as well. The middle and right hand side show the axial values of the net charge density and the electric field strength, respectively, at the same times.

space charge is defined as the width of the front on the axis of symmetry, measured between the points at which the net charge density has dropped to one half of its global maximum. The half maximum radius is defined as the maximal value of r, at which the net charge density has dropped to one half of its global maximum. From this figure, the three phases of the streamer propagation appear very clearly. During the avalanche phase, the space charge cloud widens due to diffusion. The space charge then builds up to form a fine, curved layer that enhances the field ahead of it, while shielding partially the quasi-neutral channel behind it from the background field. The width of the space charge layer decreases until saturation around $w \approx 5$, while its radius is continuously growing in time. The ration w/r_e therefore decreases in time, so that the streamer front approaches the limit of a planar front, which at some point becomes unstable and branches.

3.4.3 Influence of the refinements

Let us now consider the effect of the refinements on the streamer dynamics, as well as the effect of cutting off the densities that are below the continuum threshold. To this end, we run the simulations with the same parameters – background field, initial and boundary conditions – as in the previous subsection,

but we now allow two levels of refinement for the continuity equations, and seven levels of refinement for the Poisson equation. The finest grids in both cases have a finest mesh size $\Delta r = \Delta z = 1$. Later on in this thesis, more levels will be used.

From Sect. 3.3 we could see that, provided the leading edge of the streamer front is included in the refinement, and a quadratic interpolation is used to provide the boundary conditions for finer grids, a tolerance for the continuity equations of $\epsilon_\sigma = 10^{-3}$ is well suited. Moreover, the error in the spatial discretization of the net charge density is induced by the discretization of the drift and diffusion terms in Eq.(2.3.12), since the continuity equation for the net charge density can simply be written as

$$\frac{\partial(\sigma - \rho)}{\partial \tau} = \nabla \cdot (\sigma \mathcal{E}) + D\nabla^2 \sigma \,. \tag{3.4.3}$$

Hence it is natural to take the tolerance for the net charge density equal to that for the electron density. The choice for the tolerance for the refinement of the Poisson equation is less straightforward.

In one dimension, the second order discretization of the Poisson equation (2.3.14) reads

$$\nabla^2 \phi = \frac{\phi_{i+1} - 2\phi_i + \phi_{i-1}}{\Delta z^2} = \sigma_i - \rho_i \,, \tag{3.4.4}$$

and the discretization error then becomes

$$\delta\phi = \frac{\Delta z^2}{12} \frac{\partial^4 \phi}{\partial z^4} = \frac{\Delta z^2}{12} \frac{\partial^2 (\sigma - \rho)}{\partial z^2} \,. \tag{3.4.5}$$

Therefore, in the one-dimensional case, the curvature monitor for the net charge density will also give the error in the spatial discretization of ϕ. In higher dimensions, however, this correspondence does not strictly hold anymore. Nevertheless we assume that the tolerance for $\sigma - \rho$ will still give a good estimation for the error in the solution of the Poisson equation, and we therefore take

$$\epsilon_\phi = \epsilon_{\sigma-\rho} = \epsilon_\sigma = 10^{-3} \,. \tag{3.4.6}$$

The number of grid points in the $r-$direction contained in each fine grid for the continuity equations has been chosen as $M_0 = 32$.

The net charge density distribution and the equipotential lines at $\tau = 75$, 150, 225 and 300 are plotted in Fig. 3.17, together with the grids both on which the continuity equations and the Poisson equation, respectively, have been solved.

The influence of the refinements on the position of the streamer front on the axis of symmetry is shown in the upper plot of Fig. 3.18. It is obvious that neither the refinement of the grid for the Poisson equation, nor the refinement of the continuity equation significantly influence the position of the ionization front on the axis. The effect of the refinements on the maximal axial value of the electric field strength, shown in the lower plot of Fig. 3.18, only becomes visible

after the streamer has become unstable. We will show in Chap. 7 that, due to this instability, minor details (like the numerical grid) will affect the further evolution.

Since the streamer front is not planar anymore, it is necessary to investigate the effect of the refinements not only on the axis, but in the whole streamer. The evolution of the half maximum contours of the net charge density is depicted in Fig. 3.19. There appears to be an excellent correspondence between the uniform grid computation and the one where all grids are refined. At some places there is slight difference between the results, but this is also a consequence of the results being plotted for the coarsest grid, i.e. $\Delta r = \Delta z = 1$ for uniform

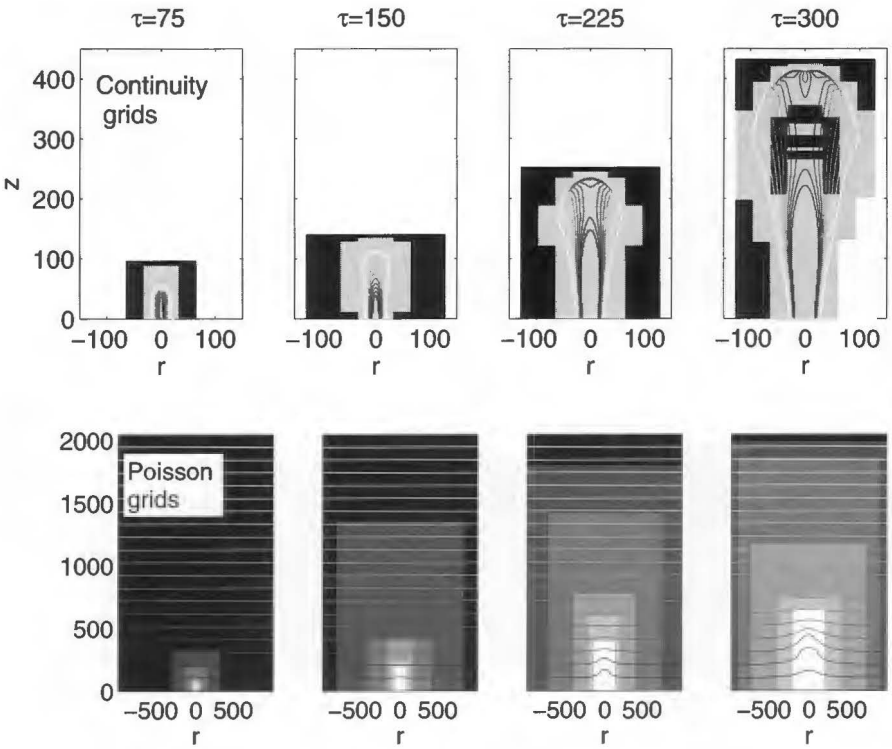

FIGURE 3.17: Grid distributions for the continuity equations (upper row), and for the Poisson equation (lower row). The times are the same as in Fig. 3.15. For the continuity grids, the black and gray regions are covered with grids with mesh sizes $\Delta r = \Delta z = 2$ and 1, respectively. The coarsest grid for the continuity equations only covers the domain on which the particles are above the continuum threshold. The two coarsest grids ($\Delta r = \Delta z = 128$ and 64) on which the Poisson equation has been solved cover the whole computational domain, which is filled in black. The finer grids with mesh sizes 32, 16, 8, 4 and 2 are plotted in lighter gray shades, the white domain is covered by the finest grid $\Delta r = \Delta z = 1$. Notice that the plots cover different spatial regions in the upper and the lower row.

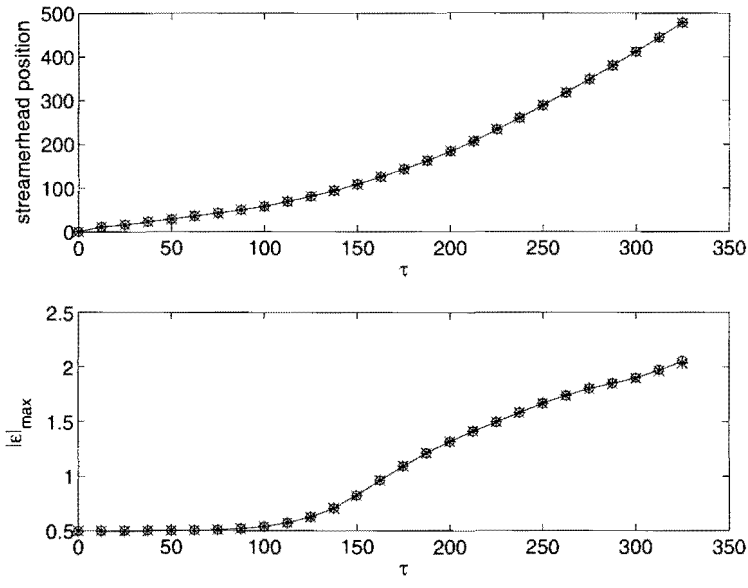

FIGURE 3.18: The position of the streamer front (maximum of the net charge density on the axis of symmetry) as a function of time. *Solid line*: uniform grid computation. +: refinement of the grids for the Poisson equation only. ○: refinement of the grids for the continuity equations only. ×: refinement of all grids.

grid, and $\Delta r = \Delta z = 2$ for the refined grids. The grid points of the plotted results therefore do not coincide, and the contours consequently might be slightly different. Up to branching, however, there is no significant error in either the radius or the width of the space charge layer. The effect of the refinement only becomes visible once the streamer has become unstable, which, as explained before, is of no major importance with regards to the onset of the instability. We notice here that, for the sake of clarity of the figure, Fig. 3.19 is not drawn in equal aspect ratio, therefore the streamer front might seem different from that of Fig. 3.16. Fig.3.19 has to be completed by the evolution of the axial charge density distribution of the streamer, in order to be sure not only of the same position of the half maximum contours, but also of the maxima themselves. This is shown in Fig. 3.20, where the axial charge density and electric field strength distributions are shown for the same times as Fig. 3.19. Again it appears that, at least up to the branching, the adaptive grid refinement method produces results that agree very well with the uniform grid computation.

Finally, because of the charge conservation during an ionization event, it should be verified that the refinements are indeed mass conserving, as has been taken care of in Sect. 3.2.3. This is shown in Fig.3.21, where we have compared a uniform grid computation where the densities below the continuum threshold have not been cut off, with the refined grid computation. It is clear that neither

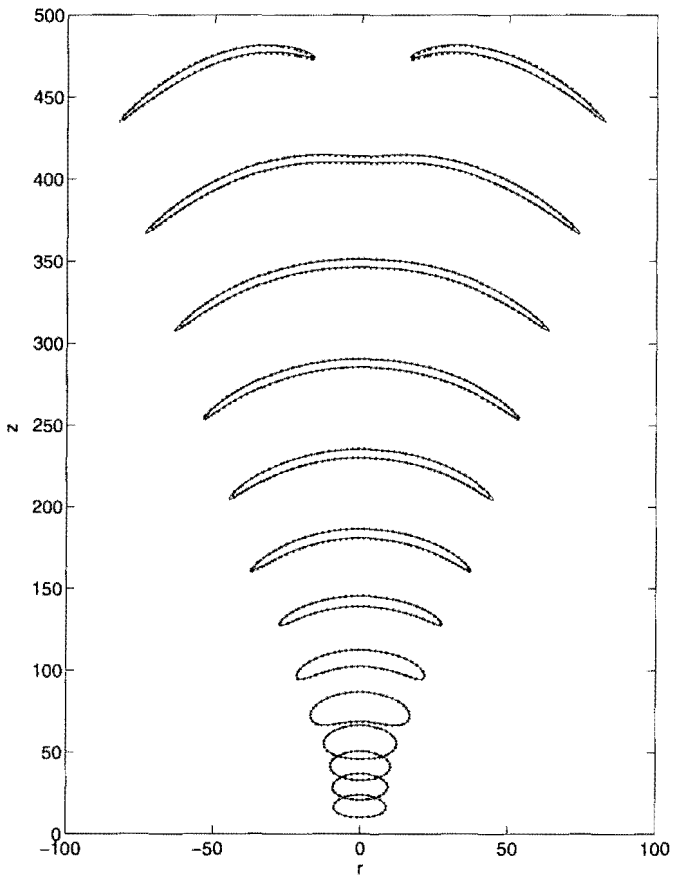

FIGURE 3.19: Contours of the half maximum of the net charge density for $\tau = 25$ to 325, with steps of 25. *Solid line*: uniform grid ($\Delta r = \Delta z = 1$). *Dots*: grid refinement ($\Delta r = \Delta z = 1, 2$). Notice that, for clarity, the plot is not equal aspect ratio.

the cut-off, nor the refinement disturb the total number of particles in a visible way.

The gain in memory obtained with the refinement method can be observed through the number of grid points that are used to solve the continuity equations and the Poisson equation. As can be seen in Fig.3.22, the number of grid points used are one to three orders of magnitude smaller than in the computations as performed in [83], where a uniform grid covers the whole computational domain.

We emphasize that in the previous test the choice for two levels of refinements has been made in order to compare the results with uniform grid computations. In later simulations we will use more refinement levels, thereby reaching much smaller mesh sizes. We can, however, extrapolate the outcome of these tests to

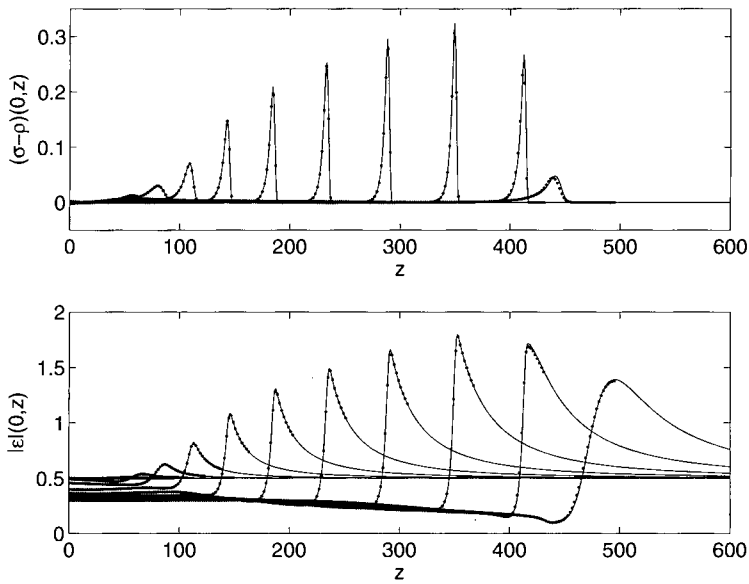

FIGURE 3.20: Axial distributions of the net charge density (upper plot) and electric field strength (lower plot) for $\tau = 25$ to 325, with steps of 25. *Solid line*: uniform grid ($\Delta r = \Delta z = 1$). *Dots*: grid refinement ($\Delta r = \Delta z = 1, 2$).

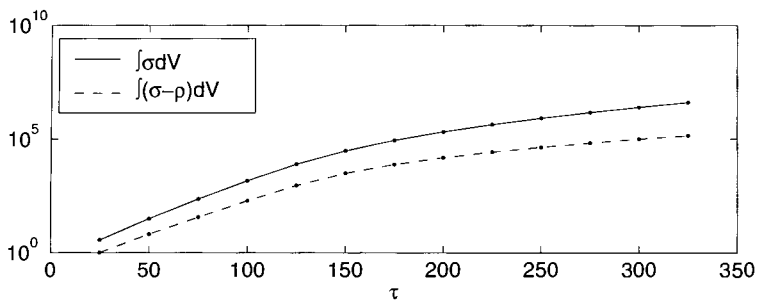

FIGURE 3.21: Evolution of the total number of electrons (solid line) and net charge (dashed line). The lines correspond to a uniform grid computation without cutting off the densities below the continuum threshold, the dots to the refined grid computation.

cases using more levels.

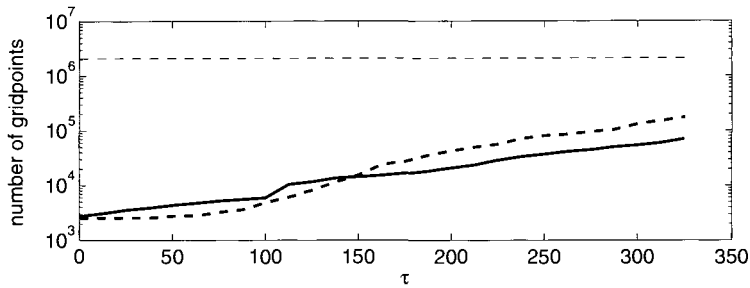

FIGURE 3.22: Number of grid points as a function of time. The thin dashed line represents the number of grid points corresponding to a grid of grid size $\Delta r = \Delta z = 1$ over the whole domain, i.e. 1024×2048. The thick lines give the temporal evolution of the number of grid points when the refinement algorithm is applied up to a finest mesh size of $\Delta r = \Delta z = 1$. *Solid line*: continuity equations, 1 level of refinement. *Dashed line*: Poisson equation, 6 levels of refinement.

3.5 Conclusions

We have presented an adaptive grid refinement strategy for the computation of the streamer propagation in a uniform background electric field, in a three dimensional geometry with radial symmetry. The refinement is based on the use of an explicit time stepping method, allowing us to refine separately the grids for the continuity equations and those for the Poisson equation. The refinement criterion of the continuity equations is based on a curvature monitor of the solution, while that of the Poisson equation is based on an error estimation. It results in two series of nested grids, one for the continuity and one for the Poisson equation, that communicate with each other using adequate restrictions and prolongations of the densities and the electric field. The refinement method has been implemented in such a way that mass, and therefore charge, is conserved during the refinements. Moreover, the densities below the continuum threshold are cut off. This will slightly influence the mass conservation, but it appears that this does not influence the streamer propagation. However it greatly improves the gain in computational memory.

The tests on a planar ionization front showed the importance of the leading edge being included in the refinements, in order for the front velocity to be well captured. These tests moreover show that a quadratic interpolation performs much better than a linear interpolation for the mapping of the boundary values.

A test on a non-planar streamer emerging from a small Gaussian ionization seed, in a relatively high background electric field, shows that the refinement method performs very well up to branching. The space charge layer, difficult to resolve because of the large spatial gradients in the charge distribution, is very well captured with the refinements. Moreover, in this test, the use of computational memory is three orders of magnitude smaller than a uniform grid computation as performed in [83]. The test on the non-planar front has

been performed with two grid levels for the continuity equation. Since further refinement is a nested iteration of the two-level case, we expect that refinement through more levels will yield reliable results as well.

This adaptive grid refinement procedure will allow us to compute the streamers of [83] with high spatial accuracy, as well as streamers in low background fields on large systems.

4

THE PHYSICAL STAGES OF STREAMER PROPAGATION

We present an overview of the evolution of an ionization seed in the electric field of a plane-parallel gap filled with a non-attaching gas. The results have been obtained with the algorithm presented in Chap. 3.

The streamer evolution is very dependent on the applied background field. We present generic results for an example of an overvolted gap and another one for on undervolted gap.

Three physical stages are passed. First, the electron avalanche phase, which is characterized by the absence of space charge effects, and therefore is *linear*. Then a space charge layer builds up around the streamer tip, altering the background electric field, and the *streamer regime* is entered, characterized by its nonlinearity. Finally the space charge layer becomes *unstable* and the streamer branches.

4.1 Introduction

The minimal streamer model derived in Chap. 2, is evaluated in a gas gap between by two plane-parallel electrodes. The gap is filled with a non-attaching gas like N_2, and the electrode configuration results in a uniform background electric field. The choice for this plane-parallel configuration has been made (i) because of its conceptual simplicity, (ii) because of its analogy with sprite discharges in the atmosphere [76].

Although a wide variety of experiments have been performed on the propagation of streamers in such gas gaps, a good theoretical understanding is still lacking, in particular regarding the influence of the gap being *overvolted* or *undervolted*. The definition of the over- and undervoltage of the gap is related to the ionization coefficient $\alpha(|\mathbf{E}|$ in the background field. For non-attaching gases like N_2, the (dimensionless) background electric field should be larger than approximately 0.2 for the gap to be overvolted.

In this thesis we present a detailed investigation of the streamer propagation, during which different physical stages are passed. Before looking at each stage in detail, we present an overview of all of them in both an under- and an overvolted gap, and give their main characteristics.

4.2 Parameters for computations in over- and undervolted gaps

We consider a gas between two planar electrodes. The simulations have been carried out in an axially symmetric coordinate system (r, z), the z-axis being the axis of symmetry, perpendicular to the electrodes. In this chapter we present two cases. One simulation has been carried out on a long, undervolted gap. This case will be designated by "(L)", referring to the relatively low electric field. The other simulation has been carried out on a short overvolted gap, and will be designated by "(H)", referring to the high background field.

4.2.1 Initial and boundary conditions

We refer to Sect. 2.3.3 for the boundary conditions for the electric potential and those for the electrons at the outflow boundaries. As an initial ionization seed we use equal Gaussian electron and positive ion distributions, as given by Eq. (2.3.16).

In case (L), the distance between the electrodes is set to $L_z = 2^{16} = 65536$, and the radial boundary is placed at $L_r = 2^{15} = 32768$. The background electric field strength is set to $|\mathcal{E}_b| = 0.15$. For N_2 at atmospheric pressure, this corresponds to an inter-electrode distance of approximately 15 cm, and a background electric field of 30 kV/cm. The height of the initial seed is set to $\sigma_0 = 1/4.7$, and its radius r_b is set to 10. In N_2 under normal conditions, this corresponds to an initial density of 10^{14}cm^{-3}, and a radius of 23 μm. The seed is placed on the cathode, at $z_0 = 0$. This high density of the initial seed has been chosen such that space charges affect the electric field rather rapidly. If one would start from a single electron, the undervoltage of the gap might never lead to the emergence of a streamer. At the cathode, we impose homogeneous Neumann boundary conditions for the electrons, permitting electrons to flow into the system.

In case (H), the distance between the electrodes is set to $L_z = 2048$ (5 mm for N_2 under normal conditions), and the radial boundary is situated at $L_r = 1024$. We use a background electric field with a strength of 0.5, which corresponds to 100 kV/cm if we consider a gap filled with N_2 at atmospheric pressure. The initial seed is placed at $z_0 = 50$, its maximal density is $\sigma_0 = 10^{-4}$, and its radius $r_b = 10$. This corresponds to a single electron placed in the bulk of the gap. Due to the overvoltage applied over the gap, this seed, in contrast to the undervolted case, turns out to lead to the emergence of the streamer. The placement of the small seed in the bulk of the gap ($z_0 \gg r_b$) results in practice

into a vanishing inflow of electrons into the system. This is further ensured by the use of homogeneous Dirichlet boundary conditions at the cathode.

4.2.2 Grid parameters

We use the algorithm described in Chap. 3 to compute the propagation of the ionization seeds. This algorithm demands the user to define a finest and coarsest mesh size for the grids on which the continuity equations and the Poisson equations will be solved. It also asks for the parameter M_0, which defines the size of the continuity grids in the radial direction. In both cases M_0 is set to 32.

In case (L) the finest mesh size for both continuity and Poisson equation is set to 2. We use 13 levels of refinement for the Poisson equation, and 6 for the continuity equations, which implies that the coarsest grids for the Poisson and the continuity equations have a mesh size of 8192 and 64, respectively.

In case (H) the coarsest grid for the Poisson solver has a mesh size of 64, while the coarsest continuity grid has a mesh size of 4. They are both refined up to a finest mesh size of $1/2$.

4.3 The linear avalanche phase

Let us first consider the high field case (H). Initially, the electrons of the initial ionization seed start drifting towards the anode under influence of the background electric field, while the ions stay immobile. During this initial phase, the space charges do build up but their effect on the electric field is still negligible, and the electric field hardly deviates from its background value, as is shown in the rightmost panel of Fig. 4.1. The equipotential lines therefore remain approximately undisturbed, as is shown in the third panel of Fig. 4.1.

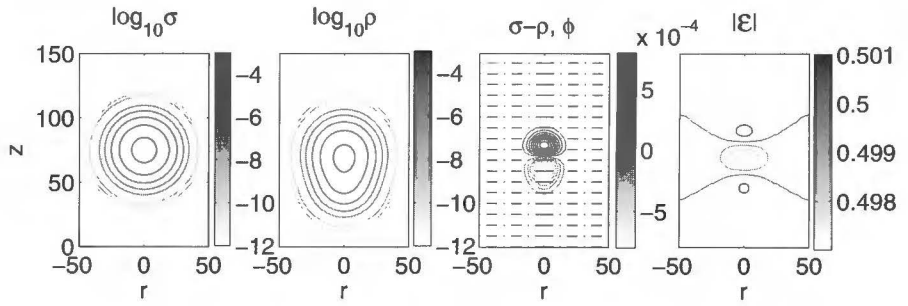

FIGURE 4.1: Avalanche regime at high fields (case (H), $|\mathcal{E}_b| = 0.5$). *From left to right*: logarithmic plot of the electron density distribution, logarithmic plot of the ion density distribution, net charge density distribution together with the equipotential lines (dash dotted lines), and electric field strength. The time of the snapshot is $\tau = 50$, which corresponds to 0.15 ns for N_2 at atmospheric pressure.

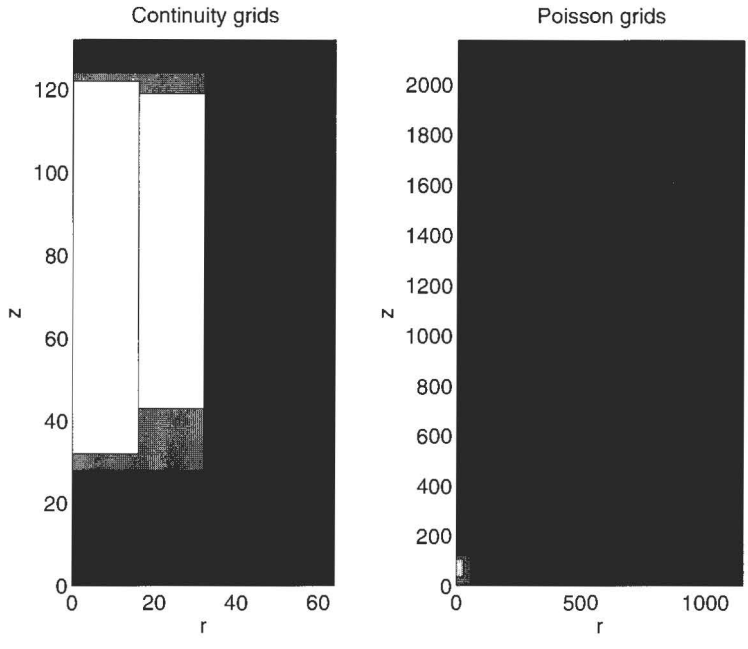

FIGURE 4.2: The grid distribution for the computation of the continuity equations (left column) and of the Poisson equation (right column) during the avalanche phase for case (H). The coarsest grids are black in both cases (the coarsest mesh size is of 2 for the continuity equations, and of 128 for the Poisson equation). Finer grids are shown in proportional shades of gray. The time of the snapshots are the same as in Fig. 4.1. The actual computational grids are shown, i.e. the region with $r > 0$. The results obtained on these grids are then mirrored around the z-axis, to obtain the plots shown in Fig. 4.1.

The leftmost panel of Fig. 4.1 shows that the electron cloud has conserved its Gaussian shape. This means that the electron cloud has indeed drifted in an almost constant and uniform background electric field, and has diffused. While they drift, the electrons also collide with neutral molecules, creating new electrons and ions. The electron cloud therefore also grows in amplitude once the reaction overcomes diffusion, (indeed, the maximal electron density in the leftmost plot of Fig. 4.1 is higher than the initial 10^{-4}). Moreover, the ions being immobile, they are left behind by the drifting electrons, which explains why the ion cloud (see the second plot of Fig. 4.1) is more extended towards the cathode than the electron cloud.

The net charge density distribution (see the third plot of Fig. 4.1) is dipole like. It consists of one negatively charged region ($\sigma - \rho > 0$) at the side of the anode (the dark region), and a positively charged counterpart (the light region). The existence of this positively charged counterpart is the result of the specific initial and boundary conditions used in this case, which, as mentioned earlier,

results in practice in a vanishing inflow of electrons into the domain. Together with the local charge conservation, this implies that the total amount of net charge in the whole system is zero as long as the streamer has not reached the domain boundaries. A negatively charged region therefore requires a positively charged counterpart for the whole system to be charge neutral. We notice that Raether [80] already developed this schematic picture of an electron avalanche (see also Fig. 1.2 in Chap. 1).

In Fig. 4.2 we show the grids on which the solution of Fig. 4.1 has been computed. The left panel gives the grid distribution for the continuity equations, the right panel that for the Poisson equation. We notice that the scales on which both distributions are plotted are different. This is due to the continuity grids only being defined on the small region where the continuum approximation for the particle densities hold, whereas the Poisson equation has to be solved on the whole computational domain. The finest grid for the continuity equation has a mesh size of $1/2$, which is equal to the finest mesh size allowed during this simulation. On the other hand, the finest grid for the Poisson equation has a mesh size of 4, which is eight times coarser than the finest mesh allowed. This also shows that the electric potential distribution only slightly deviates from its initial value.

In case (L), there is a major difference with case (H) in that the dense ionization seed is attached to the cathode (see the leftmost panel of Fig. 4.3). This electron cloud drifts towards the anode, and because of its high density it rapidly enhances the field (see the leftmost panel of Fig. 4.3). The space charges now no longer form a dipole like in case (H). Instead, there is only a negatively charged region, with relatively strong charge densities at the cathode. This is shown in the third plot of Fig. 4.3. Notice that the space charge densities have

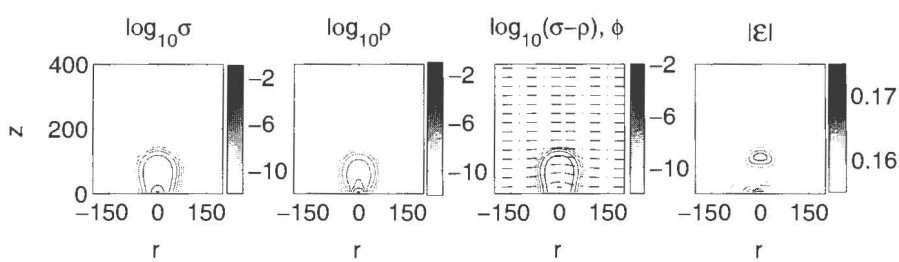

FIGURE 4.3: Initial stage of the streamer propagation at low fields (case (L), $|\mathcal{E}_b| = 0.15$). *From left to right*: logarithmic plot of the electron density distribution, logarithmic plot of the ion density distribution, logarithmic plot of the net charge density distribution together with the equipotential lines (dash dotted lines), and electric field strength. The time of the snapshot is $\tau = 500$, which corresponds to 3 ns for N_2 at atmospheric pressure. The net charge density is shown on the logarithmic rather than the linear scale because of the high space charges near the anode, which would prevent us from plotting adequately the net charge density on a linear scale.

been plotted on a logarithmic scale, this in order to capture adequately the whole space charge region.

The inflow of electrons leads to a rapid transition to the streamer regime. The two rightmost plots of Fig. 4.3 show a noticeable distortion of the equipotential lines, as well as an enhancement of the background electric field. This shows that the transition towards the streamer regime is already taking place. We emphasize that this rapid transition is due to the use of a very dense initial seed. A significant number of electrons then propagates towards the anode, leading almost immediately to the emergence of space charges that affect the background electric field. The same would be the case for the high field, while the initial conditions of the high field case in the low field would not allow a streamer to form.

The grids on which the solutions of Fig. 4.3 for case (L) have been computed are shown in Fig. 4.4. The coarsest grid for the continuity equations seems excessively extended in the radial direction, which is an effect of the fixed size of each grid in that direction, determined by $M_0 = 32$. However, the grid being extremely coarse (with a mesh size of 64), the extra amount of memory used to compute the solution on this region is negligible compared to the amount of

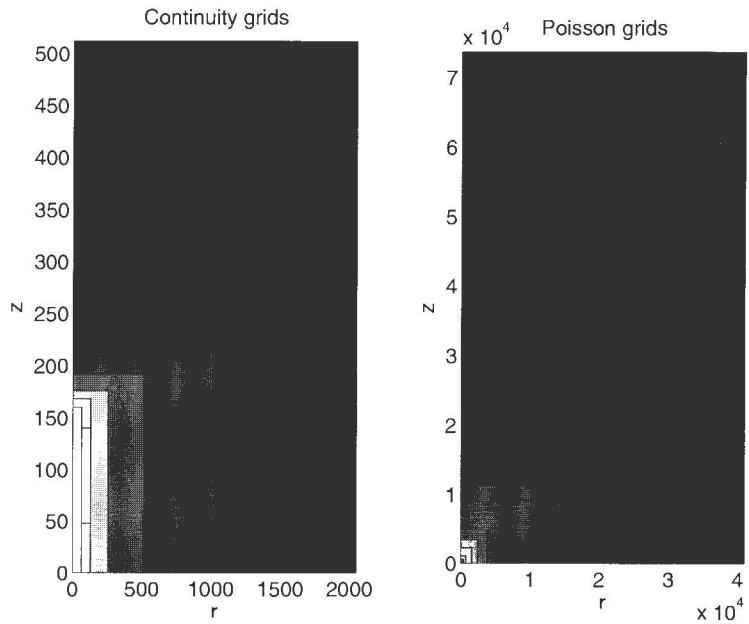

FIGURE 4.4: The grid distribution for the computation of the continuity equations (left column) and of the Poisson equation (right column) during the avalanche phase for case (L). The times of the snapshots are the same as in Fig. 4.3. Notice that, for plotting reasons, we have chosen not to use an equal aspect ratio for the continuity grids.

memory saved using this particular grid structure.

The main characteristic of the avalanche phase is the absence of space charge effects in the whole streamer. The absence of significant space charges implies that the electric field is approximately constant and equal to its background value. It is then a valid approximation to solve the streamer equations in a given background field. The evolution equations for σ and ρ in a given field are linear. The avalanche phase is thus a *linear* regime. In Chap. 5 we use this linearity to obtain analytical results on the evolution of the particles during this avalanche phase.

4.4 The non-linear streamer regime

Eventually, if the gap is sufficiently long, enough space charges build up to strongly alter the electric field. This situation in shown in Fig. 4.5 for the high field case (H), with no electron inflow.

In the left plot of Fig. 4.5, showing the logarithm of the electron density, we can now distinguish two regions: one, almost circular, with rather low densities, and one finger-shaped with high electron densities. It clearly shows that the electron cloud no longer has a Gaussian shape, which indicates that the electric field no longer is uniform.

The ions are of course still immobile, and since they are only created through

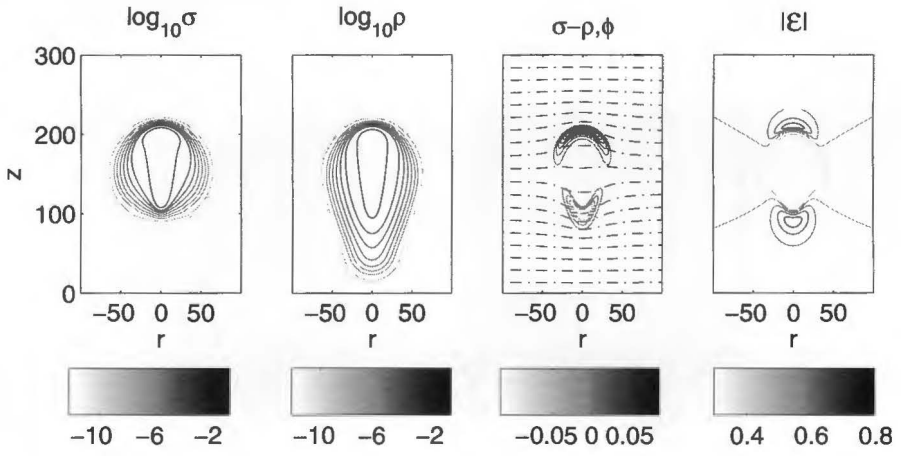

FIGURE 4.5: The non-linear regime for the high field case ($|\mathcal{E}_b| = 0.5$) with Dirichlet boundary conditions at the cathode ($z = 0$). *From left to right*: logarithmic plot of the electron density distribution, logarithmic plot of the ion density distribution, net charge density distribution together with the equipotential lines (dash dotted lines), and electric field strength. The time of the snapshot is $\tau = 200$, which corresponds to 0.6 ns for N_2 at atmospheric pressure.

ionization of neutral molecules by electrons, they in fact give the "history" of the electrons. We can observe, comparing the first and the second plot of Fig. 4.5, a region near the cathode with no electrons and a small amount of ions. The ions there will stay put, and no further ions will appear there because there are no electrons anymore to ionize the molecules in that region. This is due to the electric field being directed in the negative z-direction (and never changing sign), therefore the drift velocity will always be directed from the cathode towards the anode.

The third panel of Fig. 4.5 shows that a relatively thin and curved negatively charged region has appeared instead of the almost circular negatively charged region in the avalanche phase. Again, due to charge neutrality, a positively charged counterpart is found in the base of the streamer. In this panel we also have drawn the equipotential lines. We see that the space charges tend to exclude the equipotential lines from the streamer interior, where they are separated by a much larger distance than in the streamer exterior. For the electric field, which is defined as the gradient of the electric potential, this means

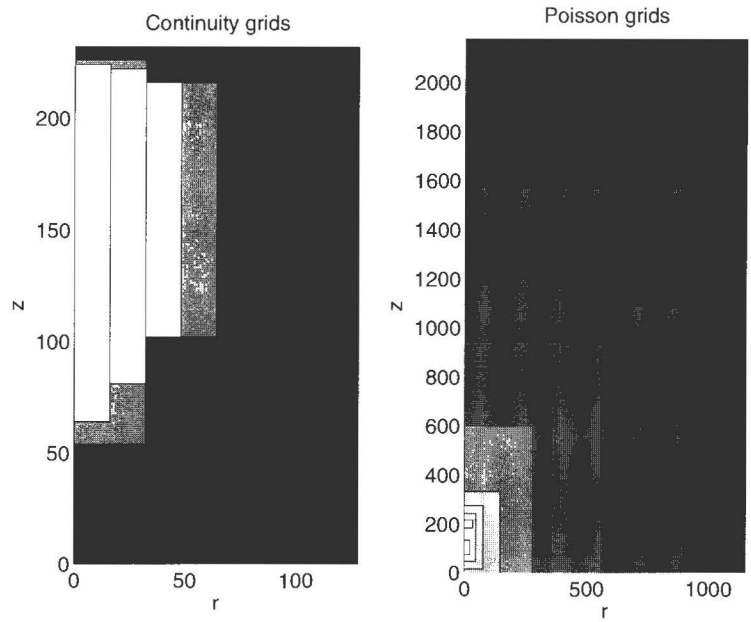

FIGURE 4.6: The grid distribution for the computation of the continuity equations (left column) and of the Poisson equation (right column) during the non-linear streamer phase for case (H). The coarsest grids are black in both cases, the white regions indicate the location of the finest grid (with a mesh size of 0.5) The times of the snapshots are the same as in Fig. 4.5. The scales on which the continuity grids are plotted are different from that of the Poisson grids.

that it is reduced in the streamer interior, and enhanced ahead of the streamer, as is shown in the rightmost plot of Fig. 4.5. This is because a conducting plasma regime has been created that tries to expel the external field as any conductor.

The grids on which the solutions of Fig. 4.5 have been computed are shown in Fig. 4.6. The grids for the continuity equations nicely follow the streamer. The grids for the Poisson equation have now been refined up to the finest level (indicated by the white regions in the rightmost panel of Fig. 4.6. Moreover, a careful look at the emplacement of the finest Poisson grids shows that they are situated around the regions with net charge densities (both positive and negative). Obviously, the source term for the Poisson equation becomes large there, and therefore the electric potential and electric field will deviate most from their background value in the neighborhood of the space charges, which in turn result in the need for a relatively high accuracy in these regions.

In the case of a streamer propagating in an undervolted gap, the impact ionization rate is much lower than in high fields. Less charged particles are therefore created during the electron avalanche. This is counteracted by using a dense initial seed, so that space charge regions can easily build up. The streamer in the non-linear regime for the low field case is shown in Fig. 4.7.

As in the high field case, two regions can be distinguished in the electron density distribution, shown in the rightmost plot of Fig. 4.7. A relatively wide region with low densities, and a dense and thin region near the axis of symmetry. The space charge layer has now clearly appeared at the tip of the streamer (see the third plot of Fig. 4.7). As in the overvolted case, these space charges enhance the field ahead of it, while in the back the field is lower than its background value, as can be seen in the rightmost picture of Fig. 4.7.

The grids for the solutions from in Fig. 4.7 are given in Fig.4.8. The advantage of the grid structure for the continuity equations is now clearly visible. Indeed, if we would not divide the region that has to be refined in small rectangles, but rather put one big rectangular grid on top of it, we quickly see that this results in huge amount of additional grid points.

We also remark that the finest grid for the Poisson grid is now as fine as the finest level imposed. However, it only occupies a small part of the streamer near the cathode, where the electrons flow in. In the streamer head, a relatively coarse grid is sufficient to compute the electric potential, whose variation around its background value is, as mentioned previously, rather smooth.

The streamer regime is characterized by the presence of a thin and curved space charge layer. This layer enhances the field ahead of it, and consequently both the ionization rate and the drift velocity are enhanced as well. The space charge layer on the other hand reduces the field in the ionized channel. Moreover, because of this nonlinear process, a length scale of the front width emerges, which is set by the ionization rate $\alpha(|\boldsymbol{\mathcal{E}}|)$ [30]. The effect of the space charge layer on the electric field is an *electrostatic* problem, and it is the distribution of the net charges that results instantaneously in a specific electric field distribution. The dynamics of the problem are due to the effect of the electric field on the electrons. A more detailed description of the features of the non-linear

regime follows in Chap. 6.

We emphasize that, although the model investigated here is minimal, which implies that it can not be used to compute cathode directed streamers (where some other mechanism has to be included to supply electrons ahead of the ionization front which then moves opposite to the electron drift direction), the occurrence of such a space charge layer is generic for both cathode and anode directed streamers. This space charge layer is required for the local field enhancement that allows streamers to propagate in undervolted gaps.

4.5 Streamer branching: the unstable regime

If we let the streamer continue to evolve in the non-linear regime, we observe that eventually the space charge layer develops from a convex to a concave form. One or more "branches" then start propagating off-axis, possibly accompanied by a branch that continues propagating along the axis.

This branching is illustrated in the lower part of Fig. 4.9 for the high field case. It clearly exhibits the off-axis propagation of the branches. The space charge layer has become very thin and unstable. The equipotential lines inside

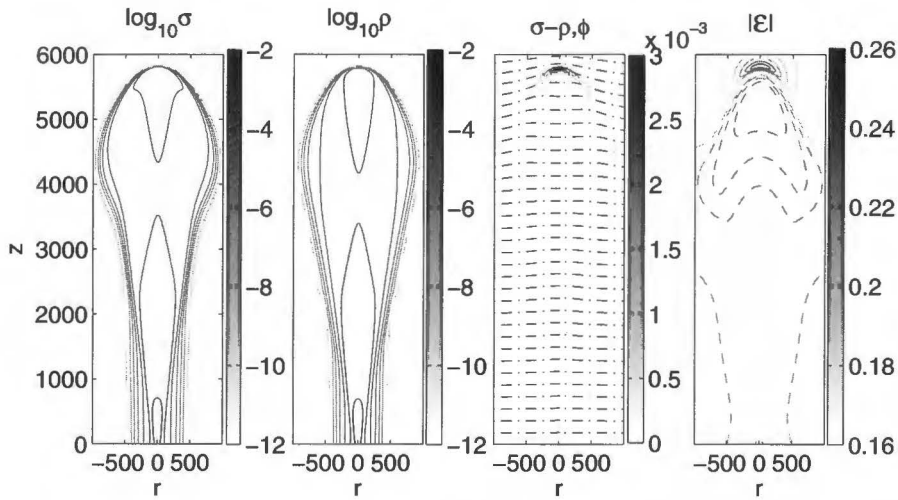

FIGURE 4.7: The non-linear regime for the low field case ($|\mathcal{E}_b| = 0.15$) with homogeneous Neumann boundary conditions at the cathode ($z = 0$). *From left to right*: logarithmic plot of the electron density distribution, logarithmic plot of the ion density distribution, net charge density distribution together with the equipotential lines (dash dotted lines), and electric field strength. The time of the snapshot is $\tau = 2.75 \cdot 10^4$, which corresponds to 82.5 ns for N_2 at atmospheric pressure. The solid lines in the rightmost plot correspond to an enhancement of the background field, the dashed lines to a field strength lower than that of the background field.

the streamer are now separated by large distances (see the third plot from the left in the upper row of Fig. 4.9). This means that the streamer body has approached the Firsov-Lozansky limit of ideal conductivity [59].

In low fields, the streamer eventually becomes unstable as well, though after a much longer propagation time (indeed, the time of branching is two orders of magnitude larger than in the high field case). This is shown in the lower row of Fig. 4.9. Again we see that the equipotential lines inside the streamer are separated by a larger distance from each other than ahead of the streamer.

These instabilities were already briefly mentioned in [24, 102], where it was shown that background ionization smears out the space charge layer, thereby stabilizing it, and suppressing the branching behavior. The branching was then qualified as the result of numerical instabilities and not looked at in more detail. In more recent work [5, 83] it was argued that the branching observed indeed was physical, and that the streamer approached the Firsov-Lozansky limit of ideal conductivity [59]. The analogy was then made with Laplacian growth problems,

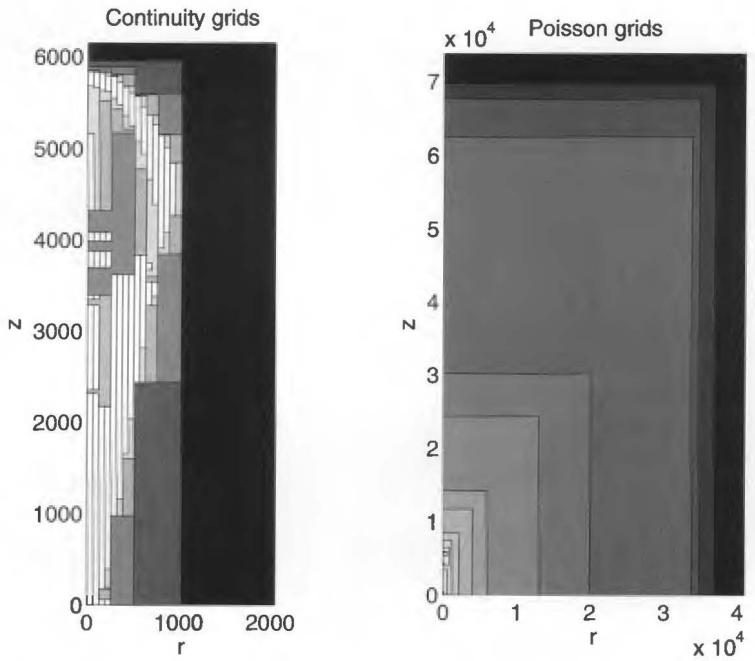

FIGURE 4.8: The grid distribution for the computation of the continuity equations (left column) and of the Poisson equation (right column) during the non-linear streamer regime for case (L). The coarsest grids are black in both cases, the white regions indicate the location of the finest grid (with a mesh size of 2) The times of the snapshots are the same as in Fig. 4.7. The scales on which the continuity grids are plotted are different from that of the Poisson grids.

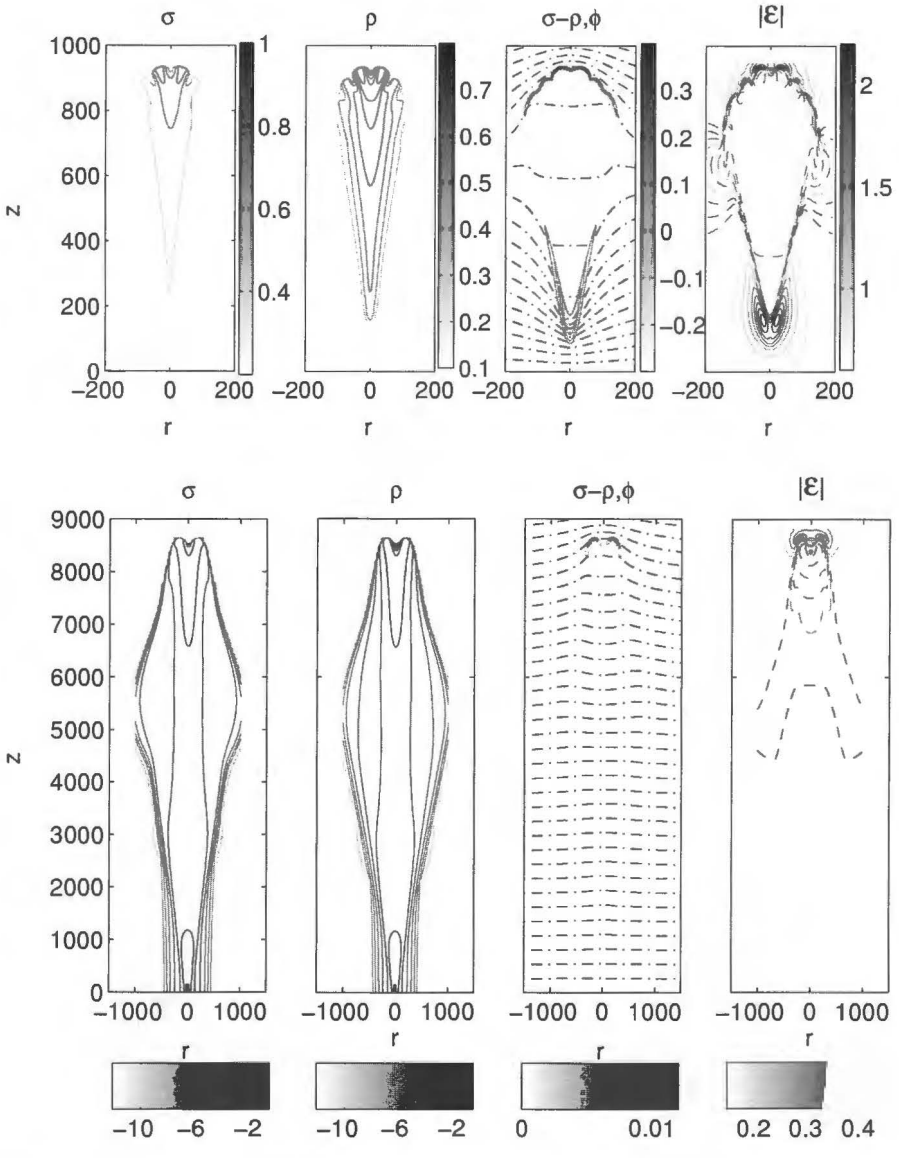

FIGURE 4.9: The branching streamer. *Upper row*: the high field case ($|\mathcal{E}_b| = 0.5$) with Dirichlet boundary conditions at the cathode ($z = 0$) at $\tau = 575$, which corresponds to 1.725 ns for N_2 at atmospheric pressure. *Lower row*: the low field case ($|\mathcal{E}_b| = 0.15$) with homogeneous Neumann boundary conditions at the cathode ($z = 0$). The time of the snapshot is $\tau = 33 \cdot 10^4$, which corresponds to 99 ns. *From left to right*: electron density distribution, ion density distribution, net charge density distribution together with the equipotential lines (dash dotted lines), and electric field strength.

such as viscous fingering, that also exhibit such interfacial instabilities.

We emphasize that in this radially symmetric setting, the streamer branches into rings, which is physically meaningless. However, it does show the appearance of an instability. Moreover, the use of a radial symmetry in fact suppresses all instability modes that are not radially symmetric. The branching time in a radially symmetric setting therefore is a upper bound for the actual three-dimensional branching [27].

4.6 Conclusions

We have presented the main characteristics of the three physical stages of the streamer propagation. During the avalanche phase, the space charge effects are negligible, and this phase is *linear*. This phase will be investigated analytically in Chap. 5.

Due to the different velocities of the fast electrons and the relatively immobile ions, the charges are separated, and a thin space charge layer builds up, characteristic for the streamer regime, and necessary for a streamer to propagate in an undervolted gap. This space charge layer enhances the field ahead of it, in the region towards which the streamer propagates. In the conducting interior of the streamer, the field is suppressed. The propagation is now nonlinear. This regime is the subject of Chap. 6.

Eventually, the streamer interior approaches the limit of ideal conductivity and becomes *unstable*. The propagation is then no longer directed along the axis of symmetry alone, and the streamer exhibits branches that evolve away from the axis. A more detailed investigation of the streamer branching follows in Chap. 7.

5

DIFFUSION CORRECTION TO THE AVALANCHE–TO–STREAMER TRANSITION

In the previous chapter it was shown that a streamer can emergence through an electron avalanche. This phase is characterized by the absence of space charge effects, which makes the propagation linear. Eventually, if the electric field system is sufficiently long, space-charge dominated streamer discharges can emerge.

We show that the required system length is not only a function of the electric field as suggested by Meek's criterion, but also of electron diffusion. We present analytical and numerical results and derive an explicit criterion for streamer formation after the emergence of the first free electron.

5.1 Problem setting and review

In narrow geometries, streamers frequently are growing from pointed electrodes, that create strong local fields in their neighborhood. At the electrodes, surface effects take place, and both positive and negative streamers can emerge [97]. On the other hand, in many natural discharges and, in particular, for sprites above thunderclouds [53], it is appropriate to assume that the electric field is homogeneous and boundary effects do not play a role. Of course, dust particles or other nucleation centers can play an additional role in discharge generation, but in this chapter we will focus on the effect of a homogeneous field on a homogeneous gas. This assumption corresponds to the case discussed previously, e.g., in [63, 82, 9].

Typically, the avalanche to streamer transition is assumed to depend on

the ionization rate α and gap length d through the dimensionless combination αd. We here first recall this statement and then reinvestigate the problem and find, that the transition depends also on electron diffusion. This dependence is analyzed quantitatively in full parameter space.

In detail, we consider a continuous discharge model with attachment and local field-dependent impact ionization rate and space charge effects. It is defined through

$$\begin{aligned}
\partial_t n_e &= D_e \nabla^2_{\mathbf{R}} n_e + \nabla_{\mathbf{R}} \cdot (\mu_e \mathbf{E}\, n_e) \\
&\quad + (\mu_e |\mathbf{E}|\, \alpha(|\mathbf{E}|) - \nu_a)\, n_e, \\
\partial_t n_+ &= \mu_e \mathbf{E}\, \alpha(|\mathbf{E}|)\, n_e, \\
\partial_t n_- &= \nu_a\, n_e, \\
\nabla^2_{\mathbf{R}} \Phi &= \frac{\mathrm{e}}{\epsilon_0} (n_e + n_- - n_+) \quad , \quad \mathbf{E} = -\nabla_{\mathbf{R}} \Phi.
\end{aligned} \tag{5.1.1}$$

Here n_e, n_+ and n_- are the particle densities of electrons, positive and negative ions, and $\mathbf{E}$ and Φ are the electric field and potential, respectively. D_e and ν_a are the electron diffusion coefficient and the electron attachment rate. We assume the impact ionization rate $\alpha(\mathbf{E})$ to be a function of the electric field, and for our numerical calculations, we use the Townsend approximation $\alpha(|\mathbf{E}|) = \alpha_0 \exp(-E_0/|\mathbf{E}|)$, in which α_0 and E_0 are parameters for the effective cross section. The positive and negative ions are considered to be immobile on the time scales investigated here . The initial ionization seed is placed in free space, and an electron avalanche drifts towards the anode.

Eventually, the charged particle density in the avalanche will become so large that space charge effects set in and change the externally applied field, and a streamer emerges from the avalanche. Essentially two criteria have been given in the literature for this emergence of a streamer from a tiny ionization seed. The first one is a necessary lower bound: the electric field has to be higher than the threshold field E_k where the impact ionization rate overcomes the attachment rate. Only for $|\mathbf{E}| > E_k$, the ionization level can grow. Here E_k is defined through

$$\mu_e\, E_k\, \alpha(E_k) = \nu_a. \tag{5.1.2}$$

The second criterion is known as Meek's criterion. As derived originally in [63], it states that for a cathode directed (i.e., positive) streamer to emerge from an anode directed avalanche, the system has to be long enough to allow for a sufficient multiplication of the drifting electron package. Then the electric field of the ions is high enough for secondary emitted electrons at the anode to drift towards the cathode. Typically, multiplication rates by 8 [55, 63] to 9 [9] decades are assumed to be sufficient. This fixes the second criterion as

$$\exp\left[\left(\alpha(|\mathbf{E}|) - \frac{\nu_a}{\mu_e |\mathbf{E}|}\right) d\right] \approx 10^8 \text{ to } 10^9, \tag{5.1.3}$$

where d is the avalanche length. In brief as a rule of thumb the criterion reads

$$\alpha(|\mathbf{E}|)\, d \approx 18 \text{ to } 21 \quad \text{according to Meek.} \tag{5.1.4}$$

Meek's criterion has been extended to the transition of the avalanche to an anode directed (i.e., negative) streamer [82, 9].

In this chapter we argue that for an avalanche originating from a tiny local seed, this criterion is not sufficient since it neglects the diffusion of the electron package. Diffusion decreases the electron density while impact ionization increases it. In low fields, diffusion stays dominant for all times which will always suppress space charge effects and consecutive streamer emergence.

The difference is particularly pronounced in non-attaching gases like nitrogen. Here Meek's criterion would suggest that streamer formation could take place as long as there is any impact ionization and the system is sufficiently long. However, electron diffusion will suppress streamer formation in low fields.

We will elaborate this argument analytically and numerically, and we will give quantitative corrections to the above criteria. First the intrinsic scales of the problem with their explicit density dependence are identified through dimensional analysis. Then analytical results for the electron density are recalled and the electron induced field is calculated. This gives a lower bound for the time and travel distance of avalanche-to-streamer transition. The ion density distribution cannot be calculated analytically, however, we found that all spatial moments of the distribution can be calculated. These moments provide the basis for an estimate of the avalanche-to-streamer transition. Fig. 5.4 on page 90 summarizes how travel time and distance at the transition depend on applied field and diffusion constant.

5.2 Dimensional analysis

Meek's criterion can be understood as an example of dimensional analysis: the effective cross-section $\alpha(|\mathbf{E}|)$ has the dimension of inverse length, hence $\alpha(|\mathbf{E}|)d$ is a dimensionless number that characterizes a certain behavior. We extend our dimensional analysis of Sect. 2.3.2 to the model (5.1.1) including attachment. Rewriting (5.1.1) in dimensionless units, we obtain the dimensionless attachment coefficient,

$$\nu = \frac{\nu_a}{\alpha_0 \mu_e E_0} \,. \tag{5.2.1}$$

This brings the system of equations (5.1.1) into the dimensionless form

$$\partial_\tau \sigma = D\nabla^2\sigma + \nabla(\boldsymbol{\mathcal{E}}\sigma) + f(|\boldsymbol{\mathcal{E}}|,\nu)\,\sigma\,, \tag{5.2.2}$$

$$\partial_\tau \rho = f(|\boldsymbol{\mathcal{E}}|,\nu)\,\sigma\,, \tag{5.2.3}$$

$$\nabla^2\phi = -\nabla\cdot\boldsymbol{\mathcal{E}} = \sigma - \rho\,, \tag{5.2.4}$$

where

$$f(|\boldsymbol{\mathcal{E}}|,\nu) = |\boldsymbol{\mathcal{E}}|e^{-1/|\boldsymbol{\mathcal{E}}|} - \nu,. \tag{5.2.5}$$

Note that ρ is now defined as

$$\rho = \frac{e(n_+ - n_-)}{\epsilon_0 \alpha_0 E_0} \,. \tag{5.2.6}$$

It is remarkable that the density of positive and negative ions $n_\pm$ enters the equations only in the form of the single dimensionless field $\rho \propto n_+ - n_-$. This is clear in the case of the Poisson equation, but holds also for the generation term proportional to $f(|\boldsymbol{\mathcal{E}}|, \nu)$.

An initial ionization seed will under influence of the background electric field advect towards the anode, diffuse and grow due to ionizing collisions with neutral atoms. At the beginning of this process the influence of space charges on the electric field is negligible. We can therefore analyze the continuity equations Eqs. (5.2.2)-(5.2.3) in a homogeneous background field $\boldsymbol{\mathcal{E}}_b$, which makes the process linear. Eventually space charges do affect the electric field, and the streamer regime is reached. Then charged layers emerge, shielding the interior of the streamer from the outer electric field. We here investigate when this will happen.

5.3 Electron distribution and field

5.3.1 Exact result for the electron distribution

We write the single electron that generates the avalanche as a localized initial density

$$\sigma(\mathbf{r}, \tau = 0) = \rho(\mathbf{r}, \tau = 0) = \sigma_0 \delta(\mathbf{r} - \mathbf{r_0}) \tag{5.3.1}$$

and consider its evolution, in a cylindrically symmetric coordinate system, under influence of a uniform field $\boldsymbol{\mathcal{E}}_b = -\mathcal{E}_b \hat{\mathbf{e}}_z$, $\hat{\mathbf{e}}_z$ being the unit vector along the axial direction.

To approximate the single electron, one has to take $\sigma_0 = 10^{-4}$ at atmospheric pressure. Indeed the integration over the whole space of the initial electron density distribution (5.3.1) is, obviously, equal to σ_0. Using the dimensional analysis introduced in the previous section, this corresponds to a total number of $(\sigma_0 n_0)/\alpha_0^3$ electrons, which is assumed to be unity (n_0 being the characteristic particle density, $n_0 = \epsilon_0 \alpha_0 E_0/e$). A substitution of the numerical values for the intrinsic scales then leads to $\sigma_0 = 10^{-4}/(N/N_0)$. For this initial condition, the electron evolution according to Eq. (5.2.2) can be given explicitly as [82]

$$\sigma(\mathbf{r}, \tau) = \sigma_0 \, e^{f\tau} \, \frac{e^{-(\mathbf{r}-\mathbf{r}_0-\boldsymbol{\mathcal{E}}_b\tau)^2/(4D\tau)}}{(4\pi D\tau)^{3/2}}; \tag{5.3.2}$$

it has the form of a Gaussian package that drifts with velocity $-\boldsymbol{\mathcal{E}}_b$, widens diffusively with half width proportional to $\sqrt{4D\tau}$, and carries a total number of electrons $e^{f\tau}$. (If the initial ionization seed consists of several electrons in some close neighborhood, the Gaussian shape is approached nevertheless for large times due to the central limit theorem.)

It should be noted that while the total number of electrons in the package grows exponentially in time, the maximum of the electron density

$$\sigma_{\max}(\tau) = \max_{\mathbf{r}} \sigma(\mathbf{r}, \tau) = \frac{\sigma_0 \, e^{f\tau}}{(4\pi D\tau)^{3/2}} \tag{5.3.3}$$

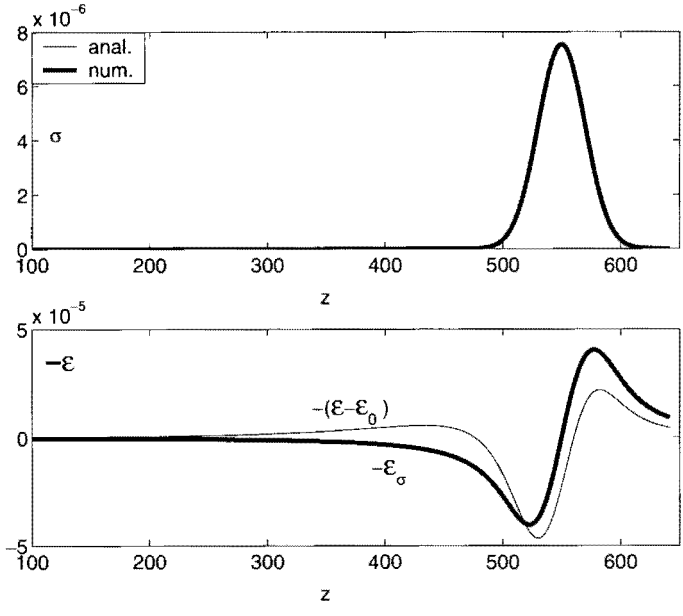

FIGURE 5.1: Numerical and analytical results at $\tau = 2000$ on the axis of symmetry z when the externally applied field is $\mathcal{E}_b = -0.25\,\hat{\mathbf{e}}_z$, and $D = 0.1$, $\nu = 0$ and $\sigma_0 = 10^{-4}$. The initial condition is located at $\mathbf{r}_0 = 50\,\hat{\mathbf{e}}_z$. The upper figure shows the electron density; the analytical expression coincides with the numerical result as it should. The lower figure shows the axial component (pointing in the same direction as $\mathcal{E}_b$) of the numerically computed field strength $\mathcal{E} - \mathcal{E}_b$ due to both electrons and ions (thick line) and the analytical result for the field $\mathcal{E}_\sigma$ induced by the electrons only (thin line).

first decreases until $\tau = 3/(2f)$ and then increases. At this moment of evolution, generation overcomes diffusion.

5.3.2 Exact result for the electron generated field $\mathcal{E}_\sigma$

While density and field of the ions can only be calculated approximately and will be treated in the next section, the electric field $\mathcal{E}_\sigma$ generated by the Gaussian electron package can be calculated exactly. The main point is that the electron density distribution (5.3.2) is spherically symmetric about the point $\mathbf{r}_0 + \mathcal{E}_b\tau$. The electric field $\mathcal{E}_\sigma(s,\tau)$ induced by the electrons at the point $\mathbf{s} = \mathbf{r} - \mathbf{r}_0 - \mathcal{E}_b\tau$ can therefore be written as $\mathcal{E}_\sigma = -\mathcal{E}_\sigma\hat{\mathbf{e}}_s$, where $\hat{\mathbf{e}}_s$ is the unit vector in the radial $\mathbf{s}$ direction. Its magnitude can be computed with Gauss' law of electrostatics:

$$\begin{aligned}\mathcal{E}_\sigma(s,\tau) &= -\frac{1}{s^2}\int_0^s \sigma_0 e^{f\tau}\,\frac{e^{-r^2/(4D\tau)}}{(4\pi D\tau)^{3/2}}\,r^2 dr \\ &= -\frac{\sigma_0 e^{f\tau}}{16\pi D\tau}\,F\left(\frac{s}{\sqrt{4D\tau}}\right), \qquad (5.3.4)\end{aligned}$$

with

$$F(x) = \frac{1}{x^2}\ \frac{4}{\sqrt{\pi}}\int_0^x y^2 e^{-y^2} dy = \frac{\text{erf}\, x}{x^2} - \frac{2}{\sqrt{\pi}}\frac{e^{-x^2}}{x}, \tag{5.3.5}$$

where erf is the error function. The spatial maximum of the field $\mathcal{E}_\sigma$ is determined by the maximum of $F(x)$; it is given by

$$\frac{2}{\sqrt{\pi}}(x + x^3)e^{-x^2} = \text{erf}\, x. \tag{5.3.6}$$

Solving this equation numerically leads to a position of the maximum of about $x \simeq 1$ and to the value $F(1) \simeq 0.4276$. The spatial maximum of the electron generated electric field becomes

$$\mathcal{E}_\sigma^{max}(\tau) \simeq \frac{\sigma_0 e^{f\tau}}{16\pi D\tau} F(1), \tag{5.3.7}$$

it is located on the sphere parameterized through

$$|\mathbf{r} - \mathbf{r}_0 - \boldsymbol{\mathcal{E}}_b\tau| \simeq \sqrt{4D\tau}. \tag{5.3.8}$$

5.3.3 A lower bound for the transition

The electric field generated by the electrons leads to a first estimate for the avalanche to streamer transition. Actually, the magnitude of the monopole field $\mathcal{E}_\sigma$ ahead of the electron cloud is an upper bound for the magnitude of the field created by the dipole of electrons on the one hand and the positive charges left behind by the electron cloud on the other hand (see lower panel in Fig. 5.1). Therefore, substantial fields arise after a shorter travel time τ_0 and distance, so that τ_0 is a lower bound for the time $\tau_{a\to s}$ of the avalanche-to-streamer transition.

The space charge generated field is measured relative to the externally applied field E_b as $|E^{max}(\tau) - E_b| \leq k|E_b|$. We will show in the next section that $k = 0.03$ is an appropriate estimate for the mid gap avalanche to streamer transition.

Finally, the lower bound τ_σ for the transition can be expressed through Eq. (5.3.7) as

$$f\tau_\sigma - \ln(\mathcal{E}_b\tau_\sigma) \simeq \ln\frac{16\pi kD}{F(1)\sigma_0}. \tag{5.3.9}$$

As travel time and travel distance are related through the drift velocity $\mathcal{E}_b$ and working the way back through dimensional analysis, $f(|\boldsymbol{\mathcal{E}}_b|, \nu)\tau_\sigma$ is found to be identical to $(\alpha(|\mathbf{E}_b|) - \nu_a/\mu_e E_b)d_\sigma$, where $d_\sigma = \mu_e E_b t_\sigma$ is the avalanche travel distance. In dimensional quantities, Eq. (5.3.9) takes the form

$$\left(\alpha(|E_b|) - \frac{\nu_a}{\mu_e E_b}\right) d_\sigma - \ln(d_\sigma\alpha_0) = \ln\frac{16\pi k 10^4}{F(1)} + \ln\frac{D_e\alpha_0}{\mu_e E_0} - \ln\frac{N}{N_0}. \tag{5.3.10}$$

For a non-attaching gas ($\nu_a = 0$) at atmospheric pressure under normal conditions with dimensionless diffusion comparable to nitrogen, inserting the numerical values for the parameters, we obtain

$$\alpha(|E_b|)d_\sigma - \ln(\alpha_0 d_\sigma) \approx 9.43. \tag{5.3.11}$$

f being a growing function of $|\mathcal{E}_b|$, Eq. (5.4.15) shows that the larger the field, the earlier the transition takes place, which is in accordance with Meek's criterion. On the other hand, the second term of in the right hand side of Eq. (5.3.10) is dependent on the diffusion coefficient in such a way that diffusion delays the transition to streamer, as expected.

The solution $\alpha(|E_b|)d_\sigma$ for N_2 at atmospheric pressure is shown in the dash-dotted line of Fig. 5.3, where it is compared to a numerical evaluation of the transition time (symbols). The latter have been obtained through a full simulation of the continuity equations (5.2.2)-(5.2.3) together with the Poisson equation (5.2.4) [83, 68]. Though the qualitative features of the transition time are well reproduced, this figure shows that the underestimation of the transition time is significant, and that it is necessary to include the field of the ion trail left behind by the electrons.

5.4 Ion distribution and field

5.4.1 Exact results on the spatial moments of the distributions

To get a more accurate estimate for the avalanche-to-streamer transition, the field generated by the positive and negative ions has to be included. In the case of the ion distribution, closed analytical results cannot be found, in contrast to the electron distribution (5.3.2). However, arbitrary spatial moments of the distribution

$$\langle \mathcal{O} \rangle_\rho = \frac{\int \mathcal{O}\, \rho\, d^3\mathbf{r}}{\int \rho\, d^3\mathbf{r}}, \quad \text{where } \mathcal{O} = z^n \text{ or } r^n, \tag{5.4.1}$$

can be derived analytically. Here z is the direction of the homogeneous field $\mathcal{E}_b$ and r is the radial direction. First, the evolution equation (5.2.3) for the ion density is integrated in time and the analytical form (5.3.2) for $\sigma(\mathbf{r}, \tau)$ is inserted. As $f = f(|\mathcal{E}_b|, \nu)$ is constant in space and time one finds

$$\rho(\mathbf{r}, \tau) - \rho(\mathbf{r}, 0) = \tag{5.4.2}$$
$$f\sigma_0 \int_0^\tau d\tau'\, e^{f\tau'} \frac{e^{-(z-z_0-\mathcal{E}_b\tau')^2/(4D\tau')}}{\sqrt{4\pi D\tau'}} \frac{e^{-r^2/(4D\tau')}}{4\pi D\tau'}.$$

Here the initial perturbation is located at z_0 on the axis $r = 0$. The moments (5.4.1) can now be derived from (5.4.2) by exchanging the order of spatial and

temporal integration. In particular, one finds

$$\int \rho \, d^3\mathbf{r} = \sigma_0 \, e^{f\tau}, \tag{5.4.3}$$

$$\int z \, \rho \, d^3\mathbf{r} = \sigma_0 \, e^{f\tau} \left(z_0 + \mathcal{E}_b \tau - \frac{1 - e^{-f\tau}}{f/\mathcal{E}_b} \right),$$

and higher moments can be calculated in the same way. For the moments of ρ, this gives

$$\langle z \rangle_\rho = z_0 + \mathcal{E}_b \left(\tau - \frac{1}{f} \right) + O\left(e^{-f\tau}\right), \tag{5.4.4}$$

$$\langle z^2 \rangle_\rho - \langle z \rangle_\rho^2 = \left(\frac{\mathcal{E}_b}{f} \right)^2 + 2D \left(\tau - \frac{1}{f} \right) + O\left(e^{-f\tau}\right).$$

The second moment of ρ in the radial direction is

$$\langle r^2 \rangle_\rho = 2D \left(\tau - \frac{1}{f} \right) + O\left(e^{-f\tau}\right). \tag{5.4.5}$$

For comparison, the moments of the Gaussian electron distribution (5.3.2) are easily found to be

$$\langle z \rangle_\sigma = z_0 + \mathcal{E}_b \tau, \tag{5.4.6}$$

$$\langle z^2 \rangle_\sigma - \langle z \rangle_\sigma^2 = 2D\tau, \tag{5.4.7}$$

$$\langle r^2 \rangle_\sigma = 2D\tau. \tag{5.4.8}$$

5.4.2 Discussion of the moments

These moments mean that the center of mass of the electron package is located at $z = z_0 + \mathcal{E}_b \tau$, and the package has a diffusive width $\sqrt{2D\tau}$ around it, both in the forward z direction and in the radial r direction. The second moment in the z direction is calculated relative to the center of mass

$$\langle z^2 \rangle_x^c := \left\langle \left(z - \langle z \rangle_x \right)^2 \right\rangle_x = \langle z^2 \rangle_x - \langle z \rangle_x^2, \quad x = \sigma, \rho. \tag{5.4.9}$$

The ion cloud shows a more complex behavior; it is evaluated close to the avalanche-to-streamer transition where $f\tau = \alpha d = O(10)$, therefore the terms of order $e^{-f\tau}$ are neglected.

First it is remarkable that the center of mass of the ion cloud shifts with precisely the same velocity as the electron cloud though the ion motion is neglected while the electrons drift, and that the ion center of mass is at an approximately constant distance $\mathcal{E}_b/f$ behind the electron center of mass. This distance

$$\ell_\alpha = \frac{\mathcal{E}_b}{f(\mathcal{E}_b)} = \frac{1}{\alpha(\mathcal{E}_b)} \tag{5.4.10}$$

in dimensional units corresponds to ionization length $1/\alpha(E_b)$.

The square of the radial width of the ion cloud $2D(\tau - 1/f)$ is $2D/f$ smaller than the one of the electron cloud. This is clear since the electron cloud also was more narrow when it left the ions behind. The ion cloud is more extended in the z direction. This comes from the ions being immobile, therefore a trace of ions along the z-axis is left behind by the electron cloud. Moreover, it can be remarked that the difference between the width and the length of the ion cloud is characterized by the same length between the centers of mass of the ion and the electron cloud, namely the ionization length ℓ_α.

5.4.3 An estimate for the transition

One can assume as in [9] that the ions have a distribution similar to the electrons, thus one could approximate them by a Gaussian with the same width as the electron cloud, but centered around $(r = 0, z = \langle z \rangle_\rho)$:

$$\rho_1(r, z, \tau) = \sigma_0 \, e^{f\tau} \, \frac{e^{-\left[(z - \langle z \rangle_\rho)^2 + r^2\right]/(4D\tau)}}{(4\pi D\tau)^{3/2}}. \tag{5.4.11}$$

In this approximation, the total electric field becomes:

$$\begin{aligned} \boldsymbol{\mathcal{E}}_1(r, z, \tau) &= \boldsymbol{\mathcal{E}}_b \\ &- \frac{\sigma_0 e^{ft}}{16\pi \, D\tau} \left[F\left(\frac{|\mathbf{s}_\sigma|}{\sqrt{4D\tau}} \right) \frac{\mathbf{s}_\sigma}{|\mathbf{s}_\sigma|} + F\left(\frac{|\mathbf{s}_\rho|}{\sqrt{4D\tau}} \right) \frac{\mathbf{s}_\rho}{|\mathbf{s}_\rho|} \right], \end{aligned} \tag{5.4.12}$$

where

$$\mathbf{s}_x \;=\; \mathbf{r} - \langle z \rangle_x \, \hat{\mathbf{e}}_z \quad \text{for} \quad x = \rho, \sigma \tag{5.4.13}$$

are the distances to the electron and ion centers of mass.

The maximum of the field $\mathcal{E}_1$ can not be computed analytically. However, in Fig. 5.1 it can be seen that the positions of the maximum of the total field and that of the electron field nearly coincide. Therefore we evaluate the field $\mathcal{E}_1$ at the maximum of $\mathcal{E}_\sigma$ as defined in Eq. (5.3.7). Moreover, it is easily seen that the maximum of the field is situated on the axis, ahead of the electron cloud. The maximum of the electric field can thus be approximated as:

$$\begin{aligned} \mathcal{E}_1^{max}(\tau) &\simeq \mathcal{E}_1(r = 0, z = z_0 + \boldsymbol{\mathcal{E}}_b \tau + \sqrt{4D\tau}, \tau) \\ &= \mathcal{E}_b + \frac{\sigma_0 e^{f\tau}}{16\pi D\tau} \left[F(1) - F\left(1 + \sqrt{\frac{\ell_\alpha^2}{4D\tau}} \right) \right]. \end{aligned} \tag{5.4.14}$$

Then $E_1^{max} - E_b = kE_b$ implies for the transition time τ_1:

$$\begin{aligned} f\tau_1 - \ln(\mathcal{E}_b \tau_1) - \ln \frac{F(1)}{F(1) - F\left(1 + \sqrt{\frac{\ell_\alpha^2}{4D\tau_1}} \right)} \\ = \ln \frac{16\pi k D}{F(1)\sigma_0} \end{aligned} \tag{5.4.15}$$

The argument of the logarithm in the third term on the right hand side being larger than 1, this criterion gives a later time for the transition than that based on the field of the electrons only. This is what we expect considering that the ions tend to reduce the field of the electrons, thus the effect of space charge. The correction given by the ion field is a function of the ratio of the ionization length ℓ_α and the diffusion length $\sqrt{2D\tau}$. At early times, this ratio goes to infinity, and the correction given by the ion cloud is negligible. However, at later times, the correction becomes more significant.

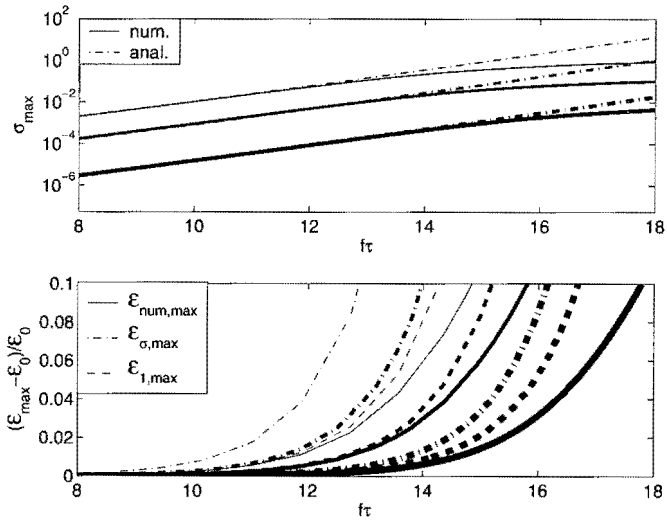

FIGURE 5.2: Evolution of the maximal electron density (upper panel) and electric field (lower panel) as a function of $f\tau$. Different values of $\mathcal{E}_b$ have been chosen: thin line: $\mathcal{E}_b = 1$, middle-thick line $\mathcal{E}_b = 0.5$ and thick line $\mathcal{E}_b = 0.25$. *Upper panel*: Numerical results (solid lines) for the maximal electron density compared with Eq. 5.3.3 (dash-dotted lines). *Lower panel*: numerical results (solid lines) are compared to maximum electric field induced by the electrons (dash-dotted lines) on the one hand and the maximal field given by Eq. (5.4.14) on the other hand (dashed lines).

Fig. 5.2 shows the influence of the correction on the field of the electrons, as well as the numerical results for the field of the ion and electron cloud together. It shows that, indeed, the correction only becomes important for larger times.

Moreover, the approximation for the maximal field ahead has now become much better than the previous approximation based on only the electron cloud. Indeed, for e.g the case of $\mathcal{E}_b = 0.5$ (corresponding to the middle thick lines), the numerically computed field (solid line) reaches the transition value ($(\mathcal{E}_{num} - \mathcal{E}_b) = 0.03\mathcal{E}_b$ at $f\tau \approx 14$. When only the field of the electrons is taken into account, this value would already be reached at $f\tau \approx 12.6$, while the correction based on the approximation of the ion cloud leads to a transition time of $f\tau \approx 13.9$. The correction becomes especially important at lower fields. In high fields,

the approximation of the ions shows somewhat larger deviations. The figure also shows that the choice of $k = 0.03$ in $E_{max} - E_b = kE_b$ is appropriate for the definition of the transition, since the maximal electron density then drops below the analytical solution with vanishing space charges.

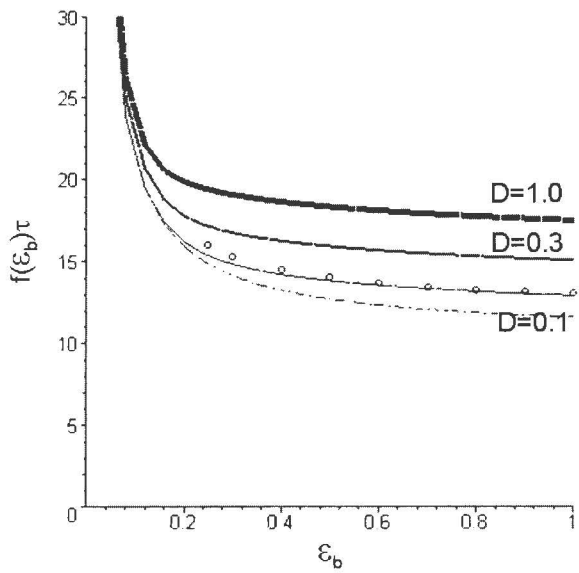

FIGURE 5.3: The transition time $f\tau$ (equivalent to the travel distance αd) as a function of the background electric field for $\sigma_0 = 10^{-4}$, $\nu = 0$ and different values of D. *Solid line*: computed with Eq. (5.4.15) for $D = 0.1$ (thin line), 0.3 (middle thin line) and 1 (thickest line). *Dash-dotted line*: computed with Eq. (5.3.9) for $D = 0.1$. *Symbols*: numerical evaluation for $D = 0.1$.

In Fig. 5.3 we compare the transition times given by Eqs. (5.3.9) and (5.4.15) with numerically evaluated transition times. It shows that the approximation of similar electron and ion distributions leads to a very good approximation of the transition time. From this figure it is also clear that the transition time $f\tau$ depends strongly on the electric field, and becomes larger towards smaller fields. Moreover, looking at the transition time for higher diffusion coefficients, it is seen that diffusion tends to delay the transition to the streamer regime. This can be expected, since diffusion will tend to broaden the electron cloud, thereby suppressing space charge effects.

For completeness, a 3-dimensional plot of the transition time approximated by Eq. (5.4.15) as a function of both background electric field and diffusion coefficients is shown in Fig. 5.4. From this figure, we see that Meek's transition criterion, that stated that $f\tau$ is approximately constant, corresponds to the case of relatively high diffusion and background field. However, realistic values of D are in the range of 0.1 to 0.3 at room temperature, and a background electric field higher than 2 also leads to unrealistic values. So in the parameter range of

real experiments, the correction given by Eq. (5.3) on Meek's criterion can not be neglected.

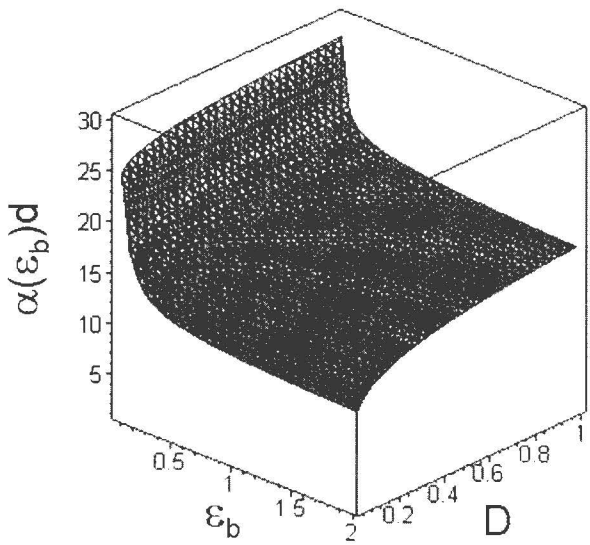

FIGURE 5.4: The transition distance αd according to Eq. (5.4.15) as a function of the background electric field $\mathcal{E}_b$ and the diffusion coefficient D for $\sigma_0 = 10^{-4}$ and $\nu = 0$.

5.4.4 A more accurate approximation for the ion density distribution

The previous approximation ρ_1 of the ion distribution leads to a relatively good approximation for the transition time in the case of a mid-gap transition. However, the real ion distribution is more narrow in the r-direction, and can be wider and asymmetrical in the z-direction. As discussed in [63], it is the field of the ion cloud that should be high to suppress the background field, so that, when the electron cloud has drifted into the anode, new electrons emitted by e.g. photoionization are drawn towards the cathode, creating a positive streamer. In this section we present another approximation for the ion distribution, which will lead to a better overall approximation of the electric field, and of the self induced field by the ion trail. However, the price to pay for this is a much more complicated analytical expression for the density and the field.

A better approximation for ρ would be an ellipsoidal Gaussian distribution centered around $(r = 0, z = \langle z \rangle_\rho)$ with width $\langle z^2 \rangle_\rho^c = \langle z^2 \rangle_\rho - \langle z \rangle_\rho^2$ and $\langle r^2 \rangle_\rho^c =$

$\langle r^2 \rangle_\rho$ in the z- and r-direction, respectively. The height of this Gaussian should be such that the total amount of ions at time t is still equal to $\sigma_0 e^{ft}$. The appropriate expression for the ion distribution is:

$$\rho(r,z,t) = \frac{\sigma_0 e^{ft}}{(2\pi)^{3/2} S_r^2 S_z} e^{-r^2/(2S_r^2) - (z-\langle z \rangle_\rho)^2/(2S_z^2)} \tag{5.4.16}$$

However, as far as we know, no closed analytical expression is known for the field of such an ellipsoidal Gaussian charge distribution. So instead, we take a spherical Gaussian distribution with the same height as the one defined in Eq. (5.4.16):

$$\rho_2(r,z,\tau) = \frac{\sigma_0 e^{f\tau}}{(2\pi)^{3/2} S_\rho^3} e^{-(r^2+(z-\langle z \rangle_\rho)^2)/(2S_\rho^2)}, \tag{5.4.17}$$

where

$$\begin{aligned} S_\rho^3 &= \langle r^2 \rangle_\rho^c \sqrt{\langle z^2 \rangle_\rho^c} \\ &= \left(2D\left(\tau - \frac{1}{f}\right)\sqrt{2D\left(\tau - \frac{1}{f}\right) + l_\alpha^2}\right). \end{aligned} \tag{5.4.18}$$

The electric field induced by this ion distribution is:

$$E_{\rho_2}(r,z,\tau) = \frac{\sigma_0 e^{f\tau}}{8\pi S_\rho^2} F\left(\sqrt{\frac{|\mathbf{s}_\rho|^2}{2S_\rho^2}}\right), \tag{5.4.19}$$

where $\mathbf{s}_\rho$ is defined in Eq. (5.4.13).

In Fig. 5.5 we compare the densities and fields given by the numerical solution and ρ_1 and ρ_2. It shows clearly that the approximation ρ_2 does not give a better approximation of the field ahead of the electron cloud. This can be explained by the fact that the region ahead of the electron cloud does not contain any ions, so that the field induced by the ions depends essentially on the total number of ions, which is the same in both ρ_1 and ρ_2. On the other hand, inside the ion cloud the approximation is much better. Therefore, evaluating the electron and ion densities with Eqs. (5.3.2) and (5.4.17) and their fields with Eqs. (5.3.4) and (5.4.19), at the transition time T_1 given by Eq. (5.4.15) will give a good approximation of the process at the time that streamer regime is entered.

5.5 Conclusions

In this chapter, the particle distributions and associated fields of an electron avalanche in a homogeneous electric field were analyzed. During the exponential growth of the total number of electrons and ions, the electrons are described by the known Gaussian distribution, but we found that the spatial moments of the ion distribution can also be calculated. As a result, we find that the

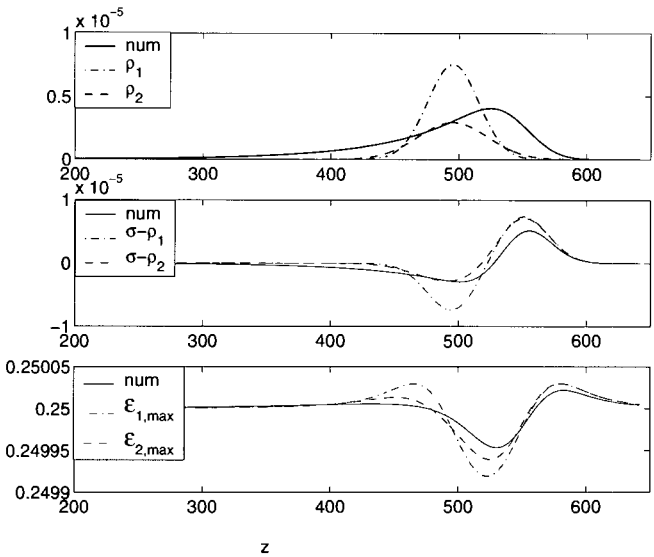

FIGURE 5.5: The ion density (upper figure), total charge density (middle figure) and electric field (lower figure) on the axis, computed with $E_0 = 0.25$, at $\tau = 2000$. *Solid lines*: numerical solution. *Dash-dotted lines*: solution corresponding to ρ_1. *Dashed lines*: solution corresponding to ρ_2.

centers of mass of electron and ion distribution both travel with the electron drift velocity within the external field. For the ions this is remarkable, since they are assumed to be immobile; their center of mass motion is therefore purely due to generation of additional ions. The distance between the centers of mass is given by the ionization length $1/\alpha(E_b)$. Furthermore, the electron cloud widens homogeneously through diffusion, so its width both in the longitudinal and in the radial direction is given by $\sqrt{2D\tau}$. The ion cloud lags behind and has the somewhat smaller "delayed" radius $\sqrt{2D\tau\,[1-1/(\alpha d)]}$ in the radial direction while its extension in the longitudinal direction can be larger, in particular, for small times, as it is characterized by $\sqrt{\ell_\alpha^2 + 2D\tau\,[1-1/(\alpha d)]}$ where ℓ_α is the dimensionless version of the ionization length $1/\alpha(E_b)$.

Furthermore, we evaluate the field of the electron cloud exactly and the field of the ion cloud approximately, and derive a criterion for the avalanche to streamer transition that takes diffusion into account. It corrects Meek's criterion that stated that $\alpha d \simeq 18 - 21$, d being the transition travel distance and α the ionization cross section of the electrons for given field. The transition distance strongly depends also on diffusion. For high fields, the transition time saturates towards $\alpha d \simeq 15$. On the other hand, for low fields, when the processes are diffusion dominated, the avalanche is much longer.

The analytical models described in this chapter give a useful tool to describe the negative streamer formation. Especially at relatively low, realistic, fields,

the present model gives an accurate description of the avalanche to streamer transition. We stress that our criterion for the transition is based on the space charges affecting the background electric field in such a way that the linearization around it no longer holds. This corresponds to the moment that the electron cloud and its ion trail start reducing sensibly the electric field strength between them. The criteria for spark breakdown derived by Meek [63], and for positive streamer formation by Bazelyan [9] are based on the space charges screening the field between the positively and negatively charged regions, i.e. $k = \mathcal{O}(1)$. However, their calculations are based on the linearization around the uniform background field, which obviously does not hold at these values of k. Moreover, the situation of complete screening might never be reached in the full nonlinear dynamics [113, 38, 24].

In [9] the diffusive widening of the electron cloud was not accounted for in the derivation of the criterion. The diffusion, however, has considerable effects on the electron and ion distribution, and especially at low fields it can considerably delay the emergence of a streamer. Indeed, in high fields, the transition to a streamer occurs after the electron cloud has traveled a much shorter distance than expected by Bazelyan.

The nonlinear streamer propagation is the subject of the following chapters. In that phase the space charges and electric field strongly interact, and the analytical study of such streamers is far more difficult than the analysis of the avalanche phase [66].

6

PROPAGATING STREAMERS: NUMERICAL EXPERIMENTS AND PREDICTIONS

We present numerical results on the propagation of streamers in N_2 under influence of a uniform electric field. The adaptive grid refinement strategy presented in Chap. 3 enables us to explore a new range of parameters. In overvolted gaps, the algorithm enables us to obtain the high accuracy required by the large spatial gradients. The only numerical work reported on negative streamers at these high fields [5, 83] uses relatively coarse, uniform grids, and their main focus is the streamer instability. We investigate in more detail the mechanisms of streamer formation and propagation, and how it depends on initial and boundary conditions. It is now also possible to compute the propagation of a streamer in very large, undervolted gaps. The formation is qualitatively different from the high field case.

6.1 Introduction

In Chap. 5 the very first stage of the streamer propagation has been investigated. This avalanche phase is characterized by its linearity, due to the absence of space charge effects on the electric field, which therefore stays constant and equal to the, in our case uniform, background electric field. It has been shown that it then is possible to solve the linear equations for the electrons analytically, while a good approximation for the ion density distribution could be derived by considering the spatial moments of the two species. Once the electric field gets altered by the space charges, the discharge enters the *non-linear streamer regime*. A curved space charge layer builds up at the streamer tip, enhancing the electric field ahead of it, while suppressing it in its back. It is then necessary to compute the complete, non-linear, minimal streamer model (2.3.12)-(2.3.14).

The simulations of streamers, particularly in high electric fields, poses a great

numerical challenge because of its multiscale nature: the non-ionized medium in which the streamer propagates is orders of magnitude larger than the ionized channel itself, which in turn is much larger than the active space charge layer at its tip. Obviously, the use of a uniform grid like in [24, 102, 5, 83] soon gives problems with computational memory. Moreover, as illustrated in Sect. 3.2.1, the FISHPAK routine used to solve the Poisson equation quickly and at low computational costs, does not provide the desired accuracy anymore when the number of grid cells exceeds a certain threshold. The grid refinement algorithm presented in Chap. 3 has been designed especially to overcome these difficulties, and can be used to run within an reasonable computational time and within the limits of the computational memory offered by a simple pc. It also enables us to obtain mesh sizes up to a fraction of the ionization length, which is much finer than the mesh sizes used up to now [24, 102, 5, 83]. We therefore have a powerful tool to investigate the dependence of the streamer propagation on a wide range of parameters.

First the influence of the grid size during the non-linear regime is investigated, enabling us to draw conclusions with respect to the minimal grid size needed for the presented results to be trusted. We use the numerical results to describe in detail the transition from the linear to the non-linear regime, when the space charge layer develops into its characteristic crescent shape. We then investigate how the streamer evolves during the non-linear regime, and how it depends on the external parameters like background field, number of seed electrons, and electron inflow. Finally we use insight given by the simulations to predict the behavior of streamers in other parameter regimes.

6.2 Accuracy requirements for the streamer simulations

6.2.1 Long streamers in a low electric field

We consider the evolution of an ionization seed that is attached to the cathode, in a long gap between two plane-parallel electrodes. Between them a low electric field is applied.

We use a three-dimensional, axially symmetric (thus effectively 2D) coordinate system (r, z). The axis of symmetry is the z-axis, perpendicular to the two electrodes.

The low voltage electrode (cathode) is placed at $z = 0$, the high voltage one (the anode) at a distance $L_z = 2^{15} = 32768$. The radial boundary is situated at $L_r = 2^{14} = 16384$. We notice that the inter-electrode distance is twice as small as that used in the undervolted gap of Chap. 4. We apply a (dimensionless) potential difference of $4.9152 \cdot 10^3$ on the electrodes, resulting in a uniform background electric field of $\boldsymbol{\mathcal{E}}_b = -|\boldsymbol{\mathcal{E}}_b|\hat{\mathbf{e}}_z$, with $|\boldsymbol{\mathcal{E}}_b| = 0.15$. For N_2 at atmospheric pressure, this corresponds approximately to an inter-electrode distance of 7.5 cm, a potential difference of 225 kV, and an electric field of 30 kV/cm.

A Gaussian initial seed (2.3.16) is placed on the cathode. The maximal initial density is $\sigma_0 = 1/4.7$ and the e-folding radius of the seed is $r_b = 100$, which correspond to 10^{14} cm^{-3} and 230 μm, respectively, for N_2 under normal conditions. This relatively dense seed enables us to bypass the avalanche phase. If we would start with a single electron at this value of the electric field, the results of Chap. 5 show that the transition to streamer would occur after the avalanche has traveled a distance $d \approx 18\alpha^{-1}(|\mathcal{E}_b|) \approx 1.4{\cdot}10^4$, which is about half of the system length. Using a dense seed accelerates considerably the transition time, thereby saving a large amount of computational time.

The width of the seed is ten times larger than that used in the example of Chap. 4. The reason for this is to investigate the accuracy requirements for the computations in this section. To this end, we will run simulations also on relatively coarse grids, that are not able to capture a narrow initial seed.

The coarsest grid for the continuity equations has a mesh size of 64, the coarsest one for the Poisson equation a size of 2048. We first present the results on the finest grid that could be obtained with the algorithm presented in Chap. 3 on a system of this size. This mesh size is 2.

The upper panel of Fig. 6.1 shows the electron density distribution on a logarithmic scale. There are two regions in the streamer: one rather wide with low electron densities, and one which is much narrower and very dense. The streamer exhibits all its characteristic. The middle panel of Fig. 6.1 clearly shows the negatively charged layer and its effect on the equipotential lines. The electric field is larger than the background electric field at the tip of the streamer, allowing the streamer to propagate into the undervolted gap. The interior field is slightly smaller than the background field (see the lower panel of Fig. 6.1). We remark that the field is only calculated in the ionized regions, therefore there is no field plotted for larger z in the lowest panel of Fig. 6.1.

Let us now compare these results with those obtained on coarser grids. We have run the simulations on grids that were refined up to mesh sizes of 4 and 8, thus the finest grids in these cases are twice respectively four times coarser than those on which the results shown in Fig. 6.1 have been obtained.

Fig. 6.2 shows the temporal evolution of the position of the streamer front obtained on each run. The position of the streamer head is defined as the location on the axis of symmetry of the maximal net charge density. It shows that, regarding the front position, and consequently the front velocity, the results are in very good accordance with each other. The streamer evolves somewhat more rapidly on the coarse grid, which is due to numerical diffusion. The differences are only visible at the very end of the non-linear regime, just before the streamer becomes unstable. This instability is the subject of a more detailed investigation in Chap. 7.

Of course, we should also consider the influence of the grid size on other quantities like densities or the field. This is done in Fig. 6.3 for the axial net charge density as well as the electric field strength on the axis of symmetry (we recall that the field has only been computed in the ionized regions). At $\tau = 500$, the run on the coarse grid (with mesh size 8) already gives convergent results. At later times, the influence of the grid becomes more visible, though

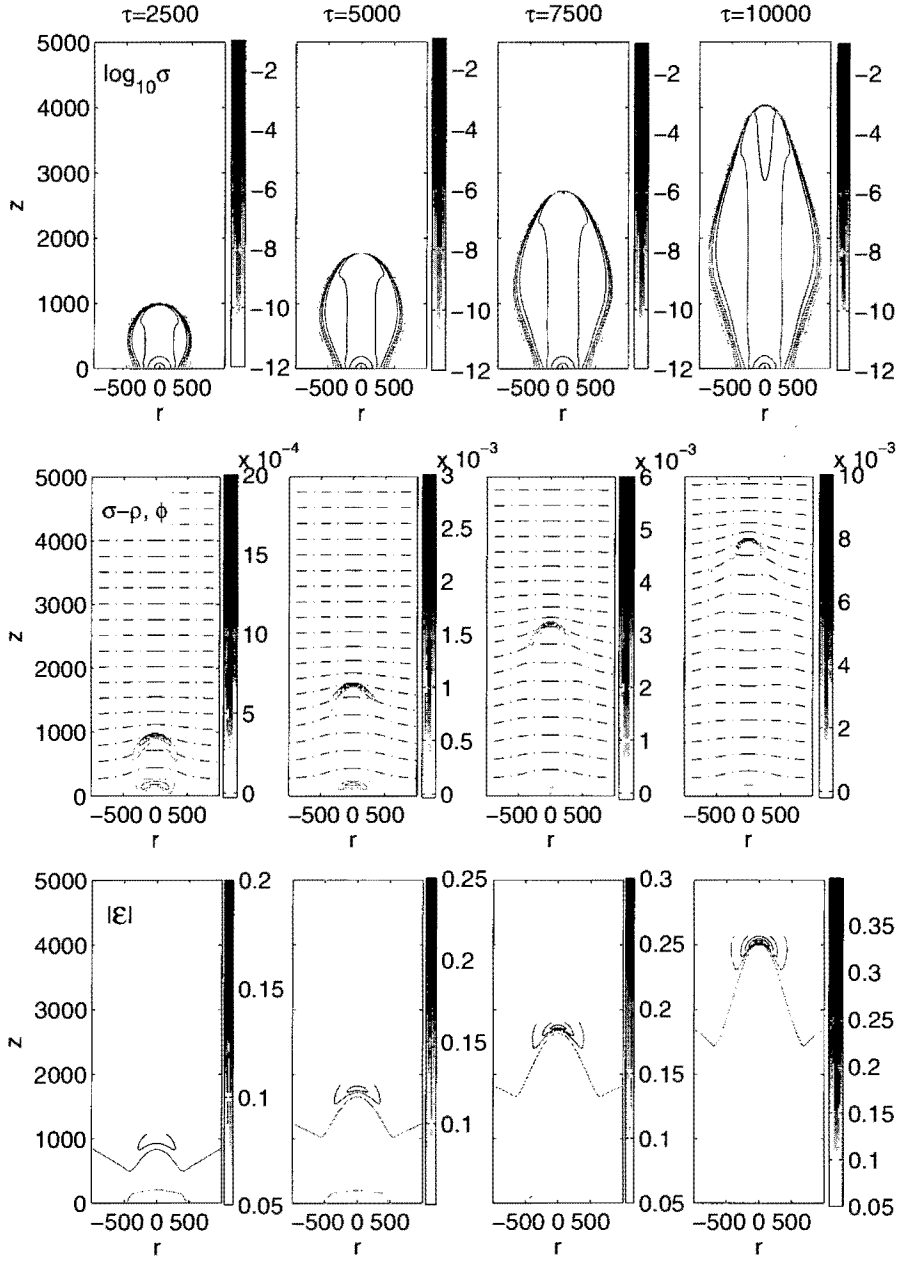

FIGURE 6.1: Evolution of a streamer during the non-linear regime in a low background electric field $|\mathcal{E}_b| = 0.15$. *Upper panel*: logarithm of the electron density. *Middle panel*: net charge density and equipotential (dash dotted) lines. *Lower panel*: electric field strength.

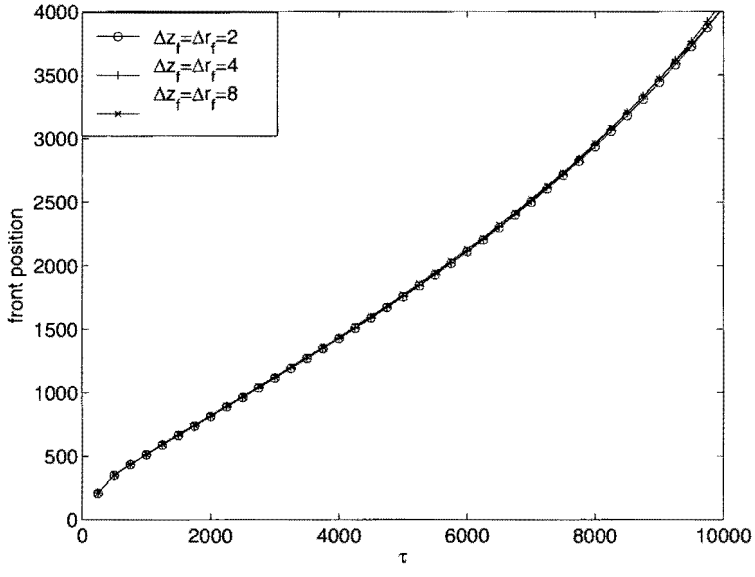

FIGURE 6.2: Influence of the grid size on the temporal evolution of the streamer head position. All simulations have been run with a coarsest grid with mesh size of 64 for the continuity equations, and with mesh size 2048 for the Poisson equation. *Solid line*: finest mesh size of 2. *Dashed line*: finest mesh size of 4. *Dash dotted line*: finest mesh size of 8.

at $\tau = 7500$ only the run on the coarsest grid gives significant errors, in that the front has moved slightly faster, and the net charge density is smaller than on smaller grids. At $\tau = 1 \cdot 10^4$ the errors on the grids with a mesh of 4 are visible as well. The front has moved too fast, although the field is smaller. This shows that it is indeed the numerical diffusion on the coarse grid that accelerates the front, rather than a erroneous computation of the electric field.

We conclude that the simulations run on a finest grid with mesh size 8 will give non-negligible errors in the results. However, one more level of refinement, leading to a finest grid with mesh size 4, already gives acceptable solutions during the streamer regime. Moreover, from these results, we can extrapolate that refining the grids even more (e.g. up to a finest mesh size of 1) will not lead to a significant correction of the results, and that the computational work required to run the simulations on such fine grids is not in proportion with the gain in accuracy.

6.2.2 Fine grid computations at a high electric field

We now consider the evolution of a streamer in short overvolted gap. The inter-electrode distance is set to 2048, corresponding to 5 mm for N_2 at atmospheric pressure. The background electric field is set to $\mathcal{E}_b = -0.5\hat{\mathbf{e}})z$, which corresponds to 100 kV/cm.

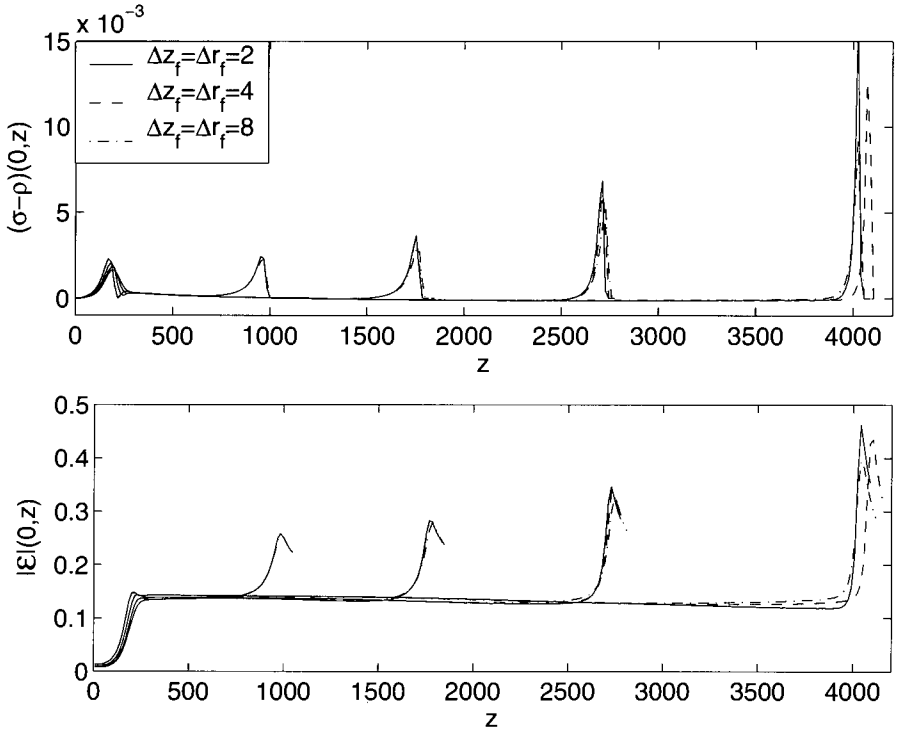

FIGURE 6.3: Influence of the grid size on the temporal evolution of the axial net charge density distribution (upper plot) and the axial electric field strength (lower plot). The results have been obtained on the same grids as Fig. 6.2. *Solid line*: finest mesh size of 2. *Dashed line*: finest mesh size of 4. *Dash dotted line*: finest mesh size of 8. The time of the snapshots are τ =2500, 5000, 7500 and 1000, and correspond to the snapshot of Fig. 6.1.

The initial seed is placed at the cathode. Because of the high electric field, a streamer will be able to emerge from a single electron. As shown in Chap. 5, we can mimic a single electron by using the initial seed (2.3.16) with a maximal density $\sigma_0 = 10^{-4}$ and an e-folding radius $r_b = 10$. In view of the small mesh sizes that will be used in the following, we use homogeneous Neumann boundary conditions at the cathode, which due to the electron inflow, will accelerate the transition to streamer.

The evolution of the streamer with the previous initial and boundary conditions during the non-linear phase is shown in Fig. 6.4. These results have been obtained on finest grids with a mesh size of 1/8 for both the continuity and the Poisson equations. The coarsest grid for the continuity equation has a mesh size of 2, the one for the Poisson equation has a size of 128.

The discharge clearly exhibits the streamer features which are, as in the

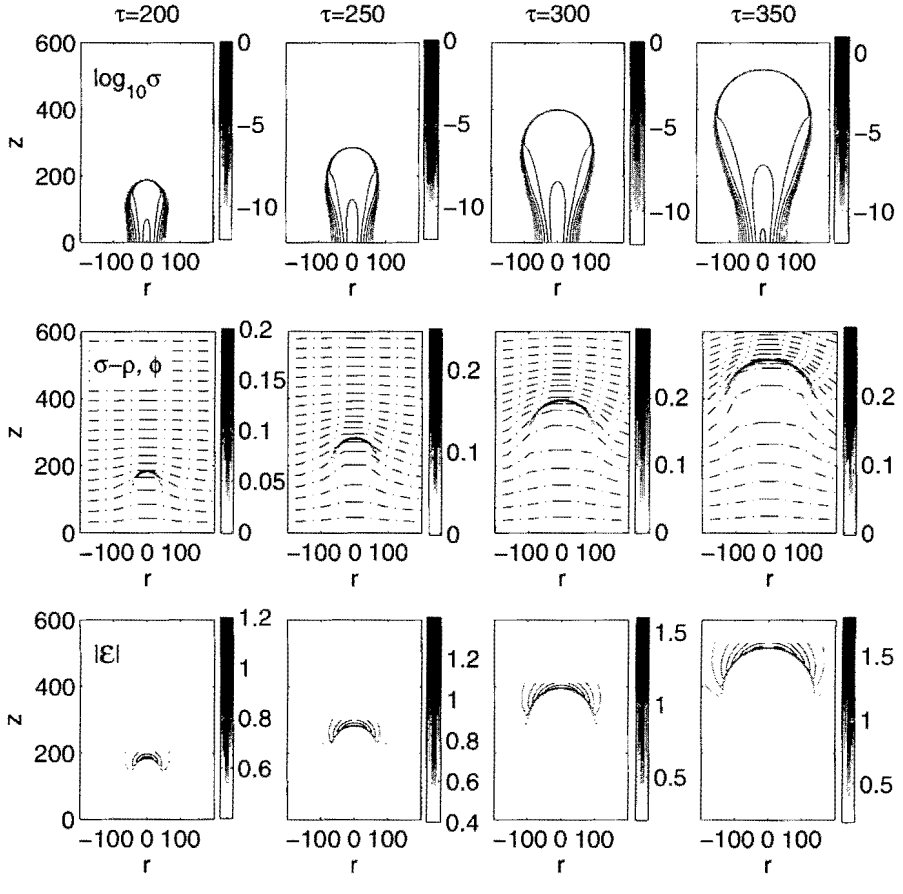

FIGURE 6.4: Evolution of a streamer during the non-linear regime in a low background electric field $|\mathcal{E}_b| = 0.5$. *Upper panel*: logarithm of the electron density. *Middle panel*: net charge density and equipotential lines. *Lower panel*: electric field strength. The results have been obtained using the adaptive grid refinement strategy presented in Chap. 3. The continuity equations are computed on grids with mesh sizes from 2 to 0.125, the Poisson equation on grids with mesh sizes from 128 to 2.

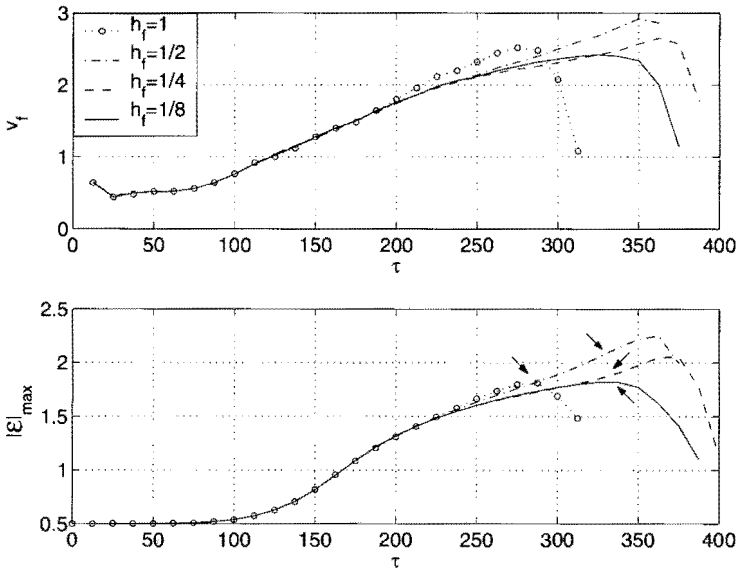

FIGURE 6.5: Temporal evolution of the front velocity (upper panel) and maximal axial electric field (lower panel) on different finest mesh sizes h_f. *Dotted line*: $h_f = 1$. *Dash-dotted line*: $h_f = 1/2$. *Solid line*: $h_f = 1/4$. *Dashed line*: $h_f = 1/8$. The arrows in the lower plot indicate the times at which the streamer becomes unstable.

low field case, a thin negatively charged layer that enhances the electric field ahead of it, and a partial screening of the interior of the streamer body from the background electric field. In contrast to the high field case, however, the electron density distribution does only exhibit a single, dense region (see the upper panel of Fig. 6.4).

A more detailed investigation of the differences between high and low field propagation follows later in this chapter, and in this section we focus on the influence of the grid size on the streamer propagation. To this end we again consider the position of the streamer head computed on coarser grids. The simulations have all been carried out with a coarsest grid with a mesh size of 2 for the continuity equations. The coarsest grid for the Poisson equation had a cell size of 128. The finest grids considered in the following have a mesh size of 1/8, 1/4, etc... up to 1.

The upper panel in Fig. 6.5 shows temporal evolution of front velocity for different grid sizes. The velocity has been computed using a numerical evaluation of the front position at equidistant time steps of 12.5. The position of the front is defined as the axial position of the maximal net charge density $\sigma - \rho$. All grids eventually show a decay of the propagation velocity. The streamer has then become unstable, and the branches no longer propagate along the axis. These instabilities will be investigated in more detail in Chap. 7, while we here

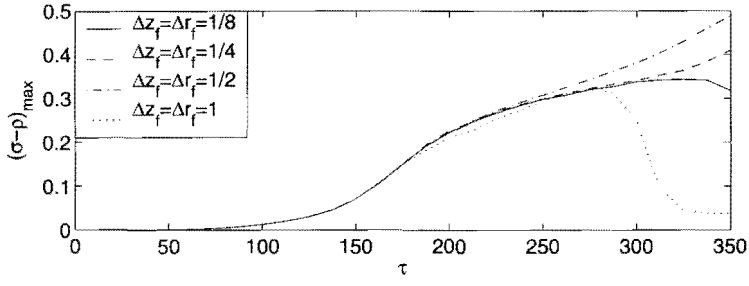

FIGURE 6.6: Influence of the grid size on the evolution of the maximal axial net charge density. *Solid line*: finest grid with mesh size 1/8. *Dashed line*: finest grid with mesh size 1/4. *Dash dotted line*: finest grid with mesh size 1/2. *Dotted line*: finest grid with mesh size 1.

focus on the streamer propagation regime.

We see that up to $\tau = 200$, the use of a grid size of 1 gives the same propagation velocity as a grid size of 1/8. After that time, the predicted front velocity on a grid size of 1 is much faster than that on the finer grids, whereas the maximal electric field does not differ that strongly from fine grid computations. This implies that the front propagates faster because of numerical diffusion.

At later times, the maximal electric field on the grid with size 1/2 and 1/4 becomes higher than that on finer grids. This results in a larger front velocity as well. This is due to branching (see also Fig. 6.7). Indeed, on a grid with size 1/8, the branching is off-axis, and the field on the axis drops. In the other two cases on the other hand one branch continues to propagate along the axis, and the field on the axis continues to grow. We notice that there is a discrepancy of the front velocity on the grids with size 1/4 and 1/8 between $\tau \approx 250$ and 325, but that the electric field is the same at these times. This discrepancy comes from the error in the calculation of the velocity, which is related to the time interval and the grid size on which the velocity is estimated. The velocities are in fact the same within the error bounds.

Let us now finally consider the error in the net charge density distribution induced by the use of too coarse grids. Fig. 6.6 shows the evolution of the maximal net charge density on the axis, obtained with the simulations on finest grids with mesh size 1 up to 1/8. On a coarse grid (with size 1), the net charge density rapidly gets underestimated. In the beginning of the non-linear phase, the run on a grid with finest mesh size of 0.5 gives good results, however a higher accuracy is required at later times for the net charge density to be quantitatively well computed.

Of course, this only provides us with information on the axial propagation. A final comparison is made in order to investigate the behavior of the streamer in the radial direction. Fig. 6.7 shows the evolution of the level lines corresponding to half the maximal net charge density. The contours have been determined at

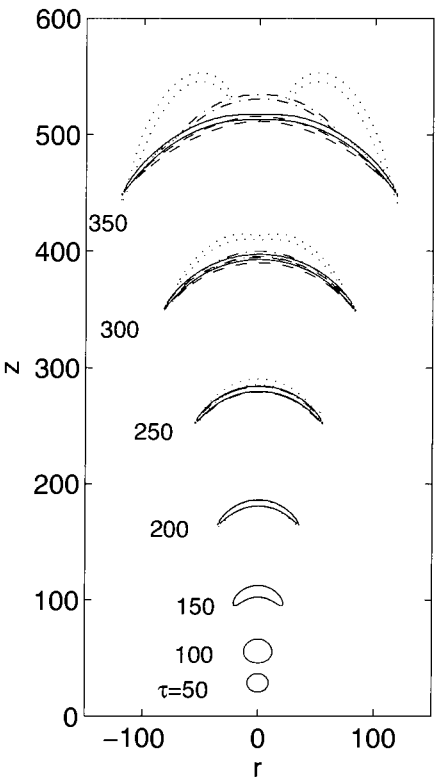

FIGURE 6.7: Influence of the grid size on the evolution of the half maximum net charge density contours. The contours have been determined from $\tau = 50$ to 350, with equidistant time steps of 50. *Solid line*: finest grid with mesh size 1/8. *Dashed line*: finest grid with mesh size 1/4. *Dash dotted line*: finest grid with mesh size 1/2. *Dotted line*: finest grid with mesh size 1.

equidistant time steps of 50.

Comparing Fig. 6.6 with Fig. 6.7, it appears that if the results concerning the *axial* distribution of the field coincide at a certain time, the results concerning the *radial* distribution coincide as well, and vice versa. Indeed, at e.g. $\tau = 200$, the contours of Fig. 6.7 are hardly discernible from each other, and so is the maximal axial net charge density computed on the different grids (see Fig. 6.6). At later times, we observed from Fig. 6.5 that the streamer computed on a grid with a finest mesh size of 0.5 starts propagating faster, which is also illustrated in Fig. 6.7. However, up to the time that the streamer becomes unstable, the results have converged with a run on a grid with finest mesh size of 1/4. The form of branching, i.e. whether it is on- or off-axis, depends on the grid that is used, and leads to the discrepancy between the results shown in Figs. 6.5 and 6.6. An off-axis branching results in a decrease of the maximal field and

densities on the axis, whereas an on-axis branching on the contrary results in an increase of these quantities.

6.2.3 Discussion and conclusions

The results show that, both in over- and undervolted gaps, negative streamers exhibit a growing enhancement of the field at their tip. The spatial gradients become larger with the field [30], requiring an increasing spatial accuracy.

The mesh sizes used here are much smaller than the ones used up to now for the simulations of streamers in an equally strong background electric field [5, 83]. Earlier simulations on negative streamers were carried out on a background field of 0.25, with a grid size of at least 2 [102]. These simulations show a field enhancement up to a value of 1, and our tests show that a finer grid size is desirable for the results to be trustworthy.

Since the characteristic scale of the inner structure of the streamer front is set by the ionization length $\alpha(|\mathcal{E}|_{max})$ [30, 4], one should take care that the grid size is fine enough to capture this length scale. **As a rule, we suggest that the grid should be at least four times smaller than the ionization length in the maximal electric field.** For our undervolted gap, where the field grows up to 0.4, this implies a maximal grid size of 3, while for our overvolted gap, in which the field grows up to 2, this rule implies that the grid size should be smaller than 0.5.

6.3 The build-up of the space charge layer

In this section we continue our description of the avalanche to streamer transition of Chap. 5 in terms of the space charge. Fig. 6.7 shows that at early times, the space charge region is almost circular, and undergoes a deformation towards its characteristic crescent shape when the streamer emerges. The evolution of this region is not straightforward, and we describe the mechanisms that result in this transition.

6.3.1 Charge neutral system

We consider the same overvolted gap as in Sect. 6.2.2. The initial seed is taken as dense and as wide as in Sect. 6.2.2. However, it is now placed in the bulk of the gap, at $z_0 = 50$, and homogeneous Dirichlet boundary at the cathode are used, thereby ensuring a vanishing inflow of electrons. The reason for this is that the aim of this section is to identify the mechanism of formation of the space large layer. It is then useful to let no electrons flow into the system, since then there is no charge inflow during the whole discharge, and hence all the charged particles sitting in the system have been created by impact ionization.

In the following we denote the (dimensionless and negative) net charge density by $q^-(\mathbf{r},\tau) = \sigma(\mathbf{r},\tau) - \rho(\mathbf{r},\tau)$. We stress that we will always refer to a negative charge density with a positive q^-.

The equation for the space charge can be derived by subtracting Eqs. (2.3.12) and (2.3.12) from each other,

$$\frac{\partial q^-}{\partial \tau} = -\nabla \cdot \mathbf{\Gamma}_e \,, \tag{6.3.1}$$

where $\mathbf{\Gamma}_e$ is the current density. It represents the charge fluxes, and is written as

$$\begin{aligned} \mathbf{\Gamma}_e &= -\sigma \boldsymbol{\mathcal{E}} - D\nabla\sigma \\ &= \mathbf{v}_b\sigma - \sigma \boldsymbol{\mathcal{E}}_q - D\nabla\sigma \\ &= \mathbf{\Gamma}_{\mathcal{E}_b} + \mathbf{\Gamma}_{\mathcal{E}_q} + \mathbf{\Gamma}_D \end{aligned} \tag{6.3.2}$$

where $\boldsymbol{\mathcal{E}}_q$ is the self induced field of the space charges,

$$\boldsymbol{\mathcal{E}}_q = \boldsymbol{\mathcal{E}} - \boldsymbol{\mathcal{E}}_b \,, \tag{6.3.3}$$

and $\mathbf{v}_b = -\boldsymbol{\mathcal{E}}_b$ is the drift velocity of the electrons in the background electric field. In Eq. (6.3.2) the fluxes have been decomposed in contributions of the background field $\mathbf{\Gamma}_{\mathcal{E}_b}$, the self induced field of the space charges $\mathbf{\Gamma}_{\mathcal{E}_q}$ and the diffusion $\mathbf{\Gamma}_D$, allowing us to determine which mechanism is most important in which phase of the evolution.

A detailed picture of the growth of the width of the layer is given in the upper plot of Fig. 6.8. We have decomposed the space charge layer into its *back*, where the densities grow, and its *front*, where the densities decay. The width is defined as the distance between the location of the maximal axial value of the net charge density, and the location where it has reached a value of 1/e of the maximal value. It clearly appears that the back of the streamer head and the front undergo different phases during the formation of the thin space charge layer. The evolution of the lateral growth, characterized by the e-folding radius of the space charge layer, is shown in the lower plot of Fig. 6.8. It shows that initially the radial growth is small, and suddenly increases around $\tau = 100$.

In order to understand what causes these changes, we look at the different sources of fluxes given in Eq. (6.3.1). The set of figures 6.9-6.12 on the following pages illustrates the evolution of the streamer at early times. Snapshots are taken at times $\tau = 50$, 87.5, 112.5 and 137.5, which correspond to the different propagation phases of the space charge layer shown in Fig. 6.8.

The upper panel in each Fig. 6.9-6.12 shows the net charge density distribution q together with a vector plot of the self induced field $\boldsymbol{\mathcal{E}}_q$, and a vector plot of the total charge current together with the negative divergence of this current field, which, as can be seen from Eq. (6.3.1), corresponds to the temporal derivative of the net charge density. The four lower pictures in each Fig. 6.9-6.12 show the vector field and the magnitude of the contributions of the background field, the self induced field of the space charges and the diffusion to the charge currents. We notice that the drift in the background electric field gives a simple translation of the electron cloud along the z-axis. The radial fluxes are set by the self induced field of the space charges and by the diffusion.

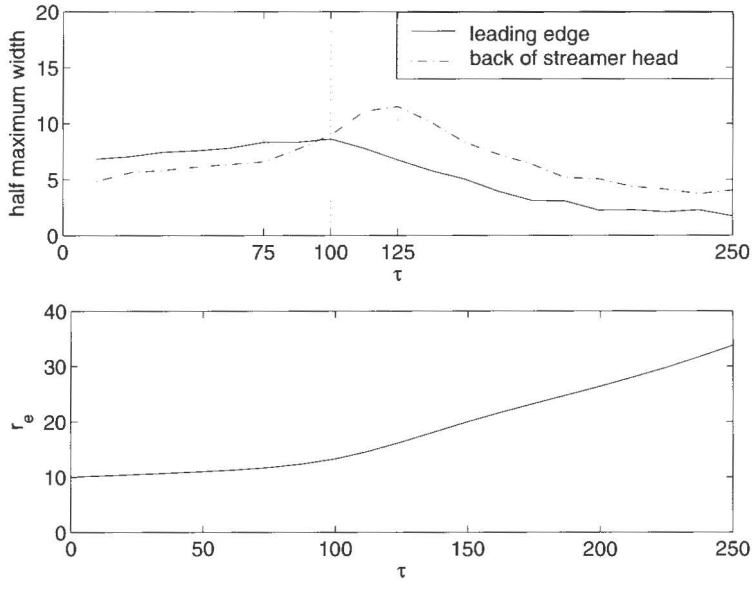

FIGURE 6.8: *Upper row*: evolution of the distance between the maximum and the half maximum position of the charge density distribution in both the leading edge (solid line) and the back of the streamer head (dash dotted line). *Lower row*: evolution of the e-folding radius of the space charge layer.

To analyze these figures, it is important to realize that the space charge density q^- grows in time in the regions where the divergence of the total fluxes $\mathbf{\Gamma}_e$ are negative, and vice versa. Also, consequently, the gradients in the space charge density grow in time in the region where the divergence of the total fluxes have negative gradients. The contour lines in the two upper plots of Figs. 6.9-6.12 therefore give the net charge density distribution together with its temporal growth rate.

At $\tau = 50$, the net charge density distribution is dipole-like (see the upper left plot of Fig. 6.9), resulting from the drifting, growing and diffusing electron cloud, leaving behind a trail of ions. These are the typical electron, ion and net charge distributions during the avalanche phase, as already introduced by Raether [80]. During this phase, the fluxes in the space charge field are negligible compared to those in the background field, and even smaller than those driven by diffusion. The radial growth of the space charge layer during this phase is set by the diffusion only, since the background field is directed axially.

At some point, the net charge densities in the dipole have become so large, that their self induced field is no longer negligible, enhancing the background field ahead of the negatively charged region, while on the contrary reducing it in between the positively and negatively charged regions. This then of course also affects the electron fluxes, shifting the location of the maximal electron

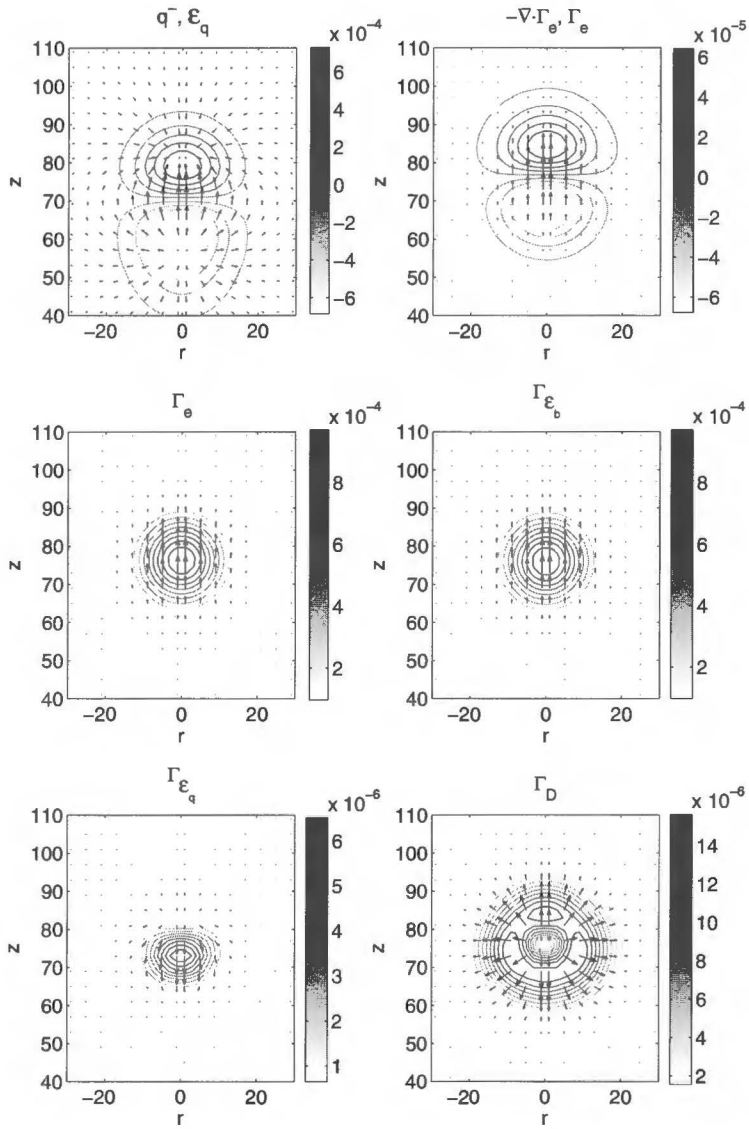

FIGURE 6.9: *Upper row*: net charge density distribution with vector plot of the self field (left) and time derivative of q with vector plots of $\mathbf{\Gamma}_e$ at $\tau = 50$. *Second row*: vector plots and absolute values of the total current density (left) and the contribution of the background field (right). *Lower row*: vector plots and absolute value of the contribution of the self induced field of the space charges to the current densities $-\sigma\mathcal{E}_q$ (left) and of the diffusion $-D\nabla\sigma$ (right).

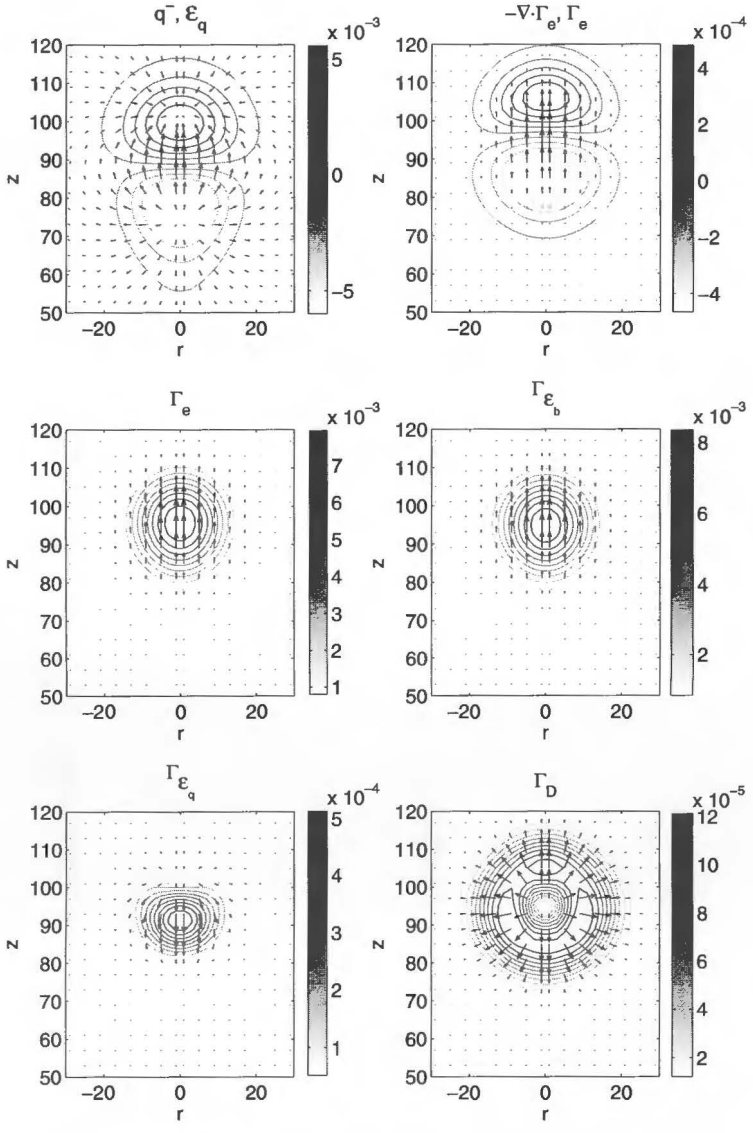

FIGURE 6.10: Same as Fig. 6.9, now for $\tau = 87.5$.

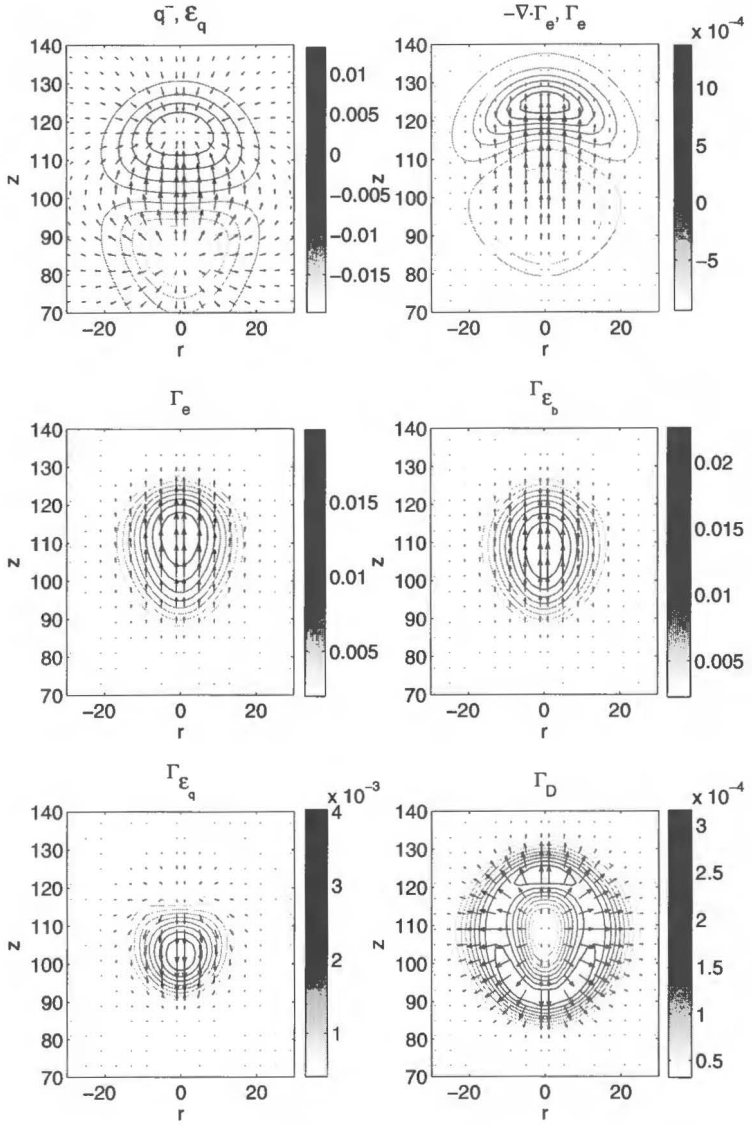

FIGURE 6.11: Same as Fig. 6.9, now for $\tau = 112.5$.

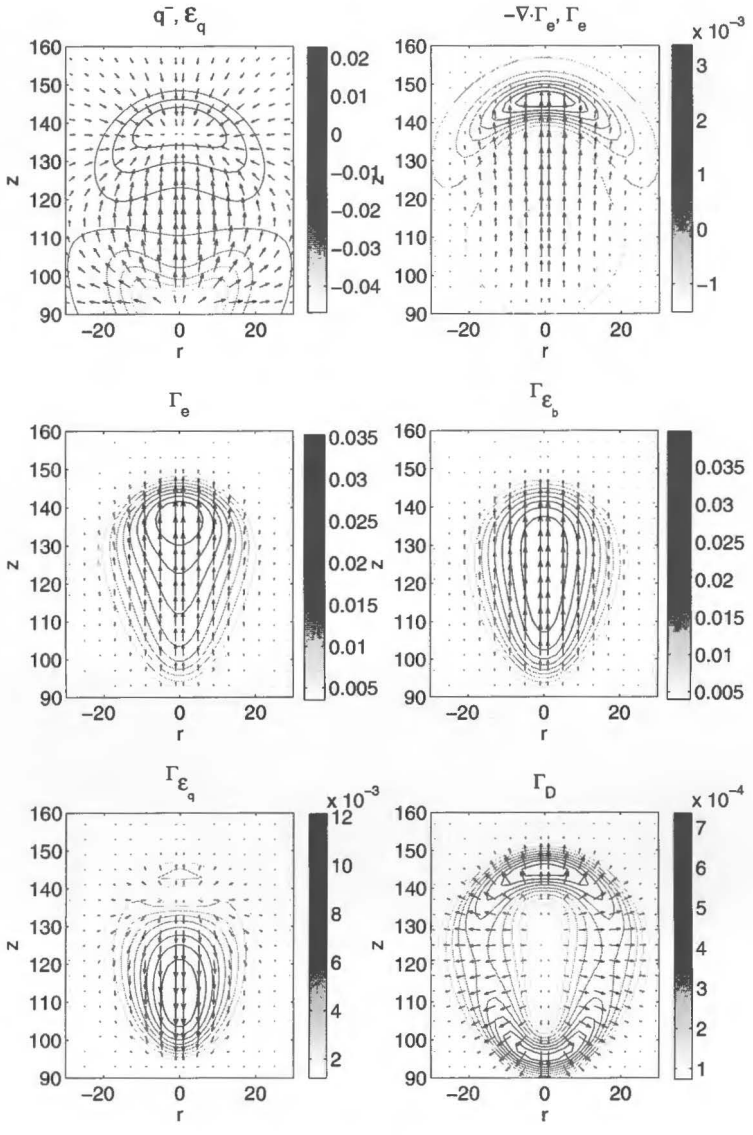

FIGURE 6.12: Same as Fig. 6.9, now for $\tau = 137.5$.

drift from the electron cloud towards the streamer head, as can be observed comparing the contours of $\mathbf{\Gamma_e}$ and $\mathbf{\Gamma}_{\mathcal{E}_b}$ in Figs. 6.10-6.12.

In a first stage, the field enhancement is still negligible, and the space charges only reduce the drift velocity of the electrons situated behind the negatively charged region. The largest transport still occurs from the electron cloud towards the negatively charged region, as can be seen from the location of the maximal fluxes in Figs. 6.10. At the same time, the field reduction leads to smaller gradients in the axial fluxes, which translate into a smaller temporal change of the net charge densities. This is the reason for the back of the streamer to become wider, as could be observed in Fig. 6.8.

Then the background field also becomes enhanced by the self induced field of the space charges, leading to larger gradients in the (axial) fluxes ahead of the negatively charged region, as illustrated in the upper right plot of Fig. 6.11. The width of the front of the space charge layer then starts decreasing (see also Fig 6.8).

Eventually, the field distortion due to the space charges becomes so strong, that the maximal charge transport no longer occurs from the electron cloud towards the back of the negatively charged region, but from the back to the front of this region, as shown in Fig. 6.12. The charge fluxes towards the back can not "refill" it, and its width then decreases.

Moreover, the field of the space charges is directed in the positive radial direction, thereby adding to the diffusion fluxes, and increasing the radial growth of the space charge layer, as is shown in the lower plot of Fig 6.8. The e-folding radius shown in this figure has been determined as the maximal radius at which the net charge density has dropped to 1/e of its axial value.

The different phases in the emergence of the space charge layer can thus be characterized by the enhancement or the reduction of the field being negligible or not.

6.3.2 Influence of the electron inflow

In the previous subsection, it has been described how the space charge layer develops when the total net charge in the system remains zero. We can now use this knowledge to understand how the emergence of the space large layer is affected when homogeneous Neumann boundary conditions are used at the cathode together with an initial seed that is attached to the cathode (we will denote this case by "(N)") instead of Dirichlet conditions at the cathode and an initial seed in the bulk of the gap (denoted by "(D)").

As mentioned before, the use of homogeneous Neumann boundary conditions together with an initial seed attached to the cathode implies that electrons are now allowed to flow into the system, and consequently the whole system is no longer charge neutral, but will accumulate negative charge. The evolution of the total number of electrons in the whole system as well as in the streamer head, for both cases (D) and (N), is shown in Fig. 6.13. Notice that at small times the total number of electrons is smaller in case (N) than in case (D). This is due to the initial condition, which was a complete Gaussian in case (D), and only

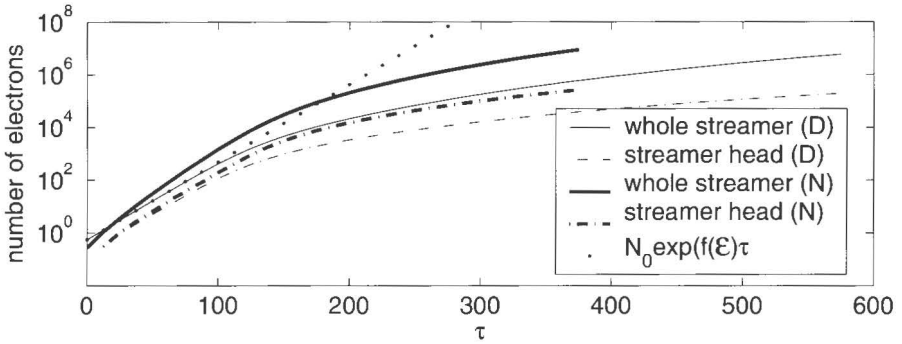

FIGURE 6.13: Influence of the electron inflow on temporal evolution of the number of electrons in the whole streamer (solid line) and in the streamer head (dash dotted line). The

half a Gaussian in case (N) because of its position on the cathode. From this figure, we see that in case (D), up to $\tau \approx 125$, the number of electrons grows as $e^{f(\mathcal{E}_b)\tau}$, as expected from Eq. (5.3.2). Since the negative net charge is found in the streamer head, we can define the total number of negative charges in the streamer head as $\int \max(\sigma - \rho, 0) d^3r$.

From $\tau \approx 125$ we see that both the total number of electrons and the total negative net charge grows less fast. This comes from the screening of the electric field in the streamer body, which leads to a reduced impact ionization, and thus to a smaller multiplication rate of the electrons in the body. This is not compensated for in the leading edge where the field enhancement leads to a larger ionization rate, this region being much smaller than the body of the streamer. Moreover, the electric field being partially screened also leads, as already mentioned before, to a reduced (though not completely annihilated) drift of electrons from the electron cloud into the streamer head. Therefore the number of negative charge in the streamer head continues to increase, though at a smaller rate.

Fig. 6.14 shows the temporal evolution of the half maximum width and radius of the space charge region in both cases of homogeneous Dirichlet and Neumann boundary conditions at the cathode. We see that the boundary condition hardly influences the radius of the space charge layer up to $\tau \approx 100$, after which the inflow of electrons apparently enhances the growth of the radius. The width of the streamer head is slightly larger when using Neumann boundary conditions. In Fig. 6.15 the charge density distribution as well as its self field and the charge current is shown at $\tau = 50$. Comparing the charge density distribution at $\tau = 50$ (upper left panel of Fig. 6.15) with that of the avalanche with Dirichlet boundary conditions (Fig. 6.9), we see that it constitutes a monopole rather than a dipole, and that the charge density in the monopole is larger than that of the dipole. This difference in space charge distribution has two consequences. First, the

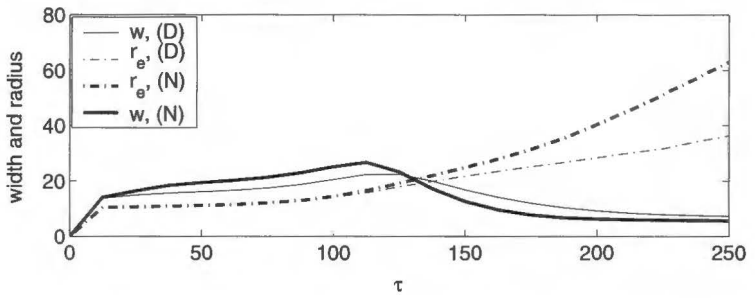

FIGURE 6.14: Comparison of the evolution of the space charge layer when using either homogeneous Dirichlet (thin lines) or homogeneous Neumann (thick lines) boundary conditions at the cathode (denoted by D and N, respectively). *Solid lines*: width of the space charge layer. *Dash dotted lines*: e-folding radius of the space charge layer.

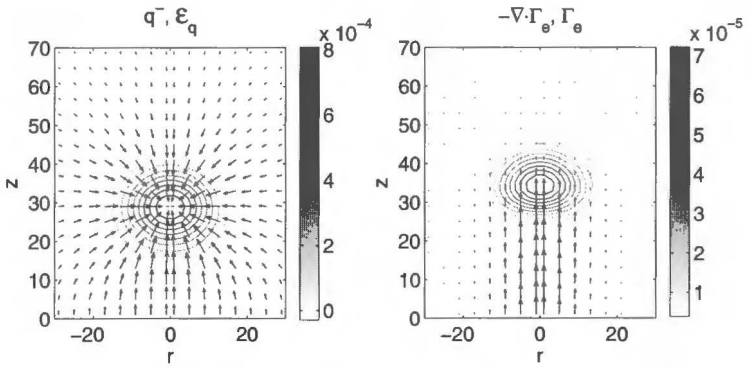

FIGURE 6.15: Net charge density distribution (right) with vector plot of the self induced field (left) at $\tau = 50$, in the case Neumann boundary conditions are used at the cathode.

field about such a monopole is radially directed, in contrast to the case with Dirichlet boundary conditions at the cathode. This causes the larger radial expansion of the streamer head in case (N) compared to case (D). Second, the field of the monopole-like charge is larger than that of the dipole with the same density, not only because of the larger net charge density, but also because of the absence of positive charges.

The field of the space charge will therefore enhance the background field at earlier times than in case (D), and the pulled front propagation will consequently be accelerated as well.

6.4 Streamers in overvolted gaps

In the previous section it has been described how the space charge layer develops into its characteristic crescent shape. It has been shown that, in this stage, it is the electric field ahead of the space charge layer that sets the dynamics of the ionization front. In this section we describe how the streamer evolves during this non-linear front regime.

6.4.1 Dirichlet boundary conditions

Let us first focus on the propagation with Dirichlet boundary conditions at the cathode. We continue the description of the streamer evolution from where we stayed at the end of Sect. 6.3.1. At that point, the space charge layer has acquired a crescent shape, whose width is decreasing in time, while its radius of curvature as well as its half maximum radius continue to grow. The further evolution of the electron and of the net charge density distributions are shown in Fig. 6.16, that of the electric field in Fig. 6.17.

The two upper panels of Fig. 6.16 show the evolution of the electron density in both logarithmic and linear scale. The plots in linear scale show the high density structure of the streamer. In the streamer head, the electron density increases with time, leading to increasingly large gradients. In the body of the streamer, the electron density is growing up to $\tau \approx 300$, and then saturates. The body of the streamer then reaches a quasi-stationary state. The electron density in the streamer reaches a value up to approximately 0.5, which corresponds to 10^{14} cm^{-3} for N_2 under normal conditions. The degree of ionization thus is low, compared to the particle density of the neutral gas, which is in the order of 10^{19} cm^{-3} at atmospheric pressure.

The lower panel of Fig. 6.16 illustrates how the positively and negatively charged regions get increasingly separated from each other, and the negatively charge streamer head, the quasi-neutral streamer body, and the positively charged base are now clearly discernible from each other. In the base of the streamer, the V-shaped positively charged region observed in Fig. 6.16 results from the trail of positive ions left behind by the electrons, the latter being advected towards the anode while the ions stay immobile. Eventually, after the electrons have been depleted from the high field region at the base, only immobile and inert ions remain there in "frozen" state. The only dynamics is a slow growth of the depleted base region by extraction of more electrons. This results in a further field enhancement in the back.

The lower panel of Fig. 6.16 also illustrates how the equipotential lines in the streamer body move further apart, getting increasingly excluded from the streamer body, which means that the streamer body becomes electrically screened. Outside the streamer, on the contrary, the equipotential lines are squeezed together, which means that the electric field is enhanced there, as can also be observed in Fig. 6.17.

Ahead and "outside" the streamer head, the axial electric field induced by the space charge layer is directed along the background field (i.e. along the

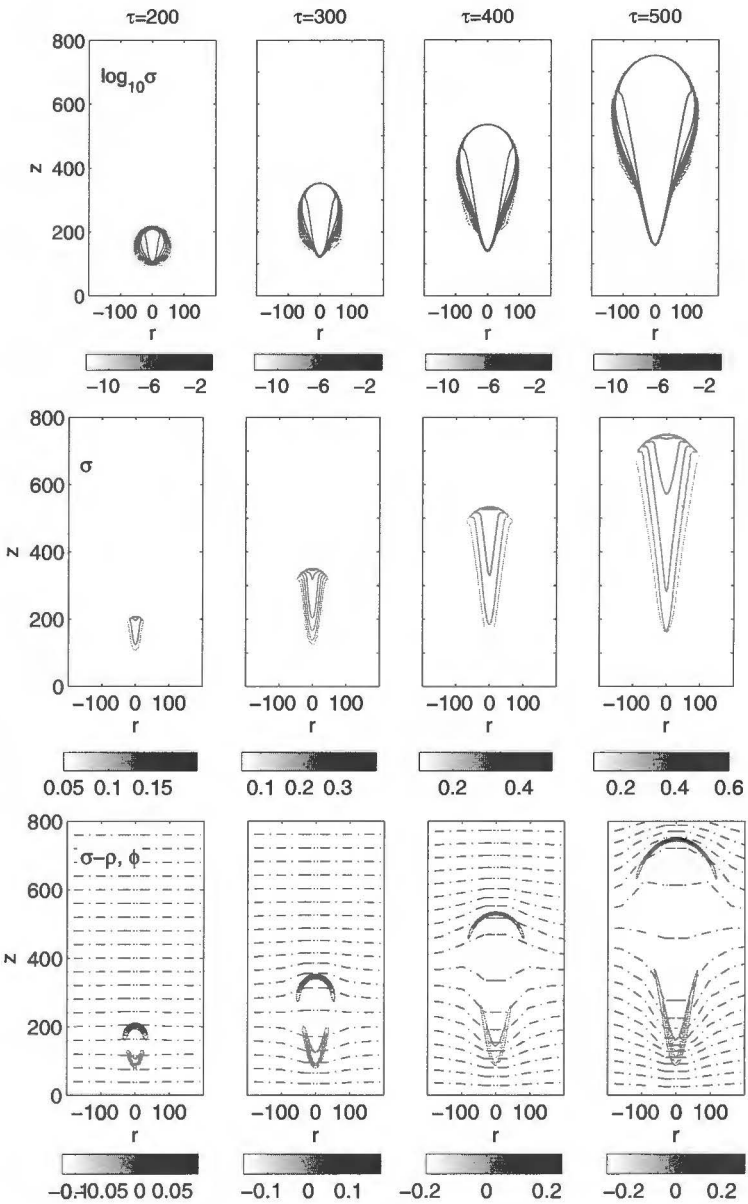

FIGURE 6.16: Evolution of the logarithm of the electron density distribution $\log_{10}\sigma$ (upper panel), the electron density on a linear scale (middle panel) and the net charge density q (lower panel) with Dirichlet conditions at the cathode. The times correspond, from left to right, to τ =200, 300, 400 and 500. The contours for $\log_{10}\sigma$ range from -12 to the maximal value with steps of 1. The contours for q start from zero both towards negative and positive values of q with steps of 0.05.

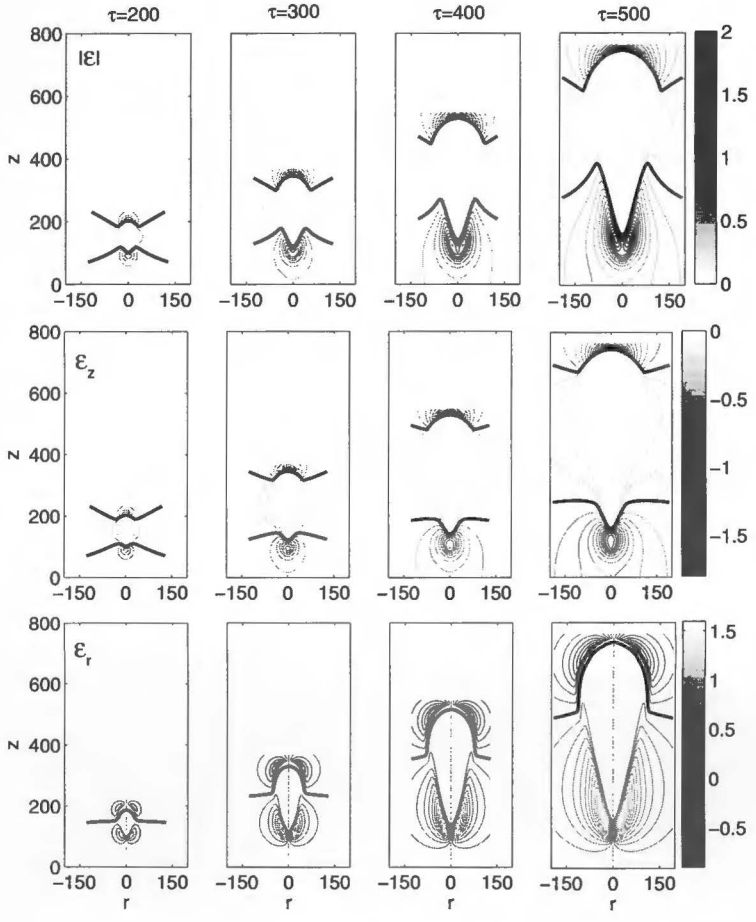

FIGURE 6.17: Evolution of the electric field distribution with Dirichlet conditions at the cathode. *From top to bottom*: electric field strength $|\mathcal{E}|$, axial field component $\mathcal{E}_z$ and radial field component $\mathcal{E}_r$. The times correspond, from left to right, to τ =200, 300, 400 and 500. The thick solid lines correspond to the unperturbed values, i.e. $|\mathcal{E}|$ =0.5, $\mathcal{E}_z = -0.5$ and $\mathcal{E}_r = 0$. The contours for $|\mathcal{E}|$ range from 0 to 2, those for $\mathcal{E}_z$ go from -1.8 to 0 and those for $\mathcal{E}_r$ from -0.9 to 1.6. All field contours are separated by an equal distance of 0.1.

negative z-direction), and it thus enhances the background field, as can be seen in the middle panel of Fig. 6.17). The lower panel of this figure shows that the radial component of the electric field is directed inwards in this region, and the current therefore is directed outwards. The electrons are thus accelerated towards the anode and away from the axis of symmetry, causing the radial expansion of the space charge layer and its propagation towards the anode.

In Fig. 6.17 we can observe that the temporal variation of the electric field in the streamer body is very small, and it reaches a value of around 0.2, which gives a shielding efficiency of approximately 60%. The interior of the streamer therefore approaches but does not reach the Firsov-Lozansky limit of ideal conductivity body [59], in which the shielding is supposed to be 100% efficient. Now, the number of charges in the space charge layer grows in time (see Fig. 6.13) and this requires a transport of charge from the streamer body towards the streamer head. Since the gradients in the electron densities in the streamer body are small, diffusion will not be able to transport a significant number of electrons, and therefore it is the drift that enables the electrons to move towards the streamer head. This explains why a non-vanishing electric field is required in the body when the head is non-stationary.

The evolution of the charge layer can be described by means of the width w and characteristic radii r_e and r_c of the half maximum contours of the net charge density. r_e has already been defined in Sect. 3.4 as the maximal $r-$coordinate of the half maximum contour, and gives a measure for how extended the layer is in radial direction. We define r_c as the radius of curvature of the layer. and therefore a measure for in how far the front approaches a planar front. More precisely, the radius of curvature of the front is defined as the radius of the circle going through the axial position of the maximal net charge density, and through the position of the maximal $r-$coordinate of the half maximum contour (see Fig. 6.18). The ratio r_c/w provides the information on the flatness of the front, We notice that it is remarkable that the circle defined with this radius of curvature indeed follows the space charge layer, and that this is not mere luck but reproducible for all kind of simulation parameters.

The radius of curvature of the front is a meaningful parameter only after the front has formed. Indeed, as we saw in Sect.6.3, at early times there is no space charge layer, only a cloud, whose radius of curvature tends towards infinity.

Up to $\tau \approx 130$, this figure shows that the space charge region is almost circular, indeed the radius r_e of the cloud is approximately half the width. This is the characteristic evolution during the avalanche regime. The layer is defined by the superposition of the Gaussian electron density and the trail of positive ions it leaves behind, and, at early times, we have shown in the previous section that this results in a dipole like distribution of the net charge density. From $\tau \approx 130$ to 200, a space charge layer forms Moreover the distance between the contours starts growing, indicating an acceleration, and thus space charge effects. The layer acquires its crescent shape, which enhances the field ahead of it while screening its back from the externally applied field. After $\tau \approx 200$, the width of the layer continues to decrease, but at a much smaller rate. We will show in Sect. 6.6 that the width of the layer is set by the ionization length

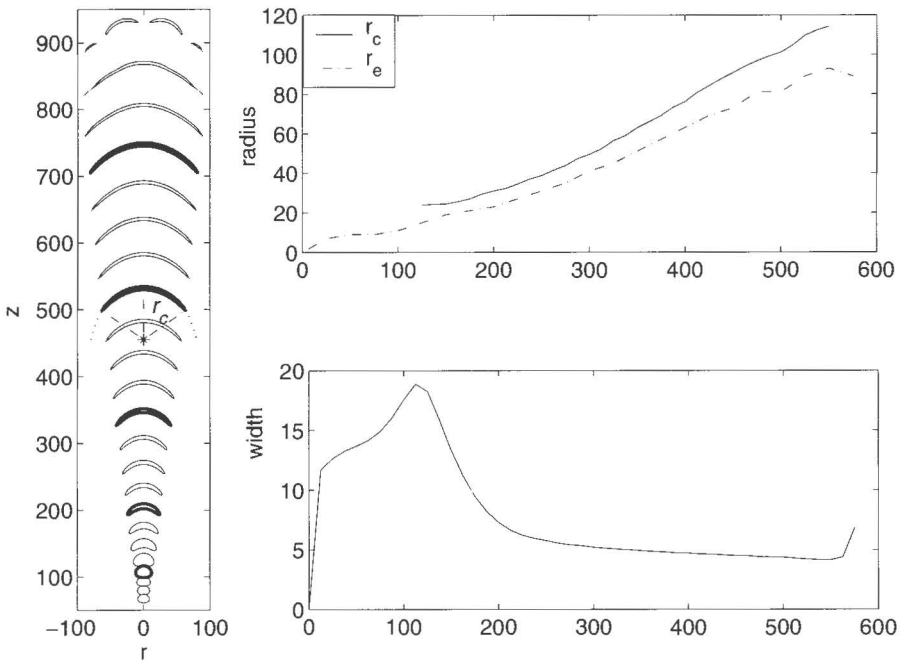

FIGURE 6.18: Left: contours of the half maximum net charge density for τ=25 to 575 with steps of 25, thick lines correspond to τ multiple of 100. r_c is illustrated for $t = 400$. The temporal evolution of the half maximum radius r_e and the radius of curvature r_c (upper right) and width w(lower right) is shown as well (for the definitions of r_e and w we refer to Fig. 3.16).

$1/\alpha(|\mathcal{E}|_{max})$, which, for increasing fields, results in shrinking. The irregularities in the width in Fig. 6.18 come from its numerical evaluation that has been carried out on the coarsest grid, whose cells have a size $\Delta r = \Delta z = 2$.

The radial growth of the space charge layer is primarily due to the field enhancement of the space charge layer, which is directed away from the axis, as is shown in Fig. 6.19.

Figs. 6.19 and 6.20 clearly show that the electron currents due to diffusion now are small compared to those due to the drift in the total electric field. Fig. 6.20 also shows that the largest diffusion fluxes occur in the streamer head, whereas in the streamer body they are quite small. However, as mentioned before, the high density streamer body is not completely screened from the external background electric field, and consequently allow electrons to flow from the streamer body to the head, thereby increasing the amount of space charges in the streamer head. The growing space charge results in an increasing enhancement of the electric field ahead of the streamer, which in turn results in a larger drift and reaction rate of the electrons. The dynamics of the space charge

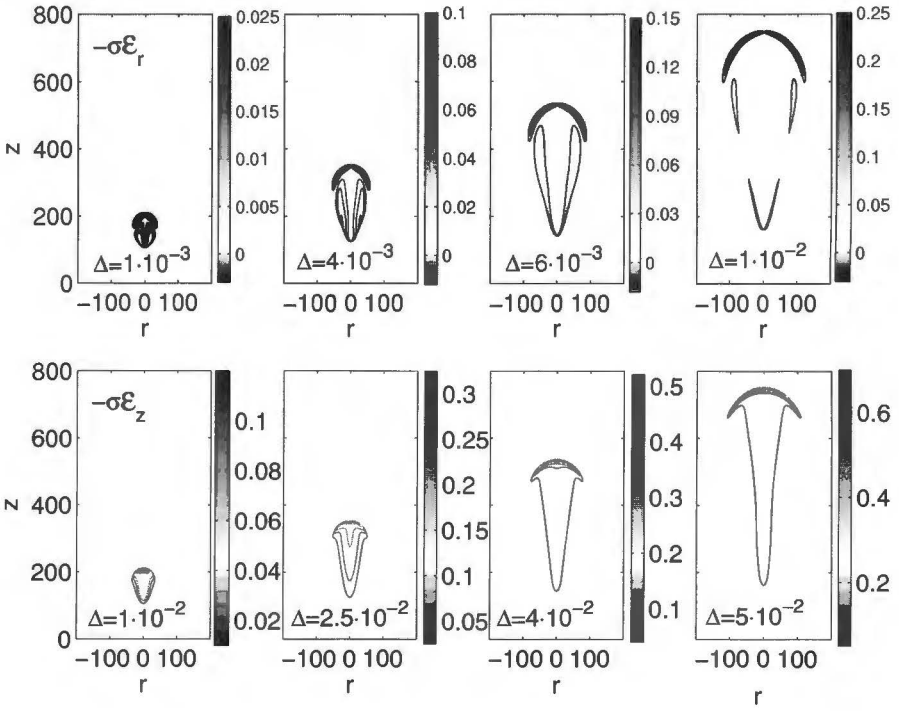

FIGURE 6.19: Distribution of the radial (upper panel) and axial (lower panel) components of the electron current density due to the drift in the total electric field. The snapshots are taken at the same times as those in Figs. 6.17 and 6.16.

layer at this stage of the evolution is mostly a redistribution of the charges in the head, at which a small amount of charge is added from the streamer body (see Fig. 6.13).

We remark that the diffusive fluxes, which are the gradients of the electron density distribution, already slightly exhibit the branching of the streamer (see Fig. 6.20) at $\tau = 500$, whereas the branching is hardly discernable in the space charge layer.

6.4.2 Effects of the initial and boundary conditions

In this section we show how the electron inflow influences the streamer propagation in the non-linear regime. To this end, we consider five cases with different initial seeds. Case 1 has Dirichlet boundary conditions, and the streamer is detached from the cathode, while in cases 2 to 5 Neumann boundary are imposed at the cathode, to which the streamer is attached.

The evolution of the total amount of electrons N_e in the system, as well as the total electron inflow per time unit I_i are shown in Fig. 6.21 for all these

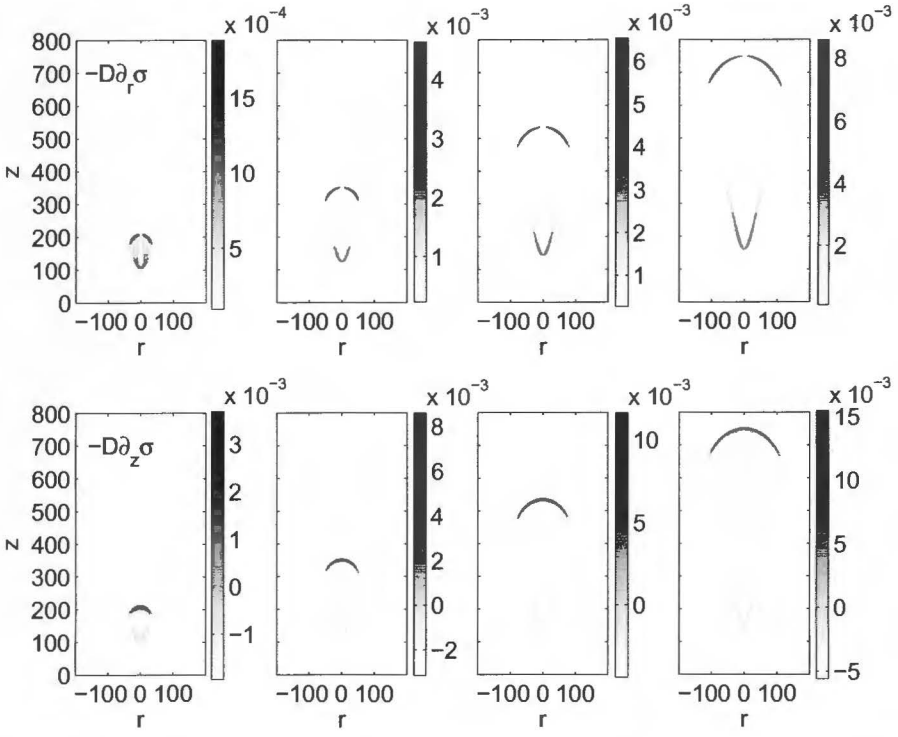

FIGURE 6.20: Distribution of the radial (upper panel) and axial (lower panel) components of the electron current density due to diffusion. The snapshots are taken at the same time as those in Fig. 6.19.

cases. I_i has been determined through the total amount of charge N_c residing in the system. Because of the charge conservation during an ionization event, N_c gives in fact the number of electrons that have flown into the system. I_i is then the time derivative of N_c. Of course, because in case (1) the seed is detached from the cathode, and therefore no charge is flowing into the system, I_i is zero in this case.

This figure now illustrates why the choice for these specific initial and boundary conditions has been made. The initial seeds of cases (1) and (2) are equally dense and have the same radius, and case (2) contains half the amount of electrons of case (1) because only half the initial Gaussian is situated inside the computational domain. The seed being attached to the cathode in case (2), electrons flow into the system, in contrast to case (1). The initial seeds of case (2) and case (3) contain the same number of electrons, but the e-folding radius of the seed of case 3 is four times larger than that for case (2). Case (2) and case (4) have a seed with the same e-folding radius, but the number of initial electrons in case (4) is much larger than in case (2). Finally, the amount of

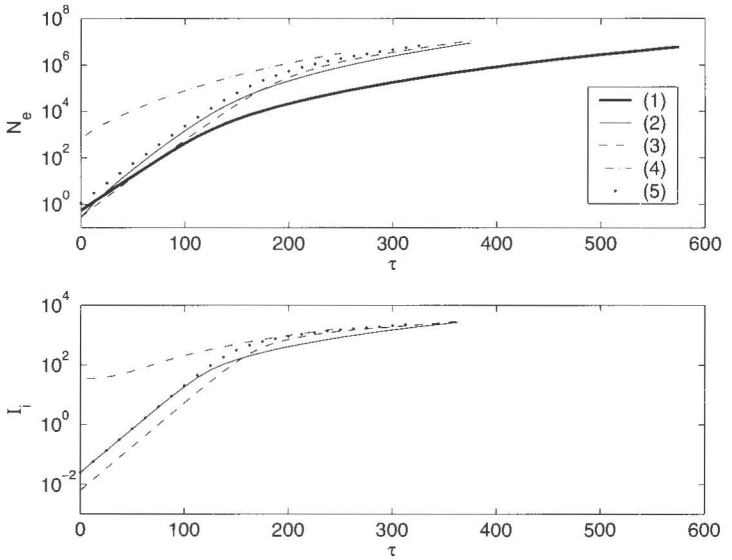

FIGURE 6.21: Temporal evolution of the total amount of electrons in the gas gap (upper panel), and the current at the cathode (lower panel) for different seeds and boundary conditions, in a background field $|\mathcal{E}_b|$=0.5. *Thick solid line*: case (1). *Thin solid line*: case (2). *Dashed line*: case (3). *Dash dotted line*: case (4). *Dots*: case (5). The electron current at the cathode is zero in case (1) and not shown due to the logarithmic scale.

electrons flowing into the system through the cathode in case (2) and case (5) are initially the same, but the seed (5) is less dense and steep. Moreover, the radius of initial seeds (1), (2) and (4) on the one hand, and of the seeds (3) and (5) on the other hand, are the same. We are thus able to investigate the influence of (i) the electron inflow, (ii) the initial number of electrons, (iii) the radius of the initial ionization seed, (iv) the initial density.

All simulations use Neumann boundary conditions at the cathode except for case (1). The density, the width and the location of the initial seeds for each case are

- Case (1):
  $\sigma_0 = 10^{-4}$, $r_b = 10$, $z_0 = 50$,
- Case (2):
  $\sigma_0 = 10^{-4}$, $r_b = 10$, $z_0 = 0$,
- Case (3):
  $\sigma_0 = \frac{1}{64}10^{-4}$, $r_b = 40$, $z_0 = 0$
- Case (4):
  $\sigma_0 = \frac{1}{4.7}$, $r_b = 10$, $z_0 = 0$

- Case (5):
  $\sigma_0 = \frac{1}{16}10^{-4}$, $r_b = 40$, $z_0 = 0$

Streamer propagation with electron inflow

Fig. 6.22 shows the evolution of the streamer in case 2 during the nonlinear regime in this case. One striking difference with the case investigated in the previous section is the absence of the positively charged region in the streamer base.

As mentioned before, the combination of a Neumann boundary condition at the cathode together with an ionization seed attached to it allows net charge to accumulate in the system. The negatively charged region therefore does not have a positive counterpart, as shown in the middle panel of Fig. 6.22.

In the streamer head, the growing amount of net charge density requires, as in the previous case, a continuous inflow of electrons from the streamer body, and therefore the electric field is not totally shielded. In fact, the minimal electric field in the body reaches a similar value in both cases, which is in the order of 0.15 just before the streamers become unstable.

Moreover, comparing the results at e.g. $\tau = 300$ in Figs. 6.16 and 6.22, we see that the densities, both of the electrons and the net charge, increase much faster than when the initial seed is not attached to the cathode. Obviously, this is due to the inflow of electrons from the cathode, which increases the electron density in the streamer body. In a similar electric field the charge fluxes are then larger as well, and the space charges consequently grow faster, thereby shortening the duration of the linear regime. **The emergence of a streamer is thus accelerated by letting electrons flow into the system.**

Propagation velocity

As we saw in the previous paragraph that the electron inflow accelerates the streamer propagation, one first thing to investigate is the influence of the electron inflow on the distance the streamer has traveled, which is shown in Fig. 6.23. The graphs in this figure end once the streamer has branched.

At very early times, the wide initial seeds drifting towards the anode, leaving behind the ion cloud, result in a maximal net charge density which is situated further from the cathode than in the case of narrow seeds. One should take care not to consider this as a faster propagation velocity, which is given by the slopes of the curves in Fig. 6.23. These indeed then show that the wide and sparse initial seeds (3) and (5) propagate slower than the narrow and dense initial seeds (1), (2) and (5).

The fact that it is electron inflow rather than the initial density of the seed which sets the propagation velocity can be easily concluded by comparing the curves for cases (1), (2) and (3). Indeed, (1) and (2) have the same initial density, however, eventually the streamer (2) accelerates compared to (1). The temporal range in which the streamer of case (3) propagates slower than case

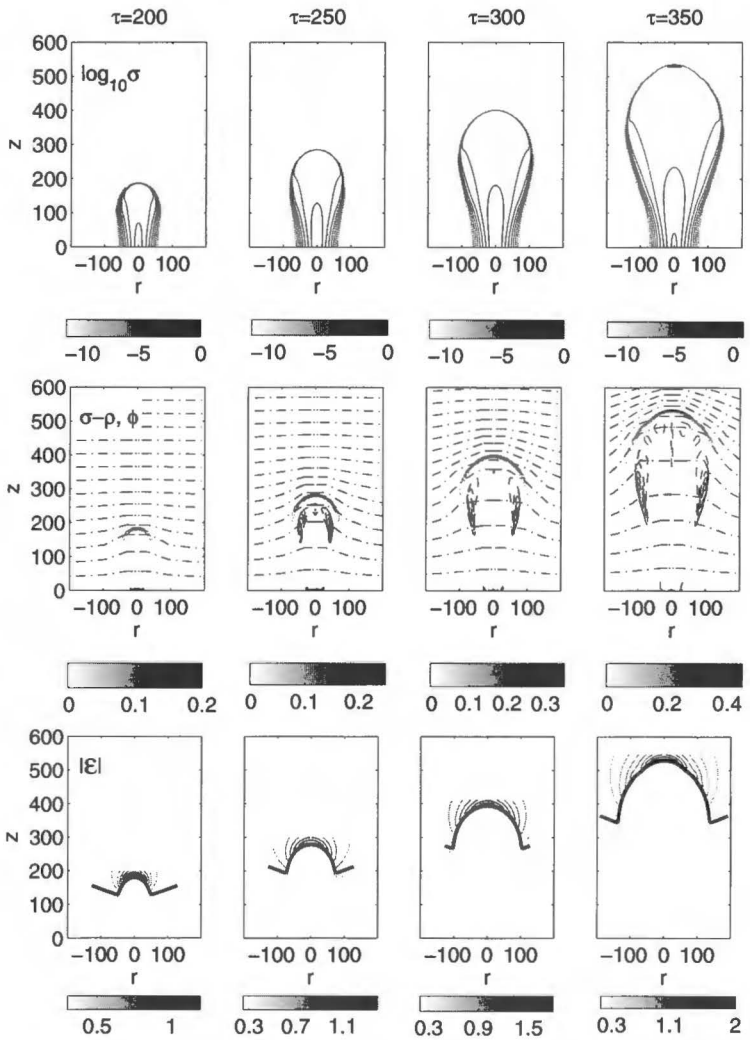

FIGURE 6.22: Evolution of the streamer with Neumann conditions at the cathode. *From top to bottom*: logarithm of the electron density, net charge density and electric field strength $|\mathcal{E}|$. The times correspond, from left to right, to τ =200, 250, 300 and 350. The ranges are the same as for distributions shown in Figs. 6.16 and Figs. 6.17. For clarity, the positively charged region is indicated by the dashed lines in the middle panel. The thick solid lines in plots for $|\mathcal{E}|$ correspond to the unperturbed value, $|\mathcal{E}|$ =0.5.

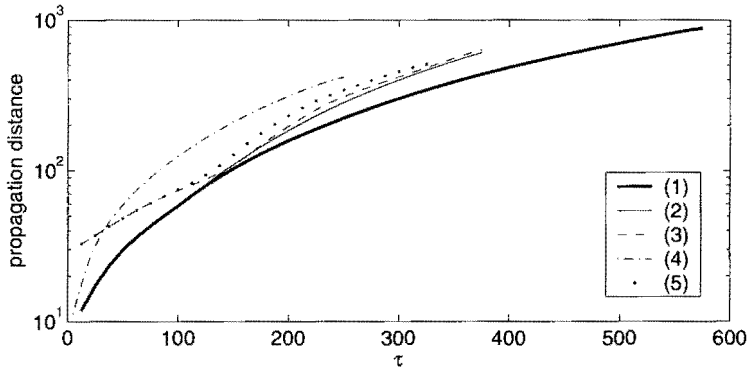

FIGURE 6.23: Travel distance of the streamer head as a function of time. This distance has been taken relative to the location of the initial ionization seed (z_0=50 for case (1), and 0 for the rest), and determined by the location of the maximal axial net charge density. *Thick solid line*: case (1). *Solid line*: case (2). *Dashed line*: case (3); *Dash dotted line*: case (4). *Dotted line*: case (5).

(2) corresponds to the times when the electron inflow of (3) is smaller (see also Fig. 6.21), and vice versa.

However, it is not only the electron inflow that sets the streamer velocity of the streamer. Indeed, in Fig. 6.21 it was shown that the seeds of cases (2) and (4) allowed for the same amount of electrons to flow into the system at the beginning of the streamer evolution. At these times, the seed of case (2), however, propagates less fast than that of case (1). This is due to less pronounced gradients in case (2), which, in a similar electric field, lead to smaller gradients in the drift and diffusive fluxes. The charge transport therefore become smaller as well, which obviously results in a slower propagation of the negatively charged region towards the anode. In case (4), the initial density and their gradients as well as the electron inflow being much larger than in all the other cases, the streamer propagates much faster, as expected.

Electron inflow as well as steep density gradients thus enhance the propagation velocity of a streamer.

Net charge density and electric field

In Fig. 6.24 the evolution of the axial maximal net charge density, together with both the maximal and the minimal axial electric field strength for the five cases (1) to (5) are shown. Comparing the evolution of the maximal electric field for cases (2), and (4) on the one hand, and those for cases (3) and (5) on the other hand, we see that, **the denser and steeper the initial seed, the faster the nonlinear regime is reached**. This is in accordance with the results of Chap. 5, and is simply due to the transport of electrons, which is proportional to the electron density in a uniform background field. The charge transport being

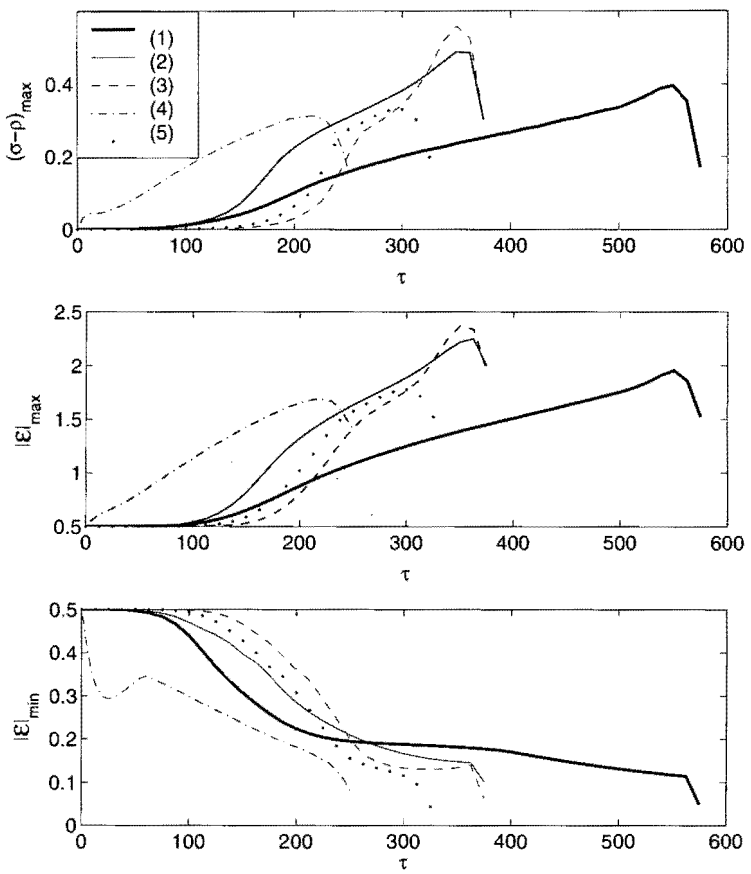

FIGURE 6.24: Evolution of the maximal net charge density on the axis (upper panel), the maximal electric field strength on the axis (middle panel), and the minimal axial electric field strength (lower panel). The time frame shown includes the electron avalanche (the maximal field is approximately equal to the background field $|\mathcal{E}_b| = 0.5$), the nonlinear regime (growing field and net charge density) and the instable phase (decreasing net charge density). *Thick solid line*: case (1). *Solid line*: case (2). *Dashed line*: case (3); *Dash dotted line*: case (4). *Dotted line*: case (5).

larger, the space charge layer builds up faster, and their effect on the electric field is visible at an earlier stage.

The evolution of the maximal net charge density and field exhibits a qualitatively similar behavior during the nonlinear regime in all cases, their growth rate being very rapid at the beginning of the nonlinear regime, and then decreasing (without turning negative). Once the space charge layer has become unstable, a different behavior sets in for cases (1), (2) and (3) on the one hand, and (4) and (5) on the other hand. In the first three cases the field and density

first increase more rapidly, then drops, whereas in the latter two cases there is no such rapid increase before the dropping of. This is due to the different form of branching, the first three acquiring a branch that propagates along the axis, leading to an even more rapid growth of the axial field and the densities before it drops off due to second splitting. The latter two on the other hand exhibit an off-axis branching, where the field and the densities become lower than those found in the stable nonlinear regime. This is illustrated in Fig. 6.25. In all cases, the streamer branches when the maximal electric field has reached a value of around 1.7.

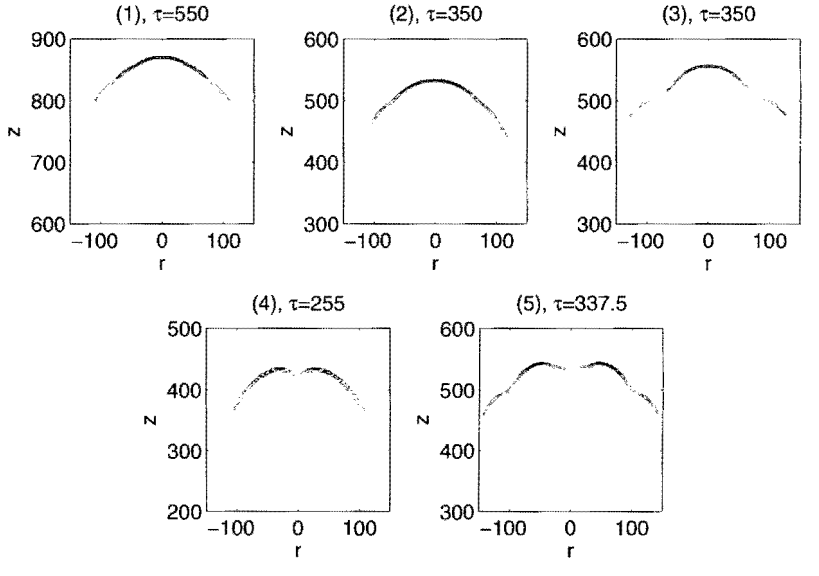

FIGURE 6.25: Net charge density distribution of the streamer head in the unstable regime. The upper three plots show the on-axis branching of cases (1), (2) and (3), the lower panel shows the off-axis branching of cases (4) and (5).

The strong increase of the space charge density at the beginning of the non linear regime is a consequence of the build-up of electric screening of the streamer body. Moreover, if the electric screening is not large enough, the ionization coefficient $\alpha(|\mathcal{E}|)$ is important, and a relatively large number of electrons (and ions) can be created in the streamer. These two things together then lead to a large increase of the net charge density. However, once the electric field screening sets in, and the interior field falls below the critical value where the ionization coefficient becomes negligible (we introduced the notion of under- and overvolted gap already in Chap. 4), the charge transport becomes smaller, resulting in a slower growth of the amount of space charges in the head.

Width and radius of the space charge layer

We have shown above how the streamer propagation is accelerated by the steepness and the density of the initial seed, as well as by the electron inflow. We now consider the influence of the initial seed on the evolution of the e-folding radius and the width of the space charge layer, shown in Fig. 6.26.

The reason for us to investigate this, is that in earlier work at low overvoltages [102] it was shown that the initial seed was "forgotten" after some time, and that the streamer therefore always evolved towards a similar structure regardless of the initial seed. The upper panel of Fig. 6.26 shows that this is the case as well in strong overvoltages. Indeed, although the radial growth differs strongly from one case to the other, the radius itself evolves towards a similar value in all cases, reaching a value of approximately 100 (which is in the order of 0.23 mm in N_2 under normal conditions) just before branching. Comparing the evolution of the radius of streamers (1) and (2), we see that **the inflow of electrons accelerates the radial growth of the streamer**. This is due to the electric field enhancement being much larger in that case because of the larger space charges, and the radial drift velocity of the electrons is therefore greater than in the case no electrons flow into the gap. For the same reason, the radial growth of the space charge layer in case (4) is much larger than in

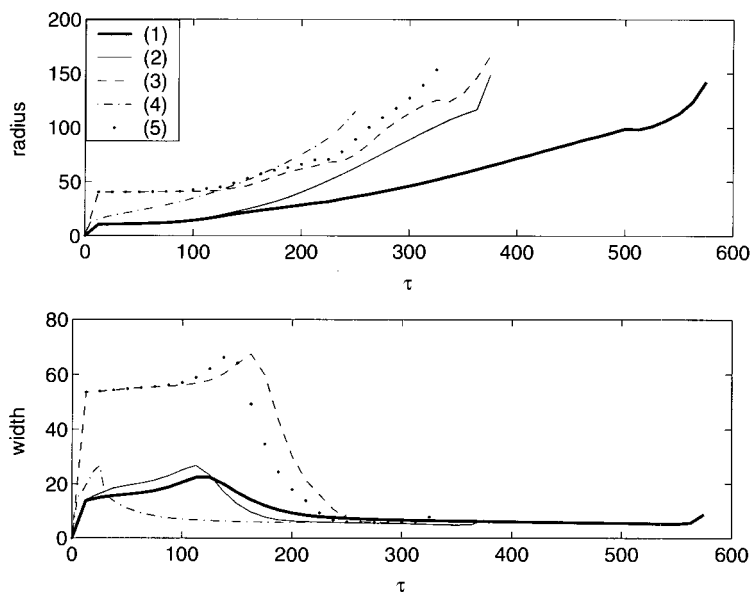

FIGURE 6.26: Evolution of the e-folding radius (upper panel) and width (lower panel) of the space charge layer for the different initial and boundary conditions. *Thick solid line*: case 1. *Solid line*: case 2. *Dashed line*: case 3. *Dash dotted line*: case 4. *Dotted line*: case 5

the other cases.

Moreover, we see that the width of the space charge layer reaches a similar value in all cases. We will see in Sect. 6.6.1 that it is the maximal electric field that sets the width of the layer. Now we have shown earlier that the streamer induces a similar field, though at a different rate, and consequently the space charge layer will shrink to a similar width.

Table 6.1 shows the characteristic values of the streamer head at the moment it becomes unstable. **It thus seems that in all cases the streamer has reached a similar state at the moment it becomes unstable.**

	$\|\mathcal{E}\|_{max}$	$\|\mathcal{E}\|_{min}$	$(\sigma-\rho)_{max}$	N_h	w	r_c
1	1.79	0.12	0.39	$1.6 \cdot 10^4$	5.23	112
2	1.96	0.15	0.40	$1.2 \cdot 10^4$	5.15	95
3	1.92	0.13	0.38	$1.7 \cdot 10^4$	5.25	120
4	1.77	0.11	0.33	$1.8 \cdot 10^4$	5.62	127
5	1.67	0.17	0.31	$7.0 \cdot 10^4$	5.69	80

Table 6.1: Characteristic values of the streamer heads in cases 1 to 5 at the moment the instability sets in. The columns contain, from left to right, the number of the case, the maximal electric field strength, the minimal field strength, the maximal net charge density, the total charge in the streamer head, the width and the radius of the space charge layer.

6.5 Streamers in low electric fields

6.5.1 Propagation of a small seed attached to the cathode

The algorithm presented in Chap. 3 has been used in the previous section to compute the propagation of a streamer in a short, strongly overvolted gap with a high spatial accuracy, needed for the large gradients induced by the strong electric field to be well resolved.

The local uniform grid refinement strategy can also be used to compute the streamer propagation in gaps longer that could be treated previously. We present the results obtained on a long gap ($L_z = 2^{16} = 65356$, in the order of 15 cm at atmospheric pressure) between two planar electrodes.

We use a rather dense initial ionization seed situated on the cathode, with height $\sigma_0 = 1/4.7$, which corresponds to 10^{14} cm^{-3} at atmospheric pressure. The e-folding radius is taken equal to 10. We recall that one needs to use a dense initial seed in order for a streamer to emerge in this undervolted gap. We use Neumann boundary conditions for the electrons at the cathode, allowing electrons to flow into the system, allowing the streamer regime to be reached even earlier. We saw in the previous section that qualitatively the electron inflow does not affect the streamer propagation. Therefore we allow ourselves to save a considerable amount of computation time by using these boundary and initial conditions.

The computational domain is extended up to $L_r = 2^{15} = 32768$ in the radial direction. From a computationally point of view it would not be effective to take L_r much smaller. Indeed, it is desirable for the computation of the Poisson equation to start on a coarse grid with as few grid points as possible, which is M_p=4 grid points in the direction of the "shortest" edge of the computational domain, in our case the radial direction. Then the number of grid points in the axial direction is $N_p = 4L_z/L_r$, and it is easily seen that the shortening the domain in the radial direction would only result in more grid points in the axial direction.

The coarsest grid for the continuity equations has a cell size of 64. They are refined up to a cell size of 2, which is a assumed to be sufficient in the low electric field. Indeed, the field will not exceed approximately 0.6, and in view of the results of Sect. 6.6.1, the e-folding width of the leading edge is not expected to decrease below $e^2 \approx 5.5$, which can be relatively well captured by this grid size.

Fig. 6.27 shows the evolution of the ionization seed. As in Sect. 6.4.1 we use the half maximum contours of the net charge density. Also, the half maximum contours of the electron density are shown, as well as those corresponding the half maximum deviation of the electric field strength from its background value.

At early times, the largest electron and net charge densities are found near the cathode. The half maximum contour lines are then concentrated near the cathode, and therefore hard to distinguish. Eventually, above $z \approx 4 \cdot 10^3$, the streamer head clearly forms.

We see that the streamer now follows a totally different evolution from that in a highly overvolted gap. It first expands radially, until the streamer has covered a distance of approximately 4000, after which it enters a phase of radial contraction. Then, when the streamer head has moved up to a distance of 8000 from the cathode, the streamer gets unstable and branches.

Also, we see from ranges of the half maximum contours that the maximal net charge density increases up to $2 \cdot 10^{-2}$, and that the maximal electron density in the streamer head grows twice as large, namely $\approx 4 \cdot 10^{-2}$. In the highly overvolted gap of Sect. 6.4, these values were one order of magnitude larger, even though the initial particle density was three orders of magnitude smaller. This is due to the very small ionization rate in this low electric field ($f(|\mathcal{E}_b|) \approx 7 \cdot 10^{-2}$ for $|\mathcal{E}_b| = 0.5$, whereas $f(0.15) \approx 2 \cdot 10^{-4}$). This is also the reason why we place a relatively high ionization seed at the cathode, and let electrons flow into the system. Otherwise indeed the initial seed might never multiply sufficiently for the nonlinear regime (and thus a sufficiently high electric field for a significant ionization rate) to be reached. This is illustrated in Fig. 6.28, where the number of electrons that have flown into the system as well as the number of electrons that have been created through ionization are plotted as a function of time.

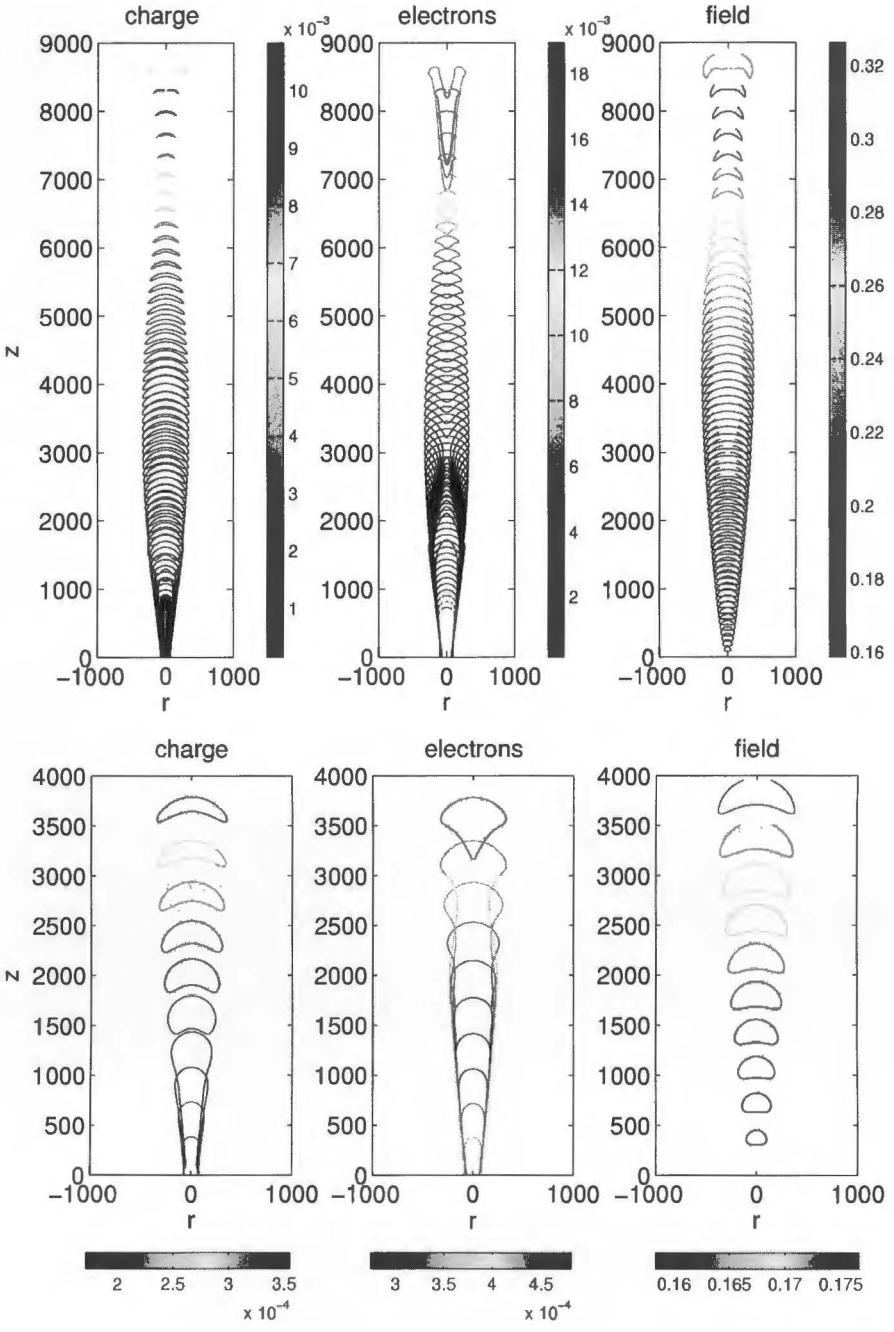

FIGURE 6.27: Evolution of an initial ionization seed in a background field $\mathcal{E}_b = -0.15$, by means of the half maximum contours of the net charge density (left), of the electron density (middle), and of the contours of the electric field defined by the half maximum deviation of the background field (right). The amplitude of the initial seed is σ_0=1./4.7 and its e-folding radius r_b=10. The temporal range covers τ from 0 to $33 \cdot 10^3$, with plotting steps of $5 \cdot 10^2$. The lower plot zooms in into the early times of the streamer evolution, from $\tau = 0$ to $2 \cdot 10^4$, with steps of $2 \cdot 10^3$.

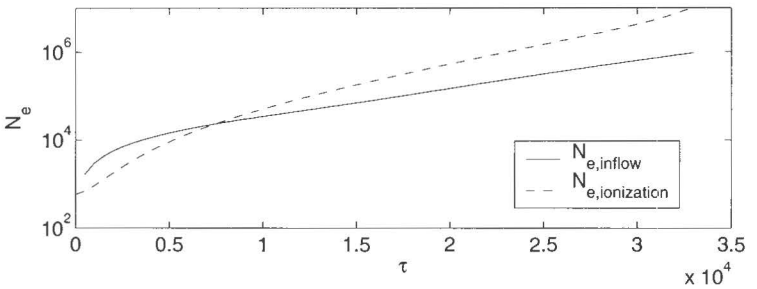

FIGURE 6.28: Temporal evolution of the number of electrons that have flown into the system (solid line) and that have been created through ionization (dashed line), when a high density initial seed attached to the cathode propagates in an undervolted gap ($|\mathcal{E}_b|$ =0.15).

6.5.2 The expansion phase

We now look in more detail at the first stage of the streamer evolution, during which the streamer head expands. The upper panel of Fig. 6.29 shows the logarithmic electron density distribution during this phase. One can distinguish two inner structures in the streamers. One is the "outer" boundary, with relatively low densities, and beyond which the density decays exponentially. The other one, situated inside the streamer, is much narrower and relatively dense. The latter is better visualized on a linear scale rather than on a logarithmic one (see the middle panel of Fig. 6.29). We will refer to the first, outer, region as the logarithmic region, and to the inner one as the linear region. This nomenclature comes from the function of the densities on which each of these regions is best plotted. The lower panel of Fig. 6.29 shows the logarithm of the net charge density distribution.

In order to characterize the radial growth of the linear and logarithmic regions, we use the radii r_1 respectively r_2, that are defined as the maximal r-coordinate at which the electron density has dropped to a value of $1/e$ and $1/100$, respectively, of its axial value. We emphasize that these radii are defined in a different way than the radius of curvature and the half maximum radius used to characterize the streamer propagation in Sect. 6.4. The reason for us to use a different radius is due to the other two being based on the maximal net charge density. Now, at the early times considered here, the streamer head has not clearly been formed yet, and the maximal net charge density is situated near the cathode and stays there. Moreover, in Sect. 6.4 the finest grids were distributed such that the base and the head of the streamer could easily be distinguished. However this is not the case here, where, up to $\tau \approx 5000$, one single grid at the finest level covers the body and the base of the streamer. The definitions for r_1 and r_2 enable us to capture in an easier way the dimension of the streamer head.

The evolution of r_1 and r_2 up to $\tau = 2.5 \cdot 10^4$ (which corresponds to 75 ns) is shown in Fig. 6.30. Up to $\tau \approx 2 \cdot 10^4$, both radii follow a similar evolution,

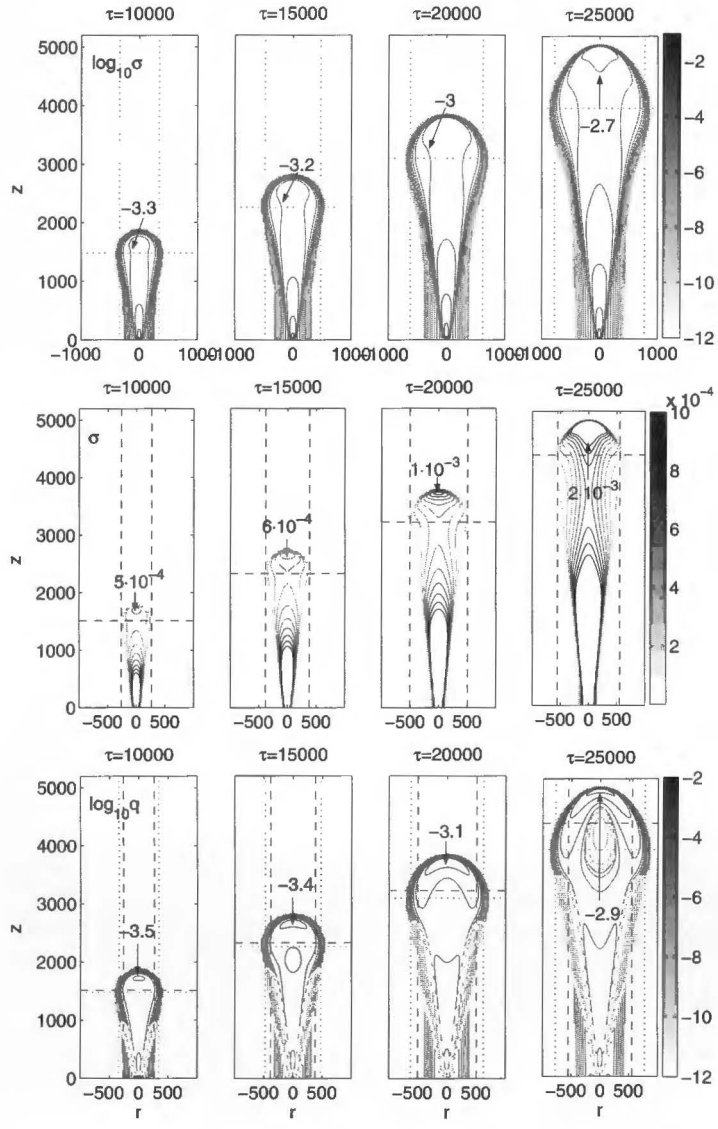

FIGURE 6.29: Expansion phase of an ionization seed in a background field field $\mathcal{E}_b = -0.15\hat{\mathbf{e}}_z$. *Upper panel*: logarithm of the electron density, the dotted lines indicate the position (r_2, z_2) of the maximal radius at which the electron density has dropped to $1/100$ of its axial value. *Middle panel*: electron density , in linear scale, The dashed lines indicate the position (r_1, z_1) of the maximal radius at which the electron density has dropped to $1/e$ of its axial value. *Lower panel*: logarithm of the net charge density distribution, the solid lines indicate negative net charge densities ($q > 0$), the dotted lines positively charged regions. The positions of the maximal radii are also shown in the lower panel. In each figure the maximal value of the corresponding quantity in the streamer head is indicated.

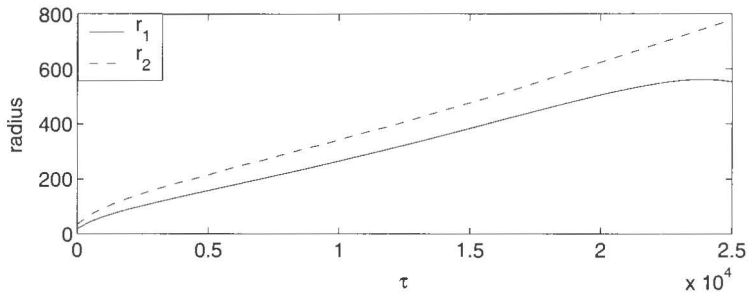

FIGURE 6.30: Evolution during the expansion phase, of the maximal e-folding radius r_1 (solid line), and the maximal radius r_2 at which the electron density has dropped to 1/100 of its axial value (dashed line).

though r_2 grows somewhat faster than the e-folding radius r_1.

To determine the contribution of the drift and the diffusion to the radial growth, we define the diffusive velocity as [102]

$$\mathbf{v}_D = \frac{1}{\sigma}\mathbf{\Gamma}_D = -\frac{1}{\sigma}D\nabla\sigma\,, \tag{6.5.1}$$

where the diffusive flux Γ_D has already been defined in Sect. 6.3.1, in Eq. (6.3.1). This definition for the diffusive velocity comes from an analogy with the drift velocity, which can be written as

$$\mathbf{v}_\mathcal{E} = -\boldsymbol{\mathcal{E}} = \frac{1}{\sigma}\mathbf{\Gamma}_\mathcal{E}\,, \tag{6.5.2}$$

where $\mathbf{\Gamma}_\mathcal{E} = \mathbf{\Gamma}_{\mathcal{E}_q} + \mathbf{\Gamma}_{\mathcal{E}_b}$ is the total contribution of the drift to the electron fluxes. In the upper panel of Fig. 6.31 we compare the radial growth $v_r = dr_1/d\tau$ together with the radial components of the drift and diffusion velocities at the position where r_1 is determined. The same is done for r_2 in the lower panel of Fig. 6.31. The irregularities in this figure are caused by the quantities being determined on a grid with grid size 16. Again it was the distribution of the grids that obliged us to choose this rather coarse grid level to evaluate he quantities considered in Fig. 6.31. However, though the results might be less "smooth" than if computed, if possible, on finer grids, the general trend is clearly shown. Another reason for the irregular shape of the curves showing v_r is its numerical evaluation on a coarse temporal grid as well. Indeed, it has not been computed at every time step of the simulation, which would have lead to very large data files, but the results at time intervals of 500 have been used.

We see that, up to $\tau \approx 1.5 \cdot 10^4$, the radial expansion of the electron cloud is very well described by the radial drift and diffusive fluxes, hence the axial velocity of the streamer does not influence the radially directed dynamics. We see indeed from the lower panel of Fig. 6.30 that both r_1 and r_2 follow the same axial evolution up to this time, and that the axial propagation is set by the background electric field.

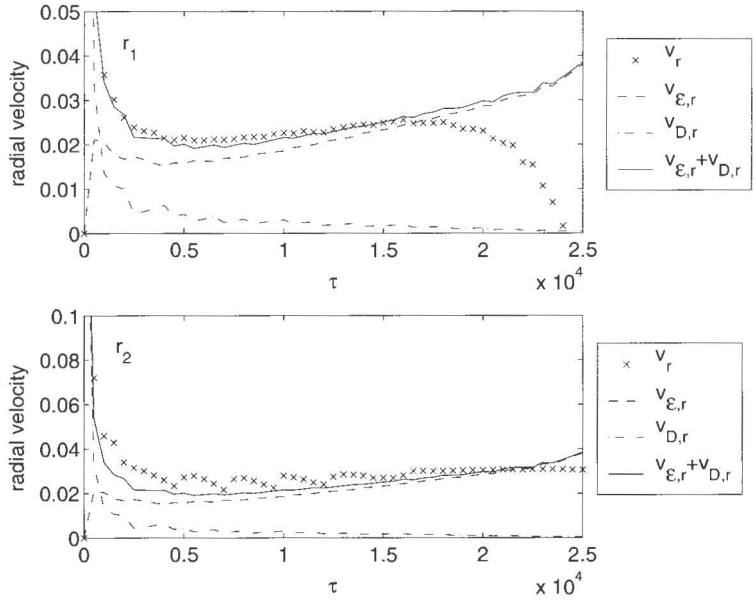

FIGURE 6.31: Evolution during the expansion phase of the radial velocities based on the e-folding radius r_1 (upper panel) and on the maximal radius r_2 at which the density drops to 1/100 of its axial value (lower panel). *Crosses*: expansion velocity v_r based on r_1 or r_2. *Dash dotted line*: radial component $v_{D,r}$ of the diffusion velocity. *Dashed line*: radial component $v_{\mathcal{E},r}$ of the drift velocity. *Solid line*: magnitude of the total radial velocity $v_{\mathcal{E},r} + v_{D,r}$. The drift and diffusive velocities are determined at the position of r_1.

At very early times ($\tau \leq 1000$), the diffusion velocity is much larger than the drift velocity, and it is the diffusion that causes the expansion. The diffusion velocity at r_1 is high because of the large gradients of the initial pulse, which is very high and narrow. This very early stage of the radial streamer propagation is thus diffusion dominated.

Moreover, from $\tau = 1000$ to approximately 5000, the radial electric field at r_1 decreases in amplitude. This is characteristic for this early phase, during which the diffusion, though not dominant, continues to decrease the maximal net charge density, as can be seen from Fig. 6.32, where the evolution of the axial electron and net charge density distribution are shown. The dots in the upper panel of this figure indicate the axial position at which r_1 has been determined, for τ multiples of 5000. We see that the radial extension of the streamer is not largest at the maximal electron density, but somewhat behind it.

Fig. 6.31 shows that, from $\tau = 5000$, the radial component of the electric field increases. From Fig. 6.32 we see that the axial electron density distribution $\sigma(0, z, \tau)$ then starts growing as well, and so does the space charge density distribution, resulting in a stronger field, both in the axial and radial direc-

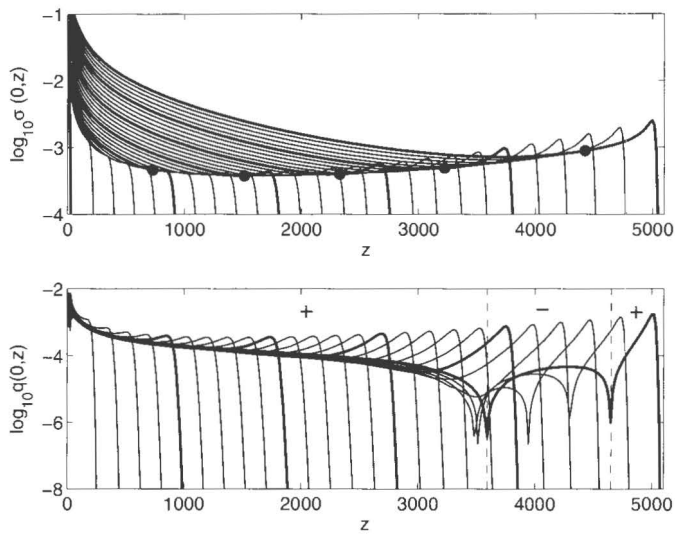

FIGURE 6.32: Evolution of the logarithm of the axial electron density $\sigma(0,z,\tau)$ (upper panel) and the axial net charge density $\sigma(0,z,\tau) - \rho(0,z,\tau)$ (lower panel) during the expansion phase, for τ=0 to 2.5·10^4. The snapshots are taken at equidistant time intervals of 1000. The thick lines correspond to τ multiple of 5000. The dots in the upper panel indicate the axial value corresponding to r_1. The discontinuities in the net charge density indicate a change of sign, which is given for τ=2.5·10^4.

tion. The diffusive velocity $v_{D,r}$ becomes smaller and smaller compared to the drift velocity $v_{\mathcal{E},r}$, although its contribution to the radial expansion can not be neglected. Indeed, Fig. 6.31 shows that the radial velocity v_r is larger than the drift velocity, and that it is in very good agreement with the sum of the contributions of both drift and diffusion up to $\tau \approx 1.5 \cdot 10^4$.

6.5.3 Transition from expansion to contraction phase

After $\tau \approx 1.5 \cdot 10^4$, Fig. 6.31 shows that the radial expansion velocity of the e-folding radius starts decreasing, and drops suddenly around $\tau \approx 2 \cdot 10^4$. At $\tau = 2.5 \cdot 10^4$ it has become negative, and the streamer enters the radial contraction phase. At that time, Fig. 6.31 shows that the radius r_2 continues growing, while the e-folding radius r_1 obviously decreases. Moreover, from $\tau \approx 1.5 \cdot 10^4$, Fig. 6.31 also shows that it is no longer set by the radial drift and the diffusion only, which indicates that the electric field has now become such that the axial velocity and the impact ionization starts playing a significant role in the radial streamer propagation. The lower panel Fig. 6.30 indeed shows that the the linear region of the streamer moves faster in the axial direction than the logarithmic region. We therefore consider the electric field that is induced by the space charges, which is shown in Fig. 6.33.

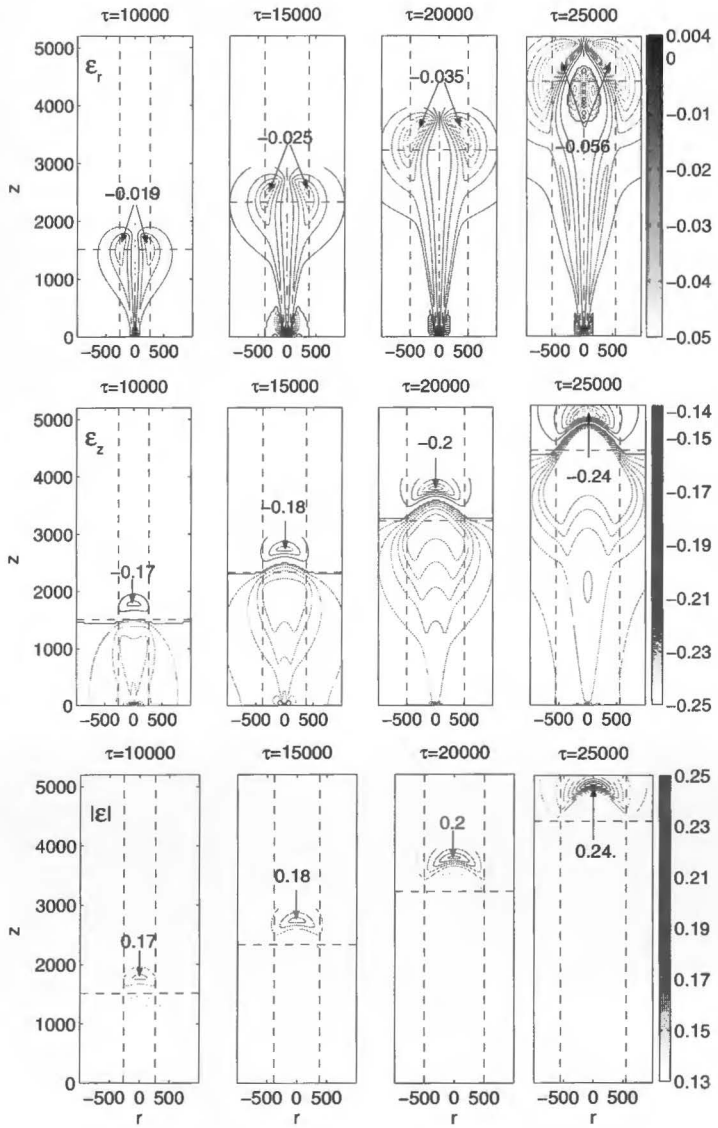

FIGURE 6.33: Electric field distribution during the expansion phase. *Upper panel*: radial component of the electric field. *Middle panel*: axial component of the field. *Lower panel*: electric field strength. The times of the snapshots are the same as in Fig. 6.30. The solid lines correspond to a field enhancement ($\mathcal{E}_r > 0$, $\mathcal{E}_z > -|\mathcal{E}_b|$ and $|\mathcal{E}| > |\mathcal{E}_b|$), the dashed lines to a field reduction.

During the first stage of the expansion phase, the space charge effects on the electric field are small. However, once the radial expansion of the linear region starts decreasing ($\tau = 2 \cdot 10^4$), this is no longer the case and the space charges screen the electric field from the streamer interior, while the field enhancement in the streamer head, is clearly visible.

Around $\tau = 2.5 \cdot 10^4$, the space charge affects the electric field significantly, resulting in a high electric field in the tip of the streamer, whereas in the streamer body the electric field is screened from its background value. Considering the dependence of the ionization rate on the field (see Fig. 6.35), we see that at these low background values ($|\boldsymbol{\mathcal{E}}| \approx 0.15$) the derivative of the ionization rate with respect to $|\boldsymbol{\mathcal{E}}|$ is much larger than at high background values. The electric field strength being largest in the streamer head near the axis, and decreasing rapidly when going to large r, the ionization rate is much larger near the axis than away from it. Moreover, the field enhancement increases in time, and so does its radial decay, resulting in a increasingly stronger radial gradients in the ionization rate as well.

It is now useful to consider the rate ω_t at which the electron density distribution changes in time. From Eq. (5.2.2) we see that this rate can, in a similar manner as was done for the fluxes in Eq. (6.3.1), be divided into contributions $\omega_{\mathcal{E}}$, ω_D and ω_i of the electric field, the diffusion, and the impact ionization, respectively,

$$\begin{aligned} \omega_{\mathcal{E}} &= -\nabla \cdot \Gamma_{\mathcal{E}} = \nabla \cdot (\sigma \boldsymbol{\mathcal{E}}) , \\ \omega_D &= -\nabla \cdot \Gamma_D = \nabla \cdot (D \nabla \sigma) , \\ \omega_i &= \sigma |\boldsymbol{\mathcal{E}}| e^{-1/|\boldsymbol{\mathcal{E}}|} , \\ \omega_t &= \omega_{\mathcal{E}} + \omega_D + \omega_i , \end{aligned} \tag{6.5.3}$$

Fig. 6.34 shows the distribution of these rates during the expansion phase and the beginning of the contraction phase. We emphasize that now, in contrast to Sect. 6.3.1, we consider the evolution of the electrons rather than that of the space charges. We therefore have to take into account the reaction rate as well.

Since r_1 defines the position at which the electron density has dropped to 1/e of its axial value, the decrease in r_1 indicates an increase in the radial gradients of the electron density in the linear region, This is indeed what can be observed in the middle panel of Fig. 6.29. In a similar way the continuous increase in r_2 indicates that the gradients in the logarithmic region continue decreasing.

Realizing that the gradients in ω give the rate of change in the gradients of σ, we can use Fig. 6.34 to understand the evolution of r_1, and why the impact ionization only influences it after some time. Indeed, we see that at early times, the gradients in ω_i are small in the interior in the streamer, and only large in the region with low electron density. Therefore the impact ionization does not affect the gradients in the streamer interior. The gradients in radial direction of $\omega_{\mathcal{E}} + \omega_D$ on the other hand are large and negative in the interior of the streamer, so that they tend to decrease the gradients in σ, resulting in a larger e-folding radius, in accordance with earlier observations of Fig. 6.31.

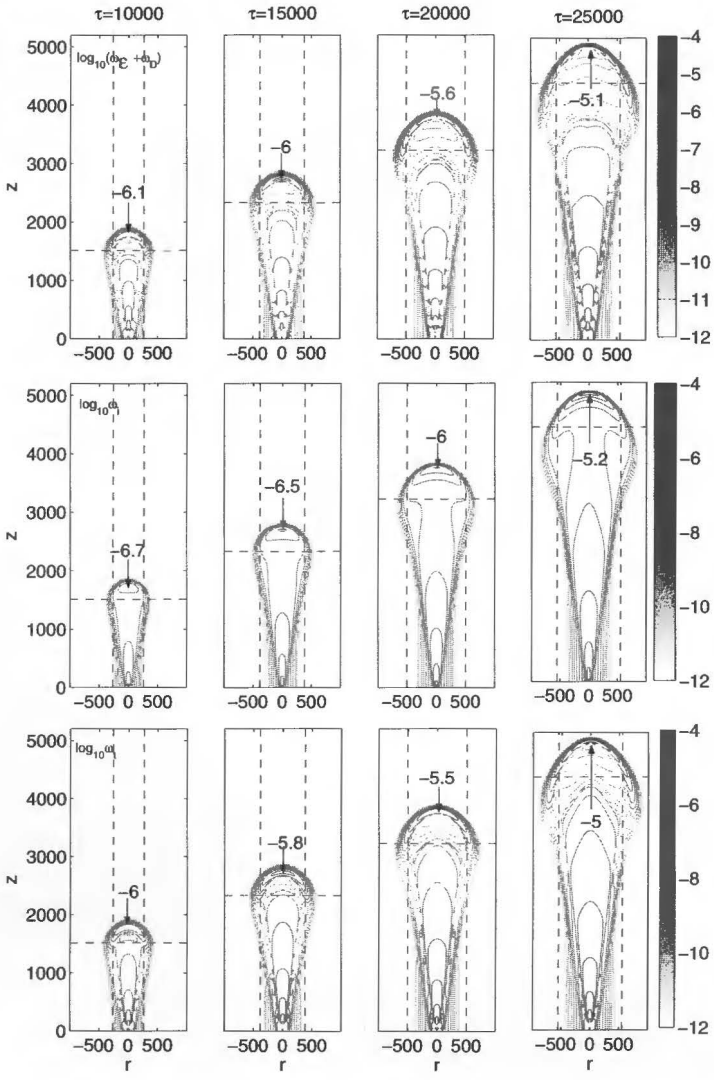

FIGURE 6.34: Logarithmic plot of the contributions of drift, diffusion and impact ionization to the rate of temporal change of the electron density during the expansion phase and the beginning of the contraction phase. *Upper panel*: $\omega_\varepsilon + \omega_D$. *Middle panel*: ω_i. *Lower panel*: ω_t. The times of the snapshots are the same as in the lower panel of Fig. 6.30. The solid lines indicate positive values of the rates, the dotted lines negative values. The dashed lines show the position at which r_1 has been determined.

However, at later times, the space charge layer results in a small region with high field ahead of the streamer. In this region, the field is sufficiently high to allow for a significant rate of impact ionization. As a consequence, the electron density grows in that region, resulting in a narrow region with relatively large particle densities, which is surrounded by a much wider region with relatively low ionization. This explains why the e-folding radius, which gives a measure for the radial extend of the region where the densities are still in the same order of magnitude as the maximal density, decreases.

The fact that the contraction phase is not observed at high overvoltages, comes from the smaller influence of the field strength on the ionization rate when the applied field is high (see Fig. 6.35). The streamer then enters a region where the radial gradients in the electric field strength have much less influence on the evolution of the radial gradients in the electron density, and consequently one can not make a clear distinction between the high and low density regions.

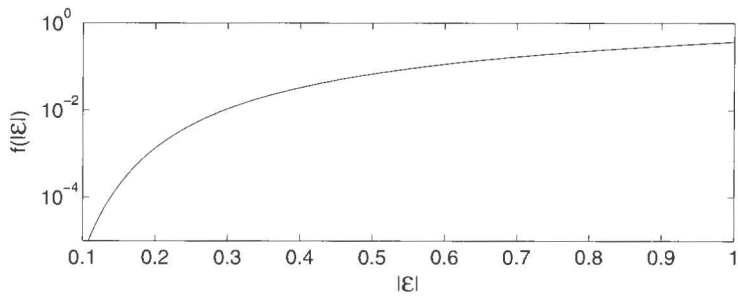

FIGURE 6.35: Ionization rate $f(|\boldsymbol{\mathcal{E}}|) = |\boldsymbol{\mathcal{E}}| \exp(-1/|\boldsymbol{\mathcal{E}}|)$ as a function of $|\boldsymbol{\mathcal{E}}|$.

At all times shown in Fig. 6.34 the growth rate due impact ionization is positive, as expected since it impact ionization can only result in a creation of charged particles. The drift and diffusion on the other hand result in an increase of the electron density in the head and in the base of the streamer, but in the streamer body they tend to decrease the electron density. At $\tau = 1 \cdot 10^4$ the impact ionization compensates for the negative values of $\omega_{\mathcal{E}} + \omega_D$, this however is not the case any longer at later times.

Moreover, at all times, the streamer interior, which gets denser, is surrounded by a region with decreasing electron density, indicated by the dotted lines in the lower panel of Fig. 6.34. This results in a positively charged region (see the lower panel of Fig. 6.29), which confines the streamer base in a small region near the axis of symmetry.

The temporal rate change of q is given by $\omega_{\mathcal{E}} + \omega_D$. In the base of the streamer, $\omega_{\mathcal{E}} + \omega_D$ is small (in the order of 10^{-8}), and the net charge density distribution is quasi-stationary (of course not really stationary since the rates are not equal to zero).

The largest absolute values of the rates $\omega_{\mathcal{E}} + \omega_D$ are found in the streamer head, as was the case in the case of a highly overvolted gap. In the streamer

head, the electric field is enhanced, and so is $\omega_{\mathcal{E}}$. The streamer head thus becomes more negatively charged.

The positive radial electric field near the cathode draws the electrons entering from the cathode towards the anode, which results in the negative reaction rate $\omega_{\mathcal{E}} + \omega_D$ that we observe in the upper panel of Fig. 6.34. This region therefore becomes less negatively charged, and eventually, around $\tau = 2.5{\cdot}10^4$, a positively charged region has formed in the streamer body.

During the expansion phase ($\tau < 2{\cdot}10^4$), the radial component of the electric field (see the upper panel of Fig. 6.33) is negative in the whole streamer – therefore the radial drift velocity is positive in the whole streamer – except for a small region near the cathode. However, when the the streamers has entered its contraction phase, at $\tau = 2.5 \cdot 10^4$ we see that, at the axial position at which r_1 has been defined, there is a region with positive radial electric field. The drift velocity in that region is thus directed towards the axis of symmetry, drawing electrons from the logarithmic part into the linear part of the streamer.

6.5.4 Contraction phase

In the previous subsection we argued that the radial contraction of the linear region of the streamer was due to the field enhancement, which is largest in the streamer head near the axis of symmetry. The logarithm of the electron and net charge density distributions during the contraction phase are shown, together with electric field strength, in Fig. 6.36.

We now clearly see that the electron density distribution consists of two regions, a narrow very dense region (the densities are in the order of 10^{-1} to 10^{-2}) situated near the axis of symmetry, and a rather wide one where densities are much lower. Their structure also differs in that the logarithmic region has its largest radial extension in the streamer body, in the region where the linear region on the contrary is thinest. The linear region then first widens when approaching the streamer head, while on the contrary the logarithmic region becomes less extended in the radial direction.

The negatively charged layer has now also become clearly visible, enhancing the field ahead of it and screening it on the contrary in the back. It surrounds a positively charged region in the body of the streamer, which corresponds to the region with high electron densities. The electron densities being highest there, the electrons tend to be drawn away from that region, leaving behind the immobile positive ions, which eventually results in this positively charged region.

In the streamer base the positive ion density is largest near the axis, attracting the electrons the electrons towards the axis, as was already observed and explained in the previous section. This results in a positively charged layer that confines the electrons in small the streamer.

The lower panel of Fig. 6.36 shows that the electric field in the streamer body is screened from the background electric field, and decays slowly with time, reaching a minimum of 80% of the background field at the moment of branching ($\tau \approx 3.25 \cdot 10^4$). The screening of the field is thus less efficient than in

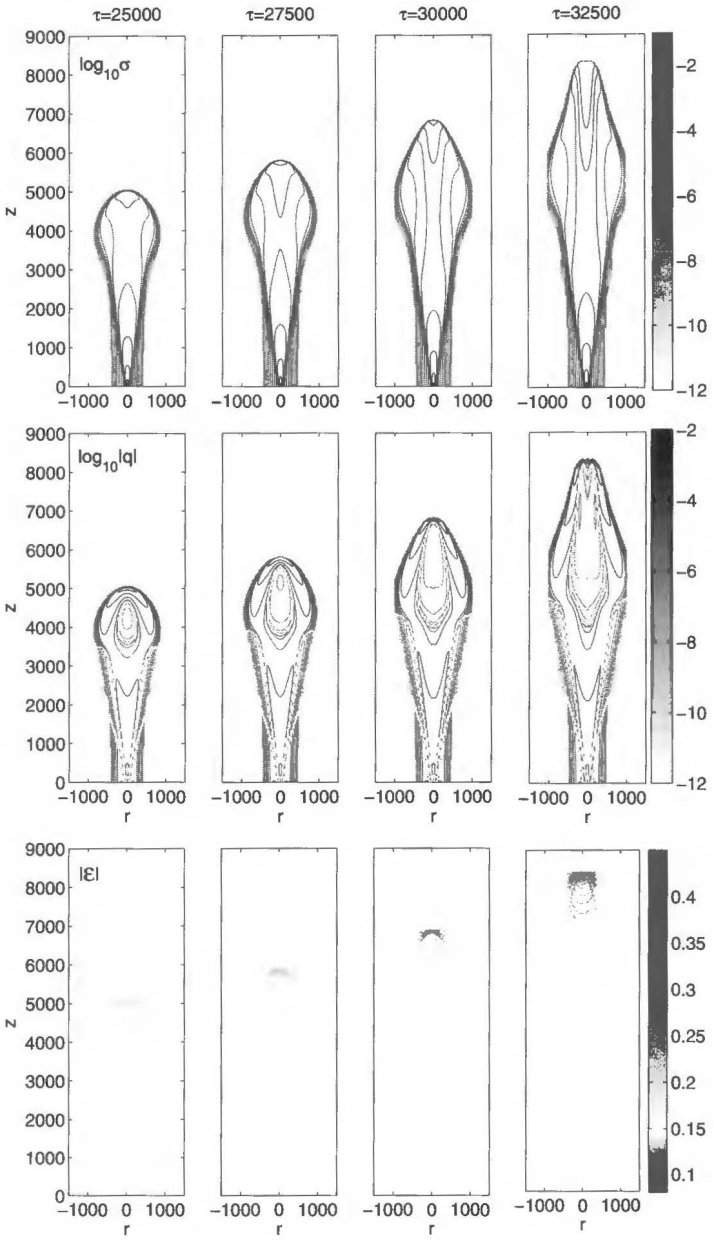

FIGURE 6.36: Logarithm of the electron density distribution (upper panel) and of the net charge density distribution (middle panel) during the contraction phase. The lower panel shows the electric field strength. The dotted lines in the middle panel indicate positively charged regions ($q < 0$). In the lower panel they indicate values of the electric field that are lower than the background electric field.

the high field case, where it reached a maximal value of 40% of the background field.

Just before the streamer branches, around ($\tau \approx 3 \cdot 10^4$), the maximal electric field strength has reached a value of more than 300% of the background value, which is less than in the high field case, where the maximal field reached a value of 400% of its background value. These lower values of the maximal field enhancement and screening are due to the much lower space charge densities occurring at these low field, as can be seen by comparing the middle panels of Fig. 6.22 and Fig. 6.36.

6.6 Interpretation of the results

In the previous sections the evolution of streamers during the nonlinear regime in both under- and overvolted gaps has been described. We now interpret the data of the numerical simulations in physical terms, and compare with previous analytical results or phenomenological concepts.

6.6.1 Screening width and impact ionization length

In Figs. 6.18 we could observe that, in the streamer regime, the width of the space charge layer initially decreases and then saturates. In Fig. 6.37 this width is plotted as a function of the maximal electric field, for various simulations in both under- and overvolted gaps.

This figure shows that, in all cases, for large field enhancements, the width of the layer becomes independent of the initial seed. The difference in width at relatively low field enhancements for $|\boldsymbol{\mathcal{E}}_b| = 0.5$ between cases (1)-(3) on the one hand and cases (4) and (5) on the other hand comes from the latter two starting from a wide ionization seed, which results in a large width of the back of the ionization front. The same can be observed for the seed with e-folding radius of 100 in the low field case. We have thus found an empirical formula that describes the e-folding width of the space charge layer as a function of the maximal electric field in the streamer head,

$$w' \approx 2\alpha^{-1}(|\boldsymbol{\mathcal{E}}|_{max}) + 4\sqrt{\frac{D}{|E|_{max}\alpha(|E|_{max})}}\,. \tag{6.6.1}$$

In dimensional units, this gives,

$$w' = \frac{2}{\alpha_0 \exp(-E_0/|E|_{max})} + 4\sqrt{\frac{D_e}{\mu_e |E|_{max}\alpha_0 \exp(-E_0/|E|_{max})}}\,. \tag{6.6.2}$$

Let us focus on the behavior of the space charge layer for large field enhancements, when the discharge has well entered the streamer regime. We use the results given by Ebert *et al.* [30], who stated that, for a planar ionization front propagating into a non-ionized region with constant electric field $\boldsymbol{\mathcal{E}}^+$, the

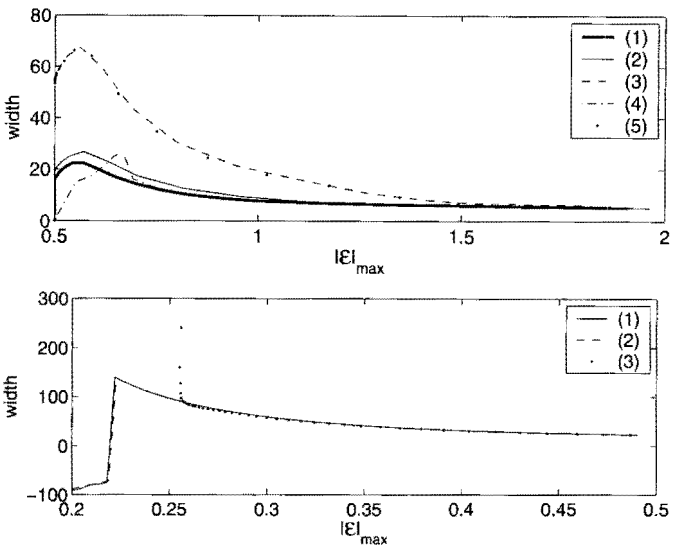

FIGURE 6.37: Width of the space layer as a function of the maximal electric field strength for various simulation parameters in overvolted (upper panel) and undervolted (lower panel) gaps. In the upper panel the graphs correspond to the 5 cases investigated in Sect. 6.4.2. The graphs in the lower panel correspond to a dense initial seed (σ_0 =1/4.7) attached to the cathode, with an e-folding radius of (1) 10, (2) 20, and (3) 100.

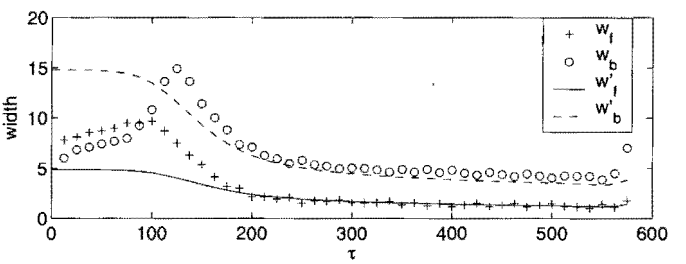

FIGURE 6.38: Comparison of the numerical evaluation of the width of the front (circles) and the back (pluses) of the space charge layer with the predictions $w'_f = \alpha^{-1}(|\mathcal{E}^+|)$ (solid line) and $w'_b = 12\Lambda(D, |\mathcal{E}^+|)$ (dashed line).

spatial decay of the net charge densities ahead of the ionization front is set by $\Lambda(D, |\mathcal{E}^+|) = \sqrt{(f(|\mathcal{E}^+|)/D)}$. Moreover, Arrayás and Ebert [4] have shown that the screening width, i.e. the width of the back of the streamer front, is set by the ionization length $\alpha^{-1}(|\mathcal{E}^+|)$.

For simulations in a background field of $|\mathcal{E}_b| = 0.5$, it appears that the width of the front of the space charge layer is very well fit by $w'_f = 4\Lambda(D, |\mathcal{E}^+|)$, while

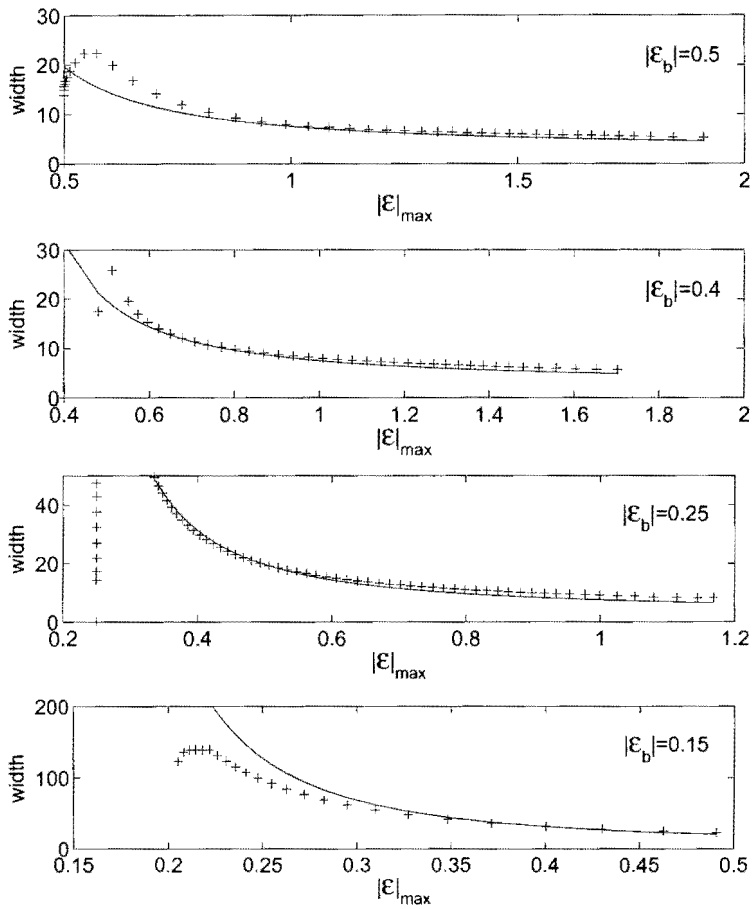

FIGURE 6.39: Comparison of the numerical evaluation of the width of the space charge layer (pluses) with the prediction $w' = 4\Lambda(D, |\boldsymbol{\mathcal{E}}^+|) + 2\alpha^{-1}(|\boldsymbol{\mathcal{E}}^+|)$, for values of the background field of, from above to below, 0.5, 0.4, 0.25 and 0.15.

that of the back of the space charge layer simply follows $w'_b = 2\alpha^{-1}(|\boldsymbol{\mathcal{E}}^+|)$, as is shown in Fig. 6.38.

These predictions are tested for various background fields in Fig. 6.39, and they show a very good agreement with the numerical results.

We can also use this knowledge to make a priori estimations of the required resolution for any background electric field. Indeed, in both the undervolted and the overvolted gap, the maximal electric field reaches a value of approximately three times its background value. We can then compute the ionization length corresponding to this background electric field, and use this as an estimation for the width the space charge layer will acquire. This then may be used to set the resolution of the computation.

6.6.2 An approximation for the maximal field enhancement

For positive streamers, Kulikovsky [44] proposed, based on one specific set of parameters, that the maximal electric field induced by the space charges at the tip of the streamer could be approximated by the field of a uniformly charged sphere with charge density q_{max}, and with a radius equal to the width w' of the space charge layer. In this approximation, the field of the space charges is written as,

$$|\mathcal{E}|_s = \frac{\sigma - \rho}{3} w \,. \tag{6.6.3}$$

In the following we derive a physically more natural approximation for the maximal electric field, by considering the specific form of the space charge layer. This gives better correspondence with the numerical results than Kulikovsky's charged sphere approximation.

Looking at the net charge density distributions in Figs. 6.16 and 6.22, it seems reasonable to compare its field with that of two oppositely, uniformly charged spheres with charge density $(\sigma - \rho)_{max}$, with radius r_c, and separated by a distance w. In this approximation, the maximal electric field strength induced by the space charge on the axis is written as as

$$|\mathcal{E}|_c = \frac{\sigma - \rho}{3} r_c \left(1 - \frac{r_c^2}{(r_c + w)^2}\right) \,. \tag{6.6.4}$$

We notice here that the choices for the density levels at which the radius and the width of space charge layer are defined are rather arbitrary. For the approximation (6.6.3) given by [44], taking the half maximum width will underestimate the field, since the total charge contained in the equivalent sphere would then be much smaller than that contained in the space charge layer. Therefore, for this approximation we use the width w based on the position at which the net charge decreased up to 1/10 of its maximal value. On the other hand, for the approximation suggested in Eq. (6.6.4) we use the e-folding width of the space charge layer. The evolution of the maximal strength together with the approximations given by Eqs. (6.6.4) and (6.6.3) are shown in Fig. 6.40, for both cases (D) and (N). The drop of the maximal field at the latest times is due to the onset of the instability, during which the streamer no longer propagates along the axis. The maximal field then is no longer found on the axis, and the maximal axial field drops.

We see that the approximation given by Eq. (6.6.4) performs very well, in that it gives qualitatively the same behavior as the numerically computed field. The approximation given by Eq. (6.6.3) behaves rather poorly at early times. The field is first highly overestimated, especially in the case of Neumann boundary conditions at the cathode. This is easily understood by realizing that, at early times, the net charge configuration was that of an almost circular monopole. Then setting the radius of the equivalent sphere equal to the width of this monopole obviously makes sense, however "filling" this sphere with the

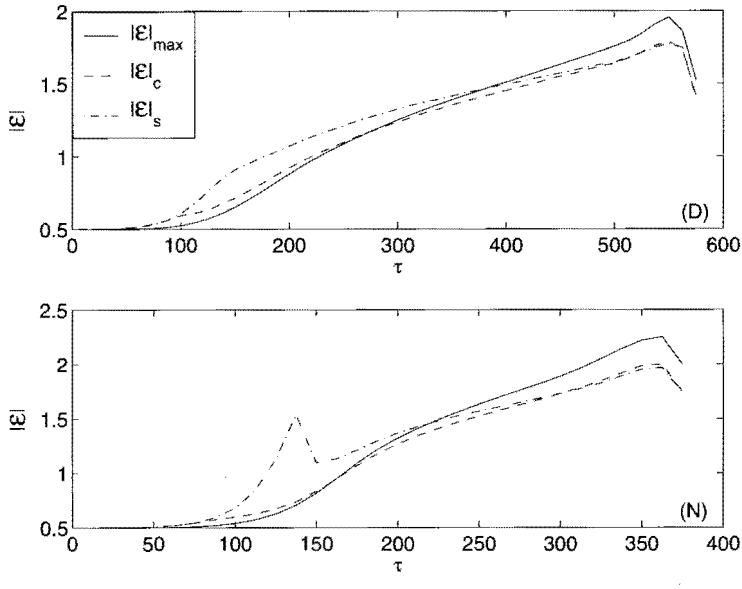

FIGURE 6.40: Temporal evolution of the self field $|\mathcal{E}|$ of the space charges (solid line) compared with that of two spheres with opposite charges ($\mathcal{E}_c$, dash-dotted line) and the approximation $\mathcal{E}_s$ for positive streamers (dotted line). The background field has been added to $\mathcal{E}_c$ and $\mathcal{E}_s$.

maximal net charge density in the monopole obviously does not, and results in the overestimation of the field.

The reason for the field to be overestimated by the approximation (6.6.3) in the case of Dirichlet boundary conditions at the cathode is different. The space charge configuration in this case is that of a dipole. The approximation (6.6.3) does not take into account the influence of any positively charged region, hence the field is easily overestimated.

On the other hand, at early times, even the quantitative behavior of approximation (6.6.4) is in very good agreement with the computed field. However, eventually the field becomes larger than would be expected by the approximation, and the error is larger in case (N) than in case (D).

The reason of the underestimation of the field by Eq. (6.6.4) is simply due to the suggested charge configuration. Indeed, the superposition of the two spheres does not only result in a negatively charged region (the streamer head), but also to a positively charged image. This positively charged region reduces the field at the outer boundary of the negatively charged region. Now in case (D), we saw that there existed a positively charged streamer base as well, but the distance between the positively and negatively charged region is larger than in the suggested configuration of two superimposed spheres. However, in case (N), we could observe previously that there was no such positively charged streamer

base. The field induced by the positive charge in the suggested configuration therefore gives relatively a stronger effect than in case (D).

At large times, the ratio of the width and the radius of curvature of the streamer head becomes increasingly small. In the limit of $w/r_c \to 0$, the field $|\boldsymbol{\mathcal{E}}_c|$ approaches the field $|\boldsymbol{\mathcal{E}}_p|$ induced by a planar front, and can be written as

$$|\boldsymbol{\mathcal{E}}|_p = \frac{2}{3} q^-_{max} w \,. \tag{6.6.5}$$

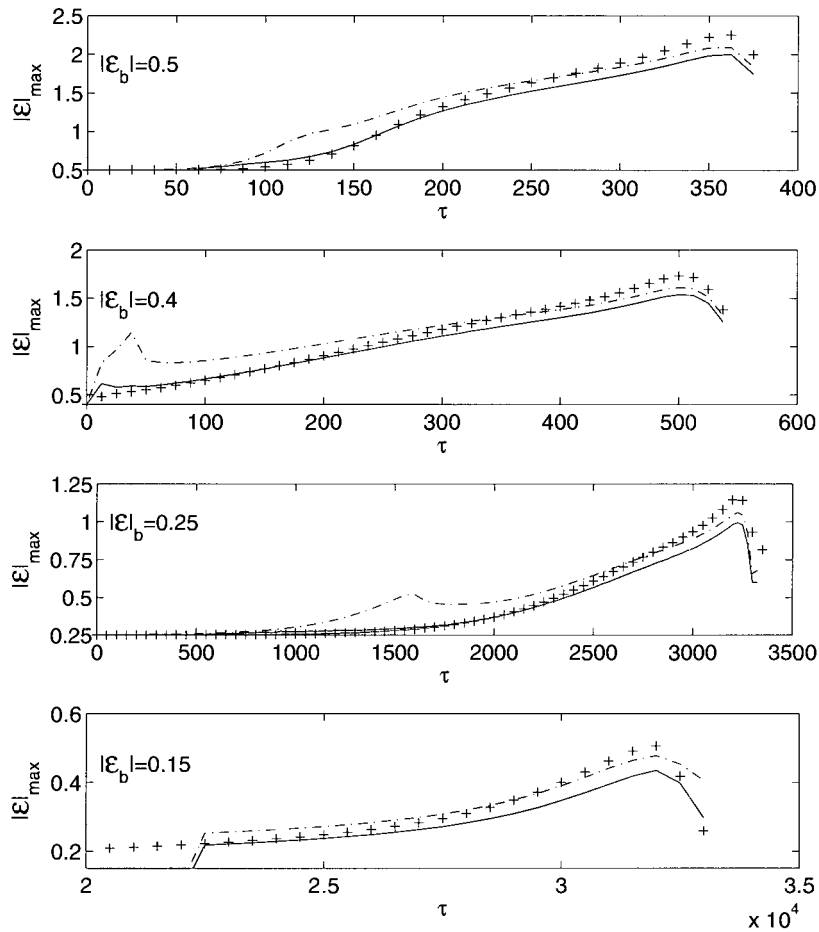

FIGURE 6.41: Evolution of the extrema of the axial electric field strength for various background fields (from top to bottom $|\boldsymbol{\mathcal{E}}_b|$ =0.5, 0.4, 0.25 and 0.15. *Symbols*: numerical result. *Solid line*: approximation (6.6.4) of the field induced by two uniformly and oppositely charged spheres, with charge density equal to the maximal net charge density in the streamer head maximal field enhancement. *Dashed line*: approximation (6.6.5) of the field induced by a planar ionization front.

In Fig. 6.41, we compare the numerical results for the evolution of the maximal electric field, together with the approximations for the curved and the planar streamer front given by Eqs. (6.6.4) and (6.6.5), respectively. This figure shows that in all cases, there is a transition below which the approximation $|\mathcal{E}|_c$ performs best, and after which the front approaches the limit of a planar ionization front, the approximation $|\mathcal{E}|_p$ giving good agreements with the numerical results.

6.6.3 Front velocity

In [29, 30] it has been shown that, for planar streamer fronts that propagate into a non-ionized medium with a fixed background electric field $\mathcal{E}^+$, the front velocity v_p is set by the diffusion coefficient and the electric field as

$$v_p = |\mathcal{E}^+| + 2\sqrt{Df(|\mathcal{E}^+|)}\,. \tag{6.6.6}$$

In Fig. 6.42 we compare our numerical results for various initial seeds in both under- and overvolted gaps with this analytical estimation.

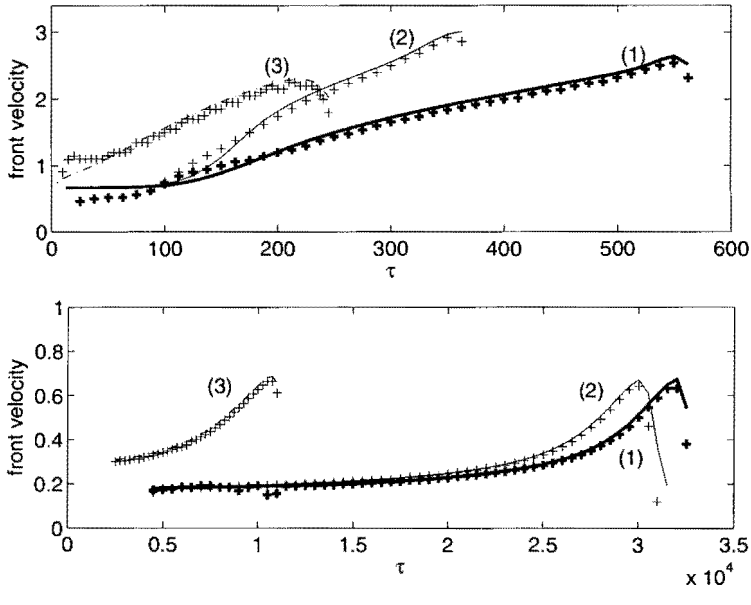

FIGURE 6.42: Evolution of the numerical front velocities (lines), compared with the analytical formula (6.6.6) (pluses). *Upper panel*: results in an overvolted gap ($|\mathcal{E}_b|$ =0.5), for (1) a seed detached from the cathode, with an e-folding radius of 10 and an amplitude of 10^{-4}, (2) a identical seed but placed at the cathode, (3) a seed attached at the cathode with the same e-folding radius but an amplitude of 1/4.7. *Lower panel*: results in undervolted gaps ($|\mathcal{E}_b|$ =0.15), for an dense initial seed (σ_0 =1/4.7) attached to the cathode, with an e-folding radius of (1) 10, (2) 20, and (3) 100.

We see that the correspondence between the numerical and the analytical results is very good. The small differences come from the planar front velocity (6.6.6) being derived for a totally relaxed and planar front, which is obviously not the case here.

6.7 Conclusions

In this chapter we have focused on the evolution of the streamer during the nonlinear phase, in both under- and overvolted gaps. We have first shown that, in order to obtain reliable results, a very high accuracy should be used, enabling us to resolve in detail the thin space charge layer, which is characteristic for the streamers in the nonlinear phase. It appeared that a resolution in the order of 1 μm was required on the high field case, whereas in a low field case a resolution of several micrometers was sufficient. This is due to the spatial density gradients being much higher in the first case. In fact, in the last section, in has been shown that the width of the space charge layer (which gives a measure for the density gradients) is set by the maximal electric field ahead of the ionization front. This in turn has been shown to reach a value of roughly three times the background electric field. This implies into spatial density gradients getting larger in larger background electric fields.

In overvolted gaps, characterized by a significant ionization rate in the background electric field, streamers have a strong radial growth, which can be enhanced even more by letting electrons flow into the system through the cathode. However, the simulations point into the direction that various initial seeds evolving in the same background electric field are attracted to the same intermediate head state before the branching instability sets in. In undervolted gaps on the other hand, the streamer first passes through a diffusive expansion phase. After a relatively long time, a sufficient number of electrons have entered the system and a contraction phase in the region with high electron densities is entered.

The use of a seed with weak spatial gradients on the other hand retards the build-up of space charges. However, in the simulations shown here, these weak gradients were set by imposing a rather wide initial condition, eventually leading to a large electron inflow, which then accelerates the streamer once it has reached the nonlinear regime.

Various electron inflows and initial seed distributions have been investigated for the overvolted gap, and we conclude (i) that the emergence of a streamer from an electron is retarded by a diffuse ionization seed, which is in accordance with experimental observations of Yi and Williams [112]; (ii) both a high initial seed density and a large electron inflow accelerate the streamer emergence and propagation. However, the values for the streamer radius, width, and the field enhancement all stay in a same range. It thus seems that there is an attractor for the dynamics of various seeds in a given background field. This hypothesis, however, requires further numerical and analytical studies.

We already mentioned in the last section that the width of the layer is set by the ionization length $\alpha^{-1}(|\mathcal{E}_{max}|)$. Moreover, an approximation for the

maximal electric field enhancement based on an electrostatic approach has been derived. This approximation, which is based on the space charge layer being mimicked by two uniformly and oppositely charged spheres, coincides better with the numerical results than that given by Kulikovsky [44], which is based on a single negatively charged sphere. It has also been shown that the velocity of the streamer was very well approached by that derived by Ebert and v. Saarloos [29, 30] for planar ionization fronts. Such planar fronts are known to be unstable, and this would explain why the curved streamer fronts, which thus approach a planar front, eventually branches. This will be investigated in more detail in Chap. 7.

7

THE BRANCHING INSTABILITY OF STREAMERS

In the previous chapters we have focused on the first stages of the streamer propagation, during which the space charge layer propagates in its self induced electric field. Eventually, the space charge layer becomes *unstable*, and the streamer branches. This branching is investigated numerically in this chapter. The numerical experiments show that the streamer branches, even in undervolted gaps, provided the gap is sufficiently long.

A qualitative matching between the numerical results and analytical work on this subject will be carried out. The numerical experiments show that the algorithm presented in Chap. 3 enables us to give a quantitative prediction for the branching.

7.1 Introduction

A negative discharge emerging from a localized ionization seed first propagates linearly during the electron avalanche phase, building up a space charge layer, which eventually becomes sufficiently dense to affect the background electric field. Then a streamer has emerged. In Chap. 6 it has been shown that the space charge layer becomes flatter and thinner, thereby approaching the limit of a planar ionization front. Eventually, the space charge layer becomes unstable and the streamer branches. Branching streamers have also been observed in experimental studies on streamers propagating in a long gap filled with either N_2 and N_2/O_2 mixtures [112].

In 1939, Raether [80] proposed a mechanism for streamer branching which was used in many textbooks. His picture is based on a uniformly charged streamer head, ahead of which stochastic processes lead to secondary avalanches, which result in the branching form. Up to now the effect of such stochastic processes has not been investigated further. It has, however, been shown in more recent work on streamers [24, 102, 44, 75] and in the previous chapter

that the streamer head is not homogeneously charged, but on the contrary that a space charge layer is necessary for a streamer to propagate. It has then been proposed by the group of Ebert [5, 83], that the streamer approaches the limit of ideal conductivity with a thin and equipotential streamer head, which exhibits a Laplacian instability and branches, in manner similar to viscous fingering.

Arrayás *et al.* [5] and Rocco *et al.* [83] have focused on the branching instability of streamers propagating into a non-ionized region filled with pure N_2, hence not taking into account photoionization, and their work lead to the proposal of the Laplacian instability mechanism mentioned above. However, their numerical codes were not able to test their branching conditions on finer grids. Moreover, the nature of the instability has been a subject of scientific discussion. The branching streamers exhibited in the simulations of [47, 5, 83] were suggested to result from numerical instabilities [48, 75]. In the present chapter we show that this is not the case.

We notice that in our radially symmetric system, the streamer branches into rings, which obviously is rather unphysical. Therefore it is not meaningful to follow the further evolution of the streamer after branching. However, the effectively two-dimensional setting suppresses unstable modes that break the radial symmetry [28], and the time of branching in a radially symmetric system will therefore give an upper bound to the actual three-dimensional branching time.

In this chapter we first investigate qualitatively and quantitatively the branching instability. We show that there is indeed a strong analogy between the branching streamers and viscous fingering. The algorithm presented in Chap. 3 enables us to run the simulations on very fine grids, and this is the first time that a conclusive investigation on the effect of grids on the branching has been carried out. The results on stepwise finer grids will enable us to give the first quantitative predictions on streamer branching as well.

7.2 Branching streamers and Laplacian instabilities

We consider the evolution of the streamer around the time when the branching instability occurs. We interpret the numerical results and show that the streamer approaches the Lozansky-Firsov limit of ideal conductivity, and that a moving boundary approximation is allowed for the streamer front.

7.2.1 The Lozansky-Firsov limit of ideally conducting bodies

We consider the evolution of an initial seed in both an undervolted gap ($|\mathcal{E}_b| = 0.15$) and an overvolted gap ($|\mathcal{E}_b| = 0.5$). The conditions are the same as those in Sect. 6.2. The results shown in this section have been computed on a finest grid with mesh size 2 in the undervolted gap, and of mesh size 1/2 in the overvolted

gap. Figs. 7.1 we shows the net charge density distribution $\sigma - \rho$ together with the equipotential lines in respectively the undervolted gap ($|\mathcal{E}_b| = 0.15$) and the overvolted gap ($|\mathcal{E}_b| = 0.5$), just before and during the streamer branching.

We see that in both cases, the distance between the equipotential lines is much larger in the interior of the streamer than ahead of the ionization front. This shows that, although the limit of ideal conductivity is not reached (in that case the equipotential lines would have completely been "pushed" out from the streamer body), it is approached. The reason for it not to be completely reached is that the growth of the space charge layer requires an electron current, and therefore an electric field, in the streamer body, which carries the charges towards the streamer head. In the streamer body, the approximation of ideal conductivity is thus approached,

$$\phi_{body} \approx const. \tag{7.2.1}$$

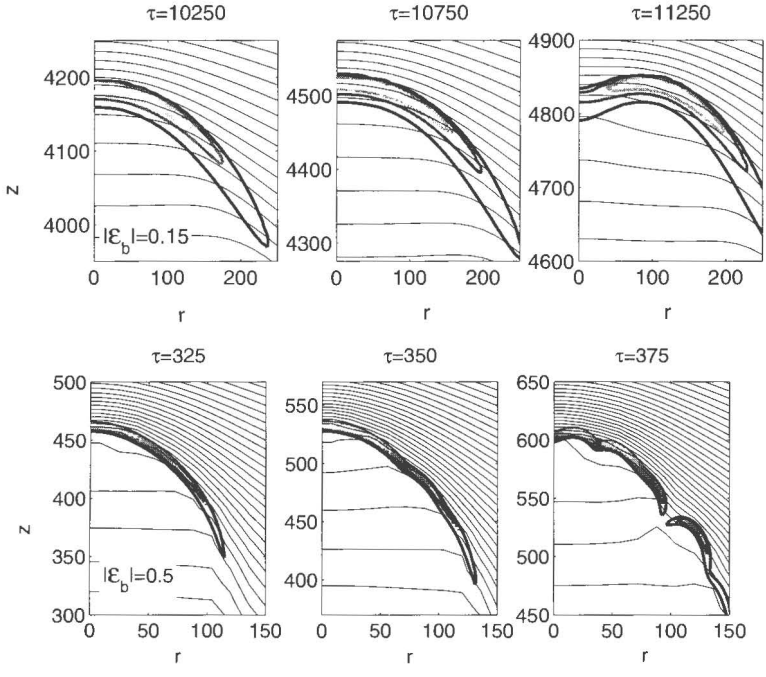

FIGURE 7.1: Enlargement of the streamer tip just before and during branching, in an undervolted gap with $|\mathcal{E}_b|$ =0.15 (upper four plots) and in an overvolted gap $|\mathcal{E}_b|$ =0.5. Both the net charge density distribution (thick lines) and the equipotential (thin) lines are shown. The contour levels for the net charge density are equally spaced with a separation of 0.004 for the low field case, and of 0.16 in the high field case. The equipotential lines are separated by a value of 5 in both cases. For clarity we only show the positive half plane on the r-axis.

7.2.2 The limit of a planar ionization front

Let us determine to what extent the space charge layer approaches the limit of a planar ionization front. A first condition for this to happen is that the radius of curvature of the layer should be much larger than its width. That this is indeed the case is shown in Fig. 7.2.

Secondly, as we have already shown in Sect. 6.6.3, the propagation velocity of the streamer could very accurately be described by that of a planar ionization front derived in [30]. We refer to Fig. 6.42, the two cases for which the branching has been investigated in Sect. 7.3 corresponding to the lines denoted by (2) in the overvolted gap, and by (3) in the undervolted gap.

Moreover, it was also shown that the maximal electric field in ahead of the streamer was very well approximated by the expression 6.6.5, which gave the limit for $w/r_c \to 0$ of the field induced by the space charge layer with width w and radius of curvature r_c.

However, we still have to verify that the jump in the field over the space charge layer can also be determined through the planar front approximation. The electric field distribution of a planar ionization front can be computed by simply integrating the Poisson equation, as was done in Sect. 3.3,

$$|\mathcal{E}| = |\mathcal{E}|_{min} - \int_{z_{min}}^{z} (\sigma - \rho) dz \tag{7.2.2}$$

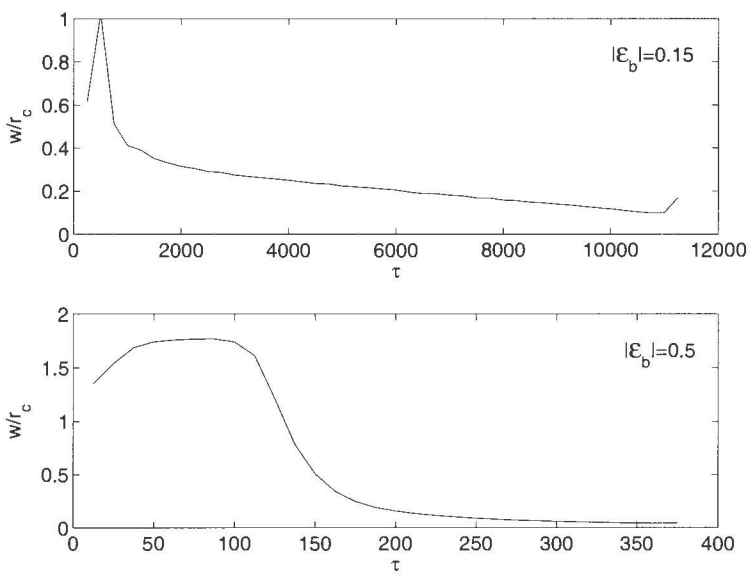

FIGURE 7.2: Evolution of the ratio between the width and the radius of curvature of the space charge layer, for the undervolted gap (upper panel) and the overvolted one (lower panel).

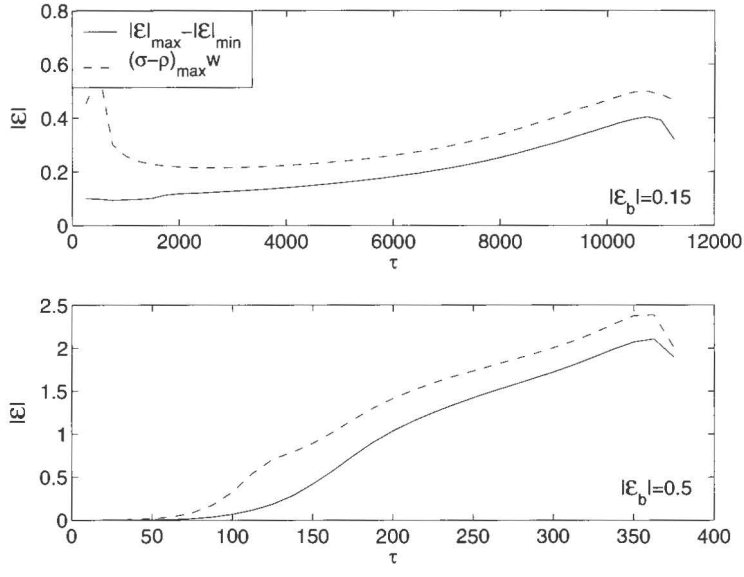

FIGURE 7.3: Evolution of the difference between the maximal and minimal electric field strength (solid line), compared with the approximation (7.2.3) (dashed line). Both the under- and overvolted gap cases are shown, respectively in the upper and in the lower panel.

where z_{min} is the location of the minimal electric field strength on the axis.

If we now assume the net charge density to be constant and equal to its maximum value over the e-folding width w of the space charge layer, and zero elsewhere, we get an approximation for the difference between the field inside and outside the streamer,

$$|\mathcal{E}|_{max} - |\mathcal{E}|_{min} \approx -(\sigma - \rho)_{max} w \,. \tag{7.2.3}$$

We have compared the numerical evaluation of $|\mathcal{E}|_{max} - |\mathcal{E}|_{min}$ with the above approximation for both the undervolted and the overvolted gap, and we show the result in Fig. 7.3. This figure shows that the planar front approximation gives, in orders of magnitude, a good estimate of the jump in the field over the streamer head. The overestimation of the jump in the field could either be due the total number of charges in the space charge layer being overestimated by the assumptions made above, or by the curvature of the space charge layer being neglected.

In order to determine which of these assumptions leads to the discrepancy between the numerical results and the approximation (7.2.3), we show in Fig. 7.4 the axial distribution of the electric field strength in the streamer head, as well as the (numerical) integration of the space charge densities over the layer, using Eq. (7.2.2). Fig. 7.4 shows that the field computed by numerical integration of

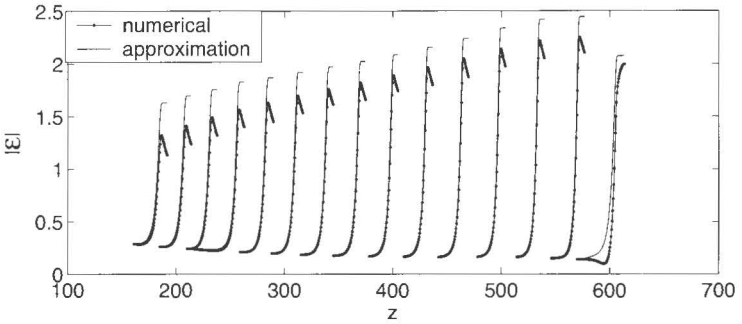

FIGURE 7.4: Evolution of the numerical evaluation of the electric field strength on the axis (dotted lines), and comparison with the field given by Eq. (7.2.2). The time at which the snapshots are taken ranges between τ=200 to 375, with equidistant intervals of 12.5.

Eq. 7.2.2 is overestimated in the streamer head, and this is due to the curvature of the front being neglected. However, comparing the results at early times with those at later times, we see that the field in the planar front approximation approaches increasingly the actual field.

We have thus shown that the width of the space charge layer decreases relative to its radius of curvature, that the propagation velocity is accurately described by that of a planar front, and that the streamer head therefore approaches the limit of planar ionization front.

7.2.3 Comparison with analytical results

In the previous section it has been shown that the ratio of the width of the streamer front and its radius of curvature decreases and reaches a value far below 1 in both under- and overvolted gaps. It is therefore admissible to treat the ionization front as a moving boundary problem. Moreover, we have shown that the streamer approaches a state, which can be described by,

$$\begin{aligned} &\phi^- \approx const.\,, \\ &v_{front} = v_{planar} = |\boldsymbol{\mathcal{E}}_{max}| + 2\sqrt{Df(|\boldsymbol{\mathcal{E}}_{max}|)} = v(\nabla\phi^+)\,, \\ &\nabla^2\phi^+ = 0\,, \end{aligned} \tag{7.2.4}$$

where the superscript "-" denotes quantities in the streamer body, while the superscript "+" denotes the quantities ahead of the ionization front. The third equation in (7.2.4) is a simple consequence of the absence of space charge in the non-ionized state into which the streamer propagates, resulting in a Laplace equation rather than a Poisson equation.

A system describing the dynamics of a moving boundary with Eqs. (7.2.4) is known to cause Laplacian instabilities. Indeed, replacing the potential ϕ by the pressure p results in the equations in which viscous fingering is observed [30].

The same model has been proposed by Lozansky and Firsov. In honor of their contributions, we have called the streamer state described by these equations the *Lozansky-Firsov limit*. However, they only identified uniformly translating parabolic shapes as solutions of the problem, and did not realize the inherent instability of the model. The relation between the simplified model approximation and the branching instability was laid by the group of Ebert [5, 66]. In [66], the propagation of the interface was solved using so-called conformal mapping techniques. The streamer then exhibited a branching behavior, the interface turning from convex to concave, as is shown in Fig. 7.5. This figure also shows that this model exhibits cusps, and recent analytical studies have identified a mechanism to regularize the interface and thereby prevent cusp formation [65].

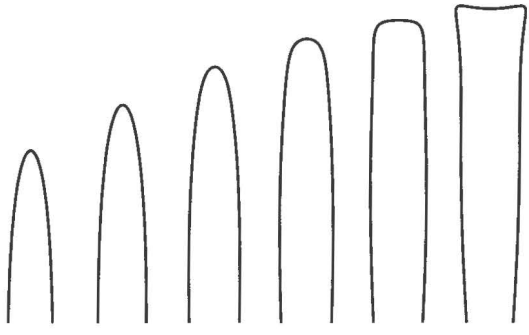

FIGURE 7.5: Temporal evolution of a streamer in the moving boundary approximation. The convex streamer becomes flatter and eventually concave. This figure can be found in [66].

7.3 Influence of the mesh on the streamer branching

In the previous section we have argued that the streamer approaches the Lozansky-Firsov limit of ideal conductivity, which exhibits Laplacian instabilities. This confirms previous findings [5, 83], in which the branching streamer was exhibited by simulations on uniform grids. However, the use of such grids made it impossible to compute the evolution of the streamer in long undervolted gaps. Besides, no quantitative predictions could be made because finer meshes could not be obtained within the limitations of computational memory on a uniform grid setting. We use the algorithm presented in Chap. 3 to reach a very high level of accuracy, and predict quantitatively the time of branching.

7.3.1 Undervolted gap

We have shown in Sect. 6.2 that for the simulations of streamers in an undervolted gap, the evolution of the streamer was already very well captured on a grid size of 4, and that differences with runs on a grid twice as fine become noticeable only just before the streamer branches.

We have determined the time at which the streamer branches on each of these grids (mesh sizes 2,4, and 8). This time of branching has been defined as the moment at which the space charge layer turns from convex to concave. This, however, is not a sudden process, but occurs gradually. It is therefore hard to determine one moment of time at which the streamer becomes unstable, and we identify a moment at which it is certain that the streamer propagates along the axis, and one at which it has certainly branched. In all cases we observe that the streamer becomes unstable between times $\tau = 1.1 \cdot 10^4$, and $\tau = 1.125 \cdot 10^4$. Moreover, in all cases, the form of branching was identical, i.e. off-axis, as shown in Fig. 7.6. We notice that in the case of a finest mesh size of 8, the electron density is roughly twice as small as in the other two cases. This is in accordance with observations made in Sect. 6.2, where it was shown that on such a coarse grid numerical diffusion would "smear out" the front, leading to larger front velocities and smaller densities. However, in the h_f=8 case the front is wider as well, and the number of space charges in the streamer head is approximately the same in all cases, as is shown in Fig. 7.7.

The branching time has thus converged in the case of this undervolted gap, and we can conclude that we have a quantitative prediction of the branching in this case.

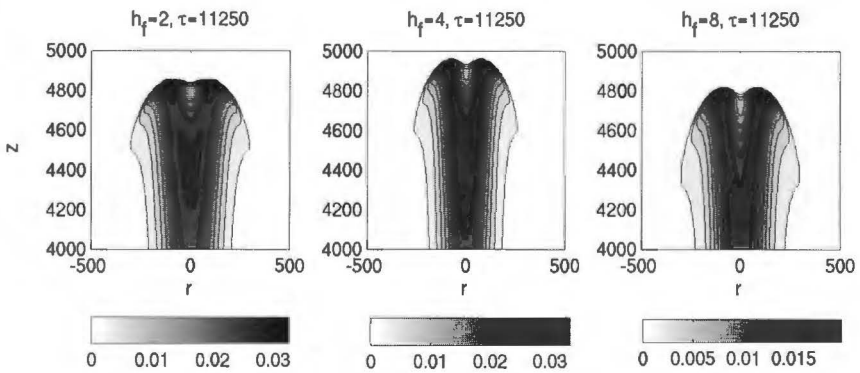

FIGURE 7.6: Electron density distribution in the streamer head just after the occurrence of the instability in a background field $|\mathcal{E}_b|$ =0.15, computed on different finest mesh sizes, h_f =8, 4 and 2, indicated in the title of each plot

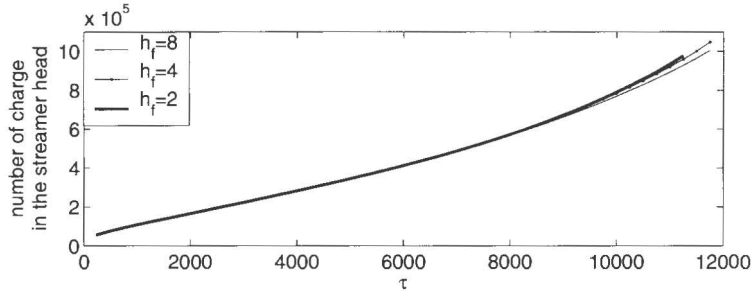

FIGURE 7.7: Evolution of the amount of space charges in the streamer head, computed on grids with finest size 8 (thin solid line), 4 (dotted line) and 2 (thick solid line).

7.3.2 Overvolted gap

In Sect. 6.2 it has been shown that, for the propagation of a streamer during the nonlinear regime in a background field $|\mathcal{E}_b| = 0.5$, a mesh size of $1/2$ is sufficient. As in the undervolted gap, we observe an influence of the mesh size only once the streamer approaches the unstable situation. In Fig. 7.8 we show the branching time as a function of the cell size of the finest grid. Because of the uncertainty in the determination of the branching time, we use error bars in this figure, which indicate a moment at which the streamer is certainly stable, and one at which it certainly has branched. This figure shows that the time at which the instability occurs is very early on coarse grid compared to fine grid computations. However, for fine grids, the time of branching converges.

However, the form into which the ionization front develops depends on the grid that is used, as can be observed in Fig. 7.9. So, although the branching time converges for smaller times, this is not the case with the form of branching. We can relate this to chaos. The streamer approaches a bifurcation point, at which minor details are decisive for the further evolution. The use of different

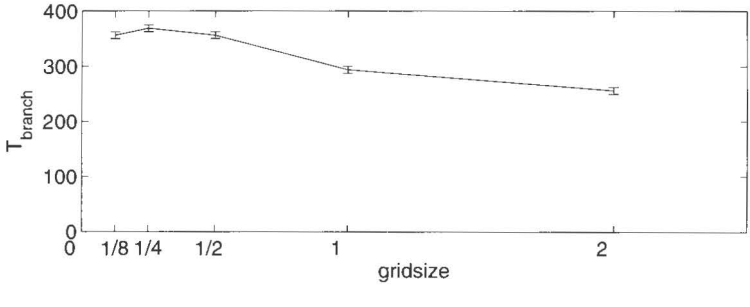

FIGURE 7.8: Time at which the instability occurs as a function of the finest mesh size on which the computation has been performed.

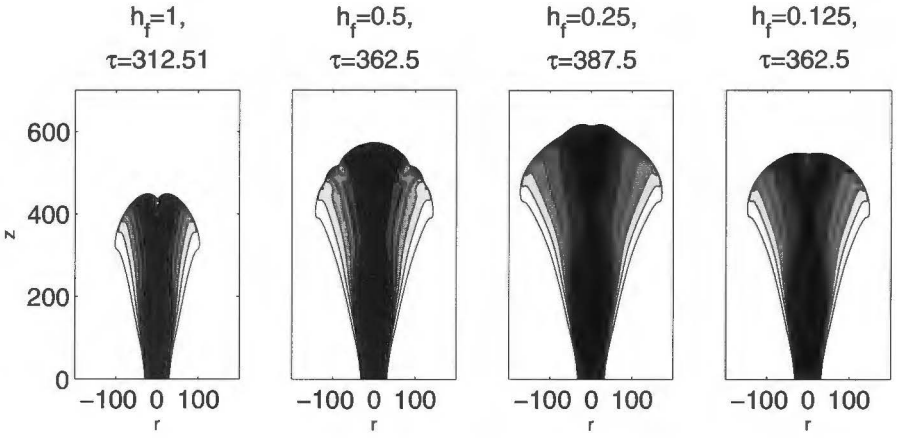

FIGURE 7.9: Electron density distribution just after the instability has occurred in a background field of 0.5, computed with different finest grids, from left to right: h_f =1, 1/2, 1/4 and 1.8.

grids results in small differences in the numerical error, and therefore in different branching forms. That this was not observed in the undervolted gap, is probably due to the relatively small spatial extent of the space charge layer running into the instability. In the overvolted gap, the space charge layer becomes much wider, and therefore more instability modes are accessible.

7.4 Conclusions

We have shown that, at the time when the space charge layer becomes unstable, the streamer approaches the Firsov-Lozansky limit of ideal conductivity, with a velocity of propagation that is set by the electric field. Furthermore, the ratio between the width and the radius of curvature of the space charge layer drops far below unity. This justifies the moving boundary approximation used in [66, 65], which shows that the branching streamer reaches a Laplacian instability, in a similar manner as viscous fingering. This explains qualitatively the appearance of the instability.

With our numerical procedure, we now also are able to predict the time of branching quantitatively. Indeed, there is a convergence of the branching time when using increasingly refined grids. In undervolted gaps, the branching is off-axis, independent of the mesh size that is used. In contrast, in overvolted gaps, the radial extent of the space charge layer is much larger, and the streamer can access various branched states. The form of branching is therefore set by minor details, like the numerical grid, and appears in various forms depending on the grid that is used. We emphasize that this does not imply that the branching is of numerical nature, but rather that the branching bifurcation is chaotic.

8

SUMMARY, CONCLUSIONS AND OUTLOOK

Throughout this thesis we have conducted numerical experiments and also an analytical investigation on the evolution of negative streamers in N_2 under influence of a uniform electric field. These streamers can be described by the minimal streamer model, which consists of continuity equations for the charged particles – including drift and impact ionization in the local electric field, and diffusion – coupled to the Poisson equation for the electric field. The phenomenon is nonlinear due to the coupling of the charged particles and the electric field.

The adaptive regridding algorithm

The simulation of streamers represents a great computational challenge because of their multiscale character, and because of the pulled character of the streamer front, which causes standard refinement strategies to fail. An adaptive grid refinement algorithm has been developed that deals efficiently with these difficulties.

The use of an explicit time stepping scheme enables us to decouple the grids for the continuity equations from those on which the Poisson equation is solved. This makes it possible to design refinement criteria specifically suited for each problem. The grids for the continuity equations are refined following a curvature monitor, which gives a good estimate of the spatial difficulty of the problem. The leading edge of the ionization front is explicitly included in the refined regions. The grids for the Poisson equations are refined following a calculation of the error in the solution on two consecutive levels.

Tests on planar and curved ionization fronts were performed successfully, showing a gain in computational memory of two orders of magnitude, as well as an important gain in computational time. The main achievement with the adaptive grid refinement is that it gives the possibility to explore a new parameter regime, in particular, high electric fields and large system sizes.

The physical stages of the streamer evolution

A streamer emerging from a single electron in a uniform electric field passes three physical stages during its evolution.

1. **The electron avalanche phase.** The electrons drift, diffuse and multiply in the undisturbed background field. The evolution during this phase is linear. Space charges build up, but not in a sufficient amount to disturb the background field.

2. **The streamer regime.** Eventually the amount of space charges has become so large that their effect on the background electric field can no longer be neglected, and the propagation has become nonlinear. The streamer is characterized by the curved and thin space charge layer around its tip, which enhances the field ahead of it. The ionization created by the ionization front increases in time, hence the conductivity of the streamer increases as well.

3. **The branching streamer.** The space charge layer around the streamer tip becomes flatter and thinner, and, provided the gap is sufficiently long, becomes unstable. The streamer then branches.

Analytical study of the avalanche phase and the transition to streamer

Raether [80] and Meek [63], independently from each other, have derived a criterion for the emergence of a streamer from an electron avalanche. They postulated that the amount of electrons should typically grow up to the order of 10^8 to 10^9 during the avalanche phase for a streamer to be formed. However, their simple estimate does not take diffusion into account.

When considering a single electron as initial seed, an explicit solution for the electron density distribution as a function of spatial and temporal coordinates exists [82]. Furthermore, we have derived explicit expressions for the spatial moments of the ion distribution, which leads to the remarkable conclusion that the center of mass of the ion cloud drifts with the same velocity as that of the electron cloud, though the ions are immobile, and that the distance between the centers of masses is fixed and equal to the ionization length in the background field. These analytical expressions enabled us to find good approximations for the electric field induced by the space charges. We use these approximations to derive a criterion for the emergence of a streamer, based on significant effect of the field distortion on the propagation of the electron cloud. This corresponds to the time when the self induced field of the space charges reaches a value of roughly 3% of the background field.

The criterion shows that diffusion tends to suppress the emergence of the streamer, whereas the use of dense initial seeds and strong electric fields on the contrary accelerates it. More specifically, the criterion derived in this thesis shows that the number of electrons at the transition saturates towards 10^6 in high fields, and that in low fields, it reaches values larger than 10^{13}.

Streamer propagation

The adaptive grid algorithm has been used to compute the propagation of streamers in a plane-parallel gap filled with N_2. This situation is comparable with that in which geophysical sprite discharges are observed.

The grid refinements allow us to investigate the propagation of streamers in both under- and overvolted gaps. We summarize the generic features and the differences in both cases.

1. **Space charge layer.** The streamer regime is characterized by a thin space charge layer around the streamer head. It enhances the field ahead it of, allowing the streamer to propagate, even in undervolted gap. The width of the space charge layer decreases in time, while the electric field immediately ahead of the streamer increases. The relation between maximal field and layer width agrees well with analytical solutions for planar fronts. The radius of curvature of the space charge layer on the other hand increases in time, and the streamer approaches the limit of a planar ionization front.

2. **Enhanced conductivity.** The electron density (and therefore the conductivity) in the streamer body increases during the propagation. As a consequence, the streamer interior is screened from the background electric field. It does, however, not reach the limit of ideal conductivity, because the amount of charges in the streamer head increases during the propagation, which requires a charge current through the streamer body.

3. **Radial growth.** In both over- and undervolted gaps, the radial growth is first governed by diffusion. When the streamer regime is entered, diffusion is overcome by drift, which leads to an enhanced radial growth of the streamer in an overvolted gap. In an undervolted gap on the contrary, after an initial phase of diffusive widening, a streamer enters a contraction phase.

4. **Propagation velocity.** The propagation velocity of the streamer is accurately described by the analytically derived velocity for planar streamer fronts [30].

5. **Intermediate attractor.** In a specific electric field, a steep and dense initial seed as well as inflow of electrons accelerates the emergence of a streamer, as well as the transition towards the branching state. However, the streamer appears to approach a similar state immediately before branching.

Branching streamer

We have shown that the streamer reaches a branching state, even in undervolted gaps, provided it is sufficiently long. Our simulations show that the time of branching converges when using finer grids. Moreover, in undervolted gaps,

the branching is of the simplest off-axis, independently of the mesh size. In overvolted gaps, the unstable streamer is more sensible to the grids, exhibiting branching at similar times, but with different forms. Apparently, several branching states can be reached. Minor differences during the bifurcation would than select one or the other state from the same symmetric unstable state.

We have shown that the front approaches the Firsov-Lozansky limit of ideal conductivity, and that the velocity is set by the maximal electric field. Moreover, the ratio of the width of the space charge layer and its radius of curvature decreases in time. The streamer front therefore approaches the limit of an infinitesimally thin layer investigated analytically through a moving boundary approximation [4, 66, 65]. Such a moving boundary indeed exhibits a Laplacian instability, similar to viscous fingering.

We have thus developed a numerical code, which is able to capture accurately the features of the streamer evolution, from its emergence from an avalanche up to the unstable state. It is, however, only a first step towards simulations of more realistic streamers. Currently a large number of projects are started to enhance our understanding of this complex phenomenon, of which we mention:

1. Development of a fully three-dimensional code, making it possible to follow the streamer evolution after the instability has occurred.

2. Inclusion of other ionization mechanisms, in particular photoionization or background ionization to investigate the propagation of streamers of both polarities in pure nitrogen or argon, as well as in composite gases like air.

3. Development of a hybrid code, in which the present code is coupled to a Monte Carlo method for the computation of the stochastic few-particle processes in the leading edge of the ionization front. The consequences of these stochastic processes for triggering the branching instability have not been investigated yet.

4. On the experimental side, the effect of the charge polarity, the applied electric field strength, the gas, and the electrode geometry on the streamer propagation are being measured. An interesting experimental feature is the influence of the power supply, that calls for theoretical understanding.

BIBLIOGRAPHY

[1] ABOU-GHAZALA, A., KATSUKI, S., SCHOENBACH, K., DOBBS, F., AND MOREIRA, K. Bacterial decontamination of water by means of pulsed-corona discharges. *IEEE Trans. Plasma Sci. 30* (200), 1449–1453.

[2] AKIYAMA, H. Streamer discharges in liquids and their applications. *IEEE Trans. Dielect. Elect. Insul. 7* (2000), 646–653.

[3] ALLEN, N., AND GHAFFAR, A. The conditions required for propagation of a cathode-directed positive streamer in air. *J. Phys. D: Appl. Phys. 29* (1996), 740–752.

[4] ARRAYÁS, M., AND EBERT, U. Stability of negative ionization fronts: Regularization by electric screening? *Phys. Rev. E 69* (2004), 036214(1–10).

[5] ARRAYÁS, M., EBERT, U., AND HUNDSDORFER, W. Spontaneous branching of anode-directed streamers between planar electrodes. *Phys. Rev. Lett. 88* (2002), 174502(1–4).

[6] BABAEVA, N., AND NAIDIS, G. Two-dimensional modelling of positive streamer dynamics in non-uniform electric fields in air. *J. Phys. D: Appl. Phys. 29* (1996), 2423–2431.

[7] BABAYAN, S., JEONG, J., TU, V., PARK, J., SELWYN, G., AND HICKS, R. Deposition of silicon dioxide films with an atmospheric-pressure plasma jet. *Plasma Source Sci. Technol. 7* (1998), 286–288.

[8] BARNES, M., COLTER, T., AND ELTA, M. Large-signal time-domain modeling of low-pressure rf glow discharges. *J. Appl. Phys. 61* (1986), 81–89.

[9] BAZELYAN, E., AND RAIZER, Y. *Spark discharge.* CRC Press, New York, 1998.

[10] BAZELYAN, E., AND RAIZER, Y. *Lightning Physics and Lightning Protection.* Institute of Physics Publishing, Bristol, U.K., 2000.

[11] BLOM, J., TROMPERT, R., AND VERWER, J. Algorithm 758: VLUGR2: A vectorizable adaptive grid solver for PDEs in 2D. *ACM Trans. Math. Softw. 22* (1996), 302–328.

[12] Bobrov, Y., and Yurghelenas, Y. Application of high-resolution schemes in the modeling of ionization waves in gas discharges. *Comp. Math. and Math. Physics 38* (1998), 1652–1661.

[13] Boeuf, J., Belenguer, P., and Hbid, T. Plasma particle interactions. *Plasma Sources Sci. Technol. 3* (1994), 407–417.

[14] Boeuf, J., Lagmich, Y., and Pitchford, L. Electrohydrodynamic force and aerodynamic flow acceleration in surface dielectric barrier discharges. In *Proc. XXVII Int. Conf. Phen. Ion. Gases* (Veldhoven, The Netherlands, 2005).

[15] Boeuf, J., and Marode, E. A Monte Carlo analysis of an electron swarm in a non-uniform field: the cathode region of a glow discharge. *J. Phys. D: Appl. Phys. 15* (1982), 2169–2187.

[16] Bogaerts, A., Neyts, E., Gijbels, R., and van der Mullen, J. Gas discharge physics and their applications. *Spectrochim Acta B 57* (2002), 609–658.

[17] Botta, E., Dekker, K., Notay, Y., van der Ploeg, A., Vuik, C., Wubs, F., and de Zeeuw, P. How fast the Laplace equation was solved in 1995. *Appl. Num. Math. 24* (1997), 439–455.

[18] Briels, T., van Veldhuizen, E., and Ebert, U. Branching of positive discharge streamers in air at varying pressures. *IEEE Trans. Plasma Sci. 33* (2005), 264–265.

[19] Briels, T., van Veldhuizen, E., and Ebert, U. Experiments on the diameter of positive streamers in air. In *Proc. XXVII Int. Conf. Phen. Ion. Gases* (Veldhoven, The Netherlands, 2005).

[20] Chalmers, I., Duffy, H., and Tedford, D. The mechanism of spark breakdown in nitrogen, oxygen and sulphur hexafluoride. *Proc. R. Soc. Lond. A 329* (1972), 171–191.

[21] Chen, F. Industrial applications of low-temperature plasma physics. *Phys. Plasmas 2* (1995), 2164–2175.

[22] Clements, J., Mizuno, A., Finney, W., and Davis, R. Combined removal of SO_2, NO_x, and fly ash from simulated flue gas using pulsed streamer corona. *IEEE Trans. Ind. Appl. 25* (1989), 62–69.

[23] Davies, A., Davies, C., and Evans, C. Computer simulation of rapidly developing gaseous discharges. *Proc. IEE 118* (1971), 816–823.

[24] Dhali, S., and Williams, P. Two-dimensional studies of streamers in gases. *J. Appl. Phys 62* (1987), 4696–4706.

[25] DINELLI, G., CIVITANO, L., AND REA, M. Industrial experiments on pulse corona simultaneous removal of NO_x and SO_2 from flue gas. *IEEE Trans. Ind. Appl. 26* (1990), 535–541.

[26] DUTTON, J. A survey of electron swarm data. *J. Phys. Chem. Ref. Data 4* (1975), 664.

[27] EBERT, U., AND HUNDSDORFER, W. Reply to the comment of A.A. Kulikovsky [48] on "Spontaneous branching of anode-directed streamers between planar electrodes". *Phys. Rev. Lett. 89* (2002), 229402.

[28] EBERT, U., ROCCO, A., HUNDSDORFER, W., AND ARRAYÁS, M. A mechanism for streamer branching. In *16th ESCAMPIG and 5th ICRP Joint Conference* (Grenoble, July 2002).

[29] EBERT, U., AND VAN SAARLOOS, W. Front propagation into unstable states: universal algebraic convergence towards uniformly translating pulled fronts. *Physica D 146* (2000), 1–99.

[30] EBERT, U., VAN SAARLOOS, W., AND CAROLI, C. Propagation and structure of planar streamer fronts. *Phys. Rev. E 55* (1997), 1530–1549.

[31] ELIASSON, B., AND KOGELSCHATZ, U. Modeling and applications of silent discharge plasmas. *IEEE Trans. Plasma Sci. 19* (1991), 309–323.

[32] EVANS, D., ROSDCHA, L., ANDERSON, G., COOGAN, J., AND KUSHNER, M. Plasma remediation of trichloroethylene in silent discharge plasmas. *J. Appl. Phys. 74* (1993), 5378–5386.

[33] FRANZ, R., NEMZEK, R., AND WINCKLER, J. Television image of a large upward electrical discharge above a thunderstorm system. *Science 249* (1990), 48–51.

[34] GERKEN, E., INAN, U., AND BARRINGTON-LEIGH, C. Telescopic imaging of sprites. *Geophys. Res. Lett. 27* (2000), 2637.

[35] GOLUB, G., AND VAN LOAN, C. *Matrix Computations*, 3 ed. John Hopkins Univ. Press, Baltimore, 1996.

[36] GOTTLIEB, S., SHU, C.-W., AND TADMOR, E. Strong stability-preserving high-order time discretization methods. *SIAM Review 43* (2001), 89–112.

[37] HEAVNER, M. *Optical Spectroscopic Observations of Sprites, Blue Jets, and Elves: Inferred Microphysical Processes and their Macrophysical Implications.* PhD thesis, Univ. Alaska, 2000.

[38] HOPWOOD, W. The positive streamer mechanism of spark breakdown. *Proc. Phys. Soc. B 62* (1949), 657–664.

[39] HUNDSDORFER, W., AND VERWER, J. *Numerical Solution of Time-Dependent Advection-Diffusion-Reaction Equations*, vol. 33 of *Series in Comp. Math.* Springer, Berlin, 2003.

[40] HUXLEY, L., AND COMPTON, R. *The Diffusion and Drift of Electrons on gases.* Series in Plasma Physics. Wiley, New York, 1974.

[41] KOGELSCHATZ, U. Industrial innovation based on fundamental physics. *Plasma Sources Sci. Technol. 11* (2002), A1–A6.

[42] KOGELSCHATZ, U. Atmospheric-pressure plasma technology. *Plasma Phys. Control. Fusion 46* (2004), B63–B75.

[43] KOSSYI, I., KOSTINSKY, A. Y., MATVEYEV, A., AND SILAKOV, V. Kinetic scheme of the non-equilibrium discharges in nitrogen-oxygen mixtures. *Plasma Sources Sci. Technol. 1* (1992), 207–220.

[44] KULIKOVSKY, A. Positive streamer between parallel plate electrodes in atmospheric pressure air. *J. Phys. D: Appl. Phys. 30* (1997), 441–450.

[45] KULIKOVSKY, A. Production of chemically active species in the air by a single positive streamer in a nonuniform field. *IEEE Trans. Plasma Sci. 25* (1997), 439–446.

[46] KULIKOVSKY, A. The role of photoionization in positive streamer dynamics. *J. Phys. D: Appl. Phys. 33* (2000), 1514–1524.

[47] KULIKOVSKY, A. The role of the absorption length of photoionizing radiation in streamer dynamics in weak fields: a characteristic scale of ionization domain. *J. Phys. D: Appl. Phys. 33* (2000), L5–L7.

[48] KULIKOVSKY, A. Comment on "Spontaneous branching of anode-directed streamers between planar electrodes". *Phys. Rev. Lett. 89* (2002), 229401.

[49] KUNHARDT, E., AND TZENG, Y. Development of an electron avalanche and its transition into streamer. *Phys. Rev. A 38* (1988), 1410–1421.

[50] KUNHARDT, E., TZENG, Y., AND BOEUF, J. Stochastic development of an electron avalanche. *Phys. Rev. A 34* (1986), 440–449.

[51] KUSHNER, M. A model for the discharge kinetics and plasma chemistry during plasma enhanced chemical vapor deposition of amorphous silicon. *J. Appl. Phys. 63* (1988), 2532–2551.

[52] LISITSYN, I., NOMIYAMA, H., KATSUKI, S., AND AKIYAMA, H. Streamer discharge reactor for water treatment by pulsed power. *Rev. Sci. Instr. 70* (1999), 3457–3462.

[53] LIU, N., AND PASKO, V. Effects of photoionization on propagation and branching of positive and negative streamers in sprites. *J. Geophys. Res 109* (2004), A04301(1–17).

[54] LOCKE, B., ICHIHASHI, A., KIM, H., AND MIZUNO, A. Diesel engine exhaust treatment with a pulsed streamer corona reactor equipped with recirculated vitreous carbon electrodes. *IEEE Trans. Plasma Sci. 37* (2001), 715–723.

[55] LOEB, L. The threshold for spark development by streamer mechanism in uniform fields. *Phys. Rev. 74* (1948), 210–212.

[56] LOEB, L. *Basic processes of gaseous electronics.* University of California Press, Berkeley, CA, 1960.

[57] LOEB, L., AND MEEK, J. The mechanism of spark discharge in air at atmospheric pressure. I. *J. Appl. Phys. 11* (1940), 438–447.

[58] LOEB, L., AND MEEK, J. The mechanism of spark discharge in air at atmospheric pressure. II. *J. Appl. Phys. 11* (1940), 459–474.

[59] LOZANSKY, E., AND FIRSOV, O. Theory of the initial stage of streamer propagation. *J. Phys. D: Appl. Phys. 6* (1973), 976–981.

[60] LYONS, W. Sprite observations above the U.S. high plains in relation to their parent thunderstorm systems. *J. Geophys. Res. 101* (1996), 29641–29652.

[61] MAKAROV, M., BONNET, J., AND PIGACHE, D. High efficiency discharge-pumped XeCl laser. *Appl. Phys. B 66* (1998), 417–426.

[62] MAZUR, V., KREHBIEL, P., AND SHAO, X. Correlated high-speed video and radio interferometric observations of a cloud-to-ground lightning flash. *J. Geophys. Res. 100* (1995), 25731–25754.

[63] MEEK, J. A theory of spark discharge. *Phys. Rev. 57* (1940), 722–728.

[64] MEEK, J., AND CRAGGS, J. *Electric breakdown of gases.* Series in Plasma Physics. Wiley, New York, 1978.

[65] MEULENBROEK, B., EBERT, U., AND SCHÄFER, L. Regularization of moving boundaries in a Laplacian field by a mixed Dirichlet-Neumann boundary condition – exact results. To appear in Phys. Rev. Lett. ca. November 2005.

[66] MEULENBROEK, B., ROCCO, A., AND EBERT, U. Streamer branching rationalized by conformal mapping techniques. *Phys. Rev. E 69* (2004), 067402(1–4).

[67] MONTIJN, C., AND EBERT, U. Avalanche to streamer transition in homogeneous fields. Tech. Rep. MAS-E0515, CWI, 2005. http://www.cwi.nl/ftp/CWIreports/MAS/MAS-E0515.pdf, http://www.arxiv.org/pdf/physics/0508109.

[68] MONTIJN, C., MEULENBROEK, B., EBERT, U., AND HUNDSDORFER, W. Numerical simulations and conformal analysis of growing and branching negative discharge streamers. *IEEE. Trans. Plasma Sc. 33* (2005), 260–261.

[69] MORGAN, W., AND PENETRANTE, B. ELENDIF: A time-dependent boltzmann solver for partially ionized plasmas. *Comp. Phys. Comm. 58* (1990), 127–152.

[70] MORROW, R., AND LOWKE, J. Streamer propagation in air. *J. Phys. D: Appl. Phys. 30* (1997), 614–627.

[71] NITSCHKE, T., AND GRAVES, D. A comparison of particle in cell and fluid model simulation of low-pressure radio frequency discharges. *J. Appl. Phys. 76* (1994), 5646–5660.

[72] ODA, A., SUGAWARA, H., SAKAI, Y., AND AKASHI, H. Estimation of the light output power and efficiency of Xe barrier discharge excimer lamps using a one-dimensional fluid model for various voltage waveforms. *J. Phys. D: Appl. Phys. 33* (2000), 1507–1513.

[73] ODA, T., KATO, T., TAKAHASHO, T., AND SHIMIZU, K. Nitric oxide decomposition in air by using nonthermal plasma processing with additives and catalyst. *IEEE Trans. Ind. Appl. 34* (1998), 268–272.

[74] PANCHESHNYI, S., STARIKOVSKAIA, S., AND STARIKOVSKII, A. Role of photoionization processes in propagation of cathode-directed streamer. *J. Phys. D: Appl. Phys. 34* (2001), 105–115.

[75] PANCHESHNYI, S., AND STARIKOVSKII, A. Two-dimensional numerical modeling of the cathode-directed streamer development in a long gap at high voltage. *J. Phys. D: Appl. Phys. 36* (2003), 2683–2691.

[76] PASKO, V., STANLEY, M., MATHEWS, J., INAN, U., AND WOOD, T. Electrical discharge from a thundercloud top to the lower ionosphere. *Nature 416* (2002), 152–154.

[77] PASKO, V., AND STENBAEK-NIELSEN, H. Diffuse and streamer regions of sprites. *Geophys. Res. Lett. 29* (2002), 82(1–4).

[78] PENNEY, G., AND HUMMERT, G. Photoionization measurements in air, oxygen, and nitrogen. *J. Appl. Phys 41* (1970), 572–577.

[79] QIN, B., AND PEDROW, P. Particle-in-cell simulation of bipolar dc corona. *IEEE. Trans. Dielect. Elect. Insulation 6* (1994), 1104–1118.

[80] RAETHER, H. The development of electron avalanche in a spark channel (from observations in a cloud chamber). *Z. Phys 112* (1939), 464.

[81] RAETHER, H. *Electron avalanches and breakdown in gases.* Butterworths, London, 1964.

[82] RAIZER, Y. *Gas Discharge Physics.* Springer, Berlin, 1991.

[83] ROCCO, A., EBERT, U., AND HUNDSDORFER, W. Branching of negative streamers in free flight. *Phys. Rev. E 66* (2002), 035102(1–4).

[84] SATO, M., OHGIYAMA, T., AND CLEMENTS, J. Formation of chemical species and their effects on microorganisms using a pulsed high voltage discharge in water. *IEEE Trans. Ind. Appl. 32* (1996), 106–112.

[85] SCHUMANN, U., AND SWEET, R. A direct method for the solution of Poisson's equation with neumann boundary conditions on a staggered grid of arbitrary size. *J. Comp. Phys 20* (1976), 171–182.

[86] SENTMAN, D., WESCOTT, E., OSBORNE, D., AND HEAVNER, M. Preliminary results from the Sprites94 campaign: Red sprites. *Geophys. Res. Lett. 22* (1995), 1205–1209.

[87] SHIMIZU, K., KINOSHITA, K., YANAGIHARA, K., RAJANIKANTH, B., KATSURA, S., AND MIZUNO, A. Pulsed-plasma treatment of polluted gas using wet-/low-temperature corona reactors. *IEEE Trans. Plasma Sci. 33* (1997), 1373–1380.

[88] SORIA, C., PONTIGA, F., AND CASTELLANOS, A. Two-dimensional numerical simulation of streamers using a particle-in-cell method. In *2000 Ann. Rep. Conf. Electr. Ins. Dielectr. Phen* (Victoria, BC, Canada, 2000).

[89] SORIA, C., PONTIGA, F., AND CASTELLANOS, A. Particle-in-cell simulation of electrical gas discharges. *J. Comp. Phys 171* (2001), 47–78.

[90] S.PASQUIERS. Removal of air pollutants by plasma catalytic processes. *Eur. Phys. J. Appl. Phys. 28* (2004), 319–324.

[91] STANLEY, M., KREHBIEL, P., BROOK, M., MOORE, C., RISON, W., AND ABRAHAMS, B. High speed video of initial sprite development. *Geophys. Res. Lett. 26* (1999), 3201–3204.

[92] STENBAEK-NIELSEN, H., MOUDRY, D., WESCOTT, E., SENTMAN, D., AND SABBAS, F. S. Sprites and possible mesospheric effects. *Geophys. Res. Lett. 27* (2000), 3827–3831.

[93] TOWNSEND, J. *The theory of ionization of gases by collision.* Constable&Company Ltd., London, 1910.

[94] TROMPERT, R., AND VERWER, J. A static-regridding method for two-dimensional parabolic partial differential equations. *Appl. Numer. Math. 8* (1991), 65–90.

[95] VAN VELDHUIZEN, E. private communication.

[96] VAN VELDHUIZEN, E., BAEDE, A., HAYASHI, D., AND RUTGERS, W. Fast imaging of streamer propagation. In *APP Spring Meeting* (Bad-Honnef, Germany, 2001).

[97] VAN VELDHUIZEN, E., KEMPS, P., AND RUTGERS, W. Streamer branching under influence of the power supply. *IEEE Trans. Plasma Sci. 30* (2002), 162–163.

[98] VAN VELDHUIZEN, E., AND RUTGERS, W. Corona discharges: fundamentals and diagnostics. In *Proc. Frontiers in Low Temp. Plasma Diagn. IV* (Kerkrade, The Netherlands, 2001), pp. 40–49.

[99] VAN VELDHUIZEN, E., AND RUTGERS, W. Pulsed positive corona streamer propagation and branching. *J. Phys. D: Appl. Phys. 35* (2002), 2169–2179.

[100] VAN VELDUIZEN, E., RUTGERS, W., AND EBERT, U. Branching of streamer type corona discharge. In *Proc. XIV Int. Conf. Gas Discharges and Appl.* (Liverpool, 2002).

[101] VITELLO, P., PENETRANTE, B., AND BARDSLEY, J. Multidimensional modeling of the dynamic morphology of streamer coronas. *Non-thermal Plasma Techniques for Pollution Control, NATO ASI Ser., Ser. G 34(A)* (1993), 249–271.

[102] VITELLO, P., PENETRANTE, B., AND BARDSLEY, J. Simulation of negative-streamer dynamics in nitrogen. *Phys. Rev. E 49* (1994), 5574–5598.

[103] WACKERS, J. A nested-grid finite-difference Poisson solver for concentrated source terms. *J. Comp. Appl. Math. 180* (2005), 1–12.

[104] WAGNER, K. Die Entwicklung der Electronenlawine in den Plasmakanal, untersucht mit Bildverstärker und Wischverschluss. *Z. Phys. 189* (1966), 465–515.

[105] WAGNER, K. Vorstadium des Funkens, untersucht mit dem Bildverstärker. *Z. Phys. 204* (1967), 177.

[106] WANG, M., AND KUNHARDT, E. Streamer dynamics. *Phys. Rev A 42* (1990), 2366–2373.

[107] WESCOTT, E., SENTMAN, D., HEAVNER, M., HAMPTON, D., AND JR., O. V. Blue jets: Their relationship to lightning and very large hailfall, and their physical mechanisms for their production. *J. Atmos. Solar-Terr. Phys. 60* (1998), 713–724.

[108] WESCOTT, E., SENTMAN, D., OSBORNE, D., AND HEAVNER, M. Preliminary results from the Sprites94 aircraft campaign: Blue jets. *Geophys. Res. Lett. 22* (1995), 1209–1213.

[109] WESSELING, P. *Principles of Computational Fluid Dynamics*, vol. 29 of *Series in Comp. Math.* Springer, Berlin, 2001.

[110] WINANDS, G., YAN, K., NAIR, A., PEMEN, A., AND VAN HEESCH, E. Evaluation of corona plasma techniques for industrial applications: HPPS and DC/AC systems. *Plasma Proc. and Polymers 2* (2005), 232–237.

[111] YAN, M., AND GOEDHEER, W. A PIC-MC simulation of the effect of frequency on the characteristics of VHF SiH_4/H_2 discharges. *Plasma Sources Sci. Technol. 8* (1999), 349–354.

[112] YI, W. J., AND WILLIAMS, P. Experimental studies of streamers in pure N_2 and N_2/O_2 mixtures and a $\simeq$ 13cm gap. *J. Phys. D: Appl. Phys. 35* (2002), 205–218.

[113] ZELENY, J. The mechanism of the electric spark. *J. Appl. Phys. 13* (1942), 444–450.

[114] ZHELEZNYAK, M., MNATSAKANYAN, A., AND SIZYKH, S. Photoionization of nitrogen and oxygen mixtures by radiation from a gas discharge. *High Temp. 20* (1982), 357–362.

SUMMARY

Plasmas are ionized media, occupying 99% of the universe. Common examples of plasmas are the sun, which is a high-temperature plasma, and neon lights, which are low-temperature plasmas. A high-temperature plasma is at thermal equilibrium, and is driven by a high pressure and temperature of the medium. A low-temperature plasma, on the other hand, is far from equilibrium, and the ionization is generated by electric or electromagnetic fields.

Streamers are transient, filamentary, low-temperature plasma channels which, under influence of the self-enhanced electric field at their tip, propagate rapidly into a non- or weakly ionized medium. They are widely used in industry, e.g. for the treatment of exhaust gasses, cleaning of polluted water, and in aerospatial engineering. Streamers are also found in nature, where they play a role in creating the path of lightning. Recent observations showed the existence of sprites, which are very large discharge structures in the higher parts of the atmosphere, composed of a multitude of streamers. One distinguishes streamers according to their polarity: in *positive* or cathode-directed streamers, positive space charges propagate in the direction of the electric field. In *negative* or anode directed streamers, on the other hand, it is negative net charge that propagates in the direction of the electron drift, i.e. opposite to the electric field.

Experiments show that positive streamers emerge more easily from a point or a wire electrode than negative ones, which require a much higher voltage to emerge. Consequently, industrial applications mainly focus on the use of positive streamers. On the other hand, when streamers emerge in free space from ionization avalanches, they can have both a positive and a negative end. Lightning as well as sprite discharges are examples of such kind of double-ended discharges. Up to now, most experimental and theoretical efforts have been devoted to positive streamers in air because of their applications. However, the cross-sections for photoionization, which is required for the propagation of positive streamers, are not well-known. To define a clear physical signature, it is therefore desirable to study a situation rather independent of photoionization: negative streamers in pure gases. High-voltage experiments to obtain such streamers are currently being set up at the Eindhoven University of Technology in collaboration with the research theme "Nonlinear Dynamics and Complex Systems" at the national research institute for Mathematics and Computer Science (CWI) in Amsterdam, where numerical and analytical research is carried out. This thesis was written at CWI and is concerned with a numerical method

for the simulation of negative streamers, and also with an analytical criterion for the emergence of such streamers.

The simulation of streamers represents a great computational challenge. First, multiple spatial scales are involved: the non-ionized region into which the streamer propagates is orders of magnitude larger than the ionized channel, which in turn is much larger than the small active region at the streamer tip, which again has an inner layered structure. Secondly, the spatial density gradients in the tip of the streamer grow during the propagation, requiring an increasing accuracy of the numerical method. Finally, another specific difficulty comes from the unstable nature of streamers: any ionized perturbation in the non-ionized, high-field region just ahead of the streamer tip will grow. The dynamics of the streamers are set in this unstable region, the *leading edge*, where the densities are very low and the density gradients therefore small. The ionization front is pulled into the non-ionized region by the leading edge, which is a main reason for the failure of standard refinement strategies to describe accurately the streamer dynamics.

We have developed a numerical algorithm that copes in an efficient way with the inherent computational difficulties. It computes the evolution of the streamer in a fluid approximation. The model consists of continuity equations for the charged particles, which, in pure nitrogen, are electrons and positive ions. These continuity equations tell us that the temporal change of the charged particles is set by their drift, diffusion, and ionization sources and sinks. The drift velocity of the particles as well as the ionization rate depend on the local electric field, which has to be determined through the so-called Poisson equation for the electric potential, whose source term is given by the space charge. This model is nonlinear because the particle motion and generation depend on the field while the field depends on the particle densities. For negative streamers in nitrogen, it is admissible to neglect ionization sources like photoionization, and the only source of charged particles is then ionization by impact of sufficiently energetic electrons with neutral particles. These mechanisms – namely the drift and impact ionization in the local electric field, the diffusion and the space charge effects – in a continuum approximation constitute the so-called *minimal streamer model*, which is analyzed in this thesis.

The algorithm is implemented for a three-dimensional system with cylindrical symmetry, which reduces the computations effectively to two spatial dimensions. The algorithm is based on a decoupling of the numerical grids for the continuity equations on the one hand, and that for the Poisson equation on the other hand. The grids are refined, according to error monitors, at each time step, thereby adapting themselves to the solution. The leading edge is explicitly included in the refinement criterion. Successful test are carried out both on planar and curved streamer fronts. This algorithm enables us to explore a new parameter regime. We can now apply large background electric fields, in which spatial gradients become very large, and still resolve the streamer in an accurate manner. It is now also possible to compute the streamer evolution in low fields and large gas gaps. The results of the simulations exhibit some very interesting features in both cases.

Following the evolution of streamers emerging from a single electron in a plane-parallel electrode geometry shows that three physical stages are passed. The emergence of a streamer can occur through an electron avalanche, characterized by the absence of space charge effects, and is therefore linear. Once the amount of space charges is sufficiently large to change significantly the background electric field, the phenomenon becomes non-linear, and a streamer emerges. If the distance to the anode is long enough, the streamer eventually becomes unstable and branches.

During the avalanche phase, the electrons drift, diffuse and multiply in the uniform background electric field. If the avalanche starts from a single electron and the field is homogeneous, the equation for the electrons has an analytical solution, which can be used to derive analytical expressions for the spatial moments of the ions. This allows us to find an analytical approximation for the electric field, and hence determine when the space charge effects have become so strong, that the transition to a streamer takes place. We have thus derived a criterion for the avalanche to streamer transition, which includes the effect of diffusion. The traditional criterion for the transition, Meek's criterion, postulates that, in a specific gas at a specific pressure, the travel time and distance of the electron avalanche before turning into a streamer only depend on the applied background field. The inclusion of diffusion shows that this is not the case and that diffusion can in fact considerably delay the emergence of a streamer.

Once the streamer has emerged, the evolution is nonlinear. At this point our grid refinement strategy provides us with a powerful tool to compute the further streamer propagation. The streamer is characterized by the enhanced conductivity of its body, which is therefore partially shielded from the exterior electric field. This shielding requires a space charge layer at the streamer tip, which in turn enhances the electric field ahead of the tip. The streamer extends in this self-enhanced field.

We investigate the evolution and branching of streamers in both cases of overvolted and undervolted gaps. These are distinguished by the ability of the background electric field to provide an electron with a sufficient amount of energy to ionize a neutral atom or molecule when colliding with it. In an overvolted gap, the background electric field is sufficiently high for this to happen, and the streamer penetrates a highly unstable state. Its radius continues to grow up to branching, giving it a conical shape. Moreover, the spatial density gradients become very steep, thereby requiring a very high accuracy from the numerical method. In an undervolted gap, the electrons only multiply in the small region ahead of the streamer where the field is sufficiently enhanced, giving the streamer a more filamentary shape. For a sufficient field enhancement, a sufficient amount of charge in the streamer head is required. The accumulation of charge in the head depends both on the initial distribution of ionization and on the boundary conditions on the electrode.

We study different cases and eventually, in all cases, the streamer branches provided the gap is sufficiently long. The branching state of the streamer has not been analyzed much up to now, mainly due to a lack of accurate numerical tools which now have become available through the work presented in this thesis.

Indeed, the refinement algorithm enables us to reach the branching state with sufficient numerical accuracy within a reasonable computational time, and more importantly, within the limits of the computational memory.

First, we here establish that the time of branching converges for identical initial and boundary conditions when using finer and finer numerical grids. Such tests were out of reach up to now. The convergence of branching times allows us now to derive quantitative predictions under given conditions. We find that the branching times converge for sufficiently fine numerical grids both for the under- and the overvolted case. An interesting detail is that in the undervolted case, the branched state is always the same while in the overvolted case, different branched states are reached on different grids after a similar evolution time. This suggests that in the second case, several branched states are accessible from the unstable head state. The outcome of such a nonlinear bifurcation process then will depend on minor details (like the numerical grid) as is well known even to the general public as the unpredictability of "chaos theory".

Another reason not to analyze the details of the branched state is the assumed cylindrical symmetry in our calculations. Within the present thesis, the streamer splits not into branches but into concentric rings as the space of linear perturbations has been restricted to cylinder symmetrical ones. When a larger space of linear perturbations is admitted, the branching instability can be expected after a similar time of evolution, but to a different state. The physically relevant question that can be answered with the present analysis is: can we characterize a generic unstable state of the streamer head that leads to branching? This indeed seems to be the case: numerical experiments in a fixed external electric field with a variety of initial ionization distributions and boundary conditions on the electrode always seem to evolve to a very similar state of the streamer head immediately before branching. This particular head state would then be an intermediate attractor of the dynamics that is followed by branching. However, this hypothesis requires further numerical and analytical studies.

There is another insight that can be gained from the present numerical studies, namely a verification of a reduced model for well developed streamers that is currently being studied analytically at CWI. Such a model for moving ionization boundaries consists of several building blocks: 1) The ionization front at the streamer tip propagates with a velocity that is a function of the electric field ahead of it. 2) The width of the space charge layer is a decreasing function of the electric field and saturates at high fields. 3) The conductivity in the interior of the streamer is so high that it approaches Lozansky and Firsov's limit of ideal conductivity. For the dependence of front velocity and width on the electric field, analytical predictions have been derived for planar fronts. Their validity for curved fronts can be tested on the numerical results. Furthermore, analytical results show that a planar front is dynamically unstable and will branch due to a Laplacian instability, while the analysis of curved fronts is underway. The limit of a planar front is never reached in the simulations, but a limit of small curvature where the radius of curvature of the streamer head is much larger than the front width does occur. Numerical studies do reveal for which curvature the Laplacian instability sets in and are therefore complementary to the analytical

studies.

We conclude that the minimal streamer model analyzed in this thesis already exhibits very complex behavior and is better adapted for explorative systematic studies than a model including many more physical features from the start. The predictions of this model should now be tested on experiments on negative streamers in nitrogen while more features like the less well-known photo-ionization should be included to predict the behavior of streamers in air. Also, the step towards fully three-dimensional simulations should be made.

SAMENVATTING

Het heelal bestaat voor 99% uit geïoniseerde media, zogeheten plasma's. Welbekende voorbeelden van plasma's zijn de zon, een hoge-temperatuur plasma, en neon verlichting, die lage-temperatuur plasma's bevat. Een hoge-temperatuur plasma is in thermisch evenwicht, en wordt aangedreven door hoge druk en hoge temperatuur. Een lage-temperatuur plasma is daarentegen ver van thermisch evenwicht en wordt gegenereerd door elektrische of elektromagnetische velden.

Streamers zijn kortstondige, lage-temperatuur plasmakanalen die zich, onder invloed van het zelf-aangemaakte elektrisch veld aan hun uiteinde, snel voortplanten in een niet of weinig geïoniseerd medium. Ze worden veelvuldig in de industrie gebruikt, bijvoorbeeld voor het reinigen van gassen en water, en in de lucht- en ruimtevaart. Streamers komen ook voor in de natuur, waar ze een rol spelen in de opbouw van bliksem. Recente waarnemingen hebben het bestaan aangetoond van sprites, zeer grote, uit vele streamers opgebouwde elektrische ontladingen in de hogere delen van de atmosfeer. Men onderscheidt streamers al naar gelang hun polariteit. In een *positieve* streamer plant positieve nettolading zich voort in de richting van het elektrisch veld, naar de kathode. In een *negatieve* of anode gerichte streamer daarentegen is het negatieve lading die zich verplaatst in de richting van de elektronendrift, dus in tegengestelde richting van het elektrisch veld.

Experimenten tonen aan dat positieve streamers gemakkelijker vanuit een punt- of draadelektrode ontstaan dan negatieve streamers, die een veel hogere elektrische spanning vergen. Dientengevolge zijn het veelal positieve streamers die gebruikt worden in industriële toepassingen. Echter, wanneer streamers in de vrije ruimte ontstaan vanuit elektronenlawines, hebben ze zowel een positief als een negatief uiteinde. Bliksem en sprites zijn voorbeelden van dergelijke ontladingen. Tot nu toe heeft het experimenteel en theoretisch onderzoek zich vooral gericht op positieve streamers vanwege hun toepassingen. De werkzame doorsneden van foto-ionisatie, die nodig is voor de ontwikkeling van positieve streamers, zijn echter slecht bekend. Om een goed gedefinieerd fysisch beeld te krijgen is het derhalve wenselijk om een situatie te bestuderen die min of meer onafhankelijk is van foto-ionisatie: negatieve streamers in pure gassen. Aan de Technische Universiteit Eindhoven wordt er momenteel gewerkt aan hoogspanningsexperimenten om dergelijke streamers te verkrijgen, in samenwerking met het onderzoeksthema "Niet-lineaire Dynamica en Complexe Systemen" van het Centrum voor Wiskunde en Informatica (CWI) in Amsterdam, waar nu-

meriek en analytisch onderzoek uitgevoerd wordt. Dit proefschrift is geschreven op het CWI en bespreekt voornamelijk een numerieke methode voor het berekenen van negatieve streamers, alsmede een analytisch criterium voor het ontstaan van dergelijke streamers.

Het simuleren van streamers is een grote numerieke uitdaging. Allereerst zijn er verschillende ruimtelijke schalen bij betrokken: het medium waarin de streamer zich voortplant kan vele ordes groter zijn dan het geïoniseerde kanaal, dat op zijn beurt veel groter is dan het kleine actieve gebied in de kop van de streamer, die zelf weer een innerlijke structuur bevat. Bovendien worden de ruimtelijke dichtheidsgradiënten in de kop steeds steiler naarmate de streamer zich verder ontwikkelt, en deze vereisen daarmee een steeds hogere nauwkeurigheid van de numerieke methode. Tenslotte komt er een moeilijkheid bij door de instabiele natuur van streamers: elke geïoniseerde verstoring in het niet-geïoniseerde gebied met hoge veldsterktes net voor de streamer kop zal groeien. De dynamica van de streamer wordt bepaald in dit instabiele gebied, de "leidende zone" (*leading edge* in het Engels), waar de dichtheden zeer laag zijn en de dichtheidsgradiënten derhalve zeer klein. Het ionisatiefront wordt als het ware het niet-geïoniseerde medium ingetrokken door deze leidende zone, en vormt één van de voornaamste oorzaken dat standaard verfijningsmethoden er niet in slagen de streamerdynamica goed weer te geven.

We hebben een numeriek algoritme ontwikkeld dat op efficiënte wijze omgaat met de inherente numerieke moeilijkheden. Het berekent de ontwikkeling van een streamer in een continuümbenadering. Het model bestaat uit continuïteitsvergelijkingen voor de geladen deeltjes, elektronen en positieve ionen in het geval van pure stikstof. Deze continuïteitsvergelijkingen leren ons dat de verandering in de tijd van de deeltjesdichtheden bepaald wordt door hun drift, diffusie en ionisatiebronnen en -putten. De driftsnelheid alsmede de ionisatiecoëfficiënt van de deeltjes worden gegeven door het lokale elektrisch veld. Deze kan berekend worden aan de hand van de zogeheten Poissonvergelijking voor de elektrische potentiaal, waarin de bronterm gegeven wordt door de ruimtelading. Dit model is niet-lineair omdat de deeltjesbeweging en -productie van het elektrisch veld afhangen terwijl het veld van de deeltjesdichtheden afhangt. In het geval van een negatieve streamer in pure stikstof, is het toegestaan ionisatiebronnen zoals foto-ionisatie te verwaarlozen, en de enige bron van geladen deeltjes is dan ionisatie door botsingen van voldoende energetische elektronen met neutrale deeltjes. Deze mechanismen – namelijk de drift en de botsingsionisatie in het lokale elektrisch veld, de diffusie en de ruimteladingseffecten – in een continuümbenadering vormen het zogeheten *minimale streamermodel*, dat in dit proefschrift bestudeerd wordt.

Het algoritme is geïmplementeerd in een driedimensionale geometrie met cylindrische symmetrie, hetgeen de berekeningen effectief naar twee dimensies reduceert. Het algoritme is gebaseerd op een ontkoppeling van de rekenroosters voor de continuïteitsvergelijkingen enerzijds en die voor de Poissonvergelijking anderzijds. Deze roosters worden op elke tijdsstap verfijnd aan de hand van foutmonitoren, waardoor ze zich aanpassen aan de oplossing. De leidende zone wordt expliciet meegenomen in het verfijningscriterium. Het algoritme is met

succes getoetst op zowel vlakke als gekromde ionisatiefronten. Het stelt ons in staat nieuwe gebieden in de parameterruimte te onderzoeken. Het is nu mogelijk om hoge achtergrondvelden in te stellen, waarin de ruimtelijke gradiënten zeer groot worden, en toch de ontwikkeling van de streamer op nauwkeurige wijze te berekenen. We kunnen bovendien ook de ontwikkeling van lange streamers in een laag achtergrondveld volgen. De resultaten van de simulaties tonen in beide gevallen interessante kenmerken.

De simulaties van streamers die uit een enkel elektron ontstaan tussen vlakke, evenwijdige elektrodes, tonen dat er drie fysische fases worden gepasseerd. Een streamer kan worden opgebouwd vanuit een elektronenlawine, die wordt gekenmerkt door de afwezigheid van ruimteladingseffecten en derhalve lineair is. Als de ruimtelading eenmaal sterk genoeg is om het achtergrondveld significant te veranderen, wordt het verschijnsel niet-lineair, en er ontstaat een streamer. Als de afstand tot de anode voldoende lang is, wordt de streamer uiteindelijk instabiel en vertakt zich.

Gedurende de lawinefase driften, diffunderen en reageren de elektronen in het uniforme achtergrondveld. Als de lawine vanuit een enkel elektron begint en het veld homogeen is, heeft de vergelijking voor de elektronen een analytische oplossing, die gebruikt kan worden om analytische uitdrukkingen te bepalen voor de ruimtelijke momenten van de ionen. Dit stelt ons in staat om een analytische benadering te vinden voor het elektrisch veld, en daarmee het tijdstip te bepalen waarop de ruimteladingseffecten zo sterk worden, dat de overgang naar de streamer plaatsvindt. We hebben hiermee een criterium afgeleid voor de overgang van lawine naar streamer, waarin rekening is gehouden met de diffusie. Het traditionele overgangscriterium, Meek's criterium, stelt dat, in een bepaald gas bij een bepaalde druk, de voortplantingsafstand van een lawine tot het moment van overgang naar streamer uitsluitend afhankelijk is van het opgelegde achtergrond elektrisch veld. Het in acht nemen van diffusie toont echter dat dit niet het geval is, en dat diffusie de overgang naar streamer in feite aanzienlijk kan vertragen.

Als de streamer eenmaal is ontstaan, is de ontwikkeling niet-lineair. De roosterverfijningsmethode verschaft ons dan een krachtig instrument om de verdere ontwikkeling van de streamer te berekenen. De streamer wordt gekenmerkt door de vergrote geleiding van het kanaal, die dientengevolge gedeeltelijk afgeschermd wordt van het achtergrond elektrisch veld. Deze afscherming vereist een ruimteladingsschil aan het uiteinde van de streamer, die op zijn beurt het elektrisch veld vlak voor de streamerkop versterkt. De streamer groeit in dit zelf-aangemaakte veld.

We hebben de streamerontwikkeling en -vertakking in zowel onder- als overvoltages bestudeerd. Deze onderscheiden zich door de mogelijkheid van het achtergrondveld om een elektron al dan niet voldoende energie te verschaffen om botsingsionisatie te veroorzaken. In het geval van overvoltage is het achtergrondveld zo sterk dat dit wel het geval is, en de streamer plant zich in dit geval in een zeer instabiele toestand voort. De diameter van de streamer blijft dan groeien tot het moment van vertakking, en de streamer is kegelvormig. Bovendien worden de ruimtelijke dischtheidsgradiënten zeer groot, en vereisen dientengevolge

een grote nauwkeurigheid van de numerieke methode. Bij ondervoltage daarentegen vermenigvuldigen de elektronen zich alleen in een klein gebied voor de streamerkop waar het veld voldoende versterkt is, en de streamer wordt daardoor eerder draadvormig. Om een afdoende veldversterking te bewerkstelligen dient er voldoende ruimtelading aanwezig te zijn in de streamerkop. De accumulatie van lading in de kop hangt zowel af van de ionisatieverdeling aan het begin als van de randvoorwaarden op de elektrode.

We bestuderen verscheidene gevallen, en in alle gevallen vertakt de streamer zich, mits de afstand tussen de elektrodes voldoende lang is. De vertakkende toestand van streamers is tot dusver niet veel bestudeerd, voornamelijk door het gebrek aan nauwkeurige numerieke middelen, die dankzij het in dit proefschrift beschreven werk nu wel beschikbaar zijn. Het verfijningsalgoritme stelt ons inderdaad in staat om de vertakkende toestand met voldoende numerieke nauwkeurigheid, binnen een redelijke rekentijd en, wat belangrijker is, binnen de grenzen van het rekengeheugen, te bereiken.

Allereerst stellen we vast dat het tijdstip van vertakken convergeert voor gelijke begin- en randvoorwaarden wanneer steeds fijnere numerieke roosters worden gebruikt. Zulke tests waren tot dusver buiten handbereik. De convergentie van het vertakkingstijdstip stelt ons in staat om kwantitatieve voorspellingen voor gegeven omstandigheden af te leiden. We zien dat de vertakkingstijdstippen convergeren voor voldoende fijne rekenroosters in zowel over- als ondervoltages. Een interessant detail is dat in het geval van ondervoltage, de vertakkingstoestand altijd dezelfde is, terwijl bij overvoltage verschillende vertakkingstoestanden worden bereikt op verschillende roosters na vergelijkbare ontwikkelingstijden. Dit suggereert dat in het tweede geval meerdere vertakkingstoestanden toegankelijk zijn vanuit de instabiele toestand van de streamerkop. De uitkomst van een dergelijk niet-lineair bifurcatieproces zal dan afhangen van kleine details (zoals het numerieke rooster), hetgeen zelfs bij een algemeen publiek bekend staat als de onvoorspelbaarheid van de "chaostheorie".

Een andere rede voor het niet bestuderen van de details van de vertakkingstoestand is de veronderstelling van cylindrische symmetrie in onze berekeningen. In dit proefschrift splitsen de streamers zich niet in takken maar in concentrische ringen, aangezien de ruimte van lineaire verstoringen beperkt is tot cylindrisch symmetrische verstoringen. Wanneer een grotere ruimte van lineaire verstoringen wordt toegestaan, kan de vertakkende instabiliteit na een vergelijkbare ontwikkelingstijd, maar in een verschillende toestand, worden verwacht. De fysisch relevante vraag die beantwoord kan worden met de huidige analyse is: kunnen we een algemene instabiele toestand van de streamerkop karakteriseren die tot vertakken leidt? Dit lijkt inderdaad het geval te zijn: numerieke experimenten in een bepaald achtergrondveld met een verscheidenheid aan beginionisatieverdelingen en randvoorwaarden op de elektrode lijken zich altijd te ontwikkelen naar een zeer vergelijkbare toestand van de streamerkop vlak voor het vertakken. Deze specifieke toestand van de kop zou dan een tussenliggende attractor zijn voor de dynamica die gevolgd wordt door vertakking. Deze hypothese vraagt echter om nader numeriek en analytisch onderzoek.

Een ander inzicht kan worden verkregen vanuit dit numeriek onderzoek,

namelijk de bevestiging van een gereduceerd model voor goed ontwikkelde streamers dat momenteel analytisch wordt onderzocht op het CWI. Een dergelijk model voor bewegende ionisatiegrensvlakken bestaat uit verschillende blokken: 1) Het ionisatiefront aan het uiteinde van de streamer plant zich voort met een snelheid die een functie is van het electrisch veld ervoor. 2) De dikte van de ruimteladingsschil is een afnemende functie van het electrisch veld en convergeert in hoge velden. 3) De geleiding in het binnenste van de streamer is zo hoog dat het Firsov en Lozansky's limiet van ideale geleiding benadert. Voor de veldafhankelijkheid van de frontsnelheid en -dikte zijn analytische voorspellingen gedaan voor vlakke fronten. Hun geldigheid voor kromme fronten kan worden nagegaan aan de hand van numerieke resultaten. Bovendien tonen analytische resultaten aan dat een vlak front dynamisch instabiel is en zal vertakken door een Laplaciaanse instabiliteit, terwijl de analyse voor kromme fronten onderweg is. De limiet van een vlak front wordt nooit bereikt in de simulaties, maar een limiet van kleine kromming waarin de krommingsstraal van de streamerkop veel groter is dan de dikte van het front komt wel degelijk voor. Numerieke simulaties wijzen uit voor welke kromming de Laplaciaanse instabiliteit optreedt, en zijn daardoor complementair aan het analytisch onderzoek.

We concluderen dat het in dit proefschrift bestudeerde minimale streamermodel al een zeer complex gedrag vertoont en beter geschikt is voor systematisch onderzoek dan een model dat vanaf het begin veel meer fysische onderdelen bevat. De voorspellingen van dit model zouden nu getoetst moeten worden aan de hand van experimenten op negatieve streamers in stikstof, terwijl meer fysische mechanismen zoals de minder goed bekende foto-ionisatie dienen worden inbegrepen om het gedrag van streamers in lucht te voorspellen. Ook zouden er stappen ondernomen moeten worden naar complete driedimenionsale simulaties.

RÉSUMÉ

Un plasma est un milieu ionisé, constituant 99% de l'univers. Des exemples bien connus de plasmas sont le soleil, lequel est un plasma chaud, et les tubes fluorescents, qui contiennent un plasma non-thermique. Un plasma chaud est en équilibre thermique et est engendré par de hautes pressions et températures. Un plasma froid est, au contraire, loin d'être en équilibre thermique et est généré par un champ électrique ou électromagnétique.

Un streamer est un canal de plasma non-thermique et éphémère lequel, en amplifiant lui-même le champ électrique à son extrémité, se propage à haute vitesse dans un milieu peu ou non-ionisé. Les applications industrielles des streamers sont répandues, par exemple, pour le traitement de gaz d'échappement et d'eau polluée, et dans l'ingénierie aérospatiale. Les streamers existent également dans la nature, où ils jouent un rôle dans la création de la trajectoire des éclairs. De récentes observations ont montré l'existence de sprites, de très grandes décharges électriques dans les hautes régions de l'atmosphère composées d'une multitude de streamers. On distingue les streamers par leur polarité : dans un streamer *positif*, une charge d'espace positive se déplace dans la direction du champ électrique, vers la cathode. Dans un streamer *négatif*, c'est une charge d'espace négative qui se déplace dans la direction d'advection des électrons, c'est-à-dire dans le sens opposé au champ électrique, vers l'anode.

Il a été démontré expérimentalement que les streamers positifs émergent plus aisément d'une électrode de type pointe ou fil que les streamers négatifs, qui nécéssitent un voltage beaucoup plus élevé. Par conséquent, les applications industrielles se concentrent principalement sur les streamers positifs. D'autre part, lorsqu'un streamer émerge d'une avalanche d'électrons dans l'espace, il possède aussi bien une extrémité positive qu'une extrémité négative. Les éclairs ainsi que les sprites sont des exemples de telles décharges. Jusqu'à présent la plupart des efforts expérimentaux et théoriques ont été consacrés aux streamers positifs en raison de leurs applications. Cependant, les sections efficaces de la photoionisation, laquelle est nécéssaire pour la propagation des streamers positifs, ne sont pas bien connues. Afin de former une image physique bien définie, il est souhaitable d'étudier une situation plus ou moins indépendente de la photoionisation : les streamers négatifs dans des gaz purs. Des expériences à haute tension sont actuellement en cours d'installation à l'Université de Technologie d'Eindhoven, en collaboration avec le thème de recherche "Dynamique Nonlinéaire et Systèmes Complexes" du Centre national de recherche Mathématique

et Informatique (CWI) à Amsterdam, où la recherche se concentre sur le calcul numérique ainsi que sur l'analyse mathématique du problème. Cette thèse a été écrite au CWI, et traite principalement d'une méthode numérique pour la simulation de streamers négatifs ainsi qu'un critère analytique pour l'émergence de ces streamers.

La simulation de streamers présente un grand défi numérique. Tout d'abord, de multiples échelles spatiales sont impliquées : le milieu peu ou non-ionisé dans lequel le streamer se déplace est des ordres de grandeur plus étendu que le canal ionisé, qui à son tour est beaucoup plus grand que la petite région active dans la tête du streamer, laquelle possède elle aussi une structure interne. De plus, au cours de la propagation, les gradients de densité spatiaux dans la tête du streamer deviennent de plus en plus importants, et demandent par conséquent une précision croissante de la méthode numérique. Finalement, une difficulté numérique supplémentaire vient de la nature instable des streamers : une perturbation ionisée dans la région non-ionisée au devant de la tête du streamer, où le champ électrique est amplifié, se développera aussi petite soit-elle au départ. La dynamique du streamer est déterminée dans cette région instable, la "zone dominante" (*leading edge* en anglais), où les densités sont très basses et où les gradients de densité spatiaux sont donc faibles. Le front d'ionisation est en quelque sorte tiré dans le médium non-ionisé par la zone dominante, ce qui est une des principales raisons pour laquelle les stratégies courantes de raffinement de maillage ne sont pas aptes à capturer de manière adéquate la dynamique des streamers.

Nous avons développé un algorithme qui traite de manière efficace les difficultés numériques inhérentes à ce problème. Il calcule l'évolution d'un streamer dans une approximation fluide. Ce modèle est basé sur les équations de continuité pour les particules chargées, c'est-à-dire électrons et ions positifs dans le cas de l'azote pur. Ces équations de continuité décrivent le changement temporel des particules chargées en fonction de leur advection et diffusion ainsi que des sources et pertes d'ionisation. La vitesse d'advection ainsi que le taux de réaction sont fixés par le champ électrique, lequel est prescrit par l'équation de Poisson pour le potentiel électrique, et dont le terme source est donné par la charge d'espace. Ce modèle est non-linéaire, puisque le mouvement et la production des particules chargées dépendent du champ électrique alors que le champ dépend des densités de particules chargées. Dans le cas des streamers négatifs dans de l'azote, il est permis de négliger des sources d'ionisation telles que la photoionisation, et la seule source de particules chargées vient dans ce cas de l'ionisation due aux collisions d'électrons suffisamment énergétiques avec des particules neutres. Ces méchanismes – c'est-à-dire l'advection et l'ionisation collisionnelle dans le champ électrique local, la diffusion en les effets de charge d'espace – dans une approximation fluide constituent ce que l'on appelle le *modèle minimal des streamers*. Ce modèle est étudié dans cette thèse.

L'algorithme est implémenté dans une géométrie à trois dimensions avec une symétrie cylindrique, ce qui réduit donc les calculs à deux dimensions. L'algorithme est basé sur un découplage des maillages pour les équations de continuité d'une part, et pour l'équation de Poisson d'autre part. Les maillages sont raf-

finés à chaque pas de temps, suivant des moniteurs d'erreur, s'adaptant ainsi à la solution. La zone dominante est inclue explicitement dans le critère de raffinement. Des tests ont été effectués avec succès, aussi bien sur des fronts d'ionisation plans que courbes. Cet algorithme nous permet d'explorer un nouveau régime pour les paramètres. Il est maintenant possible d'appliquer de très forts champs électriques, dans lesquels les gradients spatiaux peuvent devenir très importants, tout en obtenant une résolution suffisante. Nous pouvons maintenant également calculer l'évolution d'un streamer dans un grand domaine spatial sous influence d'un champ relativement faible. Les résultats des simulations montrent des caractéristiques intéressantes dans les deux cas.

Durant son évolution, un streamer émanant d'un seul électron entre deux électrodes planes et parallèles passe par trois stades physiques. Un streamer peut émerger d'une avalanche d'électrons, charactérisée par l'absence d'effets de charge d'espace; cette phase est donc linéaire. Une fois que le taux de charge d'espace est suffisant pour changer de manière significative le champ électrique externe, le phénomène devient non-linéaire, et le streamer apparaît. Si la distance jusqu'à l'anode est suffisante, le streamer finalement devient instable, et se ramifie.

Durant l'avalanche, les électrons advectent, diffusent et se multiplient dans le champ électrique externe uniforme. Si l'avalanche commence depuis un seul électron, et si le champ électrique est homogène, l'équation pour les électrons a une solution analytique qui peut être utilisée pour déduire des expressions analytiques pour les moments spatiaux de la distribution de densité d'ions. Ceci nous permet de trouver des approximations analytiques pour le champ électrique, et de déterminer ainsi le moment auquel les effets de charge d'espace deviennent si forts que la transition au streamer a lieu. Nous avons ainsi dérivé un critère pour la transition d'une avalanche vers un streamer, dans laquelle est inclu l'effet de diffusion. Le critère traditionnel pour la transition, le critère de Meek, postule que, dans un certain gaz à une certaine pression, la distance parcourue par une avalanche avant de se transformer en streamer dépend uniquement du champ électrique appliqué. L'inclusion de la diffusion montre que ceci n'est pas le cas, et que la diffusion peut en fait retarder considérablement l'apparition du streamer.

Une fois que le streamer se forme, l'évolution devient non-linéaire. A ce stade, notre stratégie de raffinement de maillage nous offre un puissant outil pour calculer l'évolution du streamer. Le streamer est caractérisé par la conductivité rehaussée du canal, qui est par conséquent partiellement protégé du champ électrique extérieur. Ceci nécéssite une couche de charge d'espace à l'extrémité du streamer, qui à son tour amplifie le champ electrique au devant de la tête du streamer. Le streamer s'étend dans ce champ auto-amplifié.

Nous avons étudié l'évolution et la ramification des streamers aussi bien avec une soustension qu'avec une surtension. Ces cas se distinguent par l'aptitude du champ électrique à donner suffisamment d'énergie à un électron pour que celui-ci puisse ioniser par impact une particule neutre. Dans un milieu soumis à une surtension, le champ électrique est si intense que ce scénario se produit, et le streamer évolue alors vers un état hautement instable. Son diamètre continue

à croître jusqu'au moment de la ramification, lui donnant une forme conique. De plus, les gradients de densité spatiaux deviennent extrêment importants, demandant de ce fait une grande précision du schéma numérique. Dans un milieu soumis à une soustension, les électrons ne peuvent se multiplier que dans une région où le champ électrique est suffisamment amplifié, et le streamer devient plutôt filamenteux. Une amplification suffisante du champ nécessite une charge suffisante dans la tête du streamer. L'accumulation de charge dans cette tête dépend aussi bien de la distribution d'ionisation initiale que des conditions aux limites aux électrodes.

Nous avons étudié de différentes situations, et dans tous les cas les streamers se ramifient à condition que la distance entre les électrodes soit suffisamment grande. La ramification des streamers n'a pas bien été analysée jusqu'à présent. Cela était principalement dû à un manque d'outils numériques précis, qui sont maintenant à notre déposition grâce aux travaux reportés dans cette thèse. En effet, l'algorithme de raffinement de maillage nous permet de décrire la ramification avec une précision suffisante, tout en utilisant un temps de calcul raisonnable et, surtout, dans les limites de la mémoire numérique.

Nous montrons que le temps de branchement converge pour des conditions initiales et aux limites identiques lorsque des maillages de plus en plus fins sont utilisés. De tels tests étaient hors d'atteinte jusqu'à présent. La convergence des temps de branchement nous permet d'obtenir des prédictions quantitatives pour des conditions données. Nous trouvons que les temps de branchement convergent sur des maillages suffisamment fins aussi bien dans le cas de soustension que de surtension. Un détail intéressant est que dans les cas de soustension, l'état de ramification est toujours le même alors que dans le cas de surtension, des ramifications différentes sont obtenues sur différents maillages après un temps d'évolution similaire. Ceci suggère que dans le deuxième cas, plusieurs états de ramifications sont accessibles depuis l'état instable de la tête du streamer. Le résultat d'un tel processus de bifurcation non-linéaire dépendra alors de détails mineurs (tels que le maillage) et est connu, même du grand public, comme l'imprévisibilité de la "théorie du chaos".

La raison pour laquelle l'état de ramification n'est pas analysée en détail est que nous avons utilisé une symétrie cylindrique dans nos calculs. Il y a une autre raison pour ne pas analyser en détail l'état de la ramification, et ceci est l'hypothèse de symétrie cylindrique dans nos calculs. Dans cette thèse, le streamer ne se divise pas en branches, mais en anneaux concentriques puisque l'espace de perturbations linéaires est restreint aux perturbations cylindriquement symétriques. Lorsqu'un plus grand espace de perturbations linéaires est admis, l'instabilité annoncée par les ramification peut survenir après un temps d'évolution similaire, mais dans un état différent. Une question importante physiquement est : pouvons-nous caractériser un état instable générique de la tête du streamer conduisant à une ramification? Une réponse peut être donnée grâce à la présente analyse : des expériences numériques dans un champ électrique externe fixe avec une variété de distributions d'ionisation initiales et de conditions aux limites aux électrodes semblent toujours évoluer vers un état très similaire de la tête du streamer immédiatement avant la ramification. Cet

état spécifique de la tête serait alors un attracteur intermédiaire de la dynamique suivi d'une ramification. Cependant, cette hypothèse nécessite de plus amples études numériques et analytiques.

La présente étude numérique peut également servir un autre but, à savoir la vérification d'un modèle réduit pour des streamers bien développés, actuellement étudié analytiquement au CWI. Un tel modèle pour des fronts d'ionisation en mouvement comprend plusieurs parties : 1) Le front d'ionisation à la tête du streamer se propage à une vitesse qui est une fonction de champs électrique à son extrémité. 2) L'épaisseur de la couche de charge d'espace est une fonction décroissante du champ électrique et sature pour de forts champs. 3) La conductivité à l'intérieur du streamer est tellement haute qu'elle approche la limite de conductivité idéale de Firsov et Lozansky. Pour la description de la vitesse et de l'épaisseur du front en fonction du champ électrique, des prédictions analytiques ont été dérivées pour des fronts plans. Leur validité pour des fronts courbes peut être vérifiée à l'aide des résultats numériques. De plus, des résultats analytiques montrent qu'un front planaire est dynamiquement instable et se ramifiera à cause d'une instabilité Laplacienne, alors que l'analyse pour des fronts courbes est en cours de traitement. La limite de front plan n'est jamais atteinte dans les simulations, mais la limite de petite courbure, où le rayon de courbure de la tête du streamer est beaucoup plus grand que l'épaisseur de front, elle est obtenue. Les études numériques révèlent pour quelle courbure l'instabilité Laplacienne se développe, et sont par conséquent complémentaires aux études analytiques.

Nous concluons que le modèle minimal des streamers analysé dans cette thèse montre déjà un comportement complexe et qu'il est mieux adapté pour des études systématiques qu'un modèle comprenant dès le début davantage de méchanismes physiques. Les prédictions de ce modèle devraient maintenant être comparées à des expériences sur des streamers négatifs dans de l'azote, et d'autres méchanismes, tels que la photoionisation, doivent être inclus pour prédire le comportement des streamers dans de l'air. Finalement, on doit s'orienter vers des simulations à trois dimensions.

ACKNOWLEDGEMENTS

Eindelijk is het dan zover, de laatste correcties zijn doorgevoerd, en het is hoog tijd om alle personen te bedanken die het voltooien (ja nu mag ik het zeggen!) van dit proefschrift hebben mogelijk gemaakt. Zonder hun hulp en steun was ik deze veelal leuke maar soms ook moeizame tijd niet zo voorspoedig doorgekomen.

Allereerst wil ik mijn grote dank betuigen aan mijn promotor, Ute Ebert, en aan mijn copromotor, Willem Hundsdorfer, voor hun inspirerende begeleiding en het nimmer aflatende geduld dat ze hebben getoond. Zonder al hun hulp – zowel op het wetenschappelijk als op het persoonlijk vlak – hun peptalks en hun af en toe strenge doch rechtvaardige woorden, had ik nu niet met zoveel plezier teruggekeken naar de afgelopen vier jaar waarin dit proefschrift tot stand is gekomen.

In het bijzonder wil ik Ute heel erg hartelijk danken voor alle moeite die ze heeft genomen voor het doorlezen van de verschillende versies van dit proefschrift (niet zelden tot in de vroege uurtjes!). Onze discussies zijn voor mij uitermate leerzaam geweest, en ik heb dankzij haar grondige correcties en duidelijke aanwijzingen met zeer veel plezier aan het voltooien van dit proefschrift gewerkt. Inderdaad, schrijven is een ding, maar goed schrijven is iets volstrekt anders, of het nou om een proefschrift of een computerprogramma gaat.

Het schrijven van de code die in dit proefschrift beschreven staat was een essentieel deel van het onderzoek, en mijn grote dank gaat uit naar Willem voor alle hulp en goede raad, evenals voor de zorg waarmee hij het numerieke gedeelte van dit proefschrift heeft gelezen. Ik heb zeer veel genoten van onze samenwerking, en dankzij hem kijk ik met veel plezier terug naar de tijd van het programmeren, dat – het moet gezegd worden – toch niet altijd even gemakkelijk ging mijnerzijds.

Wat betreft het schrijven van het computerprogramma, wil ik Jeroen Wackers bedanken voor zijn bijdrage aan de Poisson solver. Dit essentiele deel van het programmeerwerk is door hem op zeer snelle en goede wijze volbracht, zonder zijn hulp had het nóg langer geduurd om de code af te krijgen.

Mijn dank gaat ook uit naar de leden van de kern-commissie, prof. dr. ir. G.M.W. Kroesen, voor de aandacht waarmee hij mijn proefschrift heeft gelezen, prof. dr. J.G. Verwer en prof. dr. ir. B. Koren voor de interesse die ze hebben getoond in het onderzoek. I am honored and very grateful that prof. J.-P. Boeuf has agreed to be member of the thesis committee.

Graag wil ik ook Eddie van Veldhuizen, Tanja Briels en Hans Wienands van de Technische Universiteit Eindhoven bedanken voor de bijeenkomsten waarbij ik veel heb geleerd over "echte" streamers en de rondleidingen door het lab, en de mensen van EPG en ETP van de faculteit Technische Natuurkunde voor de leuke conferenties.

Verder ben ik ook dank verschuldigd aan NWO, die dit onderzoek financieel mogelijk heeft gemaakt. Dit project maakte deel uit van het onderzoeksprogramma "Computational Science", en ik heb met veel plezier de programmabijeenkomsten bezocht.

Ook gaat mijn dank uit naar het Centrum voor Wiskunde en Informatica, dat me een zeer aangename werkplek evenals een uitmuntende infrastructuur heeft geboden. Het verrichten van een promotieonderzoek kan een tamelijk eenzaam proces zijn, en de praatjes met de collega's van het CWI waren voor mij dan ook een vaak welkome afleiding. In het bijzonder wil ik mijn kamergenoten bedanken: Bob, voor de gezelligheid op de vroege morgen en het goede voorbeeld van hoe je niet gestressed de laatste maanden van het schrijven kunt doorbrengen; Jeroen, die naast een uitmuntend onderzoeker ook nog eens een leuke kamergenoot bleek te zijn; Maksat and Chao, for whom I guess I must not always have been a very nice roommate during the last months, but who were always there to have a laugh or a chat with; Ignacio, for his somewhat timid cheerfulness. Mijn dank gaat verder uit naar iedereen die de lunches, de wandelingen door de gang richting koffieautomaat of printer, of de rookpauzes altijd zo gezellig hebben gemaakt: Johannes, Mervyn, Mark, Danijela, Andrea, Anton, Ismail, Nada, Suzanne, Jason, Ben, Bernard, Arjen, Maciej, Marc, Nga, Peter, Alejandro, Laura, Stefan... A special thank to Fabian for his suggestions for the french version of the summary. Ook wil ik Daniel bedanken voor al zijn hulp als de computer weer eens niet naar me wilde luisteren, Jos voor het bewerken van vele plaatjes in dit proefschrift, en natuurlijk ook Rick en Joke, dankzij hen voelde ik me niet helemaal alleen als Feyenoorder in Amsterdam.

Aan al mijn vrienden die mijn avonden en weekenden zo rijkelijk gevuld hebben: dank jullie wel voor de bijzondere gesprekken, de steun in moeilijke tijden, de gekke feesten, maar vooral, simpelweg jullie vriendschap. In het bijzonder wil ik noemen Maartje, omdat ze er altijd is als het écht nodig is, Sjakie, voor de gezellige etentjes, Majo en Mei Lian, mijn paranimfen, voor het digitale geklets en de leuke avonden en nachten, Mike en Stef, die zo lief waren mij hun meisjes te lenen, Lucas, voor de gekke gesprekken, Bemmel, voor je uitgesproken mening en de soms heftige discussies, en Jill en Patrick, proost! Een speciale gedachte gaat uit naar Gerda die me, in de korte tijd dat ik haar heb mogen kennen, zo ontiegelijk veel heeft geleerd.

Als laatste maar zeker niet de minste, wil ik mijn ouders bedanken voor al hun liefde en vertrouwen. Hien en Jan, jullie hebben ervoor gezorgd dat ik zover kon komen. En natuurlijk mijn lieve Dico, voor je lessen in stoïcisme (go with the flow...), je geduld als het me weer eens niet lukte die lessen te volgen, maar vooral voor de heerlijke tijd die ik elke dag weer met jou doorbreng.

Haarlem, 27 Oktober 2005.

Curriculum Vitae

Carolynne Montijn was born on August 31st, 1977 in Fréjus, France. She received her secondary education at the Lycée Jean Moulin in Draguignan, France, and passed her final exam (baccalauréat) in 1994. She pursued her education at the Delft University of Technology in The Netherlands, where she studied Applied Physics. In 1999 she stayed for 6 months at the École Polytechnique in Palaiseau, France, including a scientific internship at the Laboratoire d'Hydrodynamique. She graduated in 2001 at the Laboratory for Aero and Hydrodynamics of the Delft University of Technology. The title of her Master's thesis is "Numerical simulation of the acoustic field of a turbulent, low-speed jet".

This thesis is the result of her PhD-research, which she carried out from 2001 to 2005 at the national research institute for Mathematics and Computer Science (CWI) in Amsterdam, The Netherlands. This research was part of the program "Computational Science" of the Netherlands Organisation for Scientfic Research (NWO). It was conducted under the supervision of prof.dr. U. Ebert and dr. W. Hundsdorfer.

STELLINGEN

behorende bij het proefschrift

Evolution of Negative Streamers in Nitrogen: a Numerical Investigation on Adaptive Grids

door

Carolynne-Sireeh Montijn

1. De overgang van lawine naar streamer is niet alleen afhankelijk van het opgelegde electrisch veld, maar ook van de diffusiecoëfficient van het gas. [Hoofdstuk 5]

2. Bij overvoltage groeit een streamer continu in de radiële richting. Daarentegen ondergaan streamers bij ondervoltage een fase van contractie na een initiële diffusieve expansie fase. [Hoofdstuk 6]

3. De benodigde ruimtelijke nauwkeurigheid voor het simuleren van negatieve streamers in een gegeven achtergrond electrisch veld kan vooraf bepaald worden: ze zou zodanig moeten zijn dat de botsingsionisatie- en afschermingslengte, in een veld dat viermaal zo sterk is als het achtergrondveld, goed kunnen worden weergegeven. [Hoofdstuk 6, Vgl. (6.6.1)]

4. Vertakkende streamers zijn niet het gevolg van een numerieke, maar van een fysische "Laplaciaanse" instabiliteit. [Hoofdstuk 7]

5. Een nadeel van experimenteel onderzoek is dat het moeilijk is fysische processen uit te schakelen. Een nadeel van analytisch onderzoek is dat het juist moeilijk is meer fysische processen in te schakelen. Numerieke simulaties maken het mogelijk deze kloof te overbruggen.

6. Een goed wetenschapper is niet alleen in staat tot het beantwoorden, maar ook, en vooral, tot het stellen van de goede vragen.

7. Het is niet zozeer te vrezen dat computers even intelligent worden als de mens, maar dat de mens even dom wordt als computers.

8. Een eenvoudige manier om een numeriek wiskundige van een "computational scientist" te onderscheiden is de hoeveelheid data die ze genereren te beschouwen.

9. Het doorgeven van (wetenschappelijke) kennis wordt vaak onderschat in vergelijking met het vergaren ervan.

10. Tegenslagen zijn een noodzakelijke, maar niet voldoende voorwaarde voor mensen om hun geluk op prijs te kunnen stellen.

11. Het is opmerkelijk dat de mens altijd zekerheid lijkt te zoeken, maar dat zijn grootste angst voortkomt uit de enige zekerheid die men heeft, namelijk de dood.

1. The avalanche to streamer transition does not only depend on the applied electric field, but also on the diffusion coefficient of the gas. [Chapter 5]

2. In overvolted gaps, streamers always grow radially. In contrast, streamers in undervolted gaps undergo a phase of contraction after the initial diffusive expansion phase. [Chapter 6]

3. The required spatial accuracy for the simulation of negative streamers in a given background electric field can be determined a priori: it should be such that the impact ionization and screening lengths in an electric field, which is four times stronger than the background value, can be well captured. [Chapter 6, Eq. (6.6.1)]

4. Branching negative streamers are not a result of a numerical, but of a physical "Laplacian" instability. [Chapter 7]

5. A disadvantage of experimental studies is that it is difficult to exclude physical processes. A disadvantage of analytical ones is that it is difficult to include more of them. Numerical simulations make it possible to bridge this gap.

6. A good scientist not only answers questions, but also – and especially – identifies the relevant ones.

7. We should not fear that computers get smarter than human beings, but rather that human beings become as stupid as computers.

8. An easy way to distinguish a numerical mathematician from a computational scientist is to consider the amount of data they create.

9. The importance of transferring (scientific) knowledge is often underestimated compared to that of gathering it.

10. Setbacks are a necessary but not sufficient condition for people to be able to appreciate their luck.

11. It is remarkable that mankind always seems to seek certainty, but that its biggest fear comes from the only certainty one has, namely death.

Evolution of Negative Streamers in Nitrogen: a Numerical Investigation on Adaptive Grids

Colorfigures

Carolynne Montijn

CONTENTS

3

An adaptive grid strategy for streamer simulations

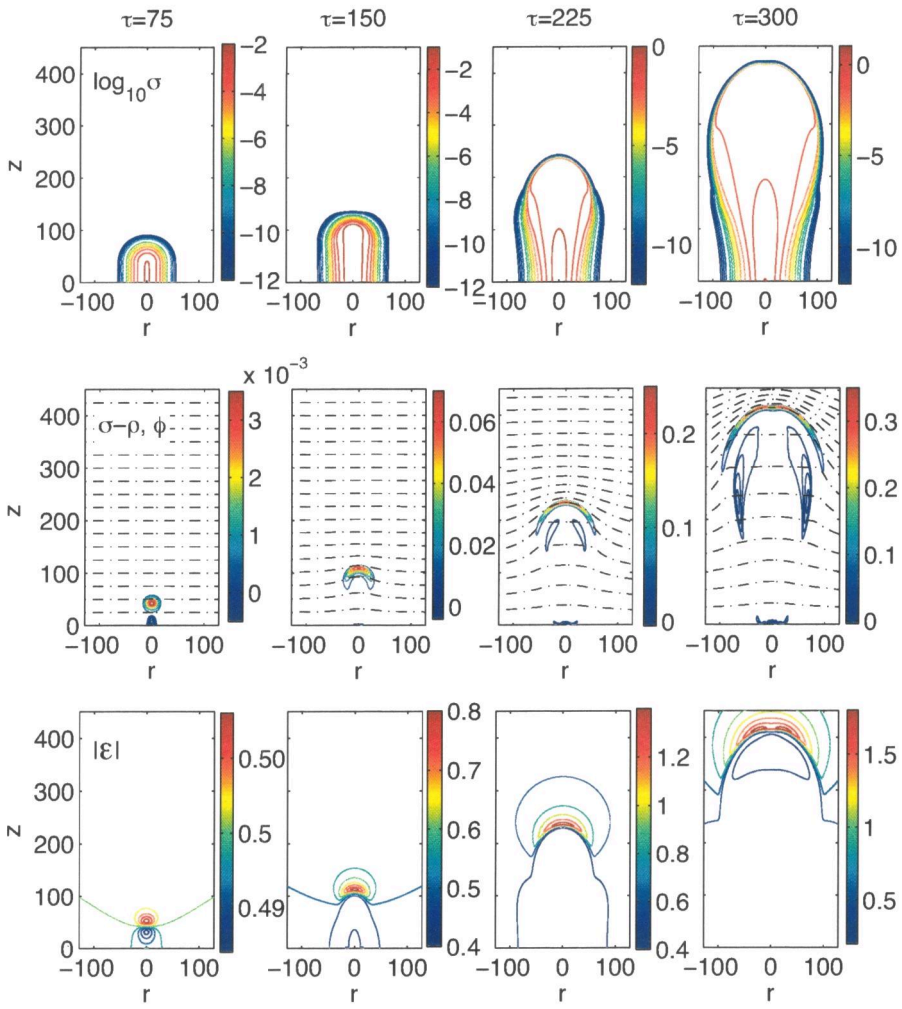

FIGURE 3.14: Propagation of a Gaussian ionization seed as given by Eq.(3.4.1) in a background field $|\mathcal{E}_b| = 0.5$. The snapshots correspond to times τ=75, 150, 225 and 300. *Upper row*: the logarithm of the electron density σ. *Middle row*: the net charge density $\sigma - \rho$. *Lower row*: the electric field strength $|\mathcal{E}|$. The grid covers the region where the particles densities are strictly positive, which is up to $z \approx 450$ for $\tau = 75$.

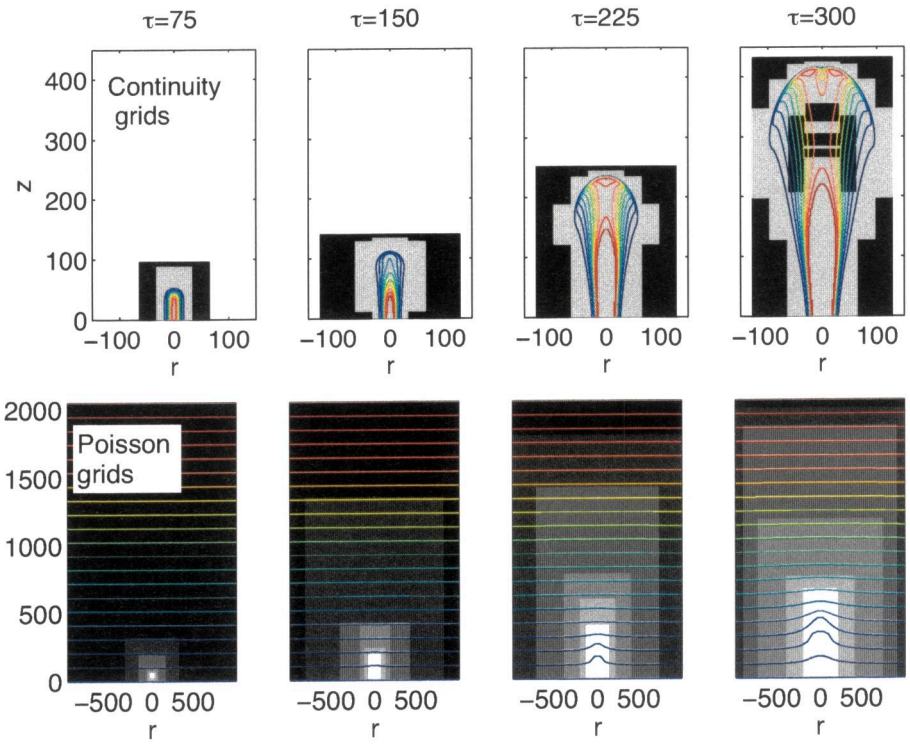

FIGURE 3.17: Grid distributions for the continuity equations (upper row), and for the Poisson equation (lower row). The times are the same as in Fig. 3.15. For the continuity grids, the black and gray regions are covered with grids with mesh sizes $\Delta r = \Delta z$ =2 and 1, respectively. The coarsest grid for the continuity equations only covers the domain on which the particles are above the continuum threshold. The two coarsest grids ($\Delta r = \Delta z$ =128 and 64) on which the Poisson equation has been solved cover the whole computational domain, which is filled in black. The finer grids with mesh sizes 32, 16, 8, 4 and 2 are plotted in lighter gray shades, the white domain is covered by the finest grid $\Delta r = \Delta z$ =1. Notice that the plots cover different spatial regions in the upper and the lower row.

4

The physical stages of streamer propagation

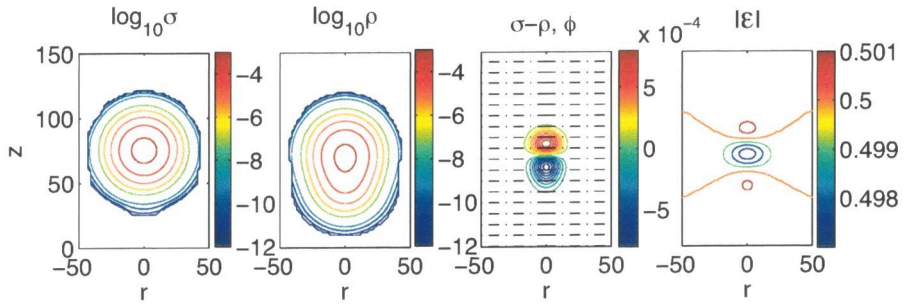

FIGURE 4.1: Avalanche regime at high fields (case (H), $|\boldsymbol{\mathcal{E}}_b| = 0.5$). *From left to right*: logarithmic plot of the electron density distribution, logarithmic plot of the ion density distribution, net charge density distribution together with the equipotential lines (dash dotted lines), and electric field strength. The time of the snapshot is $\tau = 50$, which corresponds to 0.15ns for N_2 at atmospheric pressure.

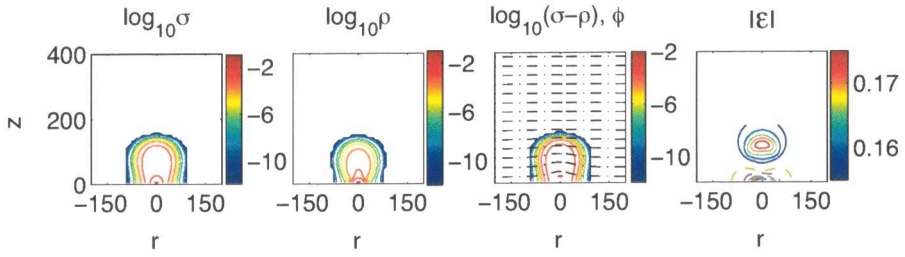

FIGURE 4.3: Initial stage of the streamer propagation at low fields (case (L), $|\boldsymbol{\mathcal{E}}_b| = 0.15$). *From left to right*: logarithmic plot of the electron density distribution, logarithmic plot of the ion density distribution, logarithmic plot of the net charge density distribution together with the equipotential lines (dash dotted lines), and electric field strength. The time of the snapshot is $\tau = 500$, which corresponds to 3 ns for N_2 at atmospheric pressure. The net charge density is shown on the logarithmic rather than the linear scale because of the high space charges near the anode, which would prevent us from plotting adequately the net charge density on a linear scale.

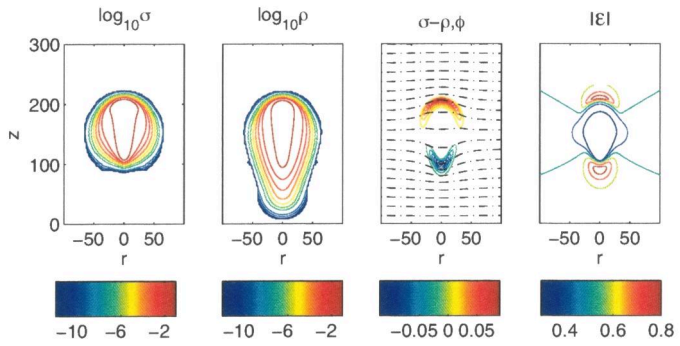

FIGURE 4.5: The non-linear regime for the high field case ($|\boldsymbol{\mathcal{E}}_b| = 0.5$) with Dirichlet boundary conditions at the cathode ($z = 0$). *From left to right*: logarithmic plot of the electron density distribution, logarithmic plot of the ion density distribution, net charge density distribution together with the equipotential lines (dash dotted lines), and electric field strength. The time of the snapshot is $\tau = 200$, which corresponds to 0.6ns for N_2 at atmospheric pressure.

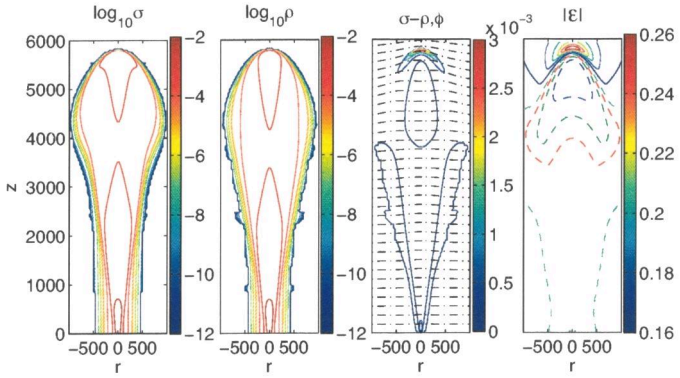

FIGURE 4.7: The non-linear regime for the low field case ($|\boldsymbol{\mathcal{E}}_b| = 0.15$) with homogeneous Neumann boundary conditions at the cathode ($z = 0$). *From left to right*: logarithmic plot of the electron density distribution, logarithmic plot of the ion density distribution, net charge density distribution together with the equipotential lines (dash dotted lines), and electric field strength. The time of the snapshot is $\tau = 2.75 \cdot 10^4$, which corresponds to 82.5 ns for N_2 at atmospheric pressure. The solid lines in the rightmost plot correspond to an enhancement of the background field, the dashed lines to a field strength lower than that of the background field.

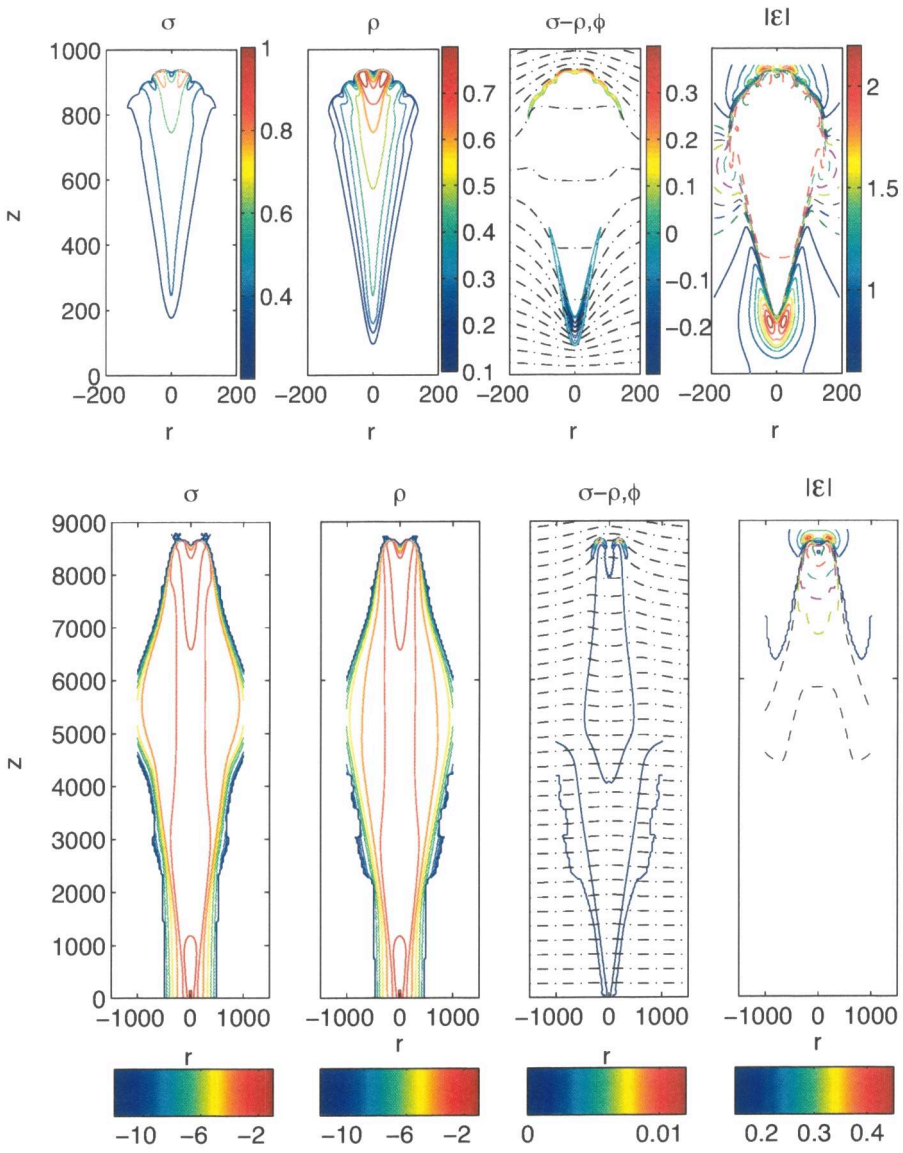

FIGURE 4.9: The branching streamer. *Upper row*: the high field case ($|\boldsymbol{\mathcal{E}}_b| = 0.5$) withDirichlet boundary conditions at the cathode ($z = 0$) at $\tau = 575$, which corresponds to 1.725 ns for N_2 at atmospheric pressure. *Lower row*: the low field case ($|\boldsymbol{\mathcal{E}}_b| = 0.15$) with homogeneous Neumann boundary conditions at the cathode ($z = 0$). The time of the snapshot is $\tau = 33 \cdot 10^4$, which corresponds to 99 ns. *From left to right*: electron density distribution, ion density distribution, net charge density distribution together with the equipotential lines (dash dotted lines), and electric field strength.

5

Diffusion correction to the avalanche–to–streamer transition

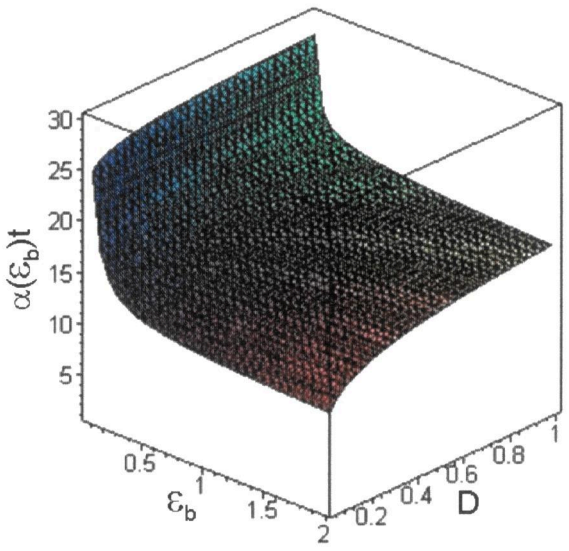

FIGURE 5.1: The transition distance αd according to Eq. (5.4.15) as a function of the background electric field $\mathcal{E}_b$ and the diffusion coefficient D for $\sigma_0 = 10^{-4}$ and $\nu = 0$.

6

Propagating streamers: numerical experiments and predictions

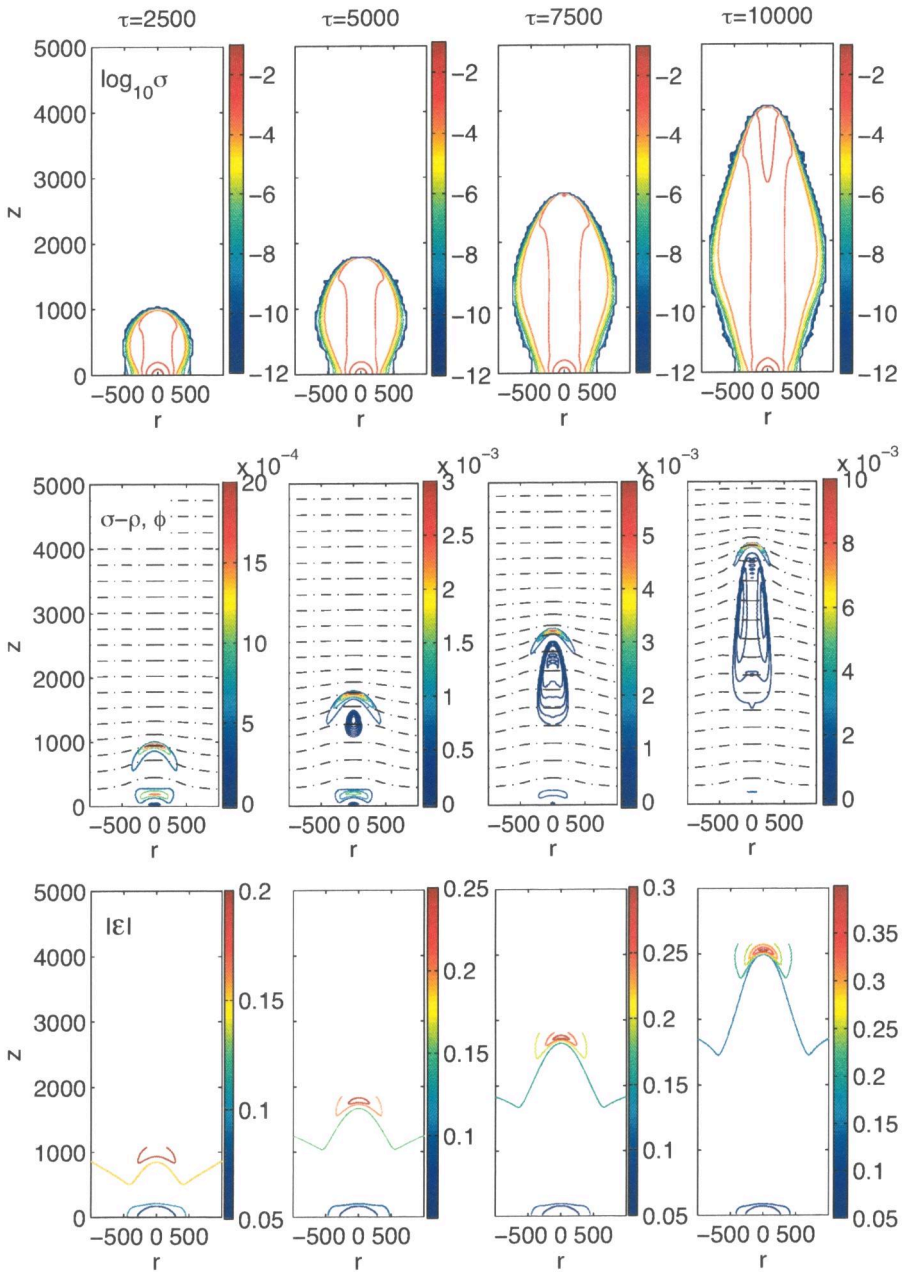

FIGURE 6.1: Evolution of a streamer during the non-linear regime in a low background electric field $|\boldsymbol{\mathcal{E}}_b| = 0.15$. *Upper panel*: logarithm of the electron density. *Middle panel*: net charge density and equipotential (dash dotted) lines. *Lower panel*: electric field strength.

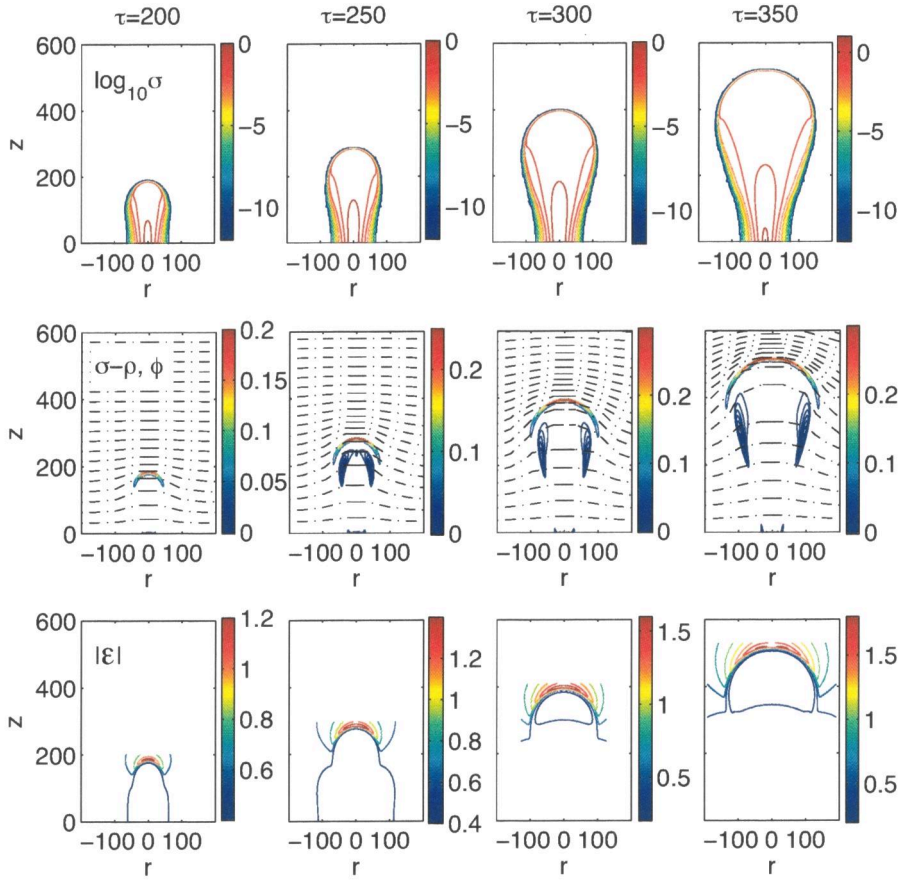

FIGURE 6.4: Evolution of a streamer during the non-linear regime in a high background electric field $|\boldsymbol{\mathcal{E}}_b| = 0.5$. *Upper panel*: logarithm of the electron density. *Middle panel*: net charge density and equipotential lines. *Lower panel*: electric field strength. The results have been obtained using the adaptive grid refinement strategy presented in Chap. 3. The continuity equations are computed on grids with mesh sizes from 2 to 0.125, the Poisson equation on grids with mesh sizes from 128 to 2.

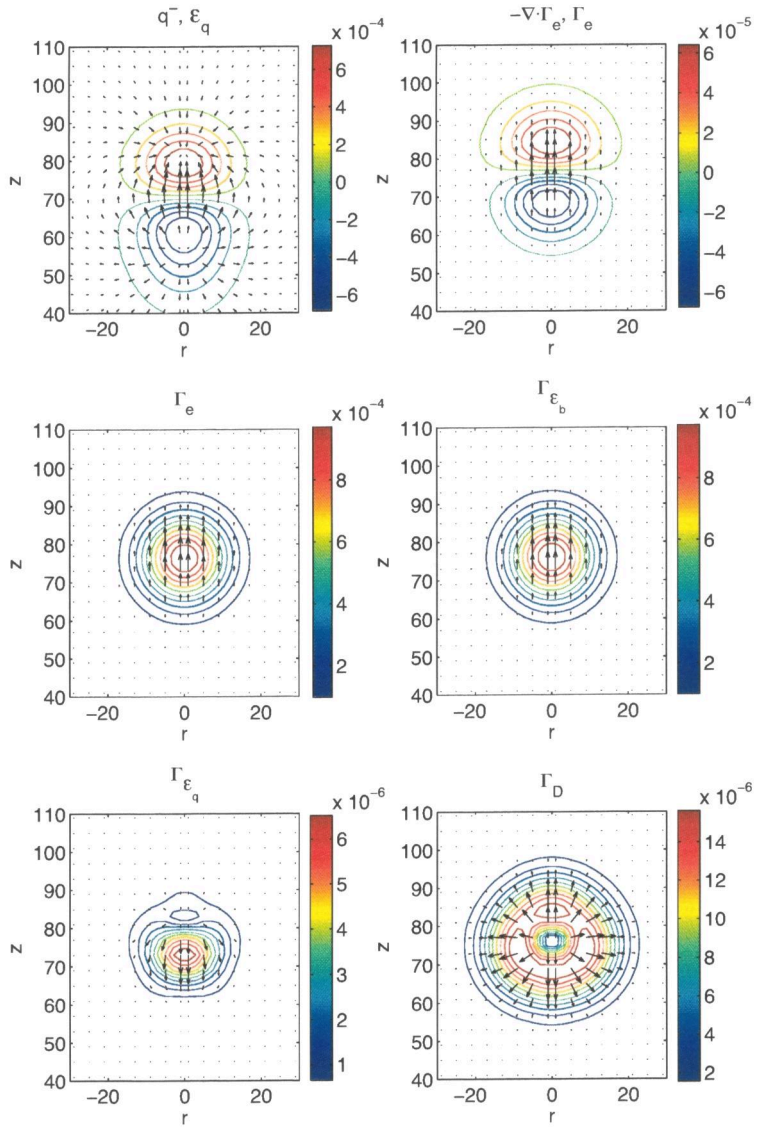

FIGURE 6.10: *Upper row*: net charge density distribution with vector plot of the self field (left) and time derivative of q with vector plots of $\mathbf{\Gamma}_e$ at $\tau = 50$. *Second row*: vector plots and absolute values of the total current density (left) and the contribution of the background field (right). *Lower row*: vector plots and absolute value of the contribution of the self induced field of the space charges to the current densities $-\sigma\boldsymbol{\mathcal{E}}_q$ (left) and of the diffusion $-D\nabla\sigma$ (right).

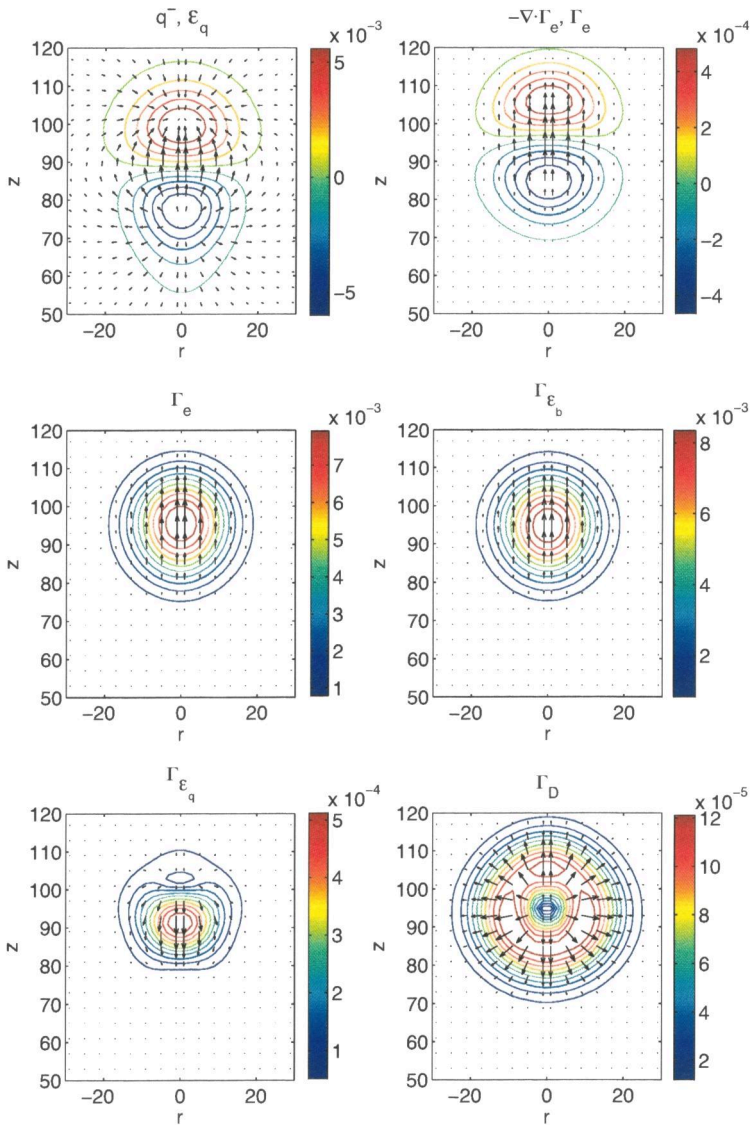

FIGURE 6.11: Same as Fig. 6.9, now for $\tau = 87.5$.

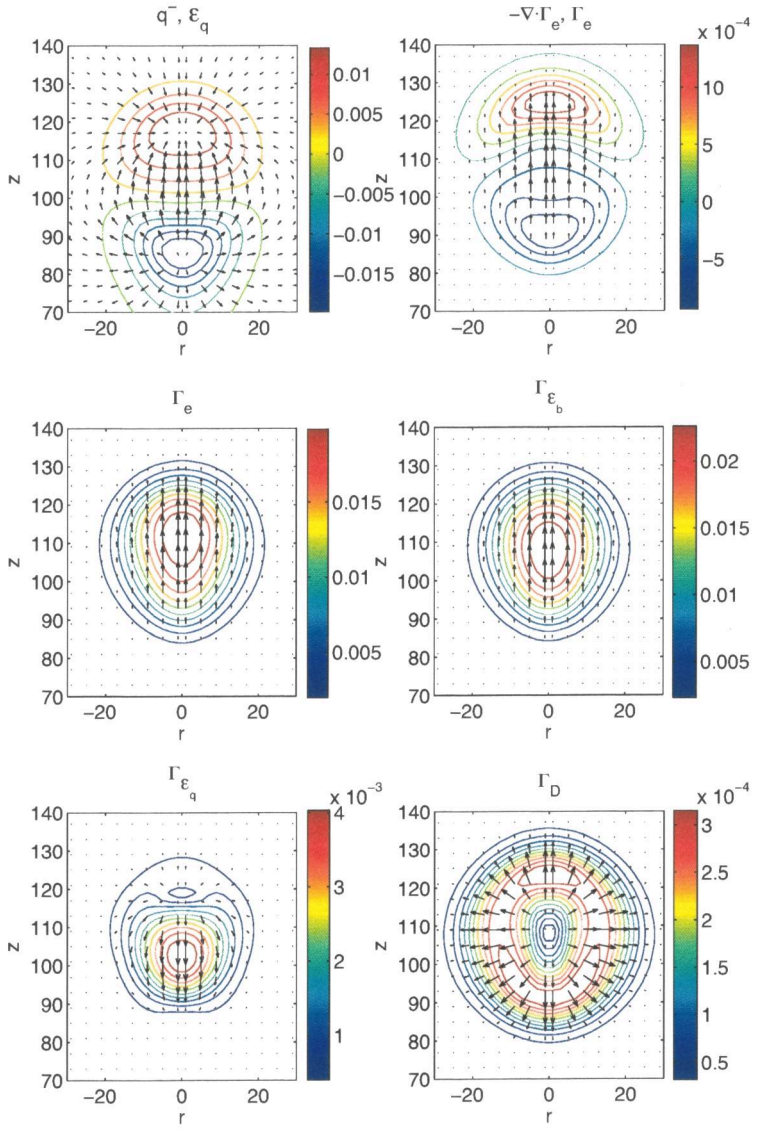

FIGURE 6.12: Same as Fig. 6.9, now for $\tau = 112.5$.

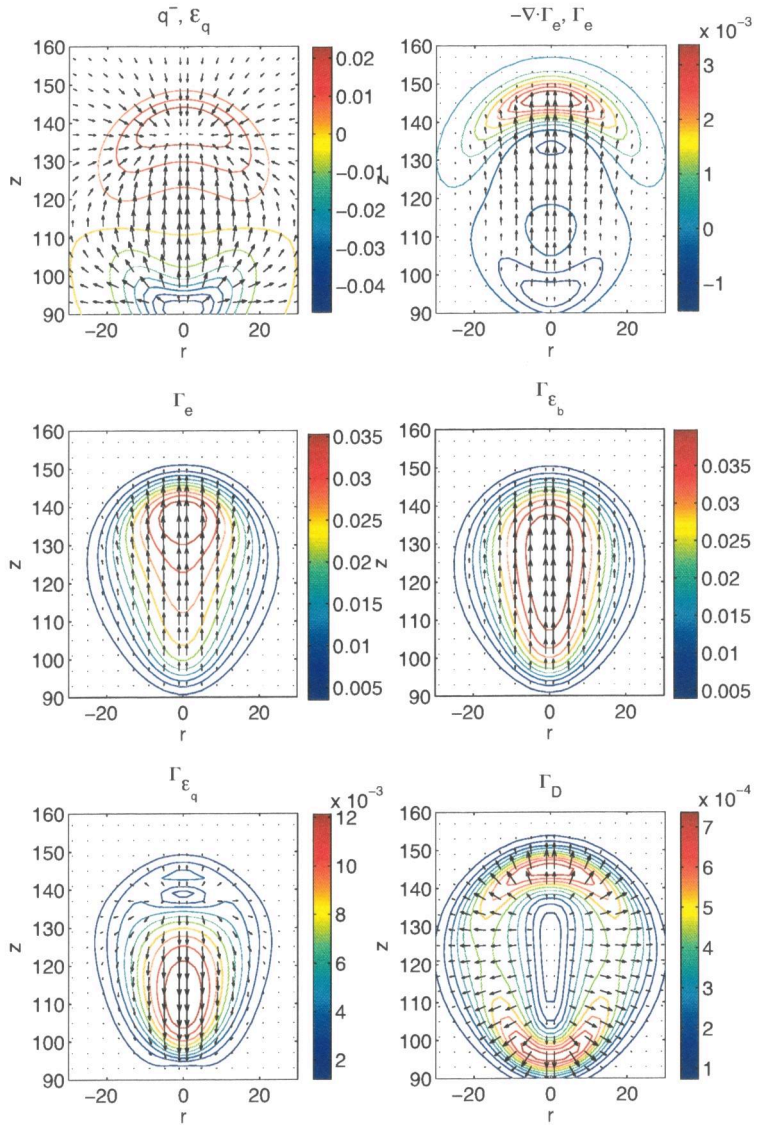

FIGURE 6.13: Same as Fig. 6.9, now for $\tau = 137.5$.

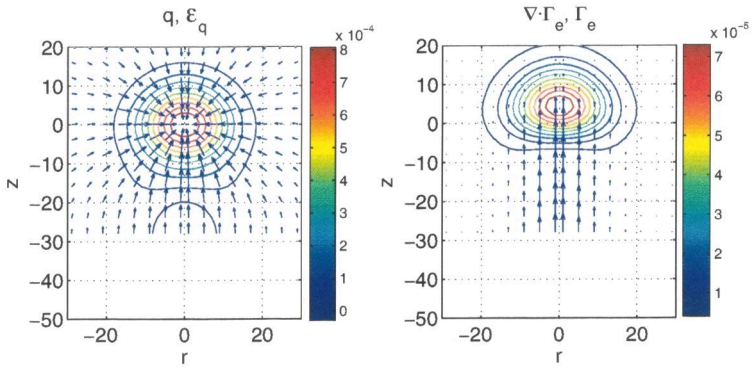

FIGURE 6.16: Net charge density distribution (right) with vector plot of the self induced field (left) at $\tau = 50$, in the case Neumann boundary conditions are used at the cathode.

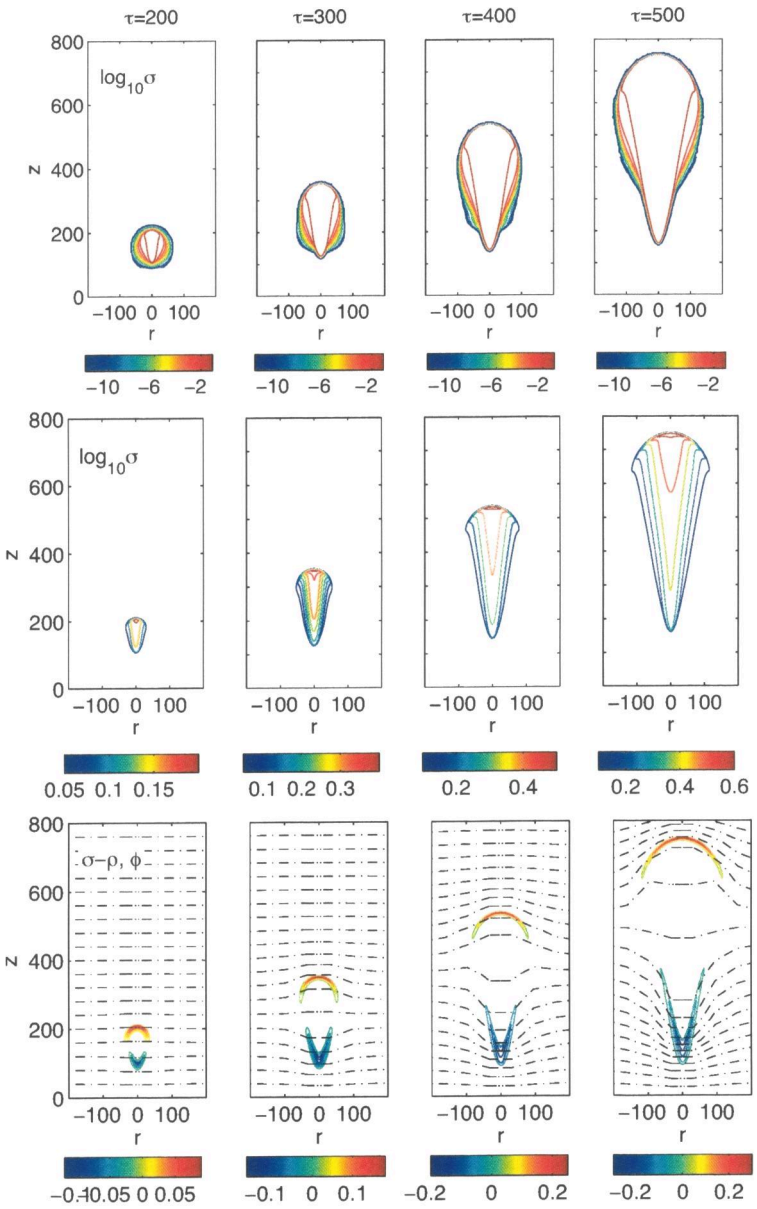

FIGURE 6.17: Evolution of the logarithm of the electron density distribution $\log_{10}\sigma$ (upper panel), the electron density on a linear scale (middle panel) and the net charge density q (lower panel) with Dirichlet conditions at the cathode. The times correspond, from left to right, to τ =200, 300, 400 and 500. The contours for $\log_{10}\sigma$ range from -12 to the maximal value with steps of 1. The contours for q start from zero both towards negative and positive values of q with steps of 0.05.

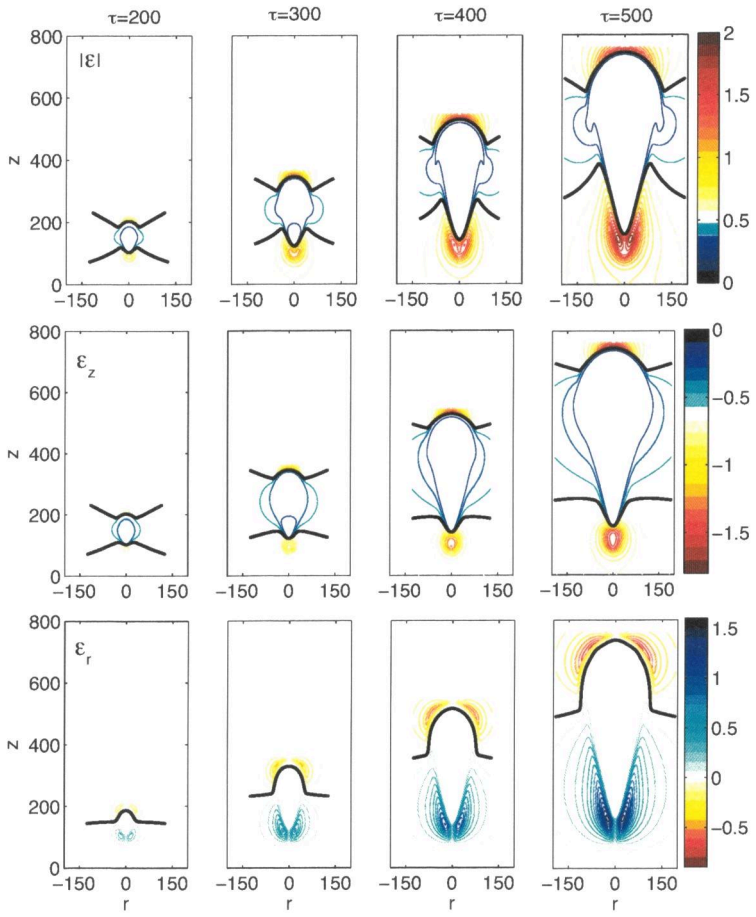

FIGURE 6.18: Evolution of the electric field distribution with Dirichlet conditions at the cathode. *From top to bottom*: electric field strength $|\boldsymbol{\mathcal{E}}|$, axial field component $\mathcal{E}_z$ and radial field component $\mathcal{E}_r$. The times correspond, from left to right, to τ =200, 300, 400 and 500. The thick solid lines correspond to the unperturbed values, i.e. $|\boldsymbol{\mathcal{E}}|$ =0.5, $\mathcal{E}_z = -0.5$ and $\mathcal{E}_r = 0$. The contours for $|\boldsymbol{\mathcal{E}}|$ range from 0 to 2, those for $\mathcal{E}_z$ go from -1.8 to 0 and those for $\mathcal{E}_r$ from -0.9 to 1.6. All field contours are separated by an equal distance of 0.1.

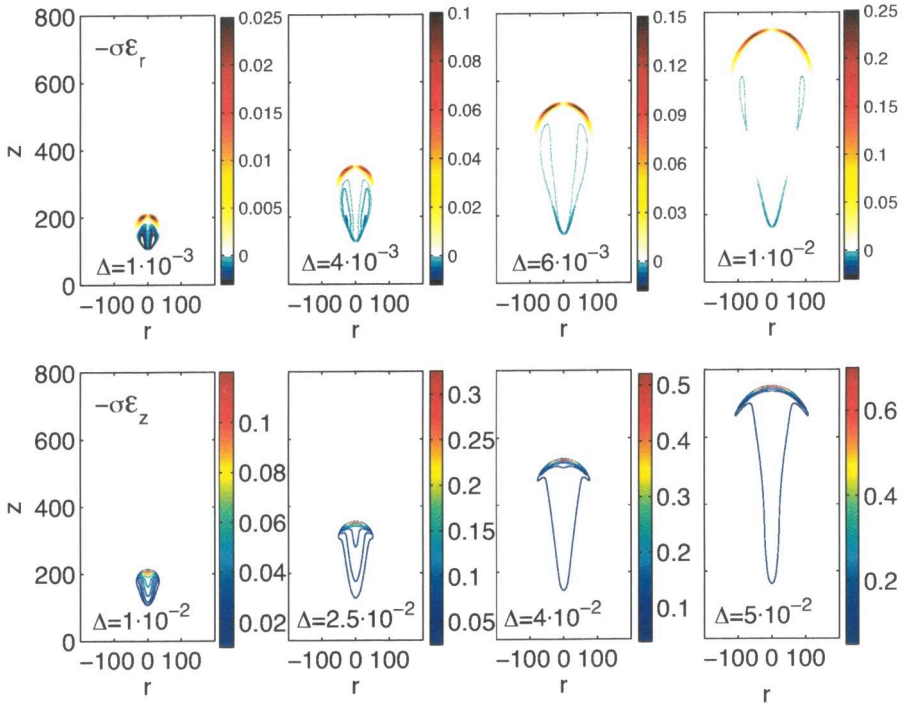

FIGURE 6.20: Distribution of the radial (upper panel) and axial (lower panel) components of the electron current density due to the drift in the total electric field. The snapshots are taken at the same times as those in Figs. 6.17 and 6.16.

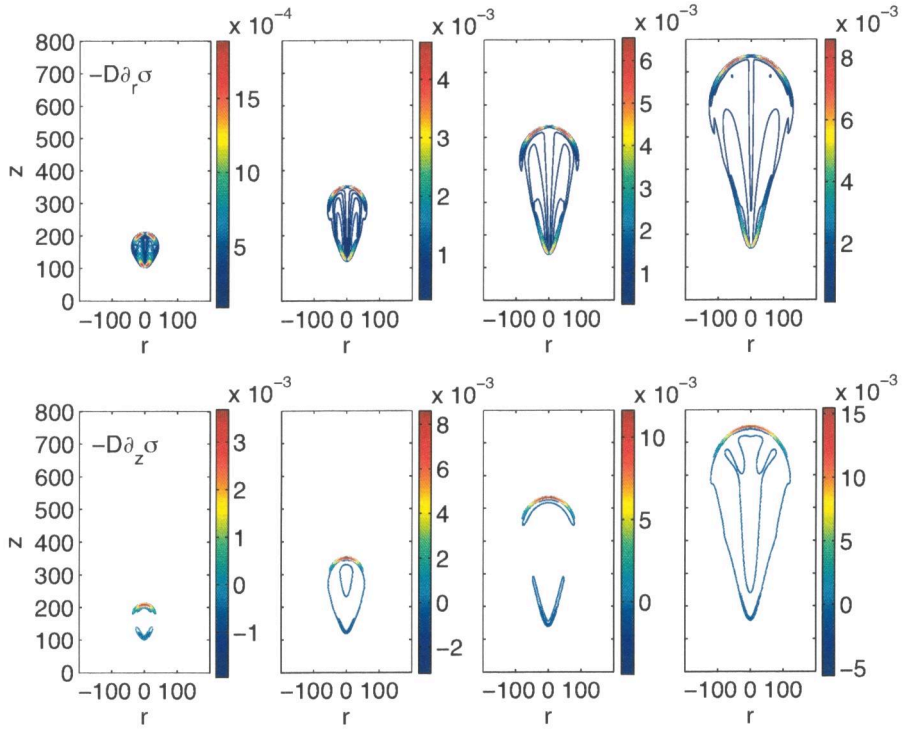

FIGURE 6.21: Distribution of the radial (upper panel) and axial (lower panel) components of the electron current density due to diffusion. The snapshots are taken at the same time as those in Fig. 6.19.

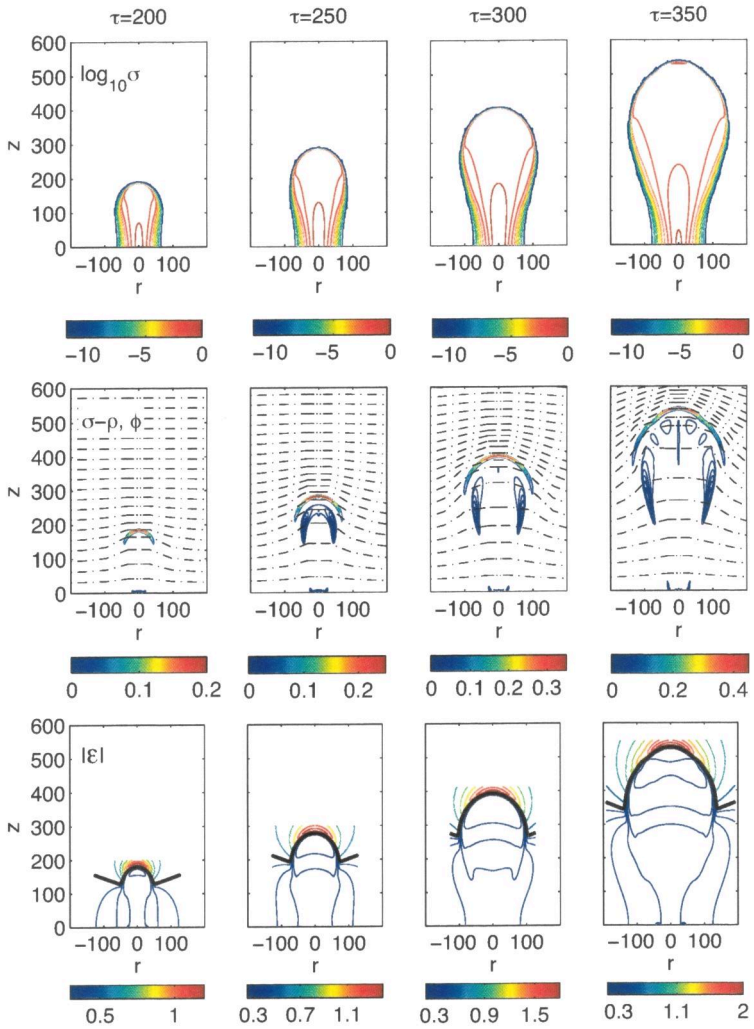

FIGURE 6.23: Evolution of the streamer with Neumann conditions at the cathode. *From top to bottom*: logarithm of the electron density, net charge density and electric field strength $|\boldsymbol{\mathcal{E}}|$. The times correspond, from left to right, to τ =200, 250, 300 and 350. The ranges are the same as for distributions shown in Figs. 6.16 and Figs. 6.17. For clarity, the positively charged region is indicated by the dashed lines in the middlepanel. The thick solid lines in plots for $|\boldsymbol{\mathcal{E}}|$ correspond to the unperturbed value, $|\boldsymbol{\mathcal{E}}|$ =0.5.

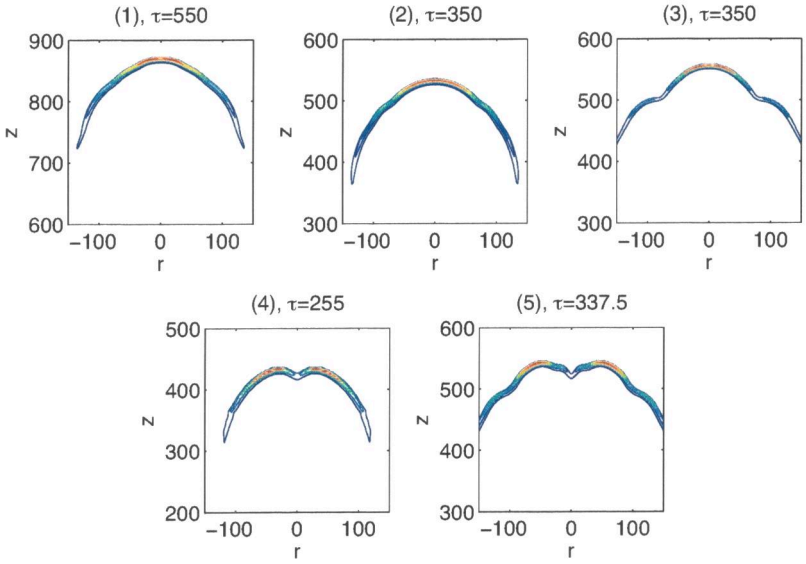

FIGURE 6.26: Net charge density distribution of the streamer head in the unstable regime. The upper three plots show the on-axis branching of cases (1), (2) and (3), the lower panel shows the off-axis branching of cases (4) and (5).

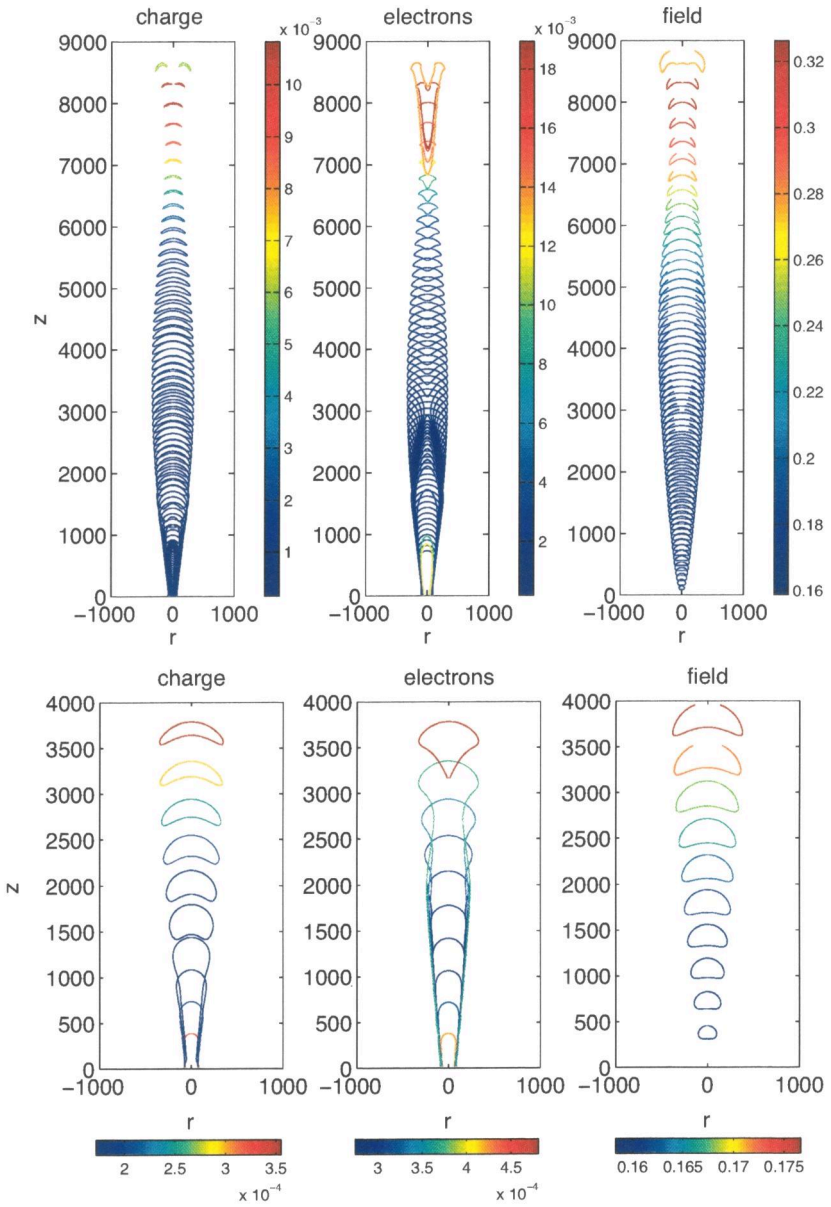

FIGURE 6.28: Evolution of an initial ionization seed in a background field $\mathcal{E}_b = -0.15$, by means of the half maximum contours of the net charge density (left), of the electron density (middle), and of the contours of the electric field defined by the half maximum deviation of the background field (right). The amplitude of the initial seed is σ_0=1./4.7 and its e-folding radius r_b=10. The temporal range covers τ from 0 to $33 \cdot 10^3$, with plotting steps of $5 \cdot 10^2$. The plot on the next page zooms in into the early times of the

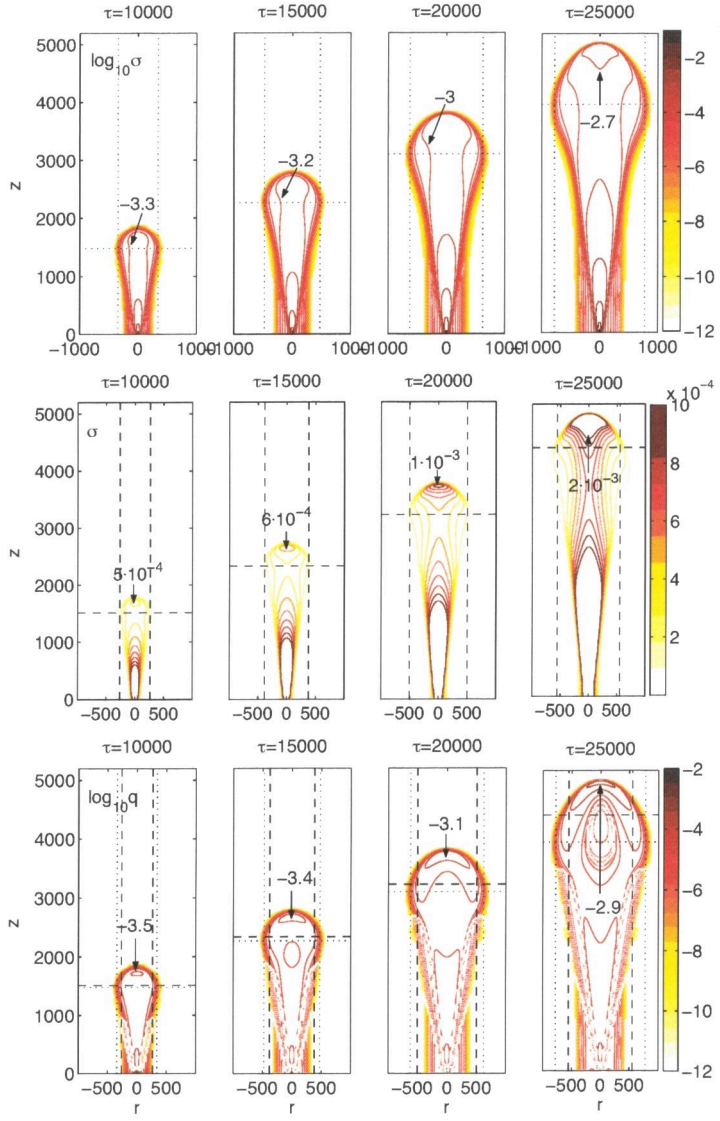

FIGURE 6.30: Expansion phase of an ionization seed in a background field field $\boldsymbol{\mathcal{E}}_b = -0.15\hat{\mathbf{e}}_z$. *Upper panel*: logarithm of the electron density, the dotted lines indicate the position (r_2, z_2) of the maximal radius at which the electron density has dropped to $1/100$ of its axial value. *Middle panel*: electron density , in linear scale, The dashed lines indicate the position (r_1, z_1) of the maximal radius at which the electron density has dropped to $1/e$ of its axial value. *Lower panel*: logarithm of the net charge density distribution, the solid lines indicate negative net charge densities ($q > 0$), the dotted lines positively charged regions. The positions of the maximal radii are also shown in the lower panel. In each figure the maximal value of the corresponding quantity in the streamer head is indicated.

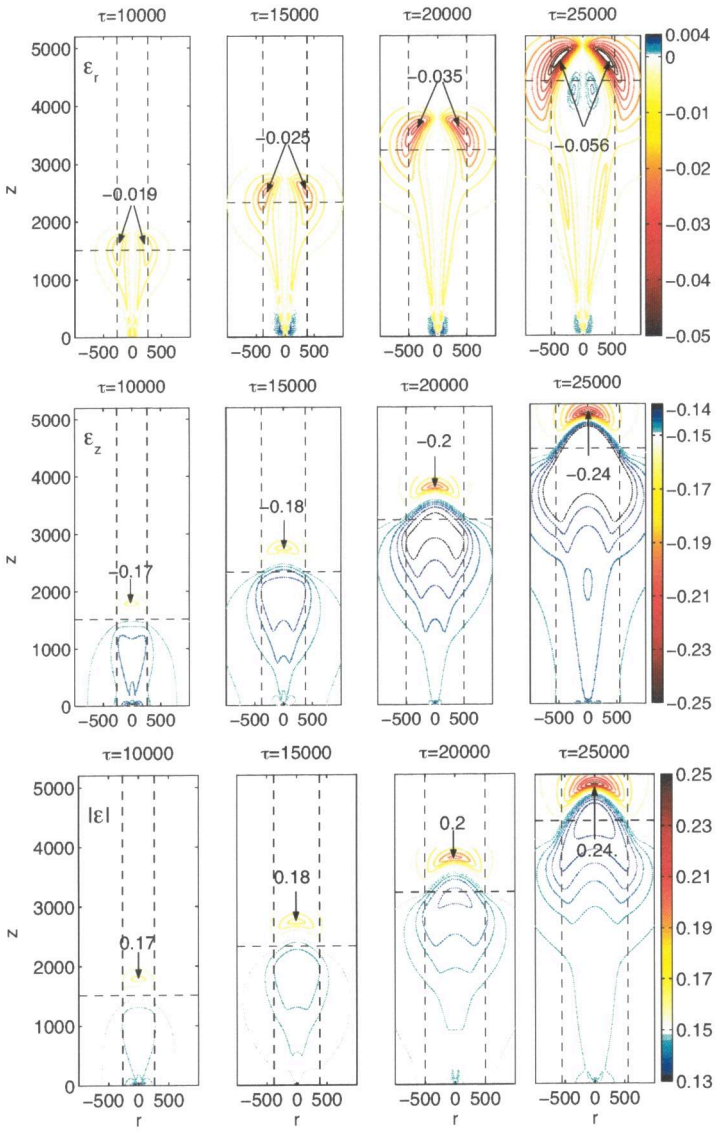

FIGURE 6.34: Electric field distribution during the expansion phase. *Upper panel*: radial component of the electric field. *Middle panel*: axial component of the field. *Lower panel*: electric field strength. The times of the snapshots are the same as in Fig. 6.30. The solid lines correspond to a field enhancement ($\mathcal{E}_r > 0$, $\mathcal{E}_z > -|\boldsymbol{\mathcal{E}}_b|$ and $|\boldsymbol{\mathcal{E}}| > |\boldsymbol{\mathcal{E}}_b|$), the dashed lines to a field reduction.

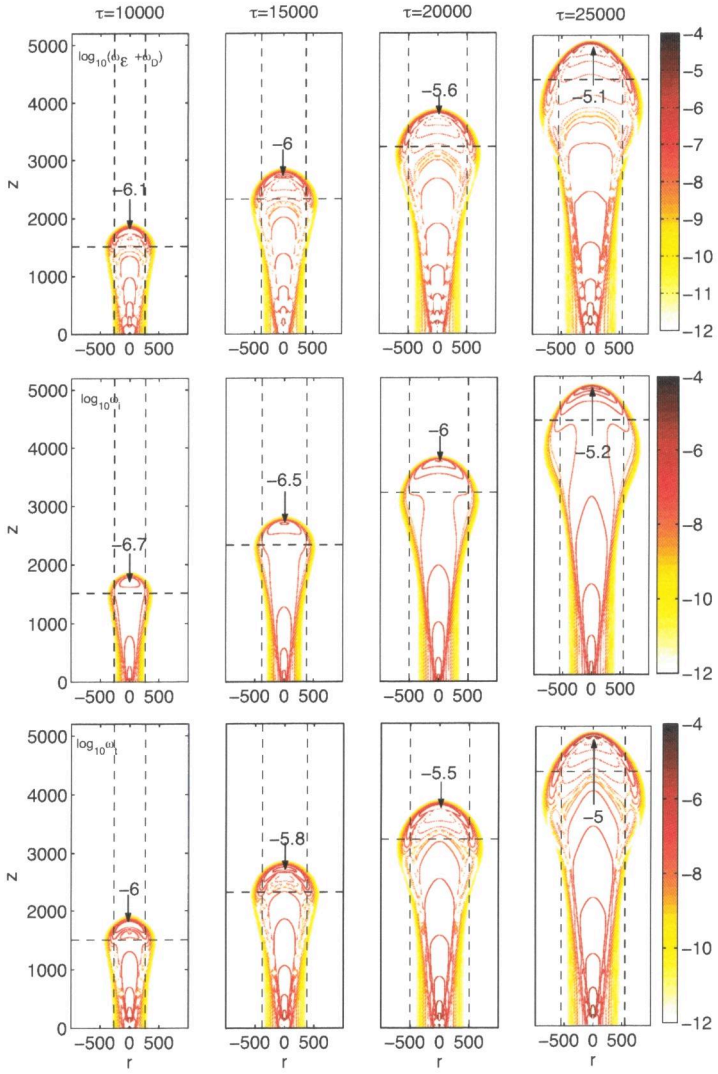

FIGURE 6.35: Logarithmic plot of the contributions of drift, diffusion and impact ionization to the rate of temporal change of the electron density during the expansion phase and the beginning of the contraction phase. *Upper panel*: $\omega_\mathcal{E} + \omega_D$. *Middle panel*: ω_i. *Lower panel*: ω_t. The times of the snapshotsare the same as in the lower panel of Fig. 6.30. The solid lines indicate positive values of the rates, the dotted lines negative values. The dashed lines show the position at which r_1 has been determined.

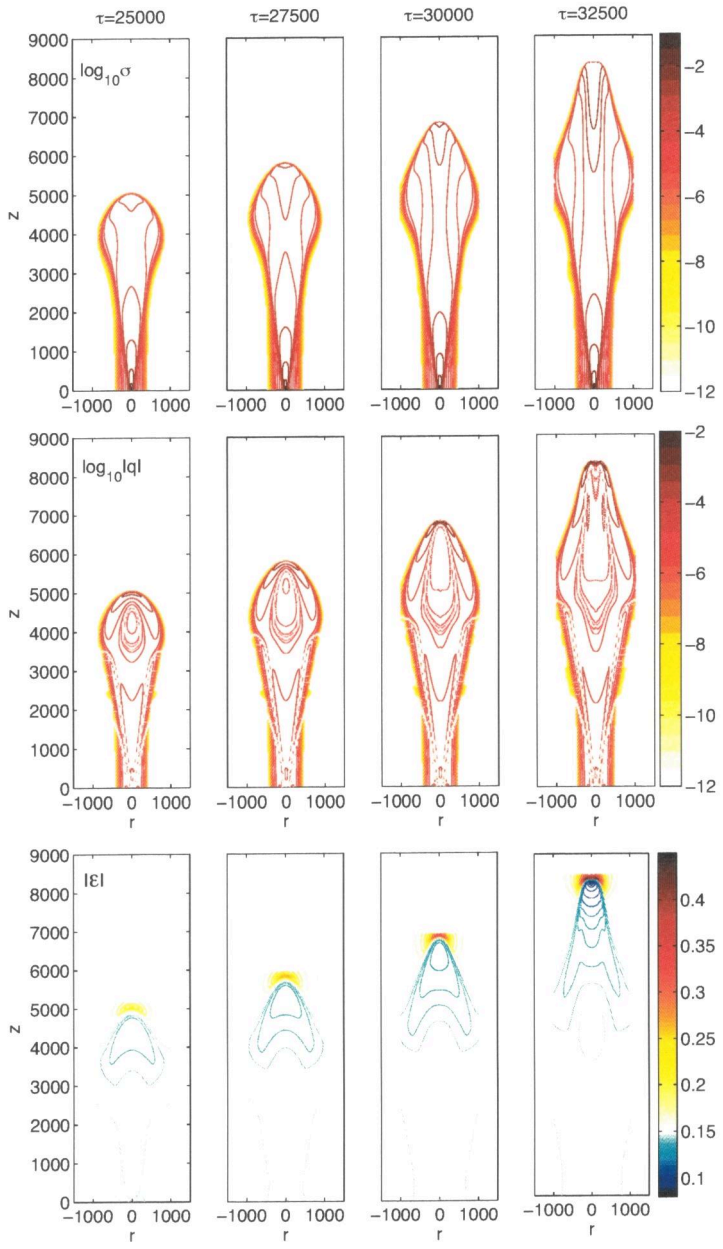

FIGURE 6.37: Logarithm of the electron density distribution (upper panel) and of the net charge density distribution (middle panel) during the contraction phase. The lower panel shows the electric field strength. The dotted lines in the middle panel indicate positively charged regions ($q < 0$). In the lower panel they indicate values of the electric field that are lower than the background electric field.

7

The branching instability of streamers

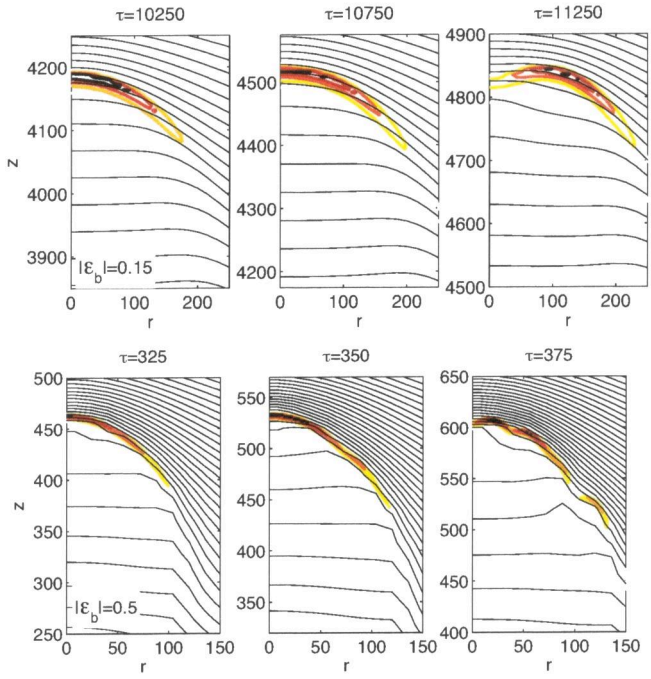

FIGURE 7.1: Enlargement of the streamer tip just before and during branching, in an undervolted gap with $|\boldsymbol{\mathcal{E}}_b|$ =0.15 (upper four plots) and in an overvolted gap $|\boldsymbol{\mathcal{E}}_b|$ =0.5. Both the net charge density distribution (thick lines) and the equipotential (thin) lines are shown. The contour levels for the net charge density are equally spaced with a separation of 0.004 for the low field case, and of 0.16 in the high field case. The equipotential lines are separated by a value of 5 in both cases. For clarity we only show the positive half plane on the r-axis.

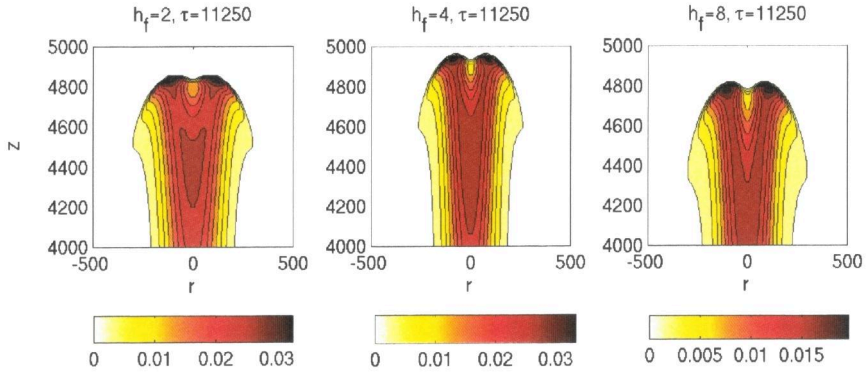

FIGURE 7.6: Electron density distribution in the streamer head just after the occurrence of the instability in a background field $|\boldsymbol{\mathcal{E}}_b|$ =0.15, computed on different finest mesh sizes, h_f =8, 4 and 2, indicated in the title of each plot.

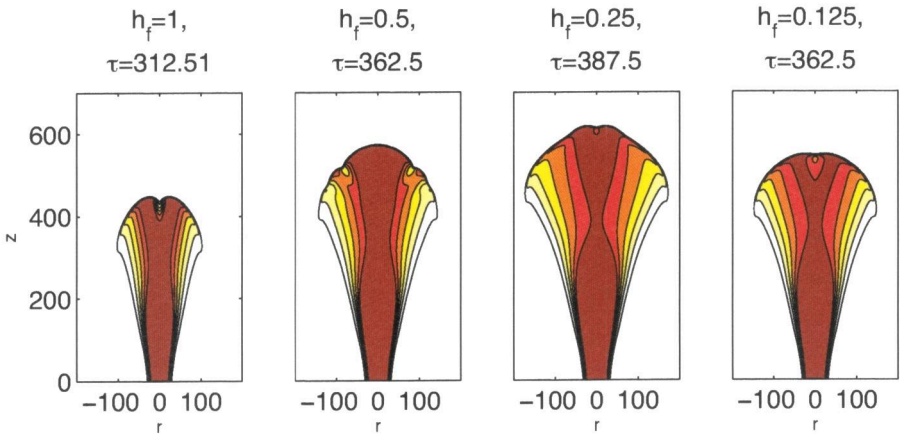

FIGURE 7.9: Electron density distribution just after the instability has occurred in a background field of 0.5, computed with different finest grids, from left to right: h_f =1, 1/2, 1/4 and 1.8.